José A. Ferreira
Sílvia Barbeiro
Gonçalo Pena
Mary F. Wheeler *Editors*

Modelling and Simulation in Fluid Dynamics in Porous Media

Springer

Springer Proceedings in Mathematics & Statistics

Volume 28

For further volumes:
http://www.springer.com/series/10533

Springer Proceedings in Mathematics & Statistics

This book series features volumes composed of select contributions from workshops and conferences in all areas of current research in mathematics and statistics, including OR and optimization. In addition to an overall evaluation of the interest, scientific quality, and timeliness of each proposal at the hands of the publisher, individual contributions are all refereed to the high quality standards of leading journals in the field. Thus, this series provides the research community with well-edited, authoritative reports on developments in the most exciting areas of mathematical and statistical research today.

José A. Ferreira • Sílvia Barbeiro • Gonçalo Pena
Mary F. Wheeler
Editors

Modelling and Simulation in Fluid Dynamics in Porous Media

Springer

Editors
José A. Ferreira
CMUC
Department of Mathematics
University of Coimbra
Coimbra, Portugal

Sílvia Barbeiro
CMUC
Department of Mathematics
University of Coimbra
Coimbra, Portugal

Gonçalo Pena
CMUC
Department of Mathematics
University of Coimbra
Coimbra, Portugal

Mary F. Wheeler
Inst. Computational Engineering
and Sciences (ICES)
University of Texas, Austin
Austin, Texas, USA

ISSN 2194-1009 ISSN 2194-1017 (electronic)
ISBN 978-1-4614-5054-2 ISBN 978-1-4614-5055-9 (eBook)
DOI 10.1007/978-1-4614-5055-9
Springer New York Heidelberg Dordrecht London

Library of Congress Control Number: 2012951311

Mathematics Subject Classification (2010): 11R23, 11S40, 14H52, 14K22, 19B28

Printed on acid-free paper

Springer is part of Springer Science+Business Media (www.springer.com)

Preface

We are pleased to introduce the readers these proceedings containing a selection of papers from invited lectures and contributed talks presented at the Workshop on Fluid Dynamics in Porous Media that was held in Coimbra, Portugal, on September 12–14, 2011.

We believe that the Workshop on Fluid Dynamics in Porous Media was an occasion of inspiration for all participants and helpful for strengthening the links between researchers working in various modeling aspects in porous media.

This book includes research work of international recognized leaders in their respective fields and presents advances in both theory and applications. The contributions are devoted to mathematical modeling, numerical simulation, and their applications. These proceedings provide the readers an overview on the latest findings and new challenges in fluid dynamics in porous media, thus making them appealing to a multidisciplinary audience, including mathematicians, engineers, physicists, and computational scientists.

We express our gratitude to all the authors for their excellent contribution. We also wish to thank the generous collaboration of anonymous reviewers. This book could not have been successfully concluded without their assistance.

We gratefully acknowledge the financial support of UT Austin|Portugal Co-Lab, the Centre of Mathematics of University of Coimbra, Fundação para a Ciência e Tecnologia through European program COMPETE/FEDER, project UTAustin/MAT/0066/2008 "Reaction-Diffusion in Porous Media," and the Department of Mathematics of University of Coimbra. We also thank Springer for agreeing to publish this work, and in particular we express our appreciation for Meredith Rich who assisted us in the edition.

Coimbra, Portugal — José A. Ferreira
Coimbra, Portugal — Sílvia Barbeiro
Coimbra, Portugal — Gonçalo Pena
Austin, TX, USA — Mary F. Wheeler

Contents

Contributors

M.R. Acharya OUAT, Bhubaneswar, India

R. Bouhlila Université de Tunis El-Manar, Tunis, Tunisia

R. Bunoiu LMAM, UMR 7122, Université de Lorraine et CNRS Ile du Saulcy, METZ Cedex 1, France

G. Cardone Department of Engineering, University of Sannio, Corso Garibaldi, Benevento, Italy

F. Civan Mewbourne School of Petroleum and Geological Engineering, The University of Oklahoma, Norman, OK, USA

V.A.F. Costa Departamento de Engenharia Mecânica, Universidade de Aveiro, Aveiro, Portugal

H. Davarzani Université de Toulouse; INPT, UPS; IMFT; Toulouse, France

G. Debenest Université de Toulouse; INPT, UPS; IMFT; Toulouse, France

M. Delshad Petroleum and Geosystems Engineering Department, The University of Texas at Austin, TX, USA

F. Dorai Université de Tunis El-Manar, Tunis, Tunisia

Université de Toulouse; INPT, UPS; IMFT; Toulouse, France

José A. Ferreira CMUC, Department of Mathematics, University of Coimbra, Coimbra, Portugal

V. Girault UPMC–Paris and CNRS, UMR, Paris Cedex 05, France

Department of Mathematics, Texas A&M University, TX, USA

J.-M. Gratien IFP Energies nouvelles, Rueil-Malmaison, France

E. Gudiño CMUC, Department of Mathematics, University of Coimbra, Coimbra, Portugal

G. Kanschat Department of Mathematics, Texas A&M University, TX, USA

X. Kong Petroleum and Geosystems Engineering Department, The University of Texas at Austin, TX, USA

F. Laouafa INERIS, Parc technologique ALATA, Verneuil-en-Halatte, France

H. Luo Université de Toulouse; INPT, UPS; IMFT; Toulouse, France

CNRS IMFT; Toulouse, France

IMFT-GEMP, Toulouse, France

A. Nayak Silicon Institute of Technology, Bhubaneswar, India

P. de Oliveira CMUC, Department of Mathematics, University of Coimbra, Coimbra, Portugal

S. Panda NIT Calicut, Calicut, India

M. Patrício CMUC, Department of Mathematics, University of Coimbra, Coimbra, Portugal

School of Technology and Management, Polytechnic Institute of Leiria, Leiria, Portugal

R. Patrício Active Space Technologies S.A., Coimbra, Portugal

C. Perugia DSBGA, University of Sannio, Benevento, Italy

M. Quintard Université de Toulouse; INPT, UPS; IMFT; Toulouse, France

B. Rivière Department of Computational and Applied Mathematics, Rice University, Houston, TX, USA

E. Sousa CMUC, Department of Mathematics, University of Coimbra, Coimbra, Portugal

A.M. Tartakovsky Pacific Northwest National Laboratory, Richland, WA, USA

D.M. Tartakovsky Department of Mechanical and Aerospace Engineering, University of California, San Diego, CA, USA

P. Wang Pacific Northwest National Laboratory, Richland, WA, USA

M.F. Wheeler Center for Subsurface Modeling, The University of Texas at Austin, TX, USA

On the Coupling of Incompressible Stokes or Navier–Stokes and Darcy Flows Through Porous Media

V. Girault, G. Kanschat, and B. Rivière

Abstract In this chapter, we present the theoretical analysis of coupled incompressible Navier–Stokes (or Stokes) flows and Darcy flows with the Beavers–Joseph–Saffman interface condition. We discuss alternative interface and porous media models. We review some finite element methods used by several authors in this coupling and present numerical experiments.

1 Introduction

Mathematical and numerical modeling of coupled Navier–Stokes (or Stokes) and Darcy flows is a topic of growing interest. Applications include the environmental problem of groundwater contamination through rivers, the problem of flows through vuggy or fractured porous media, the industrial manufacturing of filters, and the biological modeling of the coupled circulatory system with the surrounding tissue. The most widely used coupling model is based on either the Beavers–Joseph or the simpler Beavers–Joseph–Saffman interface conditions. The Beavers–Joseph condition [9], which is a Navier-type slip with a friction

V. Girault (✉)
UPMC–Paris 6 and CNRS, UMR 7598, F-75230 Paris Cedex 05, France

Department of Mathematics, Texas A&M University, College Station, TX 77843, USA
e-mail: girault@ann.jussieu.fr

G. Kanschat
Department of Mathematics, Texas A&M University, College Station, TX 77843, USA
e-mail: kanschat@tamu.edu

B. Rivière
Department of Computational and Applied Mathematics, Rice University,
Houston, TX 77005, USA
e-mail: riviere@caam.rice.edu

J.A. Ferreira et al. (eds.), *Modelling and Simulation in Fluid Dynamics in Porous Media*,
Springer Proceedings in Mathematics & Statistics 28, DOI 10.1007/978-1-4614-5055-9_1,

condition involving the interaction between the tangential velocities at the interface, was derived experimentally in 1967. In 1971, it was simplified by Saffman [53] who, observing that usually the flow in the pores is negligible with respect to the free flow, replaced the difference in these two velocities by just the free flow velocity. In 2000, via homogenization arguments, the Beavers–Joseph–Saffman model was recovered by Jäger and Mikelić [36–38], Jäger et al. [39]. Since then the theoretical and numerical coupling of Stokes and Darcy flows has been addressed by many authors with a variety of settings ranging from a primal formulation in the Stokes region and either an $\boldsymbol{H}(\mathrm{div})$ formulation or a primal formulation in the Darcy region to a fully mixed formulation in both regions. Without being exhaustive, we refer to [5, 6, 12, 22–29, 34, 42, 44, 47, 48, 51, 55]. For instance, well-posedness of the coupled problem was established by Layton et al. in [44]; the authors used continuous finite elements in the Stokes region, $\boldsymbol{H}(\mathrm{div})$ elements in the Darcy region, and coupled both regions with a mortar. Rivière and Yotov in [51] and Gatica et al. in [29] proposed a primal formulation in the Stokes region coupled with a dual formulation in the Darcy region. Discacciati et al. proposed a primal formulation in both regions; see for example [24]. In [28], Gatica et al. analyzed a fully mixed formulation in both regions, introducing the deformation tensor in the Stokes subdomain. Finally, Arbogast and Brunson in [6] use a finite element formulation with continuity requirements changing between $\boldsymbol{H}^1$ and $\boldsymbol{H}(\mathrm{div})$ as needed.

In contrast, there exists much less literature on the coupling of Navier–Stokes and Darcy flows. The readers can refer to [8, 15, 16, 32]. And finally, there exists some work on Stokes–Darcy flows coupled with the Beavers–Joseph interface condition. Albeit linear, this last problem is harder to formulate rigorously because the Darcy velocity lacks regularity at the interface; see the work of Cao et al. in [14].

Although this review focuses on the use of the Beavers–Joseph–Saffman condition to model coupled Navier–Stokes and Darcy flows, it also describes the approach of various authors in coupling Darcy or Brinkman and Stokes flows that can be easily extended to the nonlinear situation of the Navier–Stokes free flow.

2 Theoretical Analysis

2.1 Coupled Navier–Stokes and Darcy Systems

To simplify the discussion, we consider the three-dimensional problem; the two-dimensional problem is treated in the same fashion.

Let Ω be a bounded, connected Lipschitz domain of $\mathbb{R}^3$, with boundary $\partial\Omega$ and exterior unit normal vector $\boldsymbol{n}$, partitioned into two nonoverlapping regions: a porous region Ω_2 and a free fluid region Ω_1, both assumed to be Lipschitz continuous

$$\overline{\Omega} = \overline{\Omega}_1 \cup \overline{\Omega}_2.$$

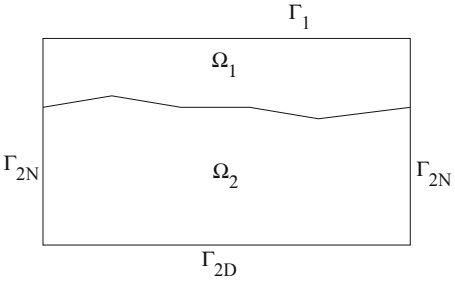

Fig. 1 Problem setting

To simplify, we assume that each region is connected as in Fig. 1, but the analysis presented in this first part easily extends to regions with several connected components. Let $\Gamma_1 = \partial\Omega_1 \cap \partial\Omega$ denote the exterior boundary of the fluid region, $\Gamma_2 = \partial\Omega_2 \cap \partial\Omega$, the exterior boundary of the porous region, and $\Gamma_{12} = \partial\Omega_1 \cap \partial\Omega_2$, the interface between the two regions. Since we are in $\mathbb{R}^3$, we also assume that the surfaces Γ_1, Γ_2, and Γ_{12} have Lipschitz continuous boundaries.

In the fluid region Ω_1, the constitutive equation for the Cauchy stress tensor $\boldsymbol{T}$ is

$$\boldsymbol{T}(\boldsymbol{u}_1, p_1) = 2\mu \boldsymbol{D}(\boldsymbol{u}_1) - p_1 \boldsymbol{I}, \tag{1}$$

where $\boldsymbol{u}_1$ is the fluid velocity, $\boldsymbol{D}(\boldsymbol{u}_1) = \frac{1}{2}\left(\nabla \boldsymbol{u}_1 + \nabla \boldsymbol{u}_1^T\right)$ is the symmetric gradient or deformation tensor, p_1 is the fluid pressure, $\boldsymbol{I}$ is the identity tensor, and $\mu > 0$ is the fluid viscosity. When substituted into the balance of linear momentum, after dividing by the constant density (keeping the same notation for the kinematic viscosity and pressure) and assuming that the flow has reached a steady state, we obtain the steady Navier–Stokes system

$$-\operatorname{div}(2\mu \boldsymbol{D}(\boldsymbol{u}_1) - p_1 \boldsymbol{I}) + \boldsymbol{u}_1 \cdot \nabla \boldsymbol{u}_1 = \boldsymbol{f}_1 \quad \text{in } \Omega_1, \tag{2}$$

where $\boldsymbol{f}_1$ is a density of fluid body forces. The conservation of mass and constant density give the incompressibility condition

$$\operatorname{div} \boldsymbol{u}_1 = 0 \quad \text{in } \Omega_1. \tag{3}$$

In the porous region Ω_2, we assume that the fluid flow is laminar; we neglect the inertial effects in the fluid and only consider friction between the pores and the fluid. By neglecting also gravity, for simplicity, this gives the Darcy law:

$$\boldsymbol{u}_2 = -\boldsymbol{K}\nabla p_2, \ \operatorname{div} \boldsymbol{u}_2 = f_2 \quad \text{in } \Omega_2, \tag{4}$$

which in divergence form reads

$$-\operatorname{div}(\boldsymbol{K}\nabla p_2) = f_2 \quad \text{in } \Omega_2, \tag{5}$$

where $\boldsymbol{u}_2$ is the fluid velocity, p_2 and the pore pressure, f_2 is a source or sink term, and $\boldsymbol{K}$ the permeability tensor divided by the viscosity, i.e.,

$$\boldsymbol{K} = \frac{\hat{\boldsymbol{K}}}{\mu},$$

with $\hat{\boldsymbol{K}}$ the intrinsic permeability. We assume that $\boldsymbol{K}$ is bounded, symmetric, and uniformly definite. When the constant gravity g is included, the relation between the velocity and pressure is expressed by

$$\boldsymbol{u}_2 = -\boldsymbol{K}\nabla(p_2 - \rho g z),$$

where $\rho > 0$ is the constant density and z is the height.

For the interface equations, let $\boldsymbol{n}_{12}$ denote the unit normal to Γ_{12} pointing in Ω_2 and $\{\boldsymbol{t}_{12}^1, \boldsymbol{t}_{12}^2\}$ an orthonormal basis on the tangent plane to Γ_{12}. The incompressibility of the fluid implies continuity of the normal velocity :

$$\boldsymbol{u}_1 \cdot \boldsymbol{n}_{12} = \boldsymbol{u}_2 \cdot \boldsymbol{n}_{12} = -\boldsymbol{K}\nabla p_2 \cdot \boldsymbol{n}_{12}. \tag{6}$$

If Γ_{12} were a permeable boundary with no porous medium beyond, (6) could be complemented by $\boldsymbol{u}_1 \cdot \boldsymbol{t}_{12}^j = 0$, $j = 1,2$. But at the interface between a fluid and a porous medium, we need conditions on the traction vector $\boldsymbol{T}\boldsymbol{n}$. The first condition is the balance of normal stresses:

$$p_2 = (\boldsymbol{T}\boldsymbol{n}_{12}) \cdot \boldsymbol{n}_{12} = ((-2\mu \boldsymbol{D}(\boldsymbol{u}_1) + p_1 \boldsymbol{I})\boldsymbol{n}_{12}) \cdot \boldsymbol{n}_{12}. \tag{7}$$

For the second condition, Beavers and Joseph [9] postulated by experiment in 1967,

$$(\boldsymbol{u}_1 - \boldsymbol{u}_2) \cdot \boldsymbol{t}_{12}^j = -G^j (\boldsymbol{T}\boldsymbol{n}_{12}) \cdot \boldsymbol{t}_{12}^j = -2\mu G^j (\boldsymbol{D}(\boldsymbol{u}_1)\boldsymbol{n}_{12}) \cdot \boldsymbol{t}_{12}^j, \ j = 1,2, \tag{8}$$

where

$$G^j = \frac{1}{\alpha} \sqrt{\frac{(\boldsymbol{K}\boldsymbol{t}_{12}^j, \boldsymbol{t}_{12}^j)}{\mu}}, \ j = 1,2, \tag{9}$$

and $\alpha > 0$ is a dimensionless constant depending on the structure of the porous medium. These are the Beavers–Joseph interface conditions. But Saffman [53], observing that $\boldsymbol{u}_2$ is often negligible with respect to $\boldsymbol{u}_1$, proposed in 1971 to replace (8) by the simpler Navier-type condition:

$$\boldsymbol{u}_1 \cdot \boldsymbol{t}_{12}^j = -2\mu G^j (\boldsymbol{D}(\boldsymbol{u}_1)\boldsymbol{n}_{12}) \cdot \boldsymbol{t}_{12}^j, \ j = 1,2. \tag{10}$$

These are the Beavers–Joseph–Saffman interface conditions; see also the references by Jäger and Mikelić [37, 38], for a derivation of these conditions by homogenization.

By eliminating the Darcy velocity and thus suppressing the index on $\boldsymbol{u}$, we obtain the following system of equations:

$$\left\{\begin{array}{r} -2\mu\,\mathrm{div}\,\boldsymbol{D}(\boldsymbol{u})+\boldsymbol{u}\cdot\nabla\boldsymbol{u}+\nabla p_1=\boldsymbol{f}_1 \\ \mathrm{div}\,\boldsymbol{u}=0 \end{array}\right\} \quad \text{in } \Omega_1, \tag{11}$$

$$-\mathrm{div}\big(\boldsymbol{K}\nabla p_2\big)=f_2 \quad \text{in } \Omega_2, \tag{12}$$

$$\left\{\begin{array}{r} \boldsymbol{u}\cdot\boldsymbol{n}_{12}=-\boldsymbol{K}\nabla p_2\cdot\boldsymbol{n}_{12} \\ -2\mu\displaystyle\sum_{j=1}^{2} G^j\big(\boldsymbol{D}(\boldsymbol{u})\boldsymbol{n}_{12}\big)\cdot\boldsymbol{t}_{12}^j=\sum_{j=1}^{2}\boldsymbol{u}\cdot\boldsymbol{t}_{12}^j \\ \big((-2\mu\boldsymbol{D}(\boldsymbol{u})+p_1\boldsymbol{I})\boldsymbol{n}_{12}\big)\cdot\boldsymbol{n}_{12}=p_2 \end{array}\right\} \quad \text{on } \Gamma_{12}. \tag{13}$$

Since we are mainly interested in the coupling, we choose simple exterior boundary conditions; we split Γ_2 into two parts Γ_{2D} and Γ_{2N}, as in Fig. 1, and we prescribe for example:

$$\begin{aligned} \boldsymbol{u}&=\boldsymbol{0} \quad \text{on } \Gamma_1, \\ p_2&=0 \quad \text{on}\,\Gamma_{2D}, \\ (\boldsymbol{K}\nabla p_2)\cdot\boldsymbol{n}_2&=0 \quad \text{on } \Gamma_{2N}. \end{aligned} \tag{14}$$

Here we assume that $|\Gamma_{2D}|>0$; otherwise, the source f_2 must satisfy the solvability condition:

$$\int_{\Omega_2} f_2\,d\boldsymbol{x}=0. \tag{15}$$

Also, since we assume that $\boldsymbol{K}$ is bounded, symmetric, and uniformly positive definite, we denote by $\lambda_{\min}>0$ and $\lambda_{\max}>0$ its extreme eigenvalues:

$$\forall\boldsymbol{x}\in\Omega_1,\forall\boldsymbol{\chi}\in\mathbb{R}^3,\ \lambda_{\min}|\boldsymbol{\chi}|^2\le\boldsymbol{K}(\boldsymbol{x})\boldsymbol{\chi}\cdot\boldsymbol{\chi}\le\lambda_{\max}|\boldsymbol{\chi}|^2, \tag{16}$$

where $|\cdot|$ denotes the Euclidean vector norm.

2.2 Challenges

This coupled problem is challenging, even without the nonlinear convection term. The first difficulty lies in the meaning to be given to the interface conditions involving the traction vector $\boldsymbol{T}\boldsymbol{n}$ when the interface is not a smooth curve. The next difficulty arises from the nonlinear term: the interface conditions do not eliminate it

from the energy balance. Finally, the numerical implementation of its discretization is problematic because the system is usually large and has different time scales and space scales in each subdomain, whence the necessity of decoupling algorithms.

2.3 Meaning of the Interface Conditions

Consider the following spaces for the data: $\boldsymbol{f}_1 \in \boldsymbol{L}^2(\Omega_1)$, $f_2 \in L^2(\Omega_2)$, and assume for the moment that a solution $(\boldsymbol{u}, p_1, p_2)$ exists. It follows easily by inspection that a reasonable choice of spaces for the solution is $\boldsymbol{u} \in \boldsymbol{H}^1(\Omega_1)$, $p_1 \in L^2(\Omega_1)$, and $p_2 \in H^1(\Omega_2)$.

Let us start with the simpler situation of the Darcy equations in Ω_2. The facts that p_2 belongs to $H^1(\Omega_2)$ and $\boldsymbol{K}$ is uniformly bounded imply that $\boldsymbol{K}\nabla p_2$ belongs to $\boldsymbol{L}^2(\Omega_2)$. Then the fact that f_2 belongs to $L^2(\Omega_2)$ and equation (12) imply that $\boldsymbol{K}\nabla p_2$ is in $\boldsymbol{H}(\mathrm{div};\Omega_2)$, where for any domain Ω,

$$\boldsymbol{H}(\mathrm{div};\Omega) = \{\boldsymbol{v} \in \boldsymbol{L}^2(\Omega);\, \mathrm{div}\,\boldsymbol{v} \in L^2(\Omega)\}.$$

Therefore $\boldsymbol{K}\nabla p_2 \cdot \boldsymbol{n}$ is in $H^{-1/2}(\partial\Omega_2)$, the normal trace space of $\boldsymbol{H}(\mathrm{div};\Omega_2)$; it is the dual space of $H^{1/2}(\partial\Omega_2)$, which in turn is the trace space of $H^1(\Omega_2)$; see [31]. In particular, $(\boldsymbol{K}\nabla p_2)\cdot\boldsymbol{n}_{12}$ is in $\big(H_{00}^{1/2}(\Gamma_{12})\big)'$, the dual space of $H_{00}^{1/2}(\Gamma_{12})$, where $H_{00}^{1/2}(\Gamma_{12})$ is the trace space of functions v in $H^1(\Omega_2)$ that vanish on portions of Γ_2 adjacent to Γ_{12}; see [46]. Hence $(\boldsymbol{K}\nabla p_2)\cdot\boldsymbol{n}_{12}$ is well defined in a weak space. On the other hand, since $\boldsymbol{u}$ is in $\boldsymbol{H}^1(\Omega_1)$, then its trace is in $\boldsymbol{H}^{1/2}(\Gamma_{12})$. Thus Sobolev's imbeddings imply that $\boldsymbol{u}\cdot\boldsymbol{n}_{12}$ is in $L^4(\Gamma_{12})$; see [1]. Therefore the equation on Γ_{12}

$$-\boldsymbol{K}\nabla p_2 \cdot \boldsymbol{n}_{12} = \boldsymbol{u}\cdot\boldsymbol{n}_{12}$$

makes sense and implies that $-\boldsymbol{K}\nabla p_2\cdot\boldsymbol{n}_{12}$ belongs in fact to $L^4(\Gamma_{12})$.

Now we turn to the Navier–Stokes equations in Ω_1. Since $\boldsymbol{u}$ belongs to $\boldsymbol{H}^1(\Omega_1)$ and p_1 to $L^2(\Omega_1)$, then $\boldsymbol{T}(\boldsymbol{u}, p_1)$ is in $\boldsymbol{L}^2(\Omega_1)$ and $\boldsymbol{u}\cdot\nabla\boldsymbol{u}$ belongs to $\boldsymbol{L}^{3/2}(\Omega_1)$. Therefore it follows from (11) that $\boldsymbol{T}$ is in $\boldsymbol{H}^{2,3/2}(\mathrm{div};\Omega_1)$, where

$$\boldsymbol{H}^{2,3/2}(\mathrm{div};\Omega_1) = \{\boldsymbol{v} \in \boldsymbol{L}^2(\Omega_1);\, \mathrm{div}\,\boldsymbol{v} \in L^{3/2}(\Omega_1)\}.$$

As the smooth functions are dense in $\boldsymbol{H}^{2,3/2}(\mathrm{div};\Omega_1)$, then the following Green's formula holds:

$$\forall\varphi \in H^1(\Omega_1), (\mathrm{div}\,\boldsymbol{v},\varphi) + (\boldsymbol{v},\nabla\varphi) = \langle \boldsymbol{v}\cdot\boldsymbol{n},\varphi\rangle_{\partial\Omega_1}.$$

This implies that $\boldsymbol{T}\boldsymbol{n}_{12}$ is well defined as an element of $\big(\boldsymbol{H}_{00}^{1/2}(\Gamma_{12})\big)'$, but if Γ_{12} has corners, the normal and tangent vectors have jumps, and the pairings $\langle \boldsymbol{T}\boldsymbol{n}_{12}, \boldsymbol{n}_{12}\rangle$ and

$\langle \boldsymbol{T}\boldsymbol{n}_{12}, \boldsymbol{t}_{12}^j \rangle$ are not defined. This difficulty can be bypassed by prescribing the last two conditions in (13) simultaneously as a single condition, instead of separately; see [32]. Indeed, set

$$\boldsymbol{g} = p_2 \boldsymbol{n}_{12} + \sum_{j=1}^{2} \frac{1}{G^j} \left(\boldsymbol{u} \cdot \boldsymbol{t}_{12}^j \right) \boldsymbol{t}_{12}^j;$$

it is easy to check that $\boldsymbol{g}$ belongs to $\boldsymbol{L}^4(\Gamma_{12})$. Since $\boldsymbol{T}\boldsymbol{n}_{12}$ is well defined, albeit in a weak space, we can prescribe on Γ_{12}:

$$\boldsymbol{T}\boldsymbol{n}_{12} = \boldsymbol{g}.$$

This condition makes sense and implies that $\boldsymbol{T}\boldsymbol{n}_{12}$ is in fact in $\boldsymbol{L}^4(\Gamma_{12})$. Then this extra regularity allows to define the above pairings and we recover the last two conditions in (13).

2.4 Variational Formulations

The boundary conditions (14) suggest that we take $\boldsymbol{u}$ and the velocity test functions in

$$\boldsymbol{H}^1_{\Gamma_1}(\Omega_1) = \left\{ \boldsymbol{v} \in \boldsymbol{H}^1(\Omega_1) \, ; \, \boldsymbol{v}|_{\Gamma_1} = \boldsymbol{0} \right\},$$

and p_2 and the pressure test functions in

$$H^1_{\Gamma_{2D}}(\Omega_2) = \left\{ q \in H^1(\Omega_2) \, ; \, q|_{\Gamma_{2D}} = 0 \right\}.$$

In these spaces, the system (11)–(14) has the equivalent variational formulation: Find $\boldsymbol{u} \in \boldsymbol{H}^1_{\Gamma_1}(\Omega_1)$, $p_1 \in L^2(\Omega_1)$, and $p_2 \in H^1_{\Gamma_{2D}}(\Omega_2)$, satisfying for all $\boldsymbol{v} \in \boldsymbol{H}^1_{\Gamma_1}(\Omega_1)$, $q_1 \in L^2(\Omega_1)$, and $q_2 \in H^1_{\Gamma_{2D}}(\Omega_2)$:

$$\begin{aligned} &2\mu \left(\boldsymbol{D}(\boldsymbol{u}), \boldsymbol{D}(\boldsymbol{v}) \right)_{\Omega_1} + \left(\boldsymbol{u} \cdot \nabla \boldsymbol{u}, \boldsymbol{v} \right)_{\Omega_1} - \left(p_1, \operatorname{div} \boldsymbol{v} \right)_{\Omega_1} + \left(\boldsymbol{K} \nabla p_2, \nabla q_2 \right)_{\Omega_2} \\ &\quad + \left(p_2, \boldsymbol{v} \cdot \boldsymbol{n}_{12} \right)_{\Gamma_{12}} - \left(q_2, \boldsymbol{u} \cdot \boldsymbol{n}_{12} \right)_{\Gamma_{12}} + \sum_{j=1}^{2} \left(\frac{1}{G^j} \boldsymbol{u} \cdot \boldsymbol{t}_{12}^j, \boldsymbol{v} \cdot \boldsymbol{t}_{12}^j \right)_{\Gamma_{12}} \\ &\quad - \left(\operatorname{div} \boldsymbol{u}, q_1 \right)_{\Omega_1} = \left(\boldsymbol{f}_1, \boldsymbol{v} \right)_{\Omega_1} + \left(f_2, q_2 \right)_{\Omega_2}. \end{aligned} \tag{17}$$

As usual, the pressure p_1 can be eliminated by restricting the test functions to

$$\boldsymbol{V} = \{ \boldsymbol{v} \in \boldsymbol{H}^1_{\Gamma_1}(\Omega_1) \, ; \, \forall q_1 \in L^2(\Omega_1), \, (\operatorname{div} \boldsymbol{u}, q_1)_{\Omega_1} = 0 \},$$

and we obtain a reduced equivalent problem: Find $\boldsymbol{u} \in \boldsymbol{V}$ and $p_2 \in H^1_{\Gamma_{2D}}(\Omega_2)$, satisfying for all $\boldsymbol{v} \in \boldsymbol{V}$ and $q_2 \in H^1_{\Gamma_{2D}}(\Omega_2)$:

$$\begin{aligned} &2\mu\left(\boldsymbol{D}(\boldsymbol{u}),\boldsymbol{D}(\boldsymbol{v})\right)_{\Omega_1} + \left(\boldsymbol{u}\cdot\nabla\boldsymbol{u},\boldsymbol{v}\right)_{\Omega_1} + \left(\boldsymbol{K}\nabla p_2,\nabla q_2\right)_{\Omega_2} \\ &\quad + \left(p_2,\boldsymbol{v}\cdot\boldsymbol{n}_{12}\right)_{\Gamma_{12}} - \left(q_2,\boldsymbol{u}\cdot\boldsymbol{n}_{12}\right)_{\Gamma_{12}} + \sum_{j=1}^{2}\left(\frac{1}{G^j}\boldsymbol{u}\cdot\boldsymbol{t}^j_{12},\boldsymbol{v}\cdot\boldsymbol{t}^j_{12}\right)_{\Gamma_{12}} \\ &= \left(\boldsymbol{f}_1,\boldsymbol{v}\right)_{\Omega_1} + \left(f_2,q_2\right)_{\Omega_2}. \end{aligned} \tag{18}$$

Equivalence follows easily from the inf-sup condition [31]: There exists $\beta > 0$ such that

$$\forall q_1 \in L^2(\Omega_1), \quad \sup_{\boldsymbol{v}\in\boldsymbol{H}^1_{\Gamma_1}(\Omega_1)} \frac{\left(\operatorname{div}\boldsymbol{v},q_1\right)_{\Omega_1}}{|\boldsymbol{v}|_{\boldsymbol{H}^1(\Omega_1)}} \geq \beta\|q_1\|_{L^2(\Omega_1)}. \tag{19}$$

2.5 *"Energy" Equality and Analysis*

The influence of the interface condition on the nonlinear term is clearly illustrated by a straightforward "energy" analysis of problem (18). Assume (18) has a solution $(\boldsymbol{u},p_2)$ and take $\boldsymbol{v}=\boldsymbol{u}$, $q_2=p_2$. Then we readily obtain

$$\begin{aligned} &2\mu\,\|\boldsymbol{D}(\boldsymbol{u})\|^2_{\boldsymbol{L}^2(\Omega_1)} + \left\|\boldsymbol{K}^{1/2}\nabla p_2\right\|^2_{\boldsymbol{L}^2(\Omega_2)} + \sum_{j=1}^{2}\left\|\left(\frac{1}{G^j}\right)^{1/2}\boldsymbol{u}\cdot\boldsymbol{t}^j_{12}\right\|^2_{L^2(\Gamma_{12})} \\ &\quad + \frac{1}{2}\int_{\Gamma_{12}}(\boldsymbol{u}\cdot\boldsymbol{n}_{12})|\boldsymbol{u}|^2 = (\boldsymbol{f}_1,\boldsymbol{u})_{\Omega_1} + (f_2,p_2)_{\Omega_2}. \end{aligned} \tag{20}$$

The integrand $(\boldsymbol{u}\cdot\boldsymbol{n}_{12})|\boldsymbol{u}|^2$ on Γ_{12} has no definite sign because $\operatorname{div}\boldsymbol{u}=0$ in Ω_1 and $\boldsymbol{u}=\boldsymbol{0}$ on Γ_1 imply that $\boldsymbol{u}\cdot\boldsymbol{n}_{12}$ changes sign on Γ_{12}. But even in the presence of other boundary conditions, one can expect exchanges of fluid at the interface. Therefore in (20) we need to control this integral on the interface.

There are different approaches for treating this integral and establishing existence of solutions. Considering that the difficulty is located on the interface, Badea et al. in [8] reduce problem (18) to a nonlinear interface problem via a nonlinear Steklov–Poincaré operator. Their main unknown is $\lambda = \boldsymbol{u}\cdot\boldsymbol{n}_{12}$ on Γ_{12}, and they require an extension operator

$$E : \lambda \in H^{1/2}_{00}(\Gamma_{12}) \mapsto \boldsymbol{v} \in \boldsymbol{H}^1(\Omega_1) \quad \text{satisfying} \quad \boldsymbol{v}\cdot\boldsymbol{n}_{12} = \lambda.$$

Unfortunately, this extension is impossible as soon as Γ_{12} has corners, because in this case $\boldsymbol{n}_{12}$ is not smooth enough to guarantee that $\boldsymbol{v}\cdot\boldsymbol{n}_{12}$ belongs to $H^{1/2}(\Gamma_{12})$. In other words, their approach does not extend to a rough boundary.

This limitation can be avoided by a direct argument (see Girault and Rivière [32]) based on a Galerkin discretization of (18), a priori estimates for restricted data, and Brouwer's fixed point theorem. More precisely, we choose and truncate a smooth basis of $\boldsymbol{V}\times L^2(\Omega_2)$, say $\boldsymbol{W}_m=\mathrm{Vect}\{(\Phi_i,\varphi_i)_{1\le i\le m}\}$, and we want to find $(\boldsymbol{u}_m,p_m)\in\boldsymbol{W}_m$ solution of

$$\begin{aligned}
&2\mu\left(\boldsymbol{D}(\boldsymbol{u}_m),\boldsymbol{D}(\Phi_k)\right)_{\Omega_1}+\left(\boldsymbol{u}_m\cdot\nabla\boldsymbol{u}_m,\Phi_k\right)_{\Omega_1}+\left(\boldsymbol{K}\nabla p_m,\nabla\varphi_k\right)_{\Omega_2}\\
&\quad+\left(p_m,\Phi_k\cdot\boldsymbol{n}_{12}\right)_{\Gamma_{12}}-\left(\varphi_k,\boldsymbol{u}_m\cdot\boldsymbol{n}_{12}\right)_{\Gamma_{12}}+\sum_{j=1}^{2}\left(\frac{1}{G^j}\boldsymbol{u}_m\cdot\boldsymbol{t}_{12}^j,\Phi_k\cdot\boldsymbol{t}_{12}^j\right)_{\Gamma_{12}}\\
&=\left(\boldsymbol{f}_1,\Phi_k\right)_{\Omega_1}+\left(f_2,\varphi_k\right)_{\Omega_2},\quad 1\le k\le m.
\end{aligned}\tag{21}$$

Clearly, any solution of (21) satisfies the energy equality (20). Hence the assumptions of Brouwer's fixed point theorem cannot be checked without restricting the data. With that in mind, it can be readily shown that there exists a constant $\mathscr{A}$ of the form

$$\mathscr{A}=C_1\|\boldsymbol{f}_1\|_{\boldsymbol{L}^2(\Omega_1)}+\sqrt{\frac{\mu}{\lambda_{\min}}}C_2\|f_2\|_{L^2(\Omega_2)},$$

with C_1 and C_2 depending only on the geometry of the domain, such that if

$$\mu^2>\mathscr{C}\mathscr{A},\tag{22}$$

where also $\mathscr{C}$ only depends on the geometry of the domain, then (21) has at least one solution $\boldsymbol{u}_m,p_m$ satisfying

$$\mu\left\|\boldsymbol{D}(\boldsymbol{u}_m)\right\|^2_{\boldsymbol{L}^2(\Omega_1)}+\left\|\boldsymbol{K}^{1/2}\nabla p_m\right\|^2_{\boldsymbol{L}^2(\Omega_2)}\le\frac{\mathscr{A}^2}{\mu}.\tag{23}$$

In other words, there exist solutions of (21) for large viscosity or small forces, or both. Furthermore, (22) and (23) imply that

$$\left\|\boldsymbol{D}(\boldsymbol{u}_m)\right\|_{\boldsymbol{L}^2(\Omega_1)}\le\frac{\mathscr{A}}{\mu}<\frac{\mu}{\mathscr{C}}\quad\text{and}\quad\left\|\boldsymbol{K}^{1/2}\nabla p_m\right\|_{\boldsymbol{L}^2(\Omega_2)}\le\frac{\mathscr{A}}{\sqrt{\mu}}<\frac{\mu^{3/2}}{\mathscr{C}}.$$

By a standard argument, these bounds are sufficient to pass to the limit in (21) as m tends to infinity. Therefore, provided (22) holds, (18) has at least one solution, and this solution satisfies

$$\left\|\boldsymbol{D}(\boldsymbol{u})\right\|_{\boldsymbol{L}^2(\Omega_1)}<\frac{\mu}{\mathscr{C}}\quad\text{and}\quad\left\|\boldsymbol{K}^{1/2}\nabla p\right\|_{\boldsymbol{L}^2(\Omega_2)}<\frac{\mu^{3/2}}{\mathscr{C}}.\tag{24}$$

Finally, it is easy to prove that (18) has no other solution satisfying (24). Existence of p_1 such that $\boldsymbol{u}, p_1, p_2$ solves (17) follows from the equivalence of these two formulations.

Remark 2.1. In the case of coupled Stokes and Darcy equations with the same interface conditions (6), (7), and (10), the argument is much simpler. Existence and uniqueness of $(\boldsymbol{u}, p_1, p_2)$ satisfying (17) without the nonlinear term are obtained unconditionally.

3 Discretization

There are several numerical methods that approximate the solution of the Stokes version of (11)–(14), either in divergence form or not. Most have straightforward extensions to the Navier–Stokes equations, although these extensions have not always been proposed. We describe some of them in this section.

3.1 A Discontinuous Galerkin Method

This method has been studied mostly by Girault, Rivière, and Yotov in [32, 49, 51]. Since the analysis presented above applies to a rough interface, we can assume that both Ω_1 and Ω_2 are polygons or polyhedra. This is a major simplification because performing the numerical analysis of problem (11)–(14) in a region with a curved interface raises very technical issues, unless the interface is flat, which is a strong limitation on the geometry.

Let $\mathscr{E}_i^h$ be a regular family (in the sense of Ciarlet [18]) of triangulations of Ω_i made of simplicial elements, i.e., there exists a constant $\gamma > 0$ independent of h, such that

$$\forall E \in \mathscr{E}_i^h, \frac{h_E}{\rho_E} = \gamma_E \leq \gamma,$$

where h_E is the diameter of E, ρ_E is the diameter of the ball inscribed in E, and h is the maximum of h_E. Hexahedral elements can also be used, but the nonlinear transformation from the reference cell makes the analysis more technical. As we work with totally discontinuous finite elements, we accept hanging nodes, but for the sake of simplicity, we assume that the triangulations are conforming, and in particular, we assume that the triangulations $\mathscr{E}_i^h$ match on the interface. However, this restriction can be easily relaxed.

The method presented here uses completely discontinuous symmetric interior penalty (SIPG) or nonsymmetric interior penalty (NIPG) everywhere for the elliptic terms; see [41, 50, 52]. This permits to prescribe weakly the essential boundary

conditions. For the nonlinear convection term, it uses discontinuous Galerkin upwinding *à la* LeSaint–Raviart; see [45]. The functions in the discrete spaces are polynomials of degrees $k_1 \geq 1$ for the fluid velocity, $k_1 - 1$ for the fluid pressure, and $k_2 \geq 1$ for the pore pressure; the spaces are

$$\boldsymbol{X}^h = \{\boldsymbol{v} \in \boldsymbol{L}^2(\Omega_1)\,;\, \forall E \in \mathscr{E}_1^h\,, \boldsymbol{v}|_E \in \mathbb{P}_{k_1}(E)^3\} \quad \text{for the fluid velocity,}$$

$$M_1^h = \{q \in L^2(\Omega_1)\,;\, \forall E \in \mathscr{E}_1^h\,, q|_E \in \mathbb{P}_{k_1-1}(E)\} \quad \text{for the fluid pressure,}$$

$$M_2^h = \{q \in L^2(\Omega_2)\,;\, \forall E \in \mathscr{E}_2^h\,, q|_E \in \mathbb{P}_{k_2}(E)\} \quad \text{for the pore pressure.}$$

As usual, we introduce the set Γ_i^h of element interfaces of $\mathscr{E}_i^h$ interior to Ω_i, and we associate a unit normal vector to each face e of Γ_i^h, say oriented from E_k to E_ℓ for $k < \ell$, and also to each face of e of Γ_i oriented away from Ω_i. Then we define the jump and average

$$[v]_e = v|_{E_k} - v|_{E_\ell}, \quad \{v\}_e = \frac{1}{2}\big(v|_{E_k} + v|_{E_\ell}\big),$$

and we associate to the face e the parameter $h_e = \max(|E_k|, |E_\ell|)$. We choose a jump penalty parameter on each face e, σ_e, and a parameter $\varepsilon_i = +1$ for a nonsymmetric formulation, -1 for a symmetric formulation, and 0 for an incomplete formulation. Then we take the following consistent approximation of $\big(\boldsymbol{D}(\boldsymbol{u}), \boldsymbol{D}(\boldsymbol{v})\big)_{\Omega_1}$ Cockburn et al. [19]:

$$\begin{aligned}
&\sum_{E \in \mathscr{E}_1^h} \big(\boldsymbol{D}(\boldsymbol{u}), \boldsymbol{D}(\boldsymbol{v})\big)_E \\
&\quad - \sum_{e \in \Gamma_1^h \cup \Gamma_1} \Big(\big(\{\boldsymbol{D}(\boldsymbol{u})\}_e \boldsymbol{n}_e, [\boldsymbol{v}]_e\big)_e - \varepsilon_1 \big(\{\boldsymbol{D}(\boldsymbol{v})\}_e \boldsymbol{n}_e, [\boldsymbol{u}]_e\big)_e \Big) + \sum_{e \in \Gamma_1^h \cup \Gamma_1} \frac{\sigma_e}{h_e} \big([\boldsymbol{u}]_e, [\boldsymbol{v}]_e\big)_e.
\end{aligned} \tag{25}$$

Similarly, for the pore pressure term $\big(\boldsymbol{K}\nabla p, \nabla q\big)_{\Omega_2}$, we use the following consistent approximation:

$$\begin{aligned}
&\sum_{E \in \mathscr{E}_2^h} \big(\boldsymbol{K}\nabla p, \nabla q\big)_E + \sum_{e \in \Gamma_2^h \cup \Gamma_2} \frac{|\boldsymbol{K}|\sigma_e}{h_e} \big([p]_e, [q]_e\big)_e \\
&\quad - \sum_{e \in \Gamma_2^h \cup \Gamma_{2D}} \Big(\big(\{\boldsymbol{K}\nabla p\}_e \cdot \boldsymbol{n}_e, [q]_e\big)_e - \varepsilon_2 \big(\{\boldsymbol{K}\nabla q\}_e \cdot \boldsymbol{n}_e, [p]_e\big)_e \Big).
\end{aligned} \tag{26}$$

For the convection term $\big(\boldsymbol{u}\cdot\nabla\boldsymbol{u},\boldsymbol{v}\big)_{\Omega_1}$, we use the LeSaint–Raviart upwind approximation [45]:

$$\sum_{E\in\mathscr{E}_1^h}\Big((\boldsymbol{u}\cdot\nabla\boldsymbol{u},\boldsymbol{v})_E+\frac{1}{2}(\operatorname{div}\boldsymbol{u},\boldsymbol{u}\cdot\boldsymbol{v})_E\Big)$$
$$+\sum_{E\in\mathscr{E}_1^h}(|\{\boldsymbol{u}\}\cdot\boldsymbol{n}_E|(\boldsymbol{u}^{\mathrm{int}}-\boldsymbol{u}^{\mathrm{ext}}),\boldsymbol{v}^{\mathrm{int}})_{\partial E_-\setminus\Gamma_{12}}-\frac{1}{2}\sum_{e\in\Gamma_1^h\cup\Gamma_1}([\boldsymbol{u}]\cdot\boldsymbol{n}_e,\{\boldsymbol{u}\cdot\boldsymbol{v}\})_e,\quad(27)$$

where $\boldsymbol{n}_E$ stands for the unit normal exterior to E, ∂E_- denotes the part of ∂E where $\{\boldsymbol{u}\}\cdot\boldsymbol{n}_E<0$, and the superscripts int and ext refer respectively to values inside and outside E. This approximation is consistent if $\operatorname{div}\boldsymbol{u}=0$, $\boldsymbol{u}$ has no jump at interfaces, and $\boldsymbol{u}$ vanishes on Γ_1. Finally, we use the consistent approximation of $\langle\nabla p_1,\boldsymbol{v}\rangle_{\Omega_1}$:

$$-\sum_{E\in\mathscr{E}_1^h}\big(p_1,\operatorname{div}\boldsymbol{v}\big)_E+\sum_{e\in\Gamma_1^h\cup\Gamma_1}\big(\{p_1\}_e,[\boldsymbol{v}]_e\cdot\boldsymbol{n}_e\big)_e.$$

It is consistent if p_1 is smooth enough. The remaining boundary terms are discretized in a straightforward way. All this leads to the numerical scheme:

$$2\mu\Bigg(\sum_{E\in\mathscr{E}_1^h}\big(\boldsymbol{D}(\boldsymbol{u}_h),\boldsymbol{D}(\boldsymbol{v}_h)\big)_E+\sum_{e\in\Gamma_1^h\cup\Gamma_1}\frac{\sigma_e}{h_e}\big([\boldsymbol{u}_h]_e,[\boldsymbol{v}_h]_e\big)_e$$
$$-\sum_{e\in\Gamma_1^h\cup\Gamma_1}\Big(\big(\{\boldsymbol{D}(\boldsymbol{u}_h)\}_e\boldsymbol{n}_e,[\boldsymbol{v}_h]_e\big)_e-\varepsilon_1\big(\{\boldsymbol{D}(\boldsymbol{v}_h)\}_e\boldsymbol{n}_e,[\boldsymbol{u}_h]_e\big)_e\Big)\Bigg)$$
$$+\sum_{E\in\mathscr{E}_2^h}\big(\boldsymbol{K}\nabla p_{2,h},\nabla q_h\big)_E+\sum_{e\in\Gamma_2^h\cup\Gamma_2}\frac{|\boldsymbol{K}|\sigma_e}{h_e}\big([p_{2,h}]_e,[q_h]_e\big)_e$$
$$-\sum_{e\in\Gamma_2^h\cup\Gamma_{2D}}\Big(\big(\{\boldsymbol{K}\nabla p_{2,h}\}_e\cdot\boldsymbol{n}_e,[q_h]_e\big)_e-\varepsilon_2\big(\{\boldsymbol{K}\nabla q_h\}_e\cdot\boldsymbol{n}_e,[p_{2,h}]_e\big)_e\Big)$$
$$+\sum_{E\in\mathscr{E}_1^h}\big((\boldsymbol{u}_h\cdot\nabla\boldsymbol{u}_h,\boldsymbol{v}_h)_E+\frac{1}{2}(\operatorname{div}\boldsymbol{u}_h,\boldsymbol{u}_h\cdot\boldsymbol{v}_h)_E\big)\quad(28)$$
$$-\frac{1}{2}\sum_{e\in\Gamma_1^h\cup\Gamma_1}([\boldsymbol{u}_h]\cdot\boldsymbol{n}_e,\{\boldsymbol{u}_h\cdot\boldsymbol{v}_h\})_e+\sum_{E\in\mathscr{E}_1^h}(|\{\boldsymbol{u}_h\}\cdot\boldsymbol{n}_E|(\boldsymbol{u}_h^{\mathrm{int}}-\boldsymbol{u}_h^{\mathrm{ext}}),\boldsymbol{v}_h^{\mathrm{int}})_{\partial E_-\setminus\Gamma_{12}}$$

$$
\begin{aligned}
&-\sum_{E\in\mathscr{E}_1^h}\left(p_{1,h},\operatorname{div}\boldsymbol{v}_h\right)_E+\sum_{e\in\Gamma_1^h\cup\Gamma_1}\left(\{p_{1,h}\}_e,[\boldsymbol{v}_h]_e\cdot\boldsymbol{n}_e\right)_e+(p_{2,h},\boldsymbol{v}_h\cdot\boldsymbol{n}_{12})_{\Gamma_{12}}\\
&-(\boldsymbol{u}_h\cdot\boldsymbol{n}_{12},q_h)_{\Gamma_{12}}+\sum_{j=1}^{2}\Big(\frac{1}{G^j}\boldsymbol{u}_h\cdot\boldsymbol{t}_{12},\boldsymbol{v}_h\cdot\boldsymbol{t}_{12}\Big)_{\Gamma_{12}}\\
&=(\boldsymbol{f}_1,\boldsymbol{v}_h)_{\Omega_1}+(f_2,q_h)_{\Omega_2},\quad\forall\boldsymbol{v}_h\in\boldsymbol{X}^h,\quad\forall q_h\in M_2^h,\\
&\quad-\sum_{E\in\mathscr{E}_1^h}(q_h,\operatorname{div}\boldsymbol{u}_h)_E+\sum_{e\in\Gamma_1^h\cup\Gamma_1}(\{q_h\},[\boldsymbol{u}_h]\cdot\boldsymbol{n}_e)_e=0,\quad\forall q_h\in M_1^h.
\end{aligned}
\tag{29}
$$

Of course the pressure $p_{1,h}$ can be eliminated by restricting the test functions $\boldsymbol{v}_h$ to those satisfying (29). The resulting reduced problem is a square nonlinear system in finite dimension that can be analyzed exactly as (21), with slightly different constants that account for the discretization. Hence, by restricting the data according to the analogue of (22), it has at least one solution $(\boldsymbol{u}_h,p_{2,h})$ that satisfies bounds similar to (24). Uniqueness and error estimates can be obtained under analogous conditions. Thus if the solution is sufficiently smooth and the data suitably restricted, the sum of the errors for $\boldsymbol{u}$ in $\boldsymbol{H}^{k_1+1}(\Omega_1)^3$, for p_1 in $H^{k_1}(\Omega_1)$, and for p_2 in $H^{k_2+1}(\Omega_2)$ is $\mathrm{O}(h^{k_1})+\mathrm{O}(h^{k_2})$, the same order as the interpolation errors.

Since it is nonlinear, computing the solution of (28), (29) requires a linearization algorithm. Assuming the sufficient conditions for uniqueness, it can be shown that if the initial guess is sufficiently small (zero can be chosen) then a simple successive approximation algorithm converges to the discrete solution. Of course other more efficient algorithms, such as Newton's algorithm, can be used. Similarly, this discontinuous Galerkin method in either one or in both regions can be replaced by a continuous Galerkin method.

Finally, computations in the two regions are coupled by the interface term $(p_{2,h},\boldsymbol{v}_h\cdot\boldsymbol{n}_{12})_{\Gamma_{12}}-(\boldsymbol{u}_h\cdot\boldsymbol{n}_{12},q_h)_{\Gamma_{12}}$. One possibility for decoupling them is the use of a two-grid algorithm.

3.2 *Decoupling by a Two-Grid Algorithm*

This algorithm was introduced by Cai et al. in [13] for a continuous finite element discretization of the coupled Navier–Stokes and Darcy equations. More recently in [17], Chidyagwai and Rivière apply the two-grid technique with a continuous Galerkin method in the fluid region Ω_1 and a discontinuous Galerkin method in the porous region Ω_2 as in Sect. 3.1. It is worth noting that the idea of using two grids of different sizes (one coarse and one fine) has been applied to various problems. The two-grid algorithm proceeds in three steps:

1. Find $(\boldsymbol{u}_H,p_{1,H},p_{2,H})$ solution of the fully coupled Navier–Stokes–Darcy system on a coarse grid with mesh size H.

2. Use the interface coarse porous pressure $p_{2,H}$ to reduce the computation to the fluid region Ω_1, use the coarse fluid velocity $\boldsymbol{u}_H$ to linearize the nonlinear Navier–Stokes convection term, and find $(\boldsymbol{u}_h, p_{1,h})$ solution of the linearized Navier–Stokes system on a fine grid with mesh size h.
3. In parallel, use the coarse fluid velocity $\boldsymbol{u}_H$ on the interface to find $p_{2,h}$ solution of the Darcy system in Ω_2 on a fine grid with mesh size h.

This algorithm solves the fully coupled problem only on a coarse grid. A complete decoupling is not straightforward, because the Darcy velocity has been eliminated in the porous region. With the same formulation, Discacciati and Quarteroni in [8] achieve their decoupling by introducing an interface equation, but, as mentioned in Sect. 2.5, their analysis cannot handle a rough boundary, and since their numerical analysis is written for a polygonal or polyhedral boundary, they can only treat a flat interface. However, a mixed formulation in the porous region that retains the Darcy velocity is more amenable to decoupling. So far, it has only been studied for Stokes–Darcy couplings, but the extension to Navier–Stokes–Darcy couplings can be handled by the analysis of Sect. 2.5.

3.3 *Discretization Based on a Mixed Formulation in the Porous Region*

Numerical discretizations of the mixed form (4) of the Darcy flow have been studied in the literature for the coupled Stokes and Darcy equations only. Most schemes can be extended to the nonlinear case. First, Rivière and Yotov in [51] consider a monolithic strategy where they keep the Darcy velocity in Ω_2: $\boldsymbol{u}_2 \in \boldsymbol{H}(\mathrm{div};\Omega_2)$. Then the velocity $\boldsymbol{u}$ is defined in the whole domain Ω, and considering the interface condition arising from the continuity (6), they prescribe continuity of $\boldsymbol{u}\cdot\boldsymbol{n}_{12}$. Thus, prescribing suitable exterior boundary conditions on $\boldsymbol{u}$, such as $\boldsymbol{u}=\boldsymbol{0}$ on Γ_1 and $\boldsymbol{u}\cdot\boldsymbol{n}=0$ on Γ_{2N}, they work in the spaces

$$\boldsymbol{V}=\{\boldsymbol{v}\in\boldsymbol{H}(\mathrm{div};\Omega)\,;\,\boldsymbol{v}|_{\Omega_1}\in\boldsymbol{H}^1(\Omega_1),\boldsymbol{v}|_{\Gamma_1}=\boldsymbol{0},(\boldsymbol{v}\cdot\boldsymbol{n})|_{\Gamma_{2N}}=0\}\quad\text{and}\quad M=L^2(\Omega).$$

Then the variational equation becomes as follows: Find $\boldsymbol{u}\in\boldsymbol{V}$ and $p\in M$ solution of

$$\begin{aligned}&2\mu\left(\boldsymbol{D}(\boldsymbol{u}_1),\boldsymbol{D}(\boldsymbol{v}_1)\right)_{\Omega_1}+\left(\boldsymbol{u}_1\cdot\nabla\boldsymbol{u}_1,\boldsymbol{v}_1\right)_{\Omega_1}-\left(p,\mathrm{div}\,\boldsymbol{v}\right)_{\Omega}+\left(q,\mathrm{div}\,\boldsymbol{u}\right)_{\Omega}\\&\quad+\left(\boldsymbol{K}^{-1}\boldsymbol{u}_2,\boldsymbol{v}_2\right)_{\Omega_2}+\sum_{j=1}^{2}\left(\frac{1}{G^j}\boldsymbol{u}\cdot\boldsymbol{t}_{12}^j,\boldsymbol{v}\cdot\boldsymbol{t}_{12}^j\right)_{\Gamma_{12}}\\&=\left(\boldsymbol{f}_1,\boldsymbol{v}\right)_{\Omega_1}+\left(f_2,q_2\right)_{\Omega_2},\quad\forall\boldsymbol{v}\in\boldsymbol{V},\forall q\in M.\end{aligned}\tag{30}$$

To discretize (30), they use a discontinuous Galerkin method in Ω_1, as in Sect. 3.1, and a mixed method in Ω_2 with Raviart–Thomas, Brezzi–Douglas–Marini, or Brezzi–Douglas–Falk–Marini elements; see [11]. The resulting discrete scheme is coupled; it can be uncoupled by relaxing the continuity of $\boldsymbol{u}\cdot\boldsymbol{n}_{12}$ by means of a Lagrange multiplier, also called mortar. This can be found in several works, such as the work of Galvis and Sarkis [26], of Layton et al. [44], of Kanschat and Rivière [42], and of Gatica et al. [29] all applied to the Stokes–Darcy coupling.

3.4 Decoupling with a Lagrange Multiplier

As an example, let us briefly present the work of Galvis and Sarkis [26]; we write it in the case of the full Navier–Stokes–Darcy coupling, although these authors study only the linear problem. The difference with (30) is that the space $\boldsymbol{V}$ is replaced by

$$\boldsymbol{W}=\{\boldsymbol{v}\in\boldsymbol{L}^2(\Omega);\boldsymbol{v}|_{\Omega_1}\in\boldsymbol{H}^1(\Omega_1),\boldsymbol{v}|_{\Omega_2}\in\boldsymbol{H}(\mathrm{div};\Omega_2),\boldsymbol{v}|_{\Gamma_1}=\boldsymbol{0},(\boldsymbol{v}\cdot\boldsymbol{n})|_{\Gamma_{2N}}=0\},$$

while the space M is unchanged. The continuity of normal traces at the interface is enforced weakly by means of a Lagrange multiplier. The more delicate choice of space Λ for the multiplier is well addressed in [26], but in the simple case of Fig. 1, where the interface is adjacent to Γ_1 and Γ_{2N}, we can take $\Lambda=H^{1/2}(\Gamma_{12})$. Then the problem reads as follows: Find $\boldsymbol{u}\in\boldsymbol{W}$, $p\in M$, and $\lambda\in\Lambda$ satisfying for all $\boldsymbol{v}\in\boldsymbol{W}$, $q\in M$, and $\mu\in\Lambda$:

$$\begin{aligned}
&2\mu\left(\boldsymbol{D}(\boldsymbol{u}),\boldsymbol{D}(\boldsymbol{v})\right)_{\Omega_1}+\left(\boldsymbol{u}\cdot\nabla\boldsymbol{u},\boldsymbol{v}\right)_{\Omega_1}-\left(p,\mathrm{div}\,\boldsymbol{v}\right)_{\Omega}+\left(\mathrm{div}\,\boldsymbol{u},q\right)_{\Omega}+\left(\boldsymbol{K}^{-1}\boldsymbol{u},\boldsymbol{v}\right)_{\Omega_2}\\
&\quad+\sum_{j=1}^{2}\left(\frac{1}{G^j}\boldsymbol{u}_1\cdot\boldsymbol{t}_{12}^j,\boldsymbol{v}_1\cdot\boldsymbol{t}_{12}^j\right)_{\Gamma_{12}}+\langle[\boldsymbol{v}\cdot\boldsymbol{n}_{12}],\lambda\rangle_{\Gamma_{12}}=\left(\boldsymbol{f}_1,\boldsymbol{v}\right)_{\Omega_1}+\left(f_2,q_2\right)_{\Omega_2},\\
&\langle[\boldsymbol{u}\cdot\boldsymbol{n}_{12}],\mu\rangle_{\Gamma_{12}}=0.
\end{aligned}\tag{31}$$

To discretize (31), they use for the velocity and pressure a Taylor–Hood $\mathbb{P}_2-\mathbb{P}_1$ finite element method in Ω_1 and a Raviart–Thomas RT_0 mixed finite element method in Ω_2. For the Lagrange multiplier, they take piecewise $\mathbb{P}_0$ functions on Γ_{12}. However, a second-order approximation of the velocity and pressure is not really necessary; it can be replaced by a mini-element.

4 Other Models

Alternatively to the system (11)–(14), different models for the interface condition as well as the porous media flow have been proposed. Among those, we discuss the Beavers–Joseph condition and the Brinkman model in the porous media. As in the previous section, these have been mostly investigated for coupling with Stokes flow but can be applied to the Navier–Stokes model as well.

4.1 The Beavers–Joseph Interface Condition

Let us investigate the meaning of the Navier–Stokes–Darcy system (11)–(13), when the second equation of (13) is replaced by the Beavers–Joseph condition (8):

$$(\boldsymbol{u}_1 - \boldsymbol{u}_2)\cdot\boldsymbol{t}_{12}^j = -G^j\big(\boldsymbol{T}\boldsymbol{n}_{12}\big)\cdot\boldsymbol{t}_{12}^j = -2\mu G^j\big(\boldsymbol{D}(\boldsymbol{u}_1)\boldsymbol{n}_{12}\big)\cdot\boldsymbol{t}_{12}^j.$$

From a theoretical point of view, this condition raises a major concern. This question is partly addressed by Cao et al. in [14], and we present our take on their proof.

Neglecting the permeability tensor $\boldsymbol{K}$ for the moment, we take $\boldsymbol{u}_2 = \nabla p_2$. Since $p_2 \in H^1(\Omega_2)$, we have $\boldsymbol{u}_2 \in \boldsymbol{H}(\mathbf{curl};\Omega_2)$, where (see [31])

$$\boldsymbol{H}(\mathbf{curl};\Omega) = \{\boldsymbol{v} \in \boldsymbol{L}^2(\Omega)\,;\, \mathbf{curl}\,\boldsymbol{v} \in \boldsymbol{L}^2(\Omega)\}.$$

Thus its tangential traces $\boldsymbol{u}_2\cdot\boldsymbol{t}_{12}^j$ are well defined in $H^{-1/2}(\partial\Omega_2)$. Since additionally, p_2 solves (12) with $f_2 \in L^2(\Omega_2)$, we have $\boldsymbol{u}_2 \in \boldsymbol{H}(\mathrm{div};\Omega_2)$, and thus its normal trace $\boldsymbol{u}_2\cdot\boldsymbol{n}_2$ is well defined in $H^{-1/2}(\partial\Omega_2)$. From the properties $\boldsymbol{u}_1 \in \boldsymbol{H}^1(\Omega_1)^3$ and $\boldsymbol{u}_2\cdot\boldsymbol{n}_{12} = \boldsymbol{u}_1\cdot\boldsymbol{n}_{12}$, Cao et al. observe, as is done in Sect. 2.3, that $\boldsymbol{u}_2\cdot\boldsymbol{n}_{12}$ is smoother than what can be expected from a function in $\boldsymbol{H}(\mathrm{div};\Omega_2)$. This fact is used to show that the difference $\boldsymbol{u}_2 - \boldsymbol{u}_1$ in Ω_2 belongs to the space

$$\boldsymbol{Y} = \{\boldsymbol{v} \in \boldsymbol{H}(\mathbf{curl};\Omega_2) \cap \boldsymbol{H}(\mathrm{div};\Omega_2)\,;\, (\boldsymbol{v}\cdot\boldsymbol{n}_2)|_{\partial\Omega_2} = 0\}.$$

As Ω_2 is a Lipschitz polyhedron, $\boldsymbol{Y}$ is continuously embedded into $\boldsymbol{H}^{1/2+s}(\Omega_2)$ for some $s > 0$; see [4]. Hence functions of $\boldsymbol{Y}$ have a trace—tangential and normal—in $\boldsymbol{H}^s(\Gamma_{12})$.

In the present case, $\boldsymbol{u}_2 = -\boldsymbol{K}\nabla p_2$; unfortunately, multiplication with an arbitrary tensor $\boldsymbol{K}$ does not preserve the zero **curl**, and therefore Cao et al. [14] treat the case when $\boldsymbol{K}(\boldsymbol{x}) = k(\boldsymbol{x})\boldsymbol{I}$, with $k \in W^{1,\infty}(\Omega_2)$. Since

$$\mathbf{curl}(\boldsymbol{K}\nabla p_2) = \nabla k \times \nabla p_2,$$

we have $\mathbf{curl}(\boldsymbol{K}\nabla p_2)$ in $\boldsymbol{L}^2(\Omega_2)$. Hence the above argument leads to a variational formulation that is similar to (17) with the interface term

$$\sum_{j=1}^{2}\left(\frac{1}{G^j}\boldsymbol{u}\cdot\boldsymbol{t}_{12}^j,\boldsymbol{v}\cdot\boldsymbol{t}_{12}^j\right)_{\Gamma_{12}}$$

replaced by

$$\sum_{j=1}^{2}\left(\frac{1}{G^j}(\boldsymbol{u}-k\nabla p_2)\cdot\boldsymbol{t}_{12}^j,\boldsymbol{v}\cdot\boldsymbol{t}_{12}^j\right)_{\Gamma_{12}}.$$

However, this term is not meaningful when p_2 is an arbitrary function in $H^1(\Omega_2)$ and the interface has corners because $\boldsymbol{v}\cdot\boldsymbol{t}_{12}^j$ is not smooth enough. Therefore the variational problem is well defined only if the interface is smooth. As a consequence, the analysis of the Stokes–Darcy coupling with an arbitrary tensor $\boldsymbol{K}$ and a rough interface appears to be an open problem.

4.2 Coupled Stokes and Brinkman Systems

If the volume fraction of the background matrix converges to zero at sufficient rate as the pore size goes to zero, the limit of the Stokes equations in the porous media is not the Darcy equation (12), but the Brinkman system

$$\left.\begin{aligned}-2\mu\,\mathrm{div}\,\boldsymbol{D}(\boldsymbol{u})+\frac{\mu}{\sigma^2}\boldsymbol{u}+\nabla p&=\boldsymbol{f}\\ \mathrm{div}\,\boldsymbol{u}&=0\end{aligned}\right\}\quad\text{in }\Omega_2,\tag{32}$$

with a typically small parameter σ. The derivation by homogenization and the exact requirements on the volume fractions and the value σ are discussed by Allaire in [2, 3]. Since the solution space for (32) is $\boldsymbol{H}^1(\Omega_2)$, the question of interface conditions is usually settled by choosing velocity fields in $\boldsymbol{H}^1(\Omega)$, thus requiring normal and tangential continuity at the interface. This causes a boundary layer, whereas the boundary layer is represented by the interface condition in the Beavers–Joseph or Beavers–Joseph–Saffman models.

Since the Brinkman model is singularly perturbed, special care has to be given to the stability of the finite element pair used for discretization; see for instance the analysis of Xie et al. in [57]. Alternatively, divergence conforming elements can be used with a discontinuous Galerkin method taking care of its inconsistency with respect to the Stokes operator, as introduced by Cockburn et al. in [20, 21]. Additional discontinuous families were suggested by Wang and Ye in [56]. Nonconforming finite element families are suggested by Karper et al. in [43] and Mardal et al. in [47]. Juntunen and Stenberg proposed continuous elements with special bubble functions in [40], while Badía and Codina in [7],

Braack and Schieweck in [10], and Burman and Hansbo in [12] propose stabilization techniques. Brinkman equation, in modeling porous media with very high porosity, is particularly suited for multiscale problems, as for instance studied by Iliev et al. in [35].

5 Numerical Examples

5.1 Convergence Rates

The numerical experiments reported in this section are set in $\mathbb{R}^2$.

In the first example, we compute numerical convergence rates for a smooth known solution. The subdomains are $\Omega_1 = (0,1)\times(1,2)$ and $\Omega_2 = (0,1)\times(0,1)$. The exact solution is

$$\boldsymbol{u}(x,y) = (-\cos(\pi x)\sin(\pi y), \sin(\pi x)\cos(\pi y)), \quad p_1(x,y) = \sin(\pi x), \quad \forall (x,y)\in\Omega_1,$$
$$p_2(x,y) = y\sin(\pi x), \quad \forall (x,y)\in\Omega_2.$$

We use the nonsymmetric discontinuous Galerkin method with penalty parameter set equal to one. The other inputs of the problem are $\mu = 1$, $\boldsymbol{K} = \boldsymbol{I}$, and the Beavers–Joseph–Saffman constant in (9) $\alpha = 10$. The nonlinear system is solved by a Picard iteration and the tolerance for stopping the iterations is 10^{-8}. We compute various numerical errors on a sequence of meshes that are successively refined uniformly. Meshes are generated using Gmsh [30], visualization is done using Tecplot [54], and the simulations are done using software developed by the authors. The Navier–Stokes velocity and Darcy pressure are approximated by polynomials of degree k and the Navier–Stokes pressure is approximated by polynomials of degree $k-1$. We vary k between 2 and 5. Figures 2–4 show the log–log plots of the energy errors versus the mesh size h: the first figure shows the convergence of $\|\nabla(\boldsymbol{u}-\boldsymbol{u}_h)\|_{\boldsymbol{L}^2(\Omega_1)}$, the second figure shows the convergence of $\|p-p_h\|_{L^2(\Omega_1)}$, and the third figure shows the convergence of $\|\nabla(p-p_h)\|_{\boldsymbol{L}^2(\Omega_2)}$. The experimental rates confirm the theoretical rate of $\mathcal{O}(h^k)$.

The errors in the L^2 norm for the Navier–Stokes velocity and Darcy pressure are shown to converge in Figs. 5 and 6. Since the nonsymmetric discontinuous Galerkin method is used, we observe that the rate is $\mathcal{O}(h^k)$ if k is odd and $\mathcal{O}(h^{k+1})$ if k is even. This loss of optimality for even degrees is well known (see for instance [33]).

5.2 Polygonal Interface

In the second example, the rectangular domain $\Omega = (0,2)\times(0,1.25)$ is partitioned into two subdomains by a polygonal interface with three successive uniform

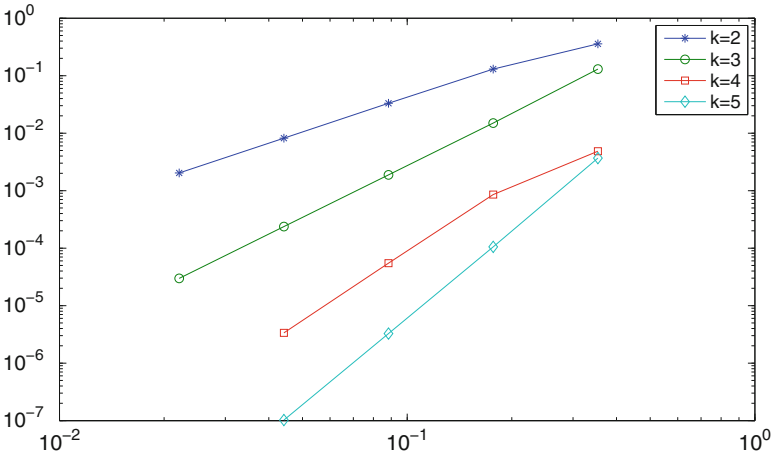

Fig. 2 Numerical error versus mesh size for the L^2 norm of the gradient of Navier–Stokes velocity for several polynomial degrees

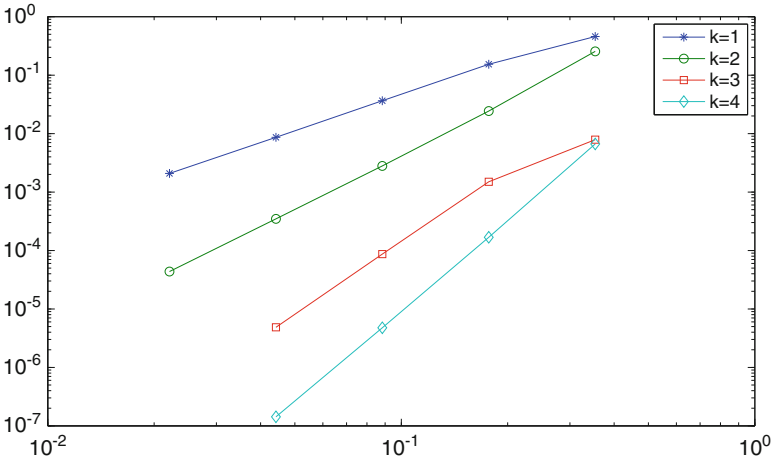

Fig. 3 Numerical error versus mesh size for the L^2 norm of the Navier–Stokes pressure for several polynomial degrees

steps (see Fig. 7). The Navier–Stokes equations are solved in Ω_1 and the Darcy equations in Ω_2. Zero Dirichlet boundary conditions are imposed on the bottom horizontal side of Ω_2 and zero Neumann boundary conditions on the remainder of $\partial\Omega_2 \setminus \Gamma_{12}$. The Navier–Stokes velocity on Γ_1 is set equal to $(-3(y-1.25)(y-0.5),0)$, which means the velocity profile is parabolic along the vertical side of Γ_1. The DG scheme is used with $\varepsilon_1 = \varepsilon_2 = -1$, $\sigma_e = 1$; see (28). As in the first example, the viscosity is equal to 1 and the Beavers–Joseph-Saffman constant α

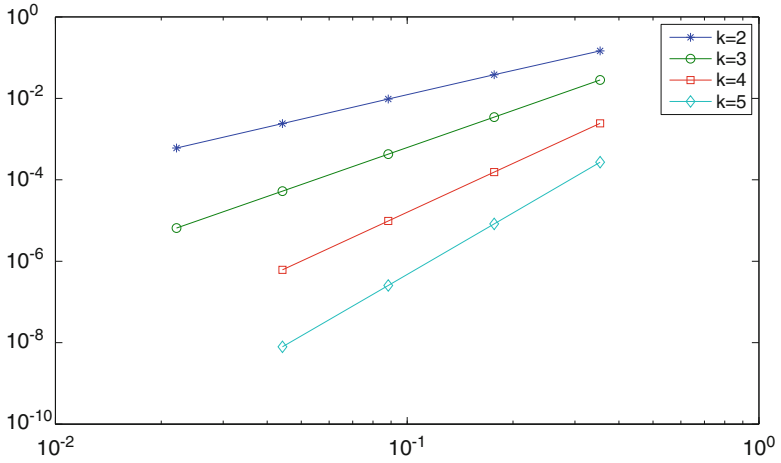

Fig. 4 Numerical error versus mesh size for the L^2 norm of the gradient of Darcy pressure for several polynomial degrees

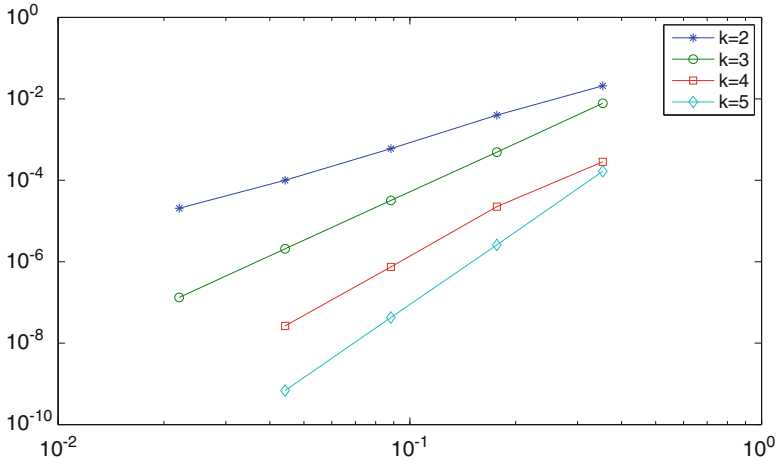

Fig. 5 Numerical error versus mesh size for the L^2 norm of the Navier–Stokes velocity

equal to 10. We fix the polynomial degrees: $k_1 = k_2 = 2$. The mesh contains 5,760 triangles of varying size so that the triangles in the neighborhood of the interface are smaller. The tolerance for stopping the Picard iterations is 10^{-7}. We vary the permeability field $\boldsymbol{K} = 10^{-n}\boldsymbol{I}$, with $n \in \{0, 2, 4, 6\}$. The contours of the x-component and y-component of the velocity are shown in Figs. 8–11.

We first observe that the normal component of the velocity is continuous across the interface, but the tangential component of the velocity is discontinuous. In

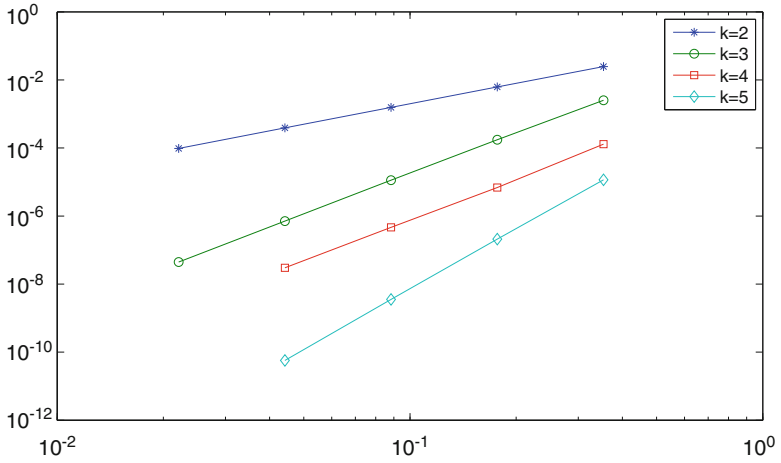

Fig. 6 Numerical error versus mesh size for the L^2 norm of Darcy pressure

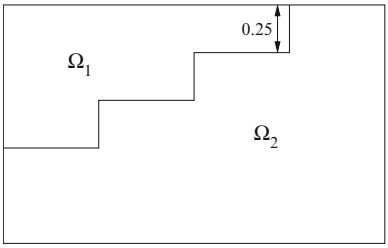

Fig. 7 Computational domain for second example

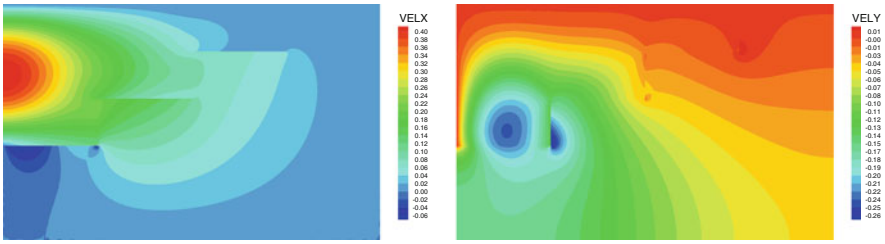

Fig. 8 Numerical solution for velocity in the case of $\boldsymbol{K} = \boldsymbol{I}$: x-component (*left figure*) and y-component (*right figure*)

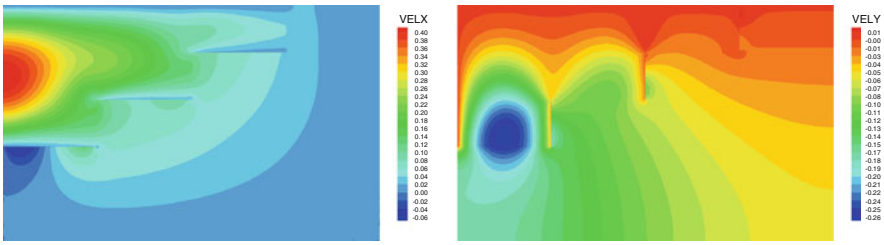

Fig. 9 Numerical solution for velocity in the case of $\boldsymbol{K} = 10^{-2}\boldsymbol{I}$: x-component (*left figure*) and y-component (*right figure*)

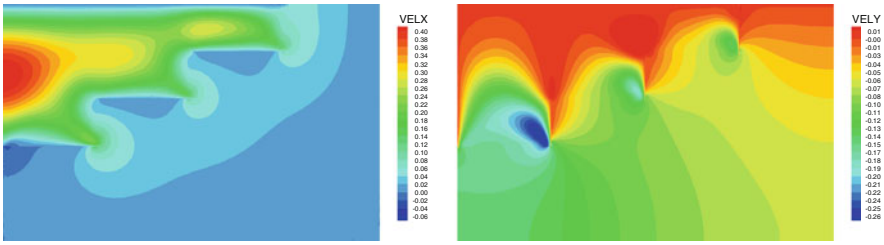

Fig. 10 Numerical solution for velocity in the case of $\boldsymbol{K} = 10^{-4}\boldsymbol{I}$: x-component (*left figure*) and y-component (*right figure*)

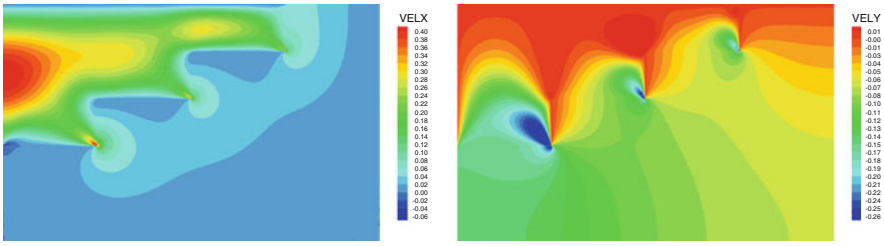

Fig. 11 Numerical solution for velocity in the case of $\boldsymbol{K} = 10^{-6}\boldsymbol{I}$: x-component (*left figure*) and y-component (*right figure*)

addition, as the permeability value decreases, the fluid from the free flow penetrates a smaller region of the porous domain.

Acknowledgements The first author acknowledges support from the UT Austin/Portugal Collaboration, Project: UT Austin/MAT/0066/2008 "Reaction-Diffusion in Porous Media." The second author acknowledges support by NSF grant no. DMS–0810387 and by KAUST award no. KUS-C1-016-04. The third author acknowledges support from NSF with the grant DMS 0810422.

References

1. Adams, R.A., Fournier, J.J.F.: Sobolev Spaces, 2nd edn. Academic (Elsevier), Amsterdam (2003)
2. Allaire, G.: Homogenization of the Navier–Stokes equations in open sets perforated with tiny holes. I. Abstract framework, a volume distribution of holes. Arch. Rational Mech. Anal. **113**, 209–259 (1991)
3. Allaire, G.: Homogenization of the Navier–Stokes equations in open sets perforated with tiny holes. II. Noncritical sizes of the holes for a volume distribution and a surface distribution of holes. Arch. Rational Mech. Anal. **113**, 261–298 (1991)
4. Amrouche, C., Bernardi, C., Dauge, M., Girault, V.: Vector potentials in three-dimensional nonsmooth domains. Math. Meth. Appl. Sci. **21**, 823–864 (1998)
5. Arbogast, T., Lehr, H.L.: Homogenization of a Darcy–Stokes system modeling vuggy porous media. Comput. Geosci. **10**, 291–302 (2006)
6. Arbogast, T., Brunson, D.: A computational method for approximating a Darcy-Stokes system governing a vuggy porous medium. Comput. Geosci. **11**, 207–218 (2007)
7. Badía, S., Codina, R.: Unified stabilized finite element formulations for the Stokes and the Darcy problems. SIAM J. Numer. Anal. **47**, 1971–2000 (2009)
8. Badea, L., Discacciati, M., Quarteroni, A.: Numerical analysis of the Navier-Stokes/Darcy coupling. Numer. Math. **115**, 195–227 (2010)
9. Beavers, G.S., Joseph, D.D.: Boundary conditions at a naturally impermeable wall. J. Fluid. Mech. **30**, 197–207 (1967)
10. Braack, M., Schieweck, F.: Equal-order finite elements with local projection stabilization for the Darcy–Brinkman equations. Comput. Methods Appl. Mech. Eng. **200**, 9–12 (2011)
11. Brezzi, F., Fortin, M.: Mixed and Hybrid Finite Element Methods. Springer, New York (1991)
12. Burman, E., Hansbo, P.: A unified stabilized method for Stokes and Darcy's equations. J. Comput. Appl. Math. **198**, 35–51 (2007)
13. Cai, M., Mu, M., Xu, J.: Numerical solution to a mixed Navier-Stokes/Darcy model by the two-grid approach. SIAM J. Numer. Anal. **47**, 3325–3338 (2009)
14. Cao, Y., Gunzburger, M., Hua, F., Wang, X.: Coupled Stokes-Darcy model with Beavers-Joseph interface boundary condition. Commun. Math. Sci. **8**, 1–25 (2010)
15. Cesmelioglu, A., Rivière, B.: Existence of a weak solution for the fully coupled Navier–Stokes/Darcy-transport problem. J. Diff. Equations. **252**, 4138–4175 (2012)
16. Chidyagwai, P., Rivière, B.: On the solution of the coupled Navier–Stokes and Darcy equations. Comput. Methods Appl. Mech. Eng. **198**, 3806–3820 (2009)
17. Chidyagwai, P., Rivière, B.: A two-grid method for coupled free flow with porous media flow. Adv. Water Resour. **34**, 1113–1123 (2011)
18. Ciarlet, P.G.: Basic error estimates for elliptic problems—finite element methods, part 1. In: Ciarlet, P.G., Lions, J.-L. (eds.) Handbook of Numerical Analysis, vol. 2, pp. 17–352. Elsevier/North-Holland, Amsterdam (1991)
19. Cockburn, B., Kanschat, G., Schoetzau, D., Schwab, C.: Local discontinuous Galerkin methods for the Stokes system. SIAM J. Numer. Anal. **40**, 319–343 (2002)
20. Cockburn, B., Kanschat, G., Schoetzau, D.: A locally conservative LDG method for the incompressible Navier–Stokes equations. Math. Comput. **74**, 1067–1095 (2005)
21. Cockburn, B., Kanschat, G., Schoetzau, D.: A note on discontinuous Galerkin divergence-free solutions of the Navier–Stokes equations. J. Sci. Comput. **31**, 61–73 (2007)
22. Discacciati, M., Quarteroni, A.: Analysis of a domain decomposition method for the coupling of Stokes and Darcy equations. In: Brezzi, F., Buffa, A., Corsaro, S., Murli, A. (eds.) Numerical Mathematics and Advanced Applications—ENUMATH 2001, pp. 3–20. Springer, Milan (2003)
23. Discacciati, M., Miglio, E., Quarteroni, A.: Mathematical and numerical models for coupling surface and groundwater flows. Appl. Numer. Math. **43**, 57–74 (2002)

24. Discacciati, M., Quarteroni, A., Valli, A.: Robin-Robin domain decomposition methods for the Stokes–Darcy coupling. SIAM J. Numer. Anal. **45**, 1246–1268 (2007)
25. Galvis, J., Sarkis, M.: Balancing domain decomposition methods for mortar coupling Stokes-Darcy systems. In: Widlund, O., Keyes, D. (eds.) Lecture Notes in Computational Science and Engineering, vol. 55, pp. 373–380. Springer, Berlin (2007)
26. Galvis, J., Sarkis, M.: Non-matching mortar discretization analysis for the coupling Stokes–Darcy equations. Electron. Trans. Numer. Anal. **26**, 350–384 (2007)
27. Gatica, G., Meddahi, S., Oyarzua, R.: A conforming mixed finite-element method for the coupling of fluid flow with porous media flow. IMA J. Numer. Anal. **29**, 86–108 (2009)
28. Gatica, G.N., Oyarzua, R., Sayas, F.-J.: Analysis of fully-mixed finite element methods for the Stokes–Darcy coupled problem. Math. Comput. **80**, 1911–1948 (2011)
29. Gatica, G.N., Oyarzua, R., Sayas, F.-J.: Convergence of a family of Galerkin discretizations for the Stokes–Darcy coupled problem. Numer. Methods Partial Differ. Equ. **27**, 721–748 (2011)
30. Geuzaine, C., Remacle, J.-F.: Gmsh: a three-dimensional finite element mesh generator with built-in pre- and post-processing facilities. Int. J. Numer. Methods Eng. **79**, 1309–1331 (2009)
31. Girault, V., Raviart, P.-A.: Finite Element Approximations of the Navier–Stokes Equations. Springer, Heidelberg (1986)
32. Girault, V., Rivière, B.: DG approximation of coupled Navier-Stokes and Darcy equations by Beaver-Joseph-Saffman interface condition. SIAM J. Numer. Anal. **47**, 2052–2089 (2009)
33. Guzman, J., Rivière, B.: Sub-optimal convergence of non-symmetric discontinuous Galerkin methods for odd polynomial approximations. J. Sci. Comput. **40**, 273–280 (2009)
34. Hanspal, N., Waghode, A., Nassehi, V., Wakeman, R.: Numerical analysis of coupled Stokes/Darcy flows in industrial filtrations. Transport Porous Med. **64**, 1573–1634 (2006)
35. Iliev, O.P., Lazarov, R.D., Willems, J.: Discontinuous Galerkin subgrid finite element method for approximation of heterogeneous Brinkman's equations. In: Lirkov, I., Margenov, S., Wasniewski, J. (eds.) Lecture Notes in Computer Science, vol. 5910, pp. 14–25. Springer, Heidelberg (2010)
36. Jaeger, W., Mikelic, A.: On the boundary conditions at the contact interface between a porous medium and a free fluid. Ann. Scuola Norm. Sup. Pisa Cl. Sci. (4). **23**, 403–465 (1996)
37. Jaeger, W., Mikelic, A.: On the interface boundary condition of Beavers, Joseph, and Saffman. SIAM J. Appl. Math. **60**, 1111–1127 (2000)
38. Jaeger, W., Mikelic, A.: Modeling effective interface laws for transport phenomena between an unconfined fluid and a porous medium using homogenization. Transport Porous Med. **78**, 489–508 (2009)
39. Jaeger, W., Mikelic, A., Neuss, N.: Asymptotic analysis of the laminar viscous flow over a porous bed. SIAM J. Sci. Comput. **22**, 2006–2028 (2000)
40. Juntunen, M., Stenberg, R.: Analysis of finite element methods for the Brinkman problem. Calcolo. **47**, 129–147 (2010)
41. Kanschat, G.: Discontinuous Galerkin Methods for Viscous Flow. Deutscher Universitätsverlag, Wiesbaden (2007)
42. Kanschat, G., Rivière, B.: A strongly conservative finite element method for the coupling of Stokes and Darcy flow. J. Comput. Phys. **229**, 5933–5943 (2010)
43. Karper, T., Mardal, K.A., Winther, R.: Unified finite element discretizations of coupled Darcy–Stokes flow. Numer. Methods Partial Differ. Equ. **25**, 311–326 (2009)
44. Layton, W.J., Schieweck, F., Yotov, I.: Coupling fluid flow with porous media flow. SIAM J. Numer. Anal. **40**, 2195–2218 (2003)
45. LeSaint, P., Raviart, P.-A.: On a finite element method for solving the neutron transport equation. In: de Boor, C. (ed.) Mathematical aspects of finite elements in partial differential equations, pp. 89–123. Academic, New York (1974)
46. Lions, J.-L., Magenes, E.: Nonhomogeneous Boundary Value Problems and Applications. Springer, Berlin (1972)
47. Mardal, K.A., Tai, X.-C., Winther, R.: A robust finite element method for Darcy–Stokes flow. SIAM J. Numer. Anal. **40**, 1605–1631 (2002)
48. Mu, M., Xu, J.: A two-grid method of a mixed Stokes–Darcy model for coupling fluid flow with porous media flow. SIAM J. Numer. Anal. **45**, 1801–1813 (2007)

49. Rivière, B.: Analysis of a discontinuous finite element method for the coupled Stokes and Darcy problems. J. Sci. Comput. **22**, 479–500 (2005)
50. Rivière, B.: Discontinuous Galerkin Methods for Solving Elliptic and Parabolic Equations. Frontiers in Applied Mathematics. SIAM, Philadelphia (2008)
51. Rivière, B., Yotov, I.: Locally conservative coupling of Stokes and Darcy flow. SIAM J. Numer. Anal. **42**, 1959–1977 (2005)
52. Rivière, B., Wheeler, M.F., Girault, V.: A priori error estimates for finite element methods based on discontinuous approximation spaces for elliptic problems. SIAM J. Numer. Anal. **39**, 902–931 (2001)
53. Saffman, P.: On the boundary condition at the surface of a porous media. Stud. Appl. Math. **50**, 292–315 (1971)
54. Tecplot, Inc. http://www.tecplot.com/
55. Vassilev, D., Yotov, I.: Coupling Stokes–Darcy flow with transport. SIAM J. Sci. Comp. **31**, 3661–3684 (2009)
56. Wang, J., Ye, X.: New finite element methods in computational fluid dynamics by $H(\mathrm{div})$ elements. SIAM J. Numer. Anal. **45**, 1269–1286 (2007)
57. Xie, X., Xu, J., Xue, G.: Uniformly-stable finite element methods for Darcy–Stokes–Brinkman models. J. Comput. Math. **26**, 437–455 (2008)

Comparison of Control Volume Analysis and Porous Media Averaging for Formulation of Porous Media Transport

F. Civan

Abstract Although the porous media averaging is frequently used it creates many difficulties in handling of the closure problems. The control volume analysis on the other hand can avoid such difficulties in a practical manner. Thus, the outstanding and complementary features of these two approaches used in the macroscopic formulation of transport through porous media are critically reviewed, compared, and evaluated. Several instructive examples are presented demonstrating their applications with various improvements.

1 Introduction

The formulation of macroscopic equations of porous media transport phenomena continues to occupy the researchers because of various unresolved issues such as the necessity of using different representative elementary volumes (REV) for different quantities and proper methods required for closure problems and reducing the complexity of the resulting equations for applications of practical importance. Although some rules of averaging have now been well established, applications in different ways may result with different formulations and their inherent limiting conditions are frequently overlooked. This includes the use of the same representative elemental volume for different quantities and assuming the volume and area averages to be the same [12]. Volume averaging of microscopic equations of transport processes may lead to extremely complicated results to be of any practical value [10, 11, 14, 18, 20]. Nevertheless, the control volume analysis can be complementary in resolving some of the difficulties of porous media volume averaging [5–7]. This chapter investigates the formulation of macroscopic transport equations

F. Civan (✉)
Mewbourne School of Petroleum and Geological Engineering, The University of Oklahoma, 100 East Boyd, SEC Room 1210 Norman, OK 73019-1003, USA
e-mail: fcivan@ou.edu

J.A. Ferreira et al. (eds.), *Modelling and Simulation in Fluid Dynamics in Porous Media*, Springer Proceedings in Mathematics & Statistics 28, DOI 10.1007/978-1-4614-5055-9_2,

by means of the porous media averaging and control volume analysis approaches and comparison of the results to determine the complementary benefits of these two different approaches. The formulations of the spontaneous transport terms and the representative volume-averaging and control volume analysis approaches are reviewed and their applications are demonstrated by various examples. The discrepancies occurring between the results obtained here and the corresponding efforts reported in the literature and their reasons are explained.

2 Spontaneous Transport

Many processes in porous media occur spontaneously because of the nonequilibrium conditions prevailing over a distance in porous media and are expressed by the following empirical gradient law [6, 7]:

$$\mathbf{j}_{jb} = \varepsilon_j \mathbf{j}_j = -\frac{1}{\varepsilon_j}\mathbf{D}_{jb} \cdot (\nabla f_{jb} - \mathbf{f}_{Rjb}) = -\frac{1}{\varepsilon_j}\mathbf{D}_{jbe} \cdot \nabla f_{jb} = -\mathbf{D}_{je} \cdot \nabla f_{jb}, \qquad (1)$$

where ε_j is the volume fraction of the j-phase present in the bulk volume of porous media, f_{jb} and f_j denote the bulk- and phase-volume averages of a property of the j-phase, respectively, $\mathbf{j}_{jb}$ and $\mathbf{j}_j$ denote the flux vectors of property f_j of the j-phase transferred across the bulk-surface area and the open-pore-surface area, respectively, $\mathbf{f}_{Rjb}$ denotes a vector representing the net internal resistance to transfer of property f_j of the j-phase through the bulk volume of porous media, and $\mathbf{D}_{jb}$, $\mathbf{D}_{jbe}$, and $\mathbf{D}_{je}$ are the various types of transport coefficients of property f_j of the j-phase appearing in Eq. (1) which are related by the following relationships:

$$\mathbf{D}_{jbe} = \left(1 - \frac{\mathbf{f}_{Rjb} \cdot \nabla f_{jb}}{\nabla f_{jb} \cdot \nabla f_{jb}}\right)\mathbf{D}_{jb}, \quad \text{when } 1 - \frac{\mathbf{f}_{Rjb} \cdot \nabla f_{jb}}{\nabla f_{jb} \cdot \nabla f_{jb}} > 0,$$

$$\mathbf{D}_{jbe} = \mathbf{0}, \quad \text{when } 1 - \frac{\mathbf{f}_{Rjb} \cdot \nabla f_{jb}}{\nabla f_{jb} \cdot \nabla f_{jb}} \leqslant 0,$$

and

$$\mathbf{D}_{je} = \frac{1}{\varepsilon_j}\mathbf{D}_{jbe}. \qquad (2)$$

The gradient law in various forms similar to Eq. (1) can be used also as an empirical means of achieving the closure for the averages of the products of deviations from the individual averages of various quantities. The empirical coefficients of transport $\mathbf{D}_{jb}$, $\mathbf{D}_{jbe}$, and $\mathbf{D}_{je}$ of various types given in Eq. (2) are referred to as the dispersion coefficients.

The gradient term appearing in Eq. (1) and elsewhere in the various formulations of porous media transport inherently involves the application of the *extrapolated limit* concept of [13] as illustrated in Fig. 1. Therefore, the gradient is expressed with

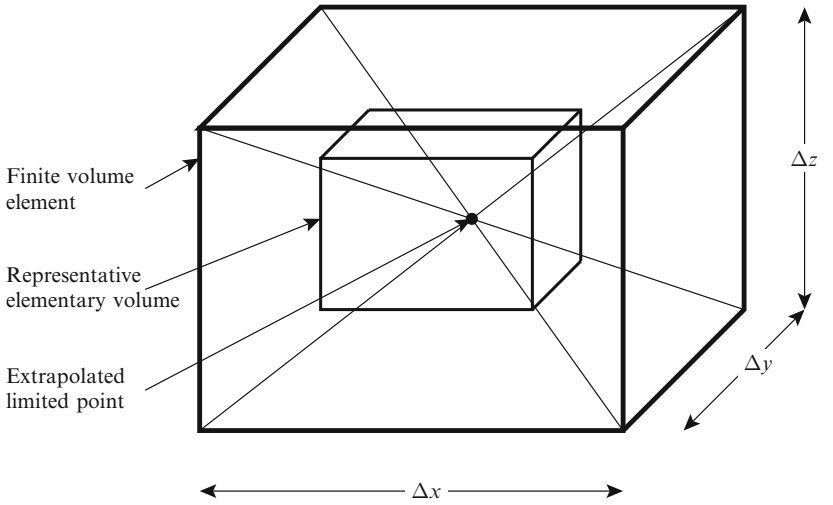

Fig. 1 Illustration of the *extrapolated limit* concept of [13]

respect to the amount of the property of interest contained in the bulk volume. This is a remedial measure because the basic definition of derivative which considers the limit as $\Delta x, \Delta y$, and $\Delta z \to 0$ is not rigorously applicable in porous media but nevertheless used in derivation of macroscopic equations. This issue is subtle and is mostly overlooked. For example, fluid tends to move from a high-density location to a low-density location at a rate proportional to the density gradient $\nabla\rho$ in the microscopic formulation of single-phase fluid systems. However, the gradient should be expressed as $\nabla(\varepsilon\rho)$ in terms of the mass of fluid contained in porous media for macroscopic formulation which is the product of the volume fraction ε and density ρ of the fluid present in porous media [4]. Consequently, the gradient law of porous media transport appears to have a problem in the special case when the fluid is incompressible. However, transport can occur in porous media averaged description even in the case of incompressible fluids when the volume fraction of the fluid varies with distance because the mass of fluid contained in porous media is different over a distance.

An application of Eq. (1) is demonstrated by derivation of Darcy's law. It should be emphasized that Darcy's law was derived with respect to the pressures applied at the outside surfaces of porous media. This bulk-volume average pressure is related to the intrinsic phase-volume average pressure by [6]

$$p_{jb} = [\alpha + (1-\alpha)c\varepsilon_j^{d/3}]p_j, \quad 0 \leqslant \alpha \leqslant 1. \tag{3}$$

Equation (3) assumes a fractal relationship between the cross-sectional area of flowing fluid and its volume fraction in porous media with a fractal coefficient of c and dimension of d, which may be replaced with other types of relationships, and

α denotes the effective stress coefficient of [1]. Equation (3) considers the effect of stress transmission through porous media depending on its elasticity.

Thus, the modified Darcy's law can be derived from Eq. (1) simply by substituting $f_{jb} \equiv p_{jb}$, $\mathbf{f}_{Rjb} \equiv \mathbf{p}_{Rjb}$, $\mathbf{j}_{jb} \equiv \mathbf{v}_{jb}$, and $\mathbf{D}_{jbe} \equiv \frac{1}{\mu_j}\mathbf{K}_{jbe}$ as

$$\begin{aligned}\mathbf{v}_{jb} = \varepsilon_j \mathbf{v}_j &= -\frac{1}{\varepsilon_j}\frac{1}{\mu_j}\mathbf{K}_{jb}\cdot(\nabla p_{jb} - \mathbf{p}_{Rjb}) \\ &= -\frac{1}{\varepsilon_j}\frac{1}{\mu_j}\mathbf{K}_{jbe}\cdot\nabla p_{jb} = -\frac{1}{\mu_j}\mathbf{K}_{je}\cdot\nabla p_{jb},\end{aligned} \tag{4}$$

where p_{jb} and p_j denote the bulk-volume average and the phase-volume average pressures, μ_j is the dynamic viscosity of the j-phase, respectively, $\mathbf{v}_{jb}$ and $\mathbf{v}_j$ denote the volumetric flux vectors of the j-phase transferred across the bulk-surface area and the open-pore-surface area, respectively, $\mathbf{p}_{Rjb}$ is a vector representing the threshold pressure gradient below which the j-phase cannot flow through porous media because of internal resistance [16], and $\mathbf{K}_{jb}$, $\mathbf{K}_{jbe}$, and $\mathbf{K}_{je}$ are the various types of effective permeability coefficients for the j-phase appearing in Eq. (4) which are related by the following relationships:

$$\mathbf{K}_{jbe} = \left(1 - \frac{\mathbf{p}_{Rjb}\cdot\nabla p_{jb}}{\nabla p_{jb}\cdot\nabla p_{jb}}\right)\mathbf{K}_{jb}, \quad \text{when } 1 - \frac{\mathbf{p}_{Rjb}\cdot\nabla p_{jb}}{\nabla p_{jb}\cdot\nabla p_{jb}} > 0,$$

$$\mathbf{K}_{jbe} = \mathbf{0}, \quad \text{when } 1 - \frac{\mathbf{p}_{Rjb}\cdot\nabla p_{jb}}{\nabla p_{jb}\cdot\nabla p_{jb}} \leqslant 0,$$

and

$$\mathbf{K}_{je} = \frac{1}{\varepsilon_j}\mathbf{K}_{jbe}. \tag{5}$$

In view of the above formulation, the law of motion introduced by [9] inherently assumes a perfectly rigid porous media for which case Biot's coefficient is given as $\alpha = 1$ [6, 15]. On the other hand, Biot's coefficient becomes $\alpha = 0$ for completely poroelastic porous media. However, its value needs to be determined empirically for natural porous materials. Further, the original Darcy's law assumes that flow occurs as long as a pressure differential is applied across porous media and therefore does not consider the need to overcome a threshold pressure gradient to initiate fluid flow.

3 Porous Media Averaging

The derivation of the macroscopic transport equations is often accomplished by averaging of the microscopic transport equations over REV [18]. The REV should be selected differently for different quantities as demonstrated by [8]. However, this issue is omitted in the following in order to avoid the additional complications so that the present discussion can focus on the issue of comparison and evaluation

of results obtained from REV-averaging and control volume analysis approaches. First, a brief review and summary of the REV-averaging rules is presented and then several applications are illustrated by various examples. The scalar, vector, and tensor properties considered in the following sections are identified using the non-bold, lowercase bold, and uppercase bold symbols.

3.1 Representative Elementary Volume-Averaging Rules

Consider the j-phase in a multiphase system containing $j = 1,2,,N$ phases (solid and fluid). The representative elementary bulk volume of porous media is V_b. The volume of the j-phase contained in the representative elementary bulk volume is V_j. The j-phase can interact with the other phases (solid and fluid) in various ways.

The bulk-volume (superficial) average of a property f of the j-phase is given by [11, 18, 20]

$$\langle f_j \rangle_b = \frac{1}{V_b} \int_{V_j} f_j \, dV. \tag{6}$$

The individual phase-volume (intrinsic) average of a property f of the j-phase is given by [11, 18, 20]

$$\langle f_j \rangle_j = \frac{1}{V_j} \int_{V_j} f_j \, dV. \tag{7}$$

The value of a property f of the j-phase at a certain point inside the REV is given as the sum of the intrinsic average value $\langle f_j \rangle_j$ and its deviation $\widehat{f}_j$ from the intrinsic average value as [11]

$$f_j = \langle f_j \rangle_j + \widehat{f}_j, \quad \langle \widehat{f}_j \rangle_j = 0 \text{ in } V_j. \tag{8}$$

The relationship between the superficial and intrinsic volume averages of a property f is given by

$$\langle f_j \rangle_b = \varepsilon_j \langle f_j \rangle_j. \tag{9}$$

Thus, the following expressions can be derived for the product of two properties and the averages of the products of two and three properties, respectively [7]:

$$\mathbf{v}_j f_j = \langle \mathbf{v}_j \rangle_j \langle f_j \rangle_j + 2\widehat{\mathbf{v}}_j \langle f_j \rangle_j + \widehat{\mathbf{v}}_j \widehat{f}_j, \tag{10}$$

$$\begin{aligned} \langle \mathbf{v}_j f_j \rangle_b &= \varepsilon_j \langle \mathbf{v}_j f_j \rangle_j = \varepsilon_j \left(\langle \mathbf{v}_j \rangle_j \langle f_j \rangle_j + \langle \widehat{\mathbf{v}}_j \widehat{f}_j \rangle_j \right) \\ &= \frac{1}{\varepsilon_j} \langle \mathbf{v}_j \rangle_b \langle f_j \rangle_b + \langle \widehat{\mathbf{v}}_j \widehat{f}_j \rangle_b, \end{aligned} \tag{11}$$

and

$$\begin{aligned}\langle \rho_j \mathbf{v}_j f_j \rangle_b &= \varepsilon_j \langle \rho_j \mathbf{v}_j f_j \rangle_j \\ &= \varepsilon_j \left(\langle \rho_j \rangle_j \langle \mathbf{v}_j \rangle_j \langle f_j \rangle_j + \langle \rho_j \rangle_j \left\langle \widehat{\mathbf{v}}_j \widehat{f}_j \right\rangle_j \right. \\ &\quad \left. + \langle \mathbf{v}_j \rangle_j \langle \widehat{\rho}_j \widehat{f}_j \rangle_j + \langle f_j \rangle_j \langle \widehat{\rho}_j \widehat{\mathbf{v}}_j \rangle_j + \langle \widehat{\rho}_j \widehat{\mathbf{v}}_j \widehat{f}_j \rangle_j \right) \\ &= \frac{1}{\varepsilon_j^2} \langle \rho_j \rangle_b \langle \mathbf{v}_j \rangle_b \langle f_j \rangle_b + \frac{1}{\varepsilon_j} \langle \rho_j \rangle_b \left\langle \widehat{\mathbf{v}}_j \widehat{f}_j \right\rangle_b + \frac{1}{\varepsilon_j} \langle \mathbf{v}_j \rangle_b \left\langle \widehat{\rho}_j \widehat{f}_j \right\rangle_b \\ &\quad + \frac{1}{\varepsilon_j} \langle f_j \rangle_b \langle \widehat{\rho}_j \widehat{\mathbf{v}}_j \rangle_b + \left\langle \widehat{\rho}_j \widehat{\mathbf{v}}_j \widehat{f}_j \right\rangle_b . \end{aligned} \tag{12}$$

The volume averages of the time derivative and gradient of a property f of the j-phase are given, respectively, by [10, 18, 20]

$$\begin{aligned}\left\langle \frac{\partial f_j}{\partial t} \right\rangle_b &= \frac{\partial \langle f_j \rangle_b}{\partial t} - \frac{1}{V_b} \int_{A_j} f_j \mathbf{v}_{Aj} \cdot \mathbf{n}_j \, dA \\ &= \frac{\partial (\varepsilon_j \langle f_j \rangle_j)}{\partial t} - \frac{1}{V_b} \int_{A_j} f_j \mathbf{v}_{Aj} \cdot \mathbf{n}_j \, dA, \end{aligned} \tag{13}$$

and

$$\langle \nabla f_j \rangle_b = \nabla \langle f_j \rangle_b + \frac{1}{V_b} \int_{A_j} f_j \mathbf{n}_j \, dA = \langle \nabla \rangle_j \left(\varepsilon_j \langle f_j \rangle_j \right) + \frac{1}{V_b} \int_{A_j} f_j \mathbf{n}_j \, dA. \tag{14}$$

Although frequently used in the literature, their derivations involve some assumptions which are not rigorously correct such as the consideration of the volumetric and area averages to be the same [12]. Here t is time and ∇ is the gradient operator. A_j is the surface area of the j-phase. $\mathbf{v}_{Aj}$ is the velocity of the surface area A_j of the j-phase at which it moves. A is the surface area variable. $\mathbf{n}_j$ is the outward unit normal vector. The symbols ∇ and $\langle \nabla \rangle_j$ denote the microscopic and macroscopic gradient operators, respectively [12]. However, in the rest of the development in this chapter simply ∇ will be used for convenience also for the macroscopic gradient operator.

However, the alternative procedure illustrated in the following yields different results than Eqs. (13) and (14), respectively, as

$$\begin{aligned}\left\langle \frac{\partial f_j}{\partial t} \right\rangle_b &= \varepsilon_j \left\langle \frac{\partial f_j}{\partial t} \right\rangle_j = \varepsilon_j \left(\frac{\partial \langle f_j \rangle_j}{\partial t} - \frac{1}{V_j} \int_{A_j} f_j \mathbf{v}_{Aj} \cdot \mathbf{n}_j \, dA \right) \\ &= \varepsilon_j \frac{\partial}{\partial t} \left(\frac{\langle f_j \rangle_b}{\varepsilon_j} \right) - \frac{1}{V_b} \int_{A_j} f_j \mathbf{v}_{Aj} \cdot \mathbf{n}_j \, dA \end{aligned} \tag{15}$$

and similarly

$$\langle \nabla f_j \rangle_b = \varepsilon_j \langle \nabla f_j \rangle_j = \varepsilon_j \left(\nabla \langle f_j \rangle_j + \frac{1}{V_j} \int_{A_j} f_j \mathbf{n}_j \, dA \right)$$
$$= \varepsilon_j \nabla \left(\frac{\langle f_j \rangle_b}{\varepsilon_j} \right) + \frac{1}{V_b} \int_{A_j} f_j \mathbf{n}_j \, dA \tag{16}$$

Notice that Eqs. (13) and (14) will be identical to Eqs. (15) and (16) only when the fluid phase-volume fraction ε_j is constant. This exercise illustrates the variation of the results by the ways of implementation of the basic rules of volume averaging.

Consider now the microscopic conservation equation for a property f of a system, given by

$$\frac{\partial f_j}{\partial t} + \nabla \cdot \mathbf{j}_{Tj} = q_j, \tag{17}$$

where q_j is a source term. The total transfer term for quantity f_j is described by

$$\mathbf{j}_{Tj} = \mathbf{v}_j f_j + \mathbf{j}_j, \; \mathbf{j}_j = -\mathbf{D}_j \cdot \nabla f_j, \tag{18}$$

where $\mathbf{j}_{Tj}$ is the total effective transport rate and $\mathbf{j}_j$ is the spontaneous transport of quantity f_j in the j-phase.

Thus, substituting Eq. (18) into Eq. (17) yields a transient-state convection/advection, dispersion, and source equation for transport of quantity f_j through porous media as

$$\frac{\partial f_j}{\partial t} + \nabla \cdot (\mathbf{v}_j f_j) = \nabla \cdot (\mathbf{D}_j \cdot \nabla f_j) + q_j. \tag{19}$$

Let ρ_j and f_j denote the density and an intensive property of the j-phase, respectively, $\mathbf{v}_j$ is the velocity vector, $\mathbf{D}_j$ is the diffusivity tensor, and q_j denotes the mass added per unit volume of the j-phase per unit time. In these equations, f_j is equal to ρ_j, $\rho_j \mathbf{v}_j$, and $H_j = \rho_j C_j T_j$ for the conservations of mass, momentum, and energy, respectively. H_j is the enthalpy, T_j denotes the temperature, and C_j is the specific heat capacity at constant pressure of the j-phase.

The volume average of Eq. (17) applying Eq. (6) yields

$$\left\langle \frac{\partial f_j}{\partial t} \right\rangle_b + \langle \nabla \cdot (\mathbf{v}_j f_j) \rangle_b = \langle \nabla \cdot (\mathbf{D}_j \cdot \nabla f_j) \rangle_b + \langle q_j \rangle_b . \tag{20}$$

The following relationships can be written using Eq. (13):

$$\langle \nabla \cdot (\mathbf{v}_j f_j) \rangle_b = \nabla \cdot \langle \mathbf{v}_j f_j \rangle_b + \frac{1}{V_b} \int_{A_j} (\mathbf{v}_j f_j) \cdot \mathbf{n}_j \, dA \tag{21}$$

and

$$\langle \nabla \cdot (\mathbf{D}_j \cdot \nabla f_j) \rangle_b = \nabla \cdot \langle \mathbf{D}_j \cdot \nabla f_j \rangle_b + \frac{1}{V_b} \int_{A_j} (\mathbf{D}_j \cdot \nabla f_j) \cdot \mathbf{n}_j \, dA. \tag{22}$$

Thus, the application of Eqs. (13), (21), and (22) to Eq. (20) yields

$$\frac{\partial}{\partial t}\left\langle f_j\right\rangle_b+\nabla\cdot\left\langle \mathbf{v}_j f_j\right\rangle_b=\nabla\cdot\left\langle \mathbf{D}_j\cdot\nabla f_j\right\rangle_b+\sum_l\frac{-1}{V_b}\int_{A_{jl}} f_j(\mathbf{v}_j-\mathbf{v}_{Ajl})\cdot\mathbf{n}_j\,dA$$
$$+\sum_l\frac{1}{V_b}\int_{A_{jl}}\mathbf{D}_j\cdot\nabla f_j\cdot\mathbf{n}_j\,dA+\left\langle q_j\right\rangle_b, \tag{23}$$

where l denotes the various phases present in porous media including the porous solid matrix which is in contact with the j-phase.

In the following, the expressions for $\left\langle \mathbf{D}_j\cdot\nabla f_j\right\rangle_b$ are derived by two alternative approaches and the results are compared. The details of the first approach are presented in the following, delineating simultaneously the application of the basic averaging rules:

$$\begin{aligned}
\left\langle \mathbf{D}_j\cdot\nabla f_j\right\rangle_b&=\varepsilon_j\left\langle \mathbf{D}_j\cdot\nabla f_j\right\rangle_j\\
&=\varepsilon_j\left\langle\left(\left\langle \mathbf{D}_j\right\rangle_j+\widehat{\mathbf{D}}_j\right)\cdot\nabla\left(\left\langle f_j\right\rangle_j+\widehat{f_j}\right)\right\rangle_j\\
&=\varepsilon_j\left(\left\langle \mathbf{D}_j\right\rangle_j\cdot\left\langle\nabla\left\langle f_j\right\rangle_j\right\rangle_j\right.\\
&\quad+\left\langle \mathbf{D}_j\right\rangle_j\cdot\left\langle\nabla\widehat{f_j}\right\rangle_j+\left\langle\widehat{\mathbf{D}}_j\right\rangle_j\cdot\left\langle\nabla\left\langle f_j\right\rangle_j\right\rangle_j+\left.\left\langle\widehat{\mathbf{D}}_j\cdot\nabla\widehat{f_j}\right\rangle_j\right)\\
&=\varepsilon_j\left(\left\langle \mathbf{D}_j\right\rangle_j\cdot\left[\nabla\left\langle\left\langle f_j\right\rangle_j\right\rangle_j+\frac{1}{V_j}\int_{A_j}\left\langle f_j\right\rangle_j\mathbf{n}_j\,dA\right]\right.\\
&\quad+\left\langle \mathbf{D}_j\right\rangle_j\cdot\left[\nabla\left\langle\widehat{f_j}\right\rangle_j+\frac{1}{V_j}\int_{A_j}\widehat{f_j}\mathbf{n}_j\,dA\right]\\
&\quad+\left.\left\langle\widehat{\mathbf{D}}_j\right\rangle_j\cdot\left\langle\nabla\left\langle f_j\right\rangle_j\right\rangle_j+\left\langle\widehat{\mathbf{D}}_j\cdot\nabla\widehat{f_j}\right\rangle_j\right)\\
&=\frac{1}{\varepsilon_j}\left\langle \mathbf{D}_j\right\rangle_b\cdot\left(\nabla\left\langle f_j\right\rangle_b+\frac{1}{V_b}\int_{A_j} f_j\mathbf{n}_j\,dA\right)+\left\langle\widehat{\mathbf{D}}_j\cdot\nabla\widehat{f_j}\right\rangle_b.
\end{aligned}\tag{24}$$

The details of the second approach are illustrated in the following:

$$\begin{aligned}
\left\langle \mathbf{D}_j\cdot\nabla f_j\right\rangle_b&=\varepsilon_j\left\langle \mathbf{D}_j\cdot\nabla f_j\right\rangle_j\\
&=\varepsilon_j\left(\left\langle \mathbf{D}_j\right\rangle_j\cdot\left\langle\nabla f_j\right\rangle_j+\left\langle\widehat{\mathbf{D}}_j\cdot\widehat{\nabla f_j}\right\rangle_j\right)\\
&=\left\langle \mathbf{D}_j\right\rangle_j\cdot\left\langle\nabla f_j\right\rangle_b+\left\langle\widehat{\mathbf{D}}_j\cdot\widehat{\nabla f_j}\right\rangle_b\\
&=\frac{1}{\varepsilon_j}\left\langle \mathbf{D}_j\right\rangle_b\cdot\left(\nabla\left\langle f_j\right\rangle_b+\frac{1}{V_b}\int_{A_j} f_j\mathbf{n}_j\,dA\right)+\left\langle\widehat{\mathbf{D}}_j\cdot\widehat{\nabla f_j}\right\rangle_b.
\end{aligned}\tag{25}$$

As can be seen, the results of Eqs. (24) and (25) are the same if $\widehat{\nabla f_j} = \nabla \widehat{f_j}$. However, the result will be different (incorrect) if the following approach is taken instead of the above approach:

$$\begin{aligned}\left\langle \mathbf{D}_j \cdot \nabla f_j \right\rangle_b &= \left\langle \mathbf{D}_j \right\rangle_b \cdot \left\langle \nabla f_j \right\rangle_b + \left\langle \widehat{\mathbf{D}}_j \cdot \widehat{\nabla f_j} \right\rangle_b \\ &= \left\langle \mathbf{D}_j \right\rangle_b \cdot \left(\nabla \left\langle f_j \right\rangle_b + \frac{1}{V_b} \int_{A_j} f_j \mathbf{n}_j \, dA \right) + \left\langle \widehat{\mathbf{D}}_j \cdot \widehat{\nabla f_j} \right\rangle_b . \end{aligned} \tag{26}$$

Substituting Eqs. (11) and (25) into Eq. (23) yields the following macroscopic conservation equation for property f_j:

$$\begin{aligned}&\frac{\partial}{\partial t} \left\langle f_j \right\rangle_b + \nabla \cdot \left(\frac{1}{\varepsilon_j} \left\langle \mathbf{v}_j \right\rangle_b \left\langle f_j \right\rangle_b + \left\langle \widehat{\mathbf{v}}_j \widehat{f}_j \right\rangle_b \right) \\ &= \nabla \cdot \left(\frac{1}{\varepsilon_j} \left\langle \mathbf{D}_j \right\rangle_b \cdot \left(\nabla \left\langle f_j \right\rangle_b + \sum_l \frac{1}{V_b} \int_{A_{jl}} f_j \mathbf{n}_j \, dA \right) + \left\langle \widehat{\mathbf{D}}_j \cdot \widehat{\nabla f_j} \right\rangle_b \right) \\ &\quad + \sum_l \frac{-1}{V_b} \int_{A_{jl}} f_j \left(\mathbf{v}_j - \mathbf{v}_{Ajl} \right) \cdot \mathbf{n}_j \, dA + \sum_l \frac{1}{V_b} \int_{A_{jl}} \mathbf{D}_j \cdot \nabla f_j \cdot \mathbf{n}_j \, dA + \left\langle q_j \right\rangle_b . \end{aligned} \tag{27}$$

In the following, first the applications of Eq. (27) are demonstrated for derivation of the mass and momentum conservation equations. Then, their simplified forms are compared with the results presented by [19] by application of their simplifying conditions.

3.2 Mass Equation

The volume average of Eq. (17) is obtained as the following by applying Eq. (27), where f_j is equal to mass density ρ_j for mass conservation:

$$\begin{aligned}&\frac{\partial}{\partial t} \left\langle \rho_j \right\rangle_b + \nabla \cdot \left(\frac{1}{\varepsilon_j} \left\langle \mathbf{v}_j \right\rangle_b \left\langle \rho_j \right\rangle_b \right) = \nabla \cdot \left(\frac{1}{\varepsilon_j} \left\langle \mathbf{D}_j \right\rangle_b \cdot \nabla \left\langle \rho_j \right\rangle_b \right) \\ &\quad - \nabla \cdot \left(\left\langle \widehat{\mathbf{v}}_j \widehat{\rho}_j \right\rangle_b \right) + \nabla \cdot \left(\frac{1}{\varepsilon_j} \left\langle \mathbf{D}_j \right\rangle_b \cdot \sum_l \frac{1}{V_b} \int_{A_{jl}} \rho_j \mathbf{n}_j \, dA \right) + \nabla \cdot \left(\left\langle \widehat{\mathbf{D}}_j \cdot \widehat{\nabla \rho_j} \right\rangle_b \right) \\ &\quad + \sum_l \frac{-1}{V_b} \int_{A_{jl}} \rho_j \left(\mathbf{v}_j - \mathbf{v}_{Ajl} \right) \cdot \mathbf{n}_j \, dA + \sum_l \frac{1}{V_b} \int_{A_{jl}} \mathbf{D}_j \cdot \nabla \rho_j \cdot \mathbf{n}_j \, dA + \left\langle q_j \right\rangle_b . \end{aligned} \tag{28}$$

Eq. (28) simplifies as the following when $\mathbf{D} = \mathbf{0}$ is substituted:

$$\frac{\partial}{\partial t}\left\langle \rho_j \right\rangle_b + \nabla \cdot \left(\frac{1}{\varepsilon_j} \left\langle \mathbf{v}_j \right\rangle_b \left\langle \rho_j \right\rangle_b + \left\langle \widehat{\mathbf{v}}_j \widehat{\rho}_j \right\rangle_b \right) = \sum_l \frac{-1}{V_b} \int_{A_{jl}} \rho_j \left(\mathbf{v}_j - \mathbf{v}_{Ajl} \right) \cdot \mathbf{n}_j \, dA + \left\langle q_j \right\rangle_b . \tag{29}$$

Expressing Eq. (29) in terms of the intrinsic fluid properties only yields

$$\frac{\partial}{\partial t}\left(\varepsilon_j \left\langle \rho_j \right\rangle_j \right) + \nabla \cdot \left(\varepsilon_j \left\langle \mathbf{v}_j \right\rangle_j \left\langle \rho_j \right\rangle_j + \varepsilon_j \left\langle \widehat{\mathbf{v}}_j \widehat{\rho}_j \right\rangle_j \right) = \sum_l \frac{-1}{V_b} \int_{A_{jl}} \rho_j \left(\mathbf{v}_j - \mathbf{v}_{Ajl} \right) \cdot \mathbf{n}_j \, dA + \varepsilon_j \left\langle q_j \right\rangle_j . \tag{30}$$

Substituting $\mathbf{v}_{Ajl} = 0$, $\left\langle q_j \right\rangle_b = 0$, assuming a no-slip condition ($\mathbf{v}_j = 0$) at the pore surface according to [19] into Eq. (28), and considering the fact that deviation quantities are zero for these constant values yields

$$\frac{\partial}{\partial t}\left\langle \rho_j \right\rangle_b + \nabla \cdot \left\langle \mathbf{v}_j \rho_j \right\rangle_b = 0. \tag{31}$$

3.3 Momentum Equation

The volume average of Eq. (17) where f_j is equal to $\rho_j \mathbf{v}_j$ for the conservation of momentum can be obtained as the following:

$$\begin{aligned} &\frac{\partial}{\partial t}\left\langle \rho_j \mathbf{v}_j \right\rangle_b + \nabla \cdot \left(\frac{1}{\varepsilon_j} \left\langle \mathbf{v}_j \right\rangle_b \left\langle \rho_j \mathbf{v}_j \right\rangle_b + \left\langle \widehat{\mathbf{v}}_j \widehat{\rho_j \mathbf{v}_j} \right\rangle_b \right) \\ &= \nabla \cdot \left(\frac{1}{\varepsilon_j} \left\langle \mathbf{D}_j \right\rangle_b \cdot \left(\nabla \left\langle \rho_j \mathbf{v}_j \right\rangle_b + \sum_l \frac{1}{V_b} \int_{A_{jl}} \rho_j \mathbf{v}_j \cdot \mathbf{n}_j \, dA \right) \right. \\ &\left. + \left\langle \widehat{\mathbf{D}}_j \cdot \widehat{\nabla \rho_j \mathbf{v}_j} \right\rangle_b \right) + \sum_l \frac{-1}{V_b} \int_{A_{jl}} \rho_j \mathbf{v}_j \left(\mathbf{v}_j - \mathbf{v}_{Ajl} \right) \cdot \mathbf{n}_j \, dA \\ &+ \sum_l \frac{1}{V_b} \int_{A_{jl}} \mathbf{D}_j \cdot \nabla \left(\rho_j \mathbf{v}_j \right) \cdot \mathbf{n}_j \, dA + \left\langle \mathbf{q}_j \right\rangle_b . \end{aligned} \tag{32}$$

Note, applying Eq. (11)

$$\left\langle \rho_j \mathbf{v}_j \right\rangle_b = \frac{1}{\varepsilon_j} \left\langle \rho_j \right\rangle_b \left\langle \mathbf{v}_j \right\rangle_b + \left\langle \widehat{\rho}_j \widehat{\mathbf{v}}_j \right\rangle_b . \tag{33}$$

Applying Eq. (33) into Eq. (32) results in

$$\begin{aligned}
&\frac{\partial}{\partial t}\left(\frac{1}{\varepsilon_j}\left\langle\rho_j\right\rangle_b\left\langle\mathbf{v}_j\right\rangle_b\right)+\nabla\cdot\left(\frac{1}{\varepsilon_j^2}\left\langle\mathbf{v}_j\right\rangle_b\left\langle\rho_j\right\rangle_b\left\langle\mathbf{v}_j\right\rangle_b\right)\\
&\quad+\frac{\partial}{\partial t}\left(\left\langle\widehat{\rho}_j\widehat{\mathbf{v}}_j\right\rangle_b\right)+\nabla\cdot\left(\frac{1}{\varepsilon_j}\left\langle\mathbf{v}_j\right\rangle_b\left\langle\widehat{\rho}_j\widehat{\mathbf{v}}_j\right\rangle_b+\left\langle\widehat{\mathbf{v}}_j\widehat{\rho_j\mathbf{v}_j}\right\rangle_b\right)\\
&\quad=\nabla\cdot\left(\frac{1}{\varepsilon_j}\left\langle\mathbf{D}_j\right\rangle_b\cdot\left(\nabla\left\langle\rho_j\mathbf{v}_j\right\rangle_b+\sum_l\frac{1}{V_b}\int_{A_{jl}}\rho_j\mathbf{v}_j\cdot\mathbf{n}_j\,dA\right)\right.\\
&\qquad\left.+\left\langle\widehat{\mathbf{D}}_j\cdot\widehat{\nabla\rho_j\mathbf{v}_j}\right\rangle_b\right)+\sum_l\frac{-1}{V_b}\int_{A_{jl}}\rho_j\mathbf{v}_j\left(\mathbf{v}_j-\mathbf{v}_{Ajl}\right)\cdot\mathbf{n}_j\,dA\\
&\qquad+\sum_l\frac{1}{V_b}\int_{A_{jl}}\mathbf{D}_j\cdot\nabla\left(\rho_j\mathbf{v}_j\right)\cdot\mathbf{n}_j\,dA+\left\langle\mathbf{q}_j\right\rangle_b. \qquad (34)
\end{aligned}$$

Alternatively, the general momentum conservation equation can be derived directly by substituting $f_j=\rho_j\mathbf{v}_j$ into Eq. (23) to obtain

$$\begin{aligned}
&\frac{\partial}{\partial t}\left\langle\rho_j\mathbf{v}_j\right\rangle_b+\nabla\cdot\left(\left\langle\rho_j\mathbf{v}_j\mathbf{v}_j\right\rangle_b\right)=\nabla\cdot\left(\left\langle\mathbf{D}_j\cdot\nabla\left(\rho_j\mathbf{v}_j\right)\right\rangle_b\right)\\
&\quad+\sum_l\frac{-1}{V_b}\int_{A_{jl}}\rho_j\mathbf{v}_j\left(\mathbf{v}_j-\mathbf{v}_{Ajl}\right)\cdot\mathbf{n}_j\,dA\\
&\quad+\sum_l\frac{1}{V_b}\int_{A_{jl}}\mathbf{D}_j\cdot\nabla\left(\rho_j\mathbf{v}_j\right)\cdot\mathbf{n}_j\,dA+\left\langle\mathbf{q}_j\right\rangle_b. \qquad (35)
\end{aligned}$$

Note that the gravity effect is included in the source terms as described later.

The stress tensor is given by the following expression for compressible Newtonian fluids [18]:

$$\mathbf{T}_j=\mathbf{D}_j\cdot\nabla\left(\rho_j\mathbf{v}_j\right)=\left(-p_j+\lambda_j\nabla\cdot\mathbf{v}_j\right)\mathbf{I}+\mu_j\left[\nabla\mathbf{v}_j+\left(\nabla\mathbf{v}_j\right)^T\right], \qquad (36)$$

where $\mathbf{I}$ is the unit tensor, $\lambda_j=\chi_j-\frac{2}{3}\mu_j$, and χ_j and μ_j denote the bulk and shear coefficients of viscosity of the j-phase, respectively. Thus, by means of Eq. (36), Eq. (35) can be written as [7]

$$\begin{aligned}
&\frac{\partial}{\partial t}\left(\left\langle\rho_j\mathbf{v}_j\right\rangle_b\right)+\nabla\cdot\left(\left\langle\rho_j\mathbf{v}_j\mathbf{v}_j\right\rangle_b\right)=\nabla\cdot\left(\left\langle\mathbf{T}_j\right\rangle_b\right)\\
&\quad+\sum_l\frac{-1}{V_b}\int_{A_{jl}}\rho_j\mathbf{v}_j\left(\mathbf{v}_j-\mathbf{v}_{Ajl}\right)\cdot\mathbf{n}_j\,dA+\sum_l\frac{1}{V_b}\int_{A_{jl}}\mathbf{T}_j\cdot\mathbf{n}_j\,dA+\left\langle\mathbf{q}_j\right\rangle_b. \qquad (37)
\end{aligned}$$

Note the following expressions can be obtained from Eqs. (11) and (12) by substituting $f_j = \rho_j$ and $f_j = \mathbf{v}_j$, respectively:

$$\left\langle \rho_j \mathbf{v}_j \right\rangle_b = \frac{1}{\varepsilon_j} \left\langle \rho_j \right\rangle_b \left\langle \mathbf{v}_j \right\rangle_b + \left\langle \widehat{\rho}_j \widehat{\mathbf{v}}_j \right\rangle_b \tag{38}$$

and

$$\begin{aligned} \left\langle \rho_j \mathbf{v}_j \mathbf{v}_j \right\rangle_b = {} & \frac{1}{\varepsilon_j^2} \left\langle \rho_j \right\rangle_b \left\langle \mathbf{v}_j \right\rangle_b \left\langle \mathbf{v}_j \right\rangle_b + \frac{1}{\varepsilon_j} \left\langle \rho_j \right\rangle_b \left\langle \widehat{\mathbf{v}}_j \widehat{\mathbf{v}}_j \right\rangle_b + \frac{1}{\varepsilon_j} \left\langle \mathbf{v}_j \right\rangle_b \left\langle \widehat{\rho}_j \widehat{\mathbf{v}}_j \right\rangle_b \\ & + \frac{1}{\varepsilon_j} \left\langle \mathbf{v}_j \right\rangle_b \left\langle \widehat{\rho}_j \widehat{\mathbf{v}}_j \right\rangle_b + \left\langle \widehat{\rho}_j \widehat{\mathbf{v}}_j \widehat{\mathbf{v}}_j \right\rangle_b . \end{aligned} \tag{39}$$

Thus, substituting Eq. (39) into Eq. (37) yields

$$\begin{aligned} & \frac{\partial}{\partial t} \left(\frac{1}{\varepsilon_j} \left\langle \rho_j \right\rangle_b \left\langle \mathbf{v}_j \right\rangle_b \right) + \nabla \cdot \left(\frac{1}{\varepsilon_j^2} \left\langle \rho_j \right\rangle_b \left\langle \mathbf{v}_j \right\rangle_b \left\langle \mathbf{v}_j \right\rangle_b \right) + \frac{\partial}{\partial t} \left(\left\langle \widehat{\rho}_j \widehat{\mathbf{v}}_j \right\rangle_b \right) \\ & + \nabla \cdot \left(\frac{1}{\varepsilon_j} \left\langle \rho_j \right\rangle_b \left\langle \widehat{\mathbf{v}}_j \widehat{\mathbf{v}}_j \right\rangle_b + \frac{1}{\varepsilon_j} \left\langle \mathbf{v}_j \right\rangle_b \left\langle \widehat{\rho}_j \widehat{\mathbf{v}}_j \right\rangle_b + \frac{1}{\varepsilon_j} \left\langle \mathbf{v}_j \right\rangle_b \left\langle \widehat{\rho}_j \widehat{\mathbf{v}}_j \right\rangle_b + \left\langle \widehat{\rho}_j \widehat{\mathbf{v}}_j \widehat{\mathbf{v}}_j \right\rangle_b \right) \\ & = \nabla \cdot \left(\left\langle \mathbf{T}_j \right\rangle_b \right) + \sum_l \frac{-1}{V_b} \int_{A_{jl}} \rho_j \mathbf{v}_j \left(\mathbf{v}_j - \mathbf{v}_{Ajl} \right) \cdot \mathbf{n}_j \, dA \\ & + \sum_l \frac{1}{V_b} \int_{A_{jl}} \mathbf{T}_j \cdot \mathbf{n}_j \, dA + \left\langle \mathbf{q}_j \right\rangle_b . \end{aligned} \tag{40}$$

Note that $\frac{\partial}{\partial t} \left\langle \widehat{\rho}_j \widehat{\mathbf{v}}_j \right\rangle_b = 0$ assuming that the deviations are spatial.

The following simplified expression for a single fluid phase flowing through porous media is obtained when the conditions of $\rho_j \equiv \left\langle \rho_j \right\rangle_j = const$, $\widehat{\rho}_j = 0$, $\varepsilon_j = const$, $\mu_j \equiv \left\langle \mu_j \right\rangle_j = const$, $\mathbf{v}_{Ajl} = \mathbf{0}$, and $\left\langle \mathbf{q}_j \right\rangle_b = \mathbf{0}$ according to [19] are substituted into Eq. (40) and considering the fact that deviation quantities are zero for these constant values

$$\begin{aligned} & \rho_j \left[\frac{\partial}{\partial t} \left\langle \mathbf{v}_j \right\rangle_b + \frac{1}{\varepsilon_j} \nabla \cdot \left(\left\langle \mathbf{v}_j \right\rangle_b \left\langle \mathbf{v}_j \right\rangle_b \right) + \nabla \cdot \left(\left\langle \widehat{\mathbf{v}}_j \widehat{\mathbf{v}}_j \right\rangle_b \right) + \frac{1}{V_b} \int_{A_{jl}} \mathbf{v}_j \mathbf{v}_j \cdot \mathbf{n}_j \, dA \right] \\ & = \nabla \cdot \left\langle \mathbf{T}_j \right\rangle_b + \frac{1}{V_b} \int_{A_{jl}} \mathbf{T}_j \cdot \mathbf{n}_j \, dA + \left\langle \mathbf{q}_j \right\rangle_b , \end{aligned} \tag{41}$$

where l denotes the porous solid matrix which is in contact with the j-phase.

Under the same above-mentioned simplifying conditions Eq. (36) simplifies as

$$\mathbf{T}_j = -p_j \mathbf{I} + \mu_j \left[\nabla \mathbf{v}_j + (\nabla \mathbf{v}_j)^T \right] . \tag{42}$$

Note according to Eq. (14)

$$\langle \nabla \mathbf{v}_j \rangle_b = \nabla \langle \mathbf{v}_j \rangle_b + \frac{1}{V_b} \int_{A_{jl}} \mathbf{v}_j \cdot \mathbf{n}_j \, dA. \tag{43}$$

Hence, the volume average of Eq. (42) and then application of Eq. (43) yield

$$\begin{aligned} \langle \mathbf{T}_j \rangle_b &= \langle -p_j \mathbf{I} \rangle_b + \left\langle \mu_j \left[\nabla \mathbf{v}_j + (\nabla \mathbf{v}_j)^T \right] \right\rangle_b \\ &= \langle -p_j \rangle_b \mathbf{I} + \mu_j \left(\nabla \langle \mathbf{v}_j \rangle_b + \frac{1}{V_b} \int_{A_{jl}} \mathbf{v}_j \cdot \mathbf{n}_j \, dA \right. \\ &\quad \left. + \left(\nabla \langle \mathbf{v}_j \rangle_b + \frac{1}{V_b} \int_{A_{jl}} \mathbf{v}_j \cdot \mathbf{n}_j \, dA \right)^T \right). \end{aligned} \tag{44}$$

Applying the no-slip boundary condition over the pore surface implies that

$$\int_{A_{jl}} \mathbf{v}_j \cdot \mathbf{n}_j \, dA = 0. \tag{45}$$

Thus, Eq. (44) simplifies by consideration of Eq. (45) as

$$\langle \mathbf{T}_j \rangle_b = \langle -p_j \rangle_b \mathbf{I} + \mu_j \left(\nabla \langle \mathbf{v}_j \rangle_b + \left(\nabla \langle \mathbf{v}_j \rangle_b \right)^T \right). \tag{46}$$

Then,

$$\begin{aligned} \nabla \cdot \langle \mathbf{T}_j \rangle_b &= -\nabla \cdot \left(\langle p_j \rangle_b \mathbf{I} \right) + \mu_j \nabla \cdot \left(\nabla \langle \mathbf{v}_j \rangle_b + \left(\nabla \langle \mathbf{v}_j \rangle_b \right)^T \right) \\ &= -\nabla \cdot \left(\langle p_j \rangle_b \mathbf{I} \right) + \mu_j \left(\nabla \cdot \nabla \langle \mathbf{v}_j \rangle_b + \nabla \cdot \left(\nabla \langle \mathbf{v}_j \rangle_b \right)^T \right). \end{aligned} \tag{47}$$

Exchanging the operators and then substituting $\nabla \cdot \langle \mathbf{v}_j \rangle_b = 0$ for incompressible fluids yields

$$\begin{aligned} \nabla \cdot \langle \mathbf{T}_j \rangle_b &= -\nabla \cdot \left(\langle p_j \rangle_b \mathbf{I} \right) + \mu_j \left(\nabla \nabla \cdot \langle \mathbf{v}_j \rangle_b + \nabla \cdot \left(\nabla \langle \mathbf{v}_j \rangle_b \right)^T \right) \\ &= -\nabla \cdot \left(\langle p_j \rangle_b \mathbf{I} \right) + \mu_j \nabla \cdot \left(\nabla \langle \mathbf{v}_j \rangle_b \right)^T. \end{aligned} \tag{48}$$

Applying Eqs. (8), (10), and (11) yields

$$\mathbf{v}_j = \langle \mathbf{v}_j \rangle_j + \widehat{\mathbf{v}}_j, \tag{49}$$

$$\mathbf{v}_j \mathbf{v}_j = \langle \mathbf{v}_j \rangle_j \langle \mathbf{v}_j \rangle_j + 2 \widehat{\mathbf{v}}_j \langle \mathbf{v}_j \rangle_j + \widehat{\mathbf{v}}_j \widehat{\mathbf{v}}_j, \tag{50}$$

and

$$\left\langle \mathbf{v}_j \mathbf{v}_j \right\rangle_b = \frac{1}{\varepsilon_j} \left\langle \mathbf{v}_j \right\rangle_b \left\langle \mathbf{v}_j \right\rangle_b + \left\langle \widehat{\mathbf{v}}_j \widehat{\mathbf{v}}_j \right\rangle_b . \tag{51}$$

Therefore, the following formulation can be carried out inferred by [19]

$$\begin{aligned} \frac{1}{V_b} \int_{A_{jl}} \mathbf{v}_j \mathbf{v}_j \cdot \mathbf{n}_j dA &= \frac{1}{V_b} \int_{A_{jl}} \left(\left\langle \mathbf{v}_j \right\rangle_j \left\langle \mathbf{v}_j \right\rangle_j + 2\widehat{\mathbf{v}}_j \left\langle \mathbf{v}_j \right\rangle_j + \widehat{\mathbf{v}}_j \widehat{\mathbf{v}}_j \right) \cdot \mathbf{n}_j \, dA \\ &= \frac{1}{V_b} \int_{A_{jl}} \widehat{\mathbf{v}}_j \widehat{\mathbf{v}}_j \cdot \mathbf{n}_j \, dA + \frac{1}{V_b} \left\langle \mathbf{v}_j \right\rangle_j \left\langle \mathbf{v}_j \right\rangle_j \cdot \int_{A_{jl}} \mathbf{n}_j \, dA \\ &\quad + \frac{2}{V_b} \left\langle \mathbf{v}_j \right\rangle_j \int_{A_{jl}} \left(\mathbf{v}_j - \left\langle \mathbf{v}_j \right\rangle_j \right) \cdot \mathbf{n}_j \, dA \\ &= -\frac{1}{V_b} \left\langle \mathbf{v}_j \right\rangle_j \left\langle \mathbf{v}_j \right\rangle_j \cdot \int_{A_{jl}} \mathbf{n}_j \, dA. \end{aligned} \tag{52}$$

Applying Eqs. (48) and (52) into Eq. (41) yields the following simplified momentum equation:

$$\begin{aligned} \rho_j \frac{\partial}{\partial t} \left\langle \mathbf{v}_j \right\rangle_b + \frac{\rho_j}{\varepsilon_j} \nabla \cdot \left(\left\langle \mathbf{v}_j \right\rangle_b \left\langle \mathbf{v}_j \right\rangle_b \right) &= -\nabla \left\langle p_j \right\rangle_b + \mu_j \nabla \cdot \left(\nabla \left\langle \mathbf{v}_j \right\rangle_b \right)^T \\ &\quad - \rho_j \left\langle \nabla \cdot \left(\widehat{\mathbf{v}}_j \widehat{\mathbf{v}}_j \right) \right\rangle_b + \frac{1}{V_b} \int_{A_{jl}} \mathbf{T}_j \cdot \mathbf{n}_j \, dA \\ &\quad + \frac{\rho_j}{V_b} \left\langle \mathbf{v}_j \right\rangle_j \left\langle \mathbf{v}_j \right\rangle_j \cdot \int_{A_{jl}} \mathbf{n}_j \, dA + \left\langle \mathbf{q}_j \right\rangle_b . \end{aligned} \tag{53}$$

Note in the above a substitution of $\left\langle p_j \right\rangle_b = \left\langle p_j \right\rangle_j$ is made assuming rigid porous media matrix material and $\left\langle p_j \right\rangle_b = \varepsilon_j \left\langle p_j \right\rangle_j$ for fully elastic porous media matrix material in accordance with Eq. (3).

Eq. (53) can be expressed in terms of the intrinsic fluid properties as

$$\begin{aligned} &\varepsilon_j \rho_j \left[\frac{\partial}{\partial t} \left\langle \mathbf{v}_j \right\rangle_j + \nabla \cdot \left(\left\langle \mathbf{v}_j \right\rangle_j \left\langle \mathbf{v}_j \right\rangle_j \right) - \left\langle \nabla \cdot \left(\widehat{\mathbf{v}}_j \widehat{\mathbf{v}}_j \right) \right\rangle_j \right] \\ &= \varepsilon_j \mu_j \nabla \cdot \left(\nabla \left\langle \mathbf{v}_j \right\rangle_j \right)^T + \frac{1}{V_b} \int_{A_{jl}} \mathbf{T}_j \cdot \mathbf{n}_j \, dA + \frac{\rho_j}{V_b} \left\langle \mathbf{v}_j \right\rangle_j \left\langle \mathbf{v}_j \right\rangle_j \cdot \int_{A_{jl}} \mathbf{n}_j \, dA \\ &\quad - \nabla \left\langle p_j \right\rangle_b + \left\langle \mathbf{q}_j \right\rangle_b . \end{aligned} \tag{54}$$

Note that Eq. (54) is different from the corresponding equation derived by [19]. Their equation in the nomenclature used in this chapter reads as

$$\rho_j \frac{\partial}{\partial t}\left\langle \mathbf{v}_j \right\rangle_b + \frac{\rho_j}{\varepsilon_j^2}\nabla\cdot\left(\left\langle \mathbf{v}_j \right\rangle_b \left\langle \mathbf{v}_j \right\rangle_b\right) = -\nabla\left\langle p_j \right\rangle_b + \mu_j \nabla\cdot\left(\nabla\left\langle \mathbf{v}_j \right\rangle_b\right)^T - \rho_j\left\langle \nabla\cdot\left(\widehat{\mathbf{v}}_j\widehat{\mathbf{v}}_j\right)\right\rangle_b + \frac{1}{V_b}\int_{A_{jl}} \mathbf{T}_j\cdot\mathbf{n}_j\, dA + \frac{\rho_j}{V_b}\left\langle \mathbf{v}_j \right\rangle_j \left\langle \mathbf{v}_j \right\rangle_j \cdot \int_{A_{jl}} \mathbf{n}_j\, dA. \tag{55}$$

The systematic error involved in the equation of [19] is explained in Appendix.

3.4 Energy Equation

Note the thermal diffusivity tensor is given by

$$\mathbf{D}_j = \frac{\boldsymbol{\kappa}_j}{\rho_j C_j}, \tag{56}$$

where $\boldsymbol{\kappa}$ denotes thermal conductivity tensor and C is specific heat capacity at constant pressure.

Applying Eq. (23) for the conservations of energy yields, where f_j is equal to the enthalpy given by $H_j = \rho_j C_j T_j$ and T_j denotes the temperature of the j-phase [3],

$$\frac{\partial}{\partial t}\left(\left\langle \rho_j C_j T_j \right\rangle_b\right) + \nabla\cdot\left(\left\langle \rho_j C_j T_j \mathbf{v}_j \right\rangle_b\right) = \nabla\cdot\left(\left\langle \mathbf{D}_j\cdot\nabla\left(\rho_j C_j T_j\right)\right\rangle_b\right) + \sum_l \frac{-1}{V_b}\int_{A_{jl}} \rho_j C_j T_j\left(\mathbf{v}_j - \mathbf{v}_{Ajl}\right)\cdot\mathbf{n}_j\, dA + \sum_l \frac{1}{V_b}\int_{A_{jl}} \mathbf{D}_j\cdot\nabla\left(\rho_j C_j T_j\right)\cdot\mathbf{n}_j\, dA + \left\langle q_j \right\rangle_b. \tag{57}$$

The averaging of the several terms appearing in Eq. (57) is explained in the following:

$$\left\langle \mathbf{D}_j\cdot\nabla\left(\rho_j C_j T_j\right)\right\rangle_b = \frac{1}{\varepsilon_j}\left\langle \mathbf{D}_j \right\rangle_b \cdot \left\langle \nabla\left(\rho_j C_j T_j\right)\right\rangle_b + \left\langle \widehat{\mathbf{D}}_j\cdot\widehat{\nabla H_j}\right\rangle_b = \frac{1}{\varepsilon_j}\left\langle \mathbf{D}_j \right\rangle_b \cdot \left(\nabla\left(\frac{1}{\varepsilon_j}\left\langle \rho_j C_j \right\rangle_b \left\langle T_j \right\rangle_b\right) + \nabla\left(\left\langle \widehat{\rho_j C_j}\widehat{T_j}\right\rangle_b\right) + \frac{1}{V_b}\int_{A_{jl}} \left(\rho_j C_j T_j\right)\mathbf{n}_j\, dA\right) + \left\langle \widehat{\mathbf{D}}_j\cdot\widehat{\nabla H_j}\right\rangle_b, \tag{58}$$

$$\left\langle \left(\rho_j C_j\right) T_j\right\rangle_b = \frac{1}{\varepsilon_j}\left\langle \rho_j C_j \right\rangle_b \left\langle T_j \right\rangle_b + \left\langle \widehat{\rho_j C_j}\widehat{T_j}\right\rangle_b, \tag{59}$$

and

$$\left\langle (\rho_j C_j)\,\mathbf{v}_j T_j \right\rangle_b = \frac{1}{\varepsilon_j^2}\left\langle \rho_j C_j \right\rangle_b \left\langle \mathbf{v}_j \right\rangle_b \left\langle T_j \right\rangle_b + \frac{1}{\varepsilon_j}\left\langle \rho_j C_j \right\rangle_b \left\langle \widehat{\mathbf{v}}_j \widehat{T}_j \right\rangle_b + \frac{1}{\varepsilon_j}\left\langle \mathbf{v}_j \right\rangle_b \left\langle \widehat{\rho_j C_j} \widehat{T}_j \right\rangle_b + \frac{1}{\varepsilon_j}\left\langle T_j \right\rangle_b \left\langle \widehat{\rho_j C_j} \widehat{\mathbf{v}}_j \right\rangle_b + \left\langle \widehat{\rho_j C_j} \widehat{\mathbf{v}}_j \widehat{T}_j \right\rangle_b . \tag{60}$$

Further, consider

$$\left\langle \rho_j C_j \right\rangle_b = \frac{1}{\varepsilon_j}\left\langle \rho_j \right\rangle_b \left\langle C_j \right\rangle_b + \left\langle \widehat{\rho}_j \widehat{C}_j \right\rangle_b . \tag{61}$$

Thus, substituting Eqs. (58)–(61) into Eq. (57) yields the volume averaged equation as

$$\begin{aligned}
&\frac{\partial}{\partial t}\left(\frac{1}{\varepsilon_j}\left(\frac{1}{\varepsilon_j}\left\langle \rho_j \right\rangle_b \left\langle C_j \right\rangle_b + \left\langle \widehat{\rho}_j \widehat{C}_j \right\rangle_b\right)\left\langle T_j \right\rangle_b + \left\langle \widehat{\rho_j C_j} \widehat{T}_j \right\rangle_b\right) \\
&\quad + \nabla\cdot\left(\left(\frac{1}{\varepsilon_j}\left\langle \rho_j \right\rangle_b \left\langle C_j \right\rangle_b + \left\langle \widehat{\rho}_j \widehat{C}_j \right\rangle_b\right)\left(\frac{1}{\varepsilon_j^2}\left\langle \mathbf{v}_j \right\rangle_b \left\langle T_j \right\rangle_b + \frac{1}{\varepsilon_j}\left\langle \widehat{\mathbf{v}}_j \widehat{T}_j \right\rangle_b\right)\right. \\
&\quad \left. + \frac{1}{\varepsilon_j}\left\langle \mathbf{v}_j \right\rangle_b \left\langle \widehat{\rho_j C_j} \widehat{T}_j \right\rangle_b + \frac{1}{\varepsilon_j}\left\langle T_j \right\rangle_b \left\langle \widehat{\rho_j C_j} \widehat{\mathbf{v}}_j \right\rangle_b + \left\langle \widehat{\rho_j C_j} \widehat{\mathbf{v}}_j \widehat{T}_j \right\rangle_b\right) \\
&= \nabla\cdot\left[\frac{1}{\varepsilon_j}\left\langle \mathbf{D}_j \right\rangle_b \cdot \left(\nabla\left(\frac{1}{\varepsilon_j}\left(\frac{1}{\varepsilon_j}\left\langle \rho_j \right\rangle_b \left\langle C_j \right\rangle_b + \left\langle \widehat{\rho}_j \widehat{C}_j \right\rangle_b\right)\left\langle T_j \right\rangle_b\right)\right.\right. \\
&\quad \left.\left. + \nabla\left(\left\langle \widehat{\rho_j C_j} \widehat{T}_j \right\rangle_b\right) + \frac{1}{V_b}\int_{A_j} (\rho_j C_j T_j)\,\mathbf{n}_j\, dA\right) + \left\langle \widehat{\mathbf{D}}_j \cdot \widehat{\nabla H_j} \right\rangle_b\right] \\
&\quad + \sum_l \frac{-1}{V_b}\int_{A_{jl}} \rho_j C_j T_j \left(\mathbf{v}_j - \mathbf{v}_{Ajl}\right)\cdot \mathbf{n}_j\, dA \\
&\quad + \sum_l \frac{1}{V_b}\int_{A_{jl}} \mathbf{D}_j \cdot \nabla\left(\rho_j C_j T_j\right)\cdot \mathbf{n}_j\, dA + \left\langle q_j \right\rangle_b .
\end{aligned} \tag{62}$$

Consequently, invoking $C_j \equiv \left\langle C_j \right\rangle_j = const$, $\rho_j \equiv \left\langle \rho_j \right\rangle_j = const$, $\varepsilon_j = const$, $\boldsymbol{\kappa}_j = const$, and $\mathbf{v}_j = \mathbf{v}_{Ajl} = 0$ according to [19] and considering the deviation quantities to be zero for these constant values yield

$$\varepsilon_j \langle \rho_j \rangle_j \langle C_j \rangle_j \left[\frac{\partial}{\partial t} \langle T_j \rangle_j + \frac{1}{\varepsilon_j} \nabla \cdot \left(\langle \mathbf{v}_j \rangle_b \langle T_j \rangle_j \right) + \nabla \cdot \left(\langle \widehat{\mathbf{v}}_j \widehat{T}_j \rangle_j \right) \right]$$
$$= \varepsilon_j \boldsymbol{\kappa}_j \cdot \nabla \cdot \nabla \langle T_j \rangle_j + \frac{1}{V_b} \boldsymbol{\kappa}_j \cdot \nabla \cdot \left(\int_{A_{jl}} T_j \mathbf{n}_j \, dA \right)$$
$$+ \frac{1}{V_b} \boldsymbol{\kappa}_j \cdot \int_{A_{jl}} \nabla T_j \cdot \mathbf{n}_j \, dA + \langle q_j \rangle_b . \tag{63}$$

But applying Eq. (8)

$$T_j = \langle T_j \rangle_j + \widehat{T}_j . \tag{64}$$

Therefore, the following expression can be written inferred by [19]

$$\frac{1}{V_b} \boldsymbol{\kappa}_j \cdot \nabla \cdot \left(\int_{A_{jl}} T_j \mathbf{n}_j \, dA \right)$$
$$= \frac{1}{V_b} \boldsymbol{\kappa}_j \cdot \nabla \cdot \left(\int_{A_{jl}} \langle T_j \rangle_j \mathbf{n}_j \, dA \right) + \frac{1}{V_b} \boldsymbol{\kappa}_j \cdot \nabla \cdot \left(\int_{A_{jl}} \widehat{T}_j \mathbf{n}_j \, dA \right) . \tag{65}$$

Then, consider the divergence theorem, given by

$$\int_{A_{jl}} \langle T_j \rangle_j \mathbf{n}_j \, dA = \int_{V_b} \nabla \langle T_j \rangle_j \, dV = 0. \tag{66}$$

Thus, substituting Eq. (66) into Eq. (65) yields [19]

$$\frac{1}{V_b} \boldsymbol{\kappa}_j \cdot \nabla \cdot \left(\int_{A_{jl}} T_j \mathbf{n}_j \, dA \right) = \frac{1}{V_b} \boldsymbol{\kappa}_j \cdot \nabla \cdot \left(\int_{A_{jl}} \widehat{T}_j \mathbf{n}_j \, dA \right) . \tag{67}$$

Consequently, the energy conservation expressed only in terms of the intrinsic fluid properties is obtained as

$$\varepsilon_j \langle \rho_j \rangle_j \langle C_j \rangle_j \left[\frac{\partial}{\partial t} \langle T_j \rangle_j + \nabla \cdot \left(\langle \mathbf{v}_j \rangle_j \langle T_j \rangle_j \right) + \nabla \cdot \langle \widehat{\mathbf{v}}_j \widehat{T}_j \rangle_j \right]$$
$$= \varepsilon_j \boldsymbol{\kappa}_j \cdot \nabla \cdot \nabla \langle T_j \rangle_j + \frac{1}{V_b} \boldsymbol{\kappa}_j \cdot \nabla \cdot \left(\int_{A_{jl}} \widehat{T}_j \mathbf{n}_j \, dA \right)$$
$$+ \frac{1}{V_b} \boldsymbol{\kappa}_j \cdot \int_{A_{jl}} \nabla T_j \cdot \mathbf{n}_j \, dA + \langle q_j \rangle_j . \tag{68}$$

Note that this result is different from the corresponding equation derived by [19]. Their equation in the nomenclature used in this chapter reads as

$$\varepsilon_j \rho_j C_j \left[\frac{\partial}{\partial t} \left\langle T_j \right\rangle_j + \frac{1}{\varepsilon_j} \nabla \cdot \left(\left\langle \mathbf{v}_j \right\rangle_j \left\langle \mathbf{T}_j \right\rangle_j \right) + \nabla \cdot \left\langle \widehat{\mathbf{v}}_j \widehat{T}_j \right\rangle_j \right]$$
$$= \varepsilon_j \boldsymbol{\kappa}_j \cdot \nabla \cdot \nabla \left\langle T_j \right\rangle_j + \frac{1}{V_b} \boldsymbol{\kappa}_j \cdot \nabla \cdot \left(\int_{A_{jl}} \widehat{T}_j \mathbf{n}_j \, dA \right) + \frac{1}{V_b} \boldsymbol{\kappa}_j \cdot \int_{A_{jl}} \nabla T_j \cdot \mathbf{n}_j \, dA. \tag{69}$$

The systematic error involved in the equation of [19] is explained in Appendix.

4 Control Volume Analyses

The control volume of the j-phase is considered to be the portion of the void space occupied by this phase in porous media. Therefore, when an element of bulk porous media $(\Delta x \Delta y \Delta z)$ with the dimensions of Δx, Δy, and Δz is considered in the x-, y-, and z- Cartesian coordinates, the j-phase contained in this element will have the *external control volume boundaries* over the external surface of this element and the *internal control volume boundaries* through which the fluid interacts at the interface with the pore surface and other phases. Thus, a general balance equation can be derived by considering the net flow through the open boundaries and the interactions at the internal pore volume and interface with other fluid phases. Thus, the following general macroscopic equation of conservation is obtained for the j-phase in the *extrapolated limit* Δx, Δy, and $\Delta z \to 0$ of [5, 6, 13]:

$$\nabla \cdot \mathbf{j}_{T\,jb} + \frac{\partial f_{jb}}{\partial t} = \sum_{CV} \dot{\mathbf{r}}_{jb}, \tag{70}$$

where $\dot{\mathbf{r}}_{jb}$ denotes the source of a property f_{jb} supplied to the j-phase per unit bulk volume of porous media and the total flux $\mathbf{j}_{T\,jb}$ of the same property is expressed by the sum of transport by convection and dispersion as

$$\mathbf{j}_{T\,jb} = \mathbf{v}_j f_{jb} + \mathbf{j}_{jb}, \quad \mathbf{j}_{jb} = -\frac{1}{\varepsilon_j} \mathbf{D}_{jb} \cdot \nabla f_{jb}, \tag{71}$$

where $\mathbf{D}_{jb}$ is a bulk-dispersion tensor.

Combining Eqs. (71) and (70) the following macroscopic transport equation is derived:

$$\nabla \cdot \left(\mathbf{v}_j f_{jb} \right) + \frac{\partial f_{jb}}{\partial t} = \nabla \cdot \left(\frac{1}{\varepsilon_j} \mathbf{D}_{jb} \cdot \nabla f_{jb} \right) + \sum_{CV} \dot{\mathbf{r}}_{jb}. \tag{72}$$

In the following, the applications of Eq. (72) are demonstrated for derivation of the mass, momentum, and energy conservation equations.

4.1 Mass Equation

The porous media mass balance equation can be derived by substituting $f_{jb} = \rho_{jb}$ in Eq. (72) to obtain

$$\nabla \cdot \left(\mathbf{v}_j \rho_{jb}\right) + \frac{\partial \rho_{jb}}{\partial t} = \nabla \cdot \left(\frac{1}{\varepsilon_j} \mathbf{D}_{jb} \cdot \nabla \rho_{jb}\right) + \sum_{CV} \dot{\mathbf{r}}_{jb}. \tag{73}$$

This equation can be manipulated as

$$\nabla \cdot \left(\frac{\mathbf{v}_{jb} \rho_{jb}}{\varepsilon_j}\right) + \frac{\partial \rho_{jb}}{\partial t} = \nabla \cdot \left(\frac{1}{\varepsilon_j} \mathbf{D}_{jb} \cdot \nabla \rho_{jb}\right) + \sum_{CV} \dot{\mathbf{r}}_{jb}. \tag{74}$$

Then, expressing in terms of the intrinsic fluid properties only yields

$$\frac{\partial}{\partial t}\left(\varepsilon_j \left\langle \rho_j \right\rangle_j\right) + \nabla \cdot \left(\varepsilon_j \left\langle \rho_j \right\rangle_j \left\langle \mathbf{v}_j \right\rangle_j\right) = \nabla \cdot \left[\frac{1}{\varepsilon_j} \mathbf{D}_{jb} \cdot \nabla \left(\varepsilon_j \left\langle \rho_j \right\rangle_j\right)\right] + \varepsilon_j \left\langle q_j \right\rangle_j. \tag{75}$$

4.2 Momentum Equation

Consider that $\mathbf{v}$ is the volume flux, μ is viscosity, p is pressure, and ρ is density of fluid. The subscripts jb and j refer to the bulk- and fluid-volume averages of the properties of the j-phase. $\mathbf{K}$ and ϕ denote the permeability tensor and porosity of porous media and $\mathbf{g}$ is the gravitational acceleration vector. ∇p_{jb} is the fluid pressure gradient, ∇p_{jbth} is the threshold or minimum fluid pressure gradient required to overcome the resistance of porous media to fluid flow [16], ϕ, D_{hx}, and τ_{hx} denote the porosity, mean-hydraulic diameter, and tortuosity of porous media, respectively, f_{kj} is a shear factor, $\mathbf{K}_{bk}$ and $\boldsymbol{\beta}_{bk}$ are the tensor effective fluid permeability (a product of relative and absolute permeability) and inertial flow coefficient, respectively, $\mathbf{T}$ is the shear stress tensor, and Φ is the flow potential, defined later.

The porous media momentum equation can be derived by substituting $f_{jb} = \varepsilon_j f_j = \varepsilon_j \rho_j \mathbf{v}_j = \frac{\rho_{jb} \mathbf{v}_{jb}}{\varepsilon_j}$, $\mathbf{v}_j = \frac{\mathbf{v}_{jb}}{\varepsilon_j}$ in Eq. (72) to obtain

$$\nabla \cdot \left(\frac{\mathbf{v}_{jb}}{\varepsilon_j} \frac{\rho_{jb} \mathbf{v}_{jb}}{\varepsilon_j}\right) + \frac{\partial}{\partial t}\left(\frac{\rho_{jb} \mathbf{v}_{jb}}{\varepsilon_j}\right) = \nabla \cdot \left(\frac{1}{\varepsilon_j} \mathbf{D}_{jb} \cdot \nabla \left(\frac{\rho_{jb} \mathbf{v}_{jb}}{\varepsilon_j}\right)\right) + \sum_{CV} \dot{\mathbf{r}}_{jb}. \tag{76}$$

Alternatively,

$$\nabla \cdot \left(\rho_j \frac{\mathbf{v}_{jb} \mathbf{v}_{jb}}{\varepsilon_j}\right) + \frac{\partial}{\partial t}\left(\rho_j \mathbf{v}_{jb}\right) = \nabla \cdot \left(\frac{1}{\varepsilon_j} \mathbf{D}_{jb} \cdot \nabla \left(\rho_j \mathbf{v}_{jb}\right)\right) + \varepsilon_j \sum_{CV} \dot{\mathbf{r}}_j. \tag{77}$$

The source term is expressed as a sum of the external and internal sources as [5]

$$\sum_{CV} \dot{\mathbf{r}}_{jb} = \sum_{CV-External} \dot{\mathbf{r}}_{jb} + \sum_{CV-Internal} \dot{\mathbf{r}}_{jb}$$
$$= [\mathbf{F}_N - \mathbf{F}_{TH} + \mathbf{F}_T + \mathbf{F}_B]_{External} + [-\mathbf{F}_S - \mathbf{F}_O - \mathbf{F}_{IF}]_{Internal}. \quad (78)$$

The various internal and external forces acting on the fluid can be expressed as the following based on the capillary-orifice model [2,5].

The forces associated with the normal and tangential stresses are given by $\mathbf{F}_N = -\nabla p_{jb}$ and $\mathbf{F}_T = -\nabla \cdot \mathbf{T}_{jb}$, respectively. $\mathbf{F}_{TH} = -\nabla p_{jbth}$ denotes the resistive force associated with the threshold pressure gradient that must be overcome to initiate flow through porous media because of the internal resistance to motion of the j-phase through porous media [16].

The gravitational body force is given by

$$\mathbf{F}_B = \varepsilon_j \rho_j \mathbf{g}. \quad (79)$$

The pore surface friction force is given by

$$\mathbf{F}_S = \varepsilon_j^2 \mu_j \mathbf{K}_{jb}^{-1} \cdot \mathbf{v}_j = \varepsilon_j \mu_j \mathbf{K}_{jb}^{-1} \cdot \mathbf{v}_{jb}. \quad (80)$$

The components of the permeability tensor are similarly expressed using the capillary-orifice model. For example, K_x is the permeability of porous medium in the x-principal direction, expressed by

$$K_x = \frac{\phi D_{hx}^2}{32\tau_{hx}}. \quad (81)$$

The pore throat orifice effect drag force is given by

$$\mathbf{F}_O = \varepsilon_j^3 \langle \rho_j \rangle_j \boldsymbol{\beta}_{jb} \cdot \left| \langle \mathbf{v}_j \rangle_j \right| \langle \mathbf{v}_j \rangle_j = \varepsilon_j \rho_j \boldsymbol{\beta}_{jb} \cdot |\mathbf{v}_{jb}| \mathbf{v}_{jb}. \quad (82)$$

The components of the inertial flow coefficient tensor are similarly expressed using the capillary-orifice model. For example, β_x is an inertial flow coefficient in the x-principal direction, given by

$$\beta_x = \frac{c_{Dx} \tau_{hx}^2}{2\phi^2 D_{hx}}, \quad (83)$$

where c_{Dx} is the drag coefficient in the x-direction.

Eliminating D_{hx} between Eqs. (81) and (83) yields

$$\beta_x = c_f \frac{1}{K_x^{1/2}}, \quad \text{or } \boldsymbol{\beta} = \mathbf{c}_f \cdot \mathbf{K}^{-1/2} \quad (84)$$

and

$$c_f = \frac{c_{Dx}}{8\sqrt{2}} \left(\frac{\tau_{hx}}{\phi} \right)^{3/2}, \tag{85}$$

where c_f is the pressure coefficient. Therefore, the pore throat drag coefficient is expressed as

$$\mathbf{F}_O = \varepsilon_j \rho_j \boldsymbol{\beta}_{jb} \cdot \left| \mathbf{v}_{jb} \right| \mathbf{v}_{jb} = \varepsilon_j \rho_j \mathbf{c}_f \cdot \mathbf{K}_{jb}^{-1/2} \cdot \left| \mathbf{v}_{jb} \right| \mathbf{v}_{jb}. \tag{86}$$

The interfacial drag force is given by, modifying the equation of [17],

$$\mathbf{F}_{IF} = \varepsilon_j \sum_{j=1, j \neq k}^{N} f_{jk} \left(\mathbf{T}_{hj} \cdot \left\langle \mathbf{v}_j \right\rangle_j - \mathbf{T}_{hk} \cdot \left\langle \mathbf{v}_k \right\rangle_k \right), \tag{87}$$

where $\mathbf{T}_{hk}$ is the tortuosity tensor.

Thus, using Eqs. (78)–(87), the source term is expressed as

$$\begin{aligned} \sum_{CV} \dot{\mathbf{r}}_{jb} &= \left[-\nabla p_{jb} + \nabla p_{jbth} - \nabla \cdot \mathbf{T}_{jb} + \varepsilon_j \rho_j \mathbf{g} \right]_{External} \\ &\quad + \Big[-\varepsilon_j^2 \mu_j \mathbf{K}_{jb}^{-1} \cdot \mathbf{v}_j - \varepsilon_j^3 \rho_j \boldsymbol{\beta}_{jb} \cdot \left| \mathbf{v}_j \right| \mathbf{v}_j \\ &\quad + \varepsilon_j \sum_{j=1, j \neq k}^{N} f_{jk} \left(\mathbf{T}_{hj} \cdot \mathbf{v}_j - \mathbf{T}_{hk} \cdot \mathbf{v}_k \right) \Big]_{Internal} \\ &= -\rho_j \nabla \Phi_{jb} - \varepsilon_j \mu_j \mathbf{K}_{jb}^{-1} \cdot \mathbf{v}_{jb} - \varepsilon_j \rho_j \boldsymbol{\beta}_{jb} \cdot \left| \mathbf{v}_{jb} \right| \mathbf{v}_{jb} \\ &\quad + \sum_{j=1, j \neq k}^{N} f_{jk} \left(\mathbf{T}_{hj} \cdot \mathbf{v}_{jb} - \mathbf{T}_{hk} \cdot \mathbf{v}_{kb} \right), \end{aligned} \tag{88}$$

where a flow potential is defined as [7]

$$\Psi_{jb} = \varepsilon_j \Psi_j = \int_{P_o}^{p} \frac{d\left(p_{jb} - p_{jbth} \right)}{\rho_j} + g\left(\varepsilon_j z - \varepsilon_{jo} z_o \right). \tag{89}$$

Thus, the following are written:

$$-\rho_j \nabla \Psi_{jb} = -\nabla p_{jb} + \nabla p_{jbth} + \varepsilon_j \rho_j \mathbf{g} \tag{90}$$

and

$$-\rho_j \nabla \Phi_{jb} = -\rho_j \nabla \Psi_{jb} - \nabla \cdot \mathbf{T}_{jb}. \tag{91}$$

The source term can be expressed in the volume-averaging nomenclature as

$$\sum_{CV}\dot{\mathbf{r}}_{jb} = -\nabla p_{jb} + \nabla p_{jbth} - \nabla\cdot\mathbf{T}_{jb} + \varepsilon_j\rho_j\mathbf{g} - \varepsilon_j^2\left\langle\mu_j\right\rangle_j\mathbf{K}_{jb}^{-1}\cdot\left\langle\mathbf{v}_j\right\rangle_j - \varepsilon_j^3\left\langle\rho_j\right\rangle_j\boldsymbol{\beta}_{jb}\cdot\left|\left\langle\mathbf{v}_j\right\rangle_j\right|\left\langle\mathbf{v}_j\right\rangle_j + \varepsilon_j\sum_{j=1,j\neq k}^{N} f_{jk}\left(\mathbf{T}_{hj}\cdot\left\langle\mathbf{v}_j\right\rangle_j - \mathbf{T}_{hk}\cdot\left\langle\mathbf{v}_k\right\rangle_k\right). \tag{92}$$

Substituting Eq. (88) into Eq. (77) yields

$$\nabla\cdot\left(\rho_j\frac{\mathbf{v}_{jb}\mathbf{v}_{jb}}{\varepsilon_j}\right) + \frac{\partial}{\partial t}\left(\rho_j\mathbf{v}_{jb}\right) = \nabla\cdot\left(\frac{1}{\varepsilon_j}\mathbf{D}_{jb}\cdot\nabla\left(\rho_j\mathbf{v}_{jb}\right)\right) - \nabla p_{jb} + \nabla p_{jbth} + \varepsilon_j\rho_j\mathbf{g} - \nabla\cdot\mathbf{T}_{jb} - \varepsilon_j\mu_j\mathbf{K}_{jb}^{-1}\cdot\mathbf{v}_{jb} - \varepsilon_j\rho_j\boldsymbol{\beta}_{jb}\cdot\left|\mathbf{v}_{jb}\right|\mathbf{v}_{jb} + \sum_{j=1,j\neq k}^{N} f_{jk}\left(\mathbf{T}_{hj}\cdot\mathbf{v}_{jb} - \mathbf{T}_{hk}\cdot\mathbf{v}_{kb}\right). \tag{93}$$

4.3 Energy Equation

The porous media energy equation can be derived by substituting $f_{jb} = \varepsilon_j f_j = \varepsilon_j\rho_j C_j T_j = \frac{\rho_{jb}C_{jb}T_{jb}}{\varepsilon_j^2}$, $\mathbf{v}_j = \frac{\mathbf{v}_{jb}}{\varepsilon_j}$ into Eq. (72) to obtain

$$\nabla\cdot\left(\frac{\mathbf{v}_{jb}}{\varepsilon_j}\frac{\rho_{jb}C_{jb}T_{jb}}{\varepsilon_j^2}\right) + \frac{\partial}{\partial t}\left(\frac{\rho_{jb}C_{jb}T_{jb}}{\varepsilon_j^2}\right) = \nabla\cdot\left[\frac{1}{\varepsilon_j}\mathbf{D}_{jb}\cdot\nabla\left(\frac{\rho_{jb}C_{jb}T_{jb}}{\varepsilon_j^2}\right)\right] + \sum_{CV}\dot{\mathbf{r}}_{jb}. \tag{94}$$

This equation can be expressed for constant fluid properties as

$$\varepsilon_j\rho_j C_j\left[\frac{\partial T_j}{\partial t} + \frac{1}{\varepsilon_j}\nabla\cdot\left(\mathbf{v}_{jb}T_j\right)\right] = \varepsilon_j\rho_j C_j\mathbf{D}_j\cdot\nabla\cdot\nabla T_j + \sum_{CV}\dot{\mathbf{r}}_{jb} = \varepsilon_j\boldsymbol{\kappa}_j\cdot\nabla\cdot\nabla T_j + \sum_{CV}\dot{\mathbf{r}}_{jb}. \tag{95}$$

5 Comparison of Porous Media Averaging and Control Volume Analysis

Comparison of the equations derived above by means of the porous media averaging and control volume analysis approaches reveals several plausible closure methods for various terms as described in the following.

5.1 Mass Equation

Comparing Eqs. (28) and (74) the following relationships can be obtained for interpretation of the two terms appearing on the right of Eq. (74):

$$\frac{1}{\varepsilon_j}\mathbf{D}_{jb}\cdot\nabla\rho_{jb}=\frac{1}{\varepsilon_j}\left\langle\mathbf{D}_j\right\rangle_b\cdot\nabla\left\langle\rho_j\right\rangle_b-\left\langle\widehat{\mathbf{v}}_j\widehat{\rho}_j\right\rangle_b+\left\langle\widehat{\mathbf{D}}_j\cdot\widehat{\nabla\rho_j}\right\rangle_b \tag{96}$$

and

$$\begin{aligned}\sum_{CV}\dot{\mathbf{r}}_{jb}=\nabla\cdot\left(\frac{1}{\varepsilon_j}\left\langle\mathbf{D}_j\right\rangle_b\cdot\sum_l\frac{1}{V_b}\int_{A_{jl}}\rho_j\mathbf{n}_j\,dA\right)\\+\sum_l\frac{-1}{V_b}\int_{A_{jl}}\rho_j\left(\mathbf{v}_j-\mathbf{v}_{Ajl}\right)\cdot\mathbf{n}_j\,dA\\+\sum_l\frac{1}{V_b}\int_{A_{jl}}\mathbf{D}_j\cdot\nabla\rho_j\cdot\mathbf{n}_j\,dA+\left\langle\mathbf{q}_j\right\rangle_b.\end{aligned} \tag{97}$$

5.2 Momentum Equation

Note the first term on the right of Eq. (76) is given by Eq. (36). Comparing Eqs. (76) and (40) the following can be obtained:

$$\begin{aligned}\nabla\cdot\left[\frac{1}{\varepsilon_j}\mathbf{D}_{jb}\cdot\nabla\cdot\left(\frac{\rho_{jb}\mathbf{v}_{jb}}{\varepsilon_j}\right)\right]=\nabla\cdot\left\langle\mathbf{T}_j\right\rangle_b-\nabla\cdot\left(\frac{1}{\varepsilon_j}\left\langle\rho_j\right\rangle_b\left\langle\widehat{\mathbf{v}}_j\widehat{\mathbf{v}}_j\right\rangle_b\right.\\\left.+\frac{2}{\varepsilon_j}\left\langle\mathbf{v}_j\right\rangle_b\left\langle\widehat{\rho}_j\widehat{\mathbf{v}}_j\right\rangle_b+\left\langle\widehat{\rho}_j\widehat{\mathbf{v}}_j\widehat{\mathbf{v}}_j\right\rangle_b\right)\end{aligned} \tag{98}$$

and

$$\sum_{CV}\dot{\mathbf{r}}_{jb}=\sum_l\frac{-1}{V_b}\int_{A_{jl}}\rho_j\mathbf{v}_j\left(\mathbf{v}_j-\mathbf{v}_{Ajl}\right)\cdot\mathbf{n}_j\,dA+\sum_l\frac{1}{V_b}\int_{A_{jl}}\mathbf{T}_j\cdot\mathbf{n}_j\,dA+\left\langle\mathbf{q}_j\right\rangle_b. \tag{99}$$

Comparing Eqs. (93) and (53) for single-phase flow with constant ε_j and ρ_j, the following expressions can be determined as a method of closure based on the control volume analysis approach:

$$-\rho_j \left\langle \nabla \cdot (\widehat{\mathbf{v}}_j \widehat{\mathbf{v}}_j) \right\rangle_b + \frac{\rho_j}{V_b} \left\langle \mathbf{v}_j \right\rangle_j \left\langle \mathbf{v}_j \right\rangle_j \cdot \int_{A_{jl}} \mathbf{n}_j \, dA = -\varepsilon_j \rho_j \boldsymbol{\beta}_{jb} \cdot \left| \mathbf{v}_{jb} \right| \mathbf{v}_{jb}, \tag{100}$$

$$\frac{1}{V_b} \int_{A_{jl}} \mathbf{T}_j \cdot \mathbf{n}_j \, dA = -\varepsilon_j \mu_j \mathbf{K}_{jb}^{-1} \cdot \mathbf{v}_{jb} \tag{101}$$

and

$$\left\langle \mathbf{q}_j \right\rangle_b = \nabla \cdot \left[\frac{1}{\varepsilon_j} \mathbf{D}_{jb} \cdot \nabla \cdot \left(\rho_j \mathbf{v}_{jb} \right) \right] + \varepsilon_j \rho_j \mathbf{g}. \tag{102}$$

5.3 Energy Equation

Comparing Eq. (95) with Eq. (63) yields

$$\sum_{CV} \dot{\mathbf{r}}_{jb} = -\varepsilon_j \left\langle \rho_j \right\rangle_j \left\langle C_j \right\rangle_j \nabla \cdot \left\langle \widehat{\mathbf{v}}_j \widehat{T}_j \right\rangle_j + \frac{1}{V_b} \boldsymbol{\kappa}_j \cdot \nabla \cdot \left(\int_{A_j} T_j \mathbf{n}_j \, dA \right)$$
$$+ \frac{1}{V_b} \boldsymbol{\kappa}_j \cdot \int_{A_j} \nabla T_j \cdot \mathbf{n}_j \, dA + \left\langle q_{je} \right\rangle_b. \tag{103}$$

Note the source term on the right of Eq. (103) can be expressed as the following:

$$\begin{aligned} \left\langle q_{je} \right\rangle_b &= \left\langle \mathbf{v}_j \cdot \nabla p_j + \frac{\partial p_j}{\partial t} \right\rangle_b \\ &= \frac{\left\langle \mathbf{v}_j \right\rangle_b \cdot \left\langle \nabla p_j \right\rangle_b}{\varepsilon_j} + \left\langle \widehat{\mathbf{v}}_j \cdot \widehat{\nabla p_j} \right\rangle_b + \frac{\partial \left\langle p_j \right\rangle_b}{\partial t} - \frac{1}{V_b} \int_{A_{jl}} p_j \mathbf{v}_{Aj} \cdot \mathbf{n}_j \, dA \\ &= \frac{\left\langle \mathbf{v}_j \right\rangle_b \cdot \nabla \left\langle p_j \right\rangle_b}{\varepsilon_j} + \frac{\partial \left\langle p_j \right\rangle_b}{\partial t} + \left\langle \widehat{\mathbf{v}}_j \cdot \widehat{\nabla p_j} \right\rangle_b \\ &\quad + \frac{\left\langle \mathbf{v}_j \right\rangle_b}{\varepsilon_j} \cdot \frac{1}{V_b} \int_{A_{jl}} p_j \mathbf{n}_j \, dA - \frac{1}{V_b} \int_{A_{jl}} p_j \mathbf{v}_{Aj} \cdot \mathbf{n}_j \, dA. \end{aligned} \tag{104}$$

6 Discussions and Conclusions

The methodology and formulations presented in this chapter for derivation of the porous media macroscopic transport equations have emphasized and demonstrated the following issues:

- The gradient law used in porous media is based on the extrapolated limit concept. This extrapolation assumes the applicability of the basic definition of derivative in the limit as Δx, Δy, and $\Delta z \to 0$. This is simply a remedial measure considered for convenience in derivation of macroscopic equations. Frequently, the point of location is mistakenly assumed to be in a certain phase when the size of the elementary volume is reduced to a point of zero volume and therefore the volume fraction of that phase at that point of location is assumed to be 100%, whereas this point of location is nothing more than an imaginary extrapolation point from the elementary finite volume of bulk porous media where the amount of a certain phase is equal to its volume fraction in the bulk volume which is less than or equal to the porosity of porous media.
- The frequently used gradient law of spontaneous transport is incorrectly defined proportionally to the gradient of the intensive property expressed at a point in a given phase which is therefore identical to the gradient considered in microscopic transport formulation. This implies that the gradient becomes zero when the phase property is constant, whereas such condition applies only for microscopic transport formulation and is not applicable in porous media averaged formulation. Thus, the correct expression of the spontaneous transport in porous media should be taken with respect to the gradient of the driving (inducing) property contained per unit bulk volume which is equal to the property multiplied by the volume fraction of the phase. Consequently, the porous media gradient becomes zero only when both the phase property and volume fraction are constant for macroscopic transport formulation. Therefore, the porous media gradient is not zero and transport can still occur if either the phase property or volume fraction, or both vary with distance in porous media.
- Control volume analysis is proven to be complementary to porous media averaging in the formulation of porous media macroscopic transport equations. Hence, comparison of the results obtained by control volume analysis and porous media averaging can be beneficial in resolving some difficulties such as developing methods for closure of various complicated terms involving the deviations of properties from their intrinsic fluid-volume averages. Proper closure methods inferred by control volume analysis can reduce the complexity of the equations obtained by porous media averaging. The control volume analysis requires creative applications to resolve various issues such as based on the capillary-orifice model used for expressing the pore surface wall friction forces and pore throat drag. This, in turn, provides valuable insights of practical importance.
- Improper applications of the basic rules of averaging may result with erroneous formulations. This explains the discrepancies between the results obtained here and the corresponding efforts reported in the literature. However, this issue is subtle and continues to be a major source of errors in porous media averaging. It is essential to apply the fluid intrinsic volume and bulk-volume-averaging rules in the derivation of macroscopic formulations in a manner such that the resulting expressions can in turn conform to these rules. This issue was illustrated for expressing the bulk-volume averages of the products of two and three properties in terms of the bulk-volume averages of the individual properties. It was shown

that only the approach based on decomposing the fluid property into its intrinsic fluid-volume average and its deviation from this average leads to a formulation which is reversibly consistent with the averaging rules.

Appendix

The equations of [19] are different from those presented in this chapter because of a systematic error involved in their derivations of the momentum and energy equations. This issue is subtle and will be explained by the following example in their choice of symbols which correspond to those used in this chapter as $\langle u\rangle^f = \langle u\rangle_j$ and $\langle u\rangle = \langle u\rangle_b$ representing the intrinsic fluid j-phase-volume and REV bulk-volume averages, respectively.

For example, the first terms in Eq. (20) of [19] read as

$$\left\langle \partial_j u_i u_j \right\rangle = \partial_j \left\langle \langle u_i\rangle^f \left\langle u_j \right\rangle^f \right\rangle + \text{ other terms.} \tag{105}$$

They arrive at the following expression of their Eq. (21) after processing Eq. (105) by considering that the average of $\langle u_i\rangle^f \left\langle u_j \right\rangle^f$ is identical to itself only over the REV bulk volume because $\langle u_i\rangle^f \left\langle u_j \right\rangle^f$ is constant:

$$\left\langle \partial_j u_i u_j \right\rangle = \partial_j \langle u_i\rangle^f \left\langle u_j \right\rangle^f + \text{ other terms.} \tag{106}$$

Therefore, their Eq. (21) leads to the following expression in the rest of their formulations, for example, in their Eq. (26), when expressed in terms of the superficial or REV bulk-volume average fluid velocity:

$$\left\langle \partial_j u_i u_j \right\rangle = \partial_j \left(\frac{\langle u_i\rangle \left\langle u_j \right\rangle}{\varepsilon^2} \right) + \text{ other terms.} \tag{107}$$

This procedure is not correct because it is not consistent with the rules of averaging. The proper procedure is described in the following.

The first terms in Eq. (20) of [19] should be processed as

$$\left\langle \partial_j u_i u_j \right\rangle = \partial_j \left\langle \langle u_i\rangle^f \left\langle u_j \right\rangle^f \right\rangle + \text{ other terms} = \partial_j \left(\varepsilon \left\langle \langle u_i\rangle^f \left\langle u_j \right\rangle^f \right\rangle^f \right) + \text{ other terms.} \tag{108}$$

Then, their Eq. (21) takes the following form after processing Eq. (105) by considering that the average of $\langle u_i\rangle^f \left\langle u_j \right\rangle^f$ is identical to itself over the fluid volume contained inside the REV bulk volume:

$$\left\langle \partial_j u_i u_j \right\rangle = \partial_j \left(\varepsilon \langle u_i\rangle^f \left\langle u_j \right\rangle^f \right) + \text{ other terms.} \tag{109}$$

Therefore, Eq. (109) takes the following form when expressed in terms of the superficial or REV bulk-volume average fluid velocity:

$$\left\langle \partial_j u_i u_j \right\rangle = \partial_j \left(\frac{\left\langle u_i \right\rangle \left\langle u_j \right\rangle}{\varepsilon} \right) + \text{ other terms.} \tag{110}$$

In view of the above explanation and illustration, the formulations of [19] require corrections of their systematic errors.

References

1. Biot, M.A.: General theory of three dimensional consolidation. J. Appl. Phys. **12**, 155–164 (1941)
2. Blick, E.F., Civan, F.: Porous media momentum equation for highly accelerated flow. SPE Reserv. Eng. **3**, 1048–1052 (1988)
3. Civan, F.: Unfrozen water content in freezing and thawing soils—kinetics and correlation. J. Cold Reg. Eng. **14**, 146–156 (2000)
4. Civan, F.: Implications of alternative macroscopic descriptions illustrated by general balance and continuity equations. J. Porous Media. **5**, 271–282 (2002)
5. Civan, F.: Generalized Darcy's law by control volume analysis including capillary and orifice effects. J. Can. Petrol. Tech. **47**, 1–7 (2008)
6. Civan, F.: Modeling transport in porous media by control volume analysis. J. Porous Media **13**, 855–873 (2010)
7. Civan, F.: Porous Media Transport Phenomena. Wiley, Hoboken, New Jersey (2011)
8. Civan, F., Evans, R.D.: Determining the parameters of the Forchheimer equation from pressure-squared vs. pseudo-pressure Formulations. SPE Reserv. Eval. Eng. **1**, 43–46 (1998)
9. Darcy, H.: Les Fontaines Publiques de la Ville de Dijon. Victor Dalmont, Paris (1856)
10. de Lemos, M.J.S.: Analysis of turbulent flows in fixed and moving permeable media. Acta Geophys. **56**, 562–583 (2008)
11. Gray, W.G.: A derivation of the equations for multiphase transport. Chem. Eng. Sci. **30**, 229–233 (1975)
12. Hsu, C.-T.: Dynamic modeling of convective heat transfer. In: Vafai, K. (ed.) Porous Media, Handbook of Porous Media, 2nd edn., pp. 39–80. CRC Press, Taylor & Francis, LLC, Boca Raton (2005)
13. Hubbert, M.K.: Darcy's law and the field equations of the flow of underground fluids. Petrol. Trans. AIME **207**, 222–239 (1956)
14. Lasseux, D., Ahmadi, A., Arani, A.A.A.: Two-phase inertial flow in homogeneous porous media: a theoretical derivation of a macroscopic model. Transport Porous Med. **75**, 371–400 (2008)
15. Liu, S., Masliyah, J.H.: Dispersion in porous media. In: Vafai, K. (ed.) Porous Media, Handbook of Porous Media, 2nd edn., pp. 81–140. CRC Press, Taylor & Francis Group, LLC, Boca Raton (2005)
16. Prada, A., Civan, F.: Modification of Darcy's law for the threshold pressure gradient. J. Petrol. Sci. Eng. **22**, 237–240 (1999)
17. Schulenberg, T., Muller U.: An improved model for two-phase flow through beds of coarse particles. Int. J. Multiphase Flow. **13**, 87–97 (1987)
18. Slattery, J.C.: Momentum, Energy and Mass Transfer in Continua. McGraw-Hill, New York (1972)
19. Sozer, E., Shyy, W.: Multi-scale thermo-fluid transport in porous media. Int. J. Numer. Meth. Heat Fluid Flow **18**, 883–899 (2008)
20. Whitaker, S.: The Method of Volume Averaging. Kluwer Academic Publishers, Boston (1999)

On the Energy Conservation Formulation for Flows in Porous Media Including Viscous Dissipation Effects

V.A.F. Costa

Abstract Energy conservation formulation needs to be carefully conducted when dealing with natural or mixed convection problems if viscous dissipation is considered. A violation of the Energy Conservation Principle exists if only the viscous dissipation term is considered, and if its counterpart, the work of pressure forces is not also considered in the internal energy conservation equation. This is true both for flows in clear fluid domains and for flows in fluid-saturated porous domains. In this chapter general detailed energy conservation formulations are conducted, first for flows in clear fluid domains and then for flows in fluid-saturated porous domains. Main conclusions obtained from the model for flows in clear fluid domains are equally relevant for flows in fluid-saturated porous domains. Considering an enclosure of rigid walls where steady natural convection takes place, it is shown that, when integrating over the overall domain, the viscous dissipation (energy source) has its symmetric on the work of pressure forces (energy sink). Globally heat entering the enclosure equals the heat leaving it, no matter the thermal boundary conditions considered at the enclosure walls. It is shown in an exact way that this result applies both for domains filled with a clear fluid or filled with a fluid-saturated porous medium. Main conclusions concerning verification of the Energy Conservation Principle are extracted from what happens in steady natural convection in enclosures filled with fluid-saturated porous domains and then to what happens in steady natural convection in open fluid-saturated porous domains, in unsteady natural convection problems in fluid-saturated porous domains, and also in steady or unsteady mixed convection problems in fluid-saturated porous domains.

V.A.F. Costa (✉)
Departamento de Engenharia Mecânica, Universidade de Aveiro, Campus Universitário de Santiago, 3810 - 193 Aveiro, Portugal
e-mail: v.costa@ua.pt

J.A. Ferreira et al. (eds.), *Modelling and Simulation in Fluid Dynamics in Porous Media*, Springer Proceedings in Mathematics & Statistics 28, DOI 10.1007/978-1-4614-5055-9_3,

1 Introduction

Energy conservation formulation needs to be carefully conducted if viscous dissipation is considered in the energy conservation equation, both for flows in clear fluid domains and for flows in fluid-saturated porous domains. This is an ongoing research topic, as shown by the amount of recent works dealing with it [1–8]. This problem is crucial when natural or mixed convection is present, as in this case the work of pressure forces needs to be considered in the energy conservation equation if the viscous dissipation is considered in that equation. If this is not the case the Energy Conservation Principle is violated and the energy model is not correct, as well as any eventual results obtained using such unrealistic energy formulation.

In previous works [1, 2, 5, 7] the author tried to clarify this question, but it is still being debated in the literature [5–8], and energy models continue being proposed and results obtained and presented in the literature violating the Energy Conservation Principle (energy being created from nothing or destructed to nothing).

Present contribution aims to present and discuss the exact energy conservation formulation for flows in clear fluid domains and emphasize the relative importance of the work of pressure forces and viscous dissipation in some particular cases and in particular in natural or mixed convection problems. Some new exact developments are presented, regarding the literature on the field, thus trying to solve some controversial questions debated in the recent literature. This is done going back to the basic principles embodied by the conservation equations. It is emphasized that both the viscous dissipation and the work of pressure forces need to be considered together in the internal energy conservation equation, the unique consistent energy conservation formulation respecting the Energy Conservation Principle. Main conclusions obtained for flows in clear fluid domains are also applied to the energy conservation formulation when dealing with flows in fluid-saturated porous domains.

Main basic physical principles needed to establish the aforementioned consistent energy conservation formulation are taken essentially from [9, 10]. In what follows, Sect. 2 deals with mass conservation, Sect. 3 with the momentum, kinetic, and mechanical energy balance equations, Sect. 4 with the total (mechanical plus internal) energy balance equation, Sect. 5 with the different forms of the internal energy balance equation, Sect. 6 with the analysis and consequences of the previous equations, and Sect. 7 deals with the most usual forms of the thermal energy balance equation.

2 Mass Conservation Equation

Fluid flow and natural, mixed, or forced convection occur in a certain domain V, where all variables are defined.

The *mass conservation equation* (continuity equation) for a flow in a clear fluid domain can be written as in [9]

$$\frac{\partial \rho}{\partial t} + (\nabla \cdot \rho \mathbf{v}) = 0. \tag{1}$$

Equation (1) can be rewritten as

$$\frac{D\rho}{Dt} + \rho (\nabla \cdot \mathbf{v}) = 0, \tag{2}$$

where the material, or substantial, derivative of the generic variable ϕ is obtained as in [9]

$$\frac{D\phi}{Dt} = \frac{\partial \phi}{\partial t} + (\mathbf{v} \cdot \nabla \phi). \tag{3}$$

For a fluid-saturated porous domain of uniform porosity ε, the similar equations for the fluid phase become

$$\frac{\partial}{\partial t}(\rho \varepsilon) + (\nabla \cdot \rho \mathbf{v}) = 0. \tag{4}$$

Equation (2) is valid for clear fluids and for fluid-saturated porous domains, and the analogous of Eq. (3) for fluid-saturated porous domains is

$$\frac{D\phi}{Dt} = \varepsilon \frac{\partial \phi}{\partial t} + (\mathbf{v} \cdot \nabla \phi). \tag{5}$$

3 Momentum, Kinetic, and Mechanical Energy Balance Equations

The *momentum balance equations* for a flow in a clear fluid domain can be expressed compactly as in [9]:

$$\frac{\partial}{\partial t}(\rho \mathbf{v}) + [\nabla \cdot \rho \mathbf{v}\mathbf{v}] = -\nabla p - [\nabla \cdot \tau] + \rho \mathbf{g}. \tag{6}$$

For fluid-saturated porous domains of uniform porosity ε and permeability K, the similar equation for the fluid phase becomes (see [11])

$$\frac{1}{\varepsilon}\frac{\partial}{\partial t}(\rho \mathbf{v}) + \frac{1}{\varepsilon^2}[\nabla \cdot \rho \mathbf{v}\mathbf{v}] = -\nabla p - [\nabla \cdot \tau_{eff}] + \rho \mathbf{g} - \left(\frac{\mu}{K} + \frac{\rho c_F}{\sqrt{K}}|\mathbf{v}|\right)\mathbf{v}, \tag{7}$$

where the inertial, Brinkman (viscous), Darcy, and Forchheimer terms have been considered. In this case τ_{eff} is used instead of simply τ, i.e., the effective stress tensor in the fluid-saturated porous medium.

If the flow in the fluid-saturated porous domain takes place with low velocity and $Re_{\sqrt{K}} = \rho|\mathbf{v}|\sqrt{K}/\mu \lesssim 1$, the simpler Darcy flow model can be used, and the *momentum equation* reduces to

$$0 = -\nabla p + \rho\mathbf{g} - \frac{\mu}{K}\mathbf{v}, \tag{8}$$

or, in the most usual form, written to provide velocity as

$$\mathbf{v} = -\frac{K}{\mu}\left[\nabla p - \rho\mathbf{g}\right]. \tag{9}$$

The foregoing momentum equations can be multiplied by $\mathbf{v}$ (scalar product) to give the *kinetic energy conservation equation* for the flow in a clear fluid domain as [9]

$$\begin{aligned}\frac{\partial}{\partial t}\left(\frac{1}{2}\rho\left|\mathbf{v}\right|^2\right) + \left(\nabla\cdot\frac{1}{2}\rho\left|\mathbf{v}\right|^2\mathbf{v}\right) = &-\left(\nabla\cdot p\mathbf{v}\right) - p\left(-\nabla\cdot\mathbf{v}\right)\\ &-\left(\nabla\cdot\left[\boldsymbol{\tau}\cdot\mathbf{v}\right]\right) - \left(-\boldsymbol{\tau}:\nabla\mathbf{v}\right) + \rho\left(\mathbf{v}\cdot\mathbf{g}\right).\end{aligned} \tag{10}$$

For fluid-saturated porous domains, the similar kinetic energy conservation equation for the fluid phase becomes

$$\begin{aligned}\varepsilon\frac{\partial}{\partial t}\left(\frac{1}{2}\rho\frac{\left|\mathbf{v}\right|^2}{\varepsilon^2}\right) + \left(\nabla\cdot\frac{1}{2}\rho\frac{\left|\mathbf{v}\right|^2}{\varepsilon^2}\mathbf{v}\right) = &-\left(\nabla\cdot p\mathbf{v}\right) - p\left(-\nabla\cdot\mathbf{v}\right)\\ &-\left(\nabla\cdot\left(\tau_{eff}\cdot\mathbf{v}\right)\right) - \left(-\tau_{eff}:\nabla\mathbf{v}\right)\\ &+\rho\left(\mathbf{v}\cdot\mathbf{g}\right) - \left(\frac{\mu}{K} + \frac{\rho c_F}{\sqrt{K}}\left|\mathbf{v}\right|\right)\left|\mathbf{v}\right|^2,\end{aligned} \tag{11}$$

and if the Darcy flow model can be used, the corresponding equation becomes simply

$$0 = -\left(\nabla\cdot p\mathbf{v}\right) - p\left(-\nabla\cdot\mathbf{v}\right) + \rho\left(\mathbf{v}\cdot\mathbf{g}\right) - \left(\frac{\mu}{K}\right)\left|\mathbf{v}\right|^2. \tag{12}$$

Another possible way to write the foregoing equations is to consider the gravitational potential energy by unit mass as $\hat{\phi}$, defined by $\mathbf{g} = -\nabla\hat{\phi}$. In this way, the gravitational term in Eqs. (10)–(12) can be written as

$$\begin{aligned}\rho\left(\mathbf{v}\cdot\mathbf{g}\right) = -\rho\left(\mathbf{v}\cdot\nabla\hat{\phi}\right) &= -\left(\nabla\cdot\rho\mathbf{v}\hat{\phi}\right) + \hat{\phi}\left(\nabla\cdot\rho\mathbf{v}\right) = -\left(\nabla\cdot\rho\mathbf{v}\hat{\phi}\right) - \hat{\phi}\frac{\partial\rho}{\partial t}\\ &= -\left(\nabla\cdot\rho\mathbf{v}\hat{\phi}\right) - \frac{\partial\left(\rho\hat{\phi}\right)}{\partial t},\end{aligned} \tag{13}$$

assuming that $\hat{\phi}$ is independent of time, Eq. (10) can be written as

$$\frac{\partial}{\partial t}\left(\frac{1}{2}\rho\left|\mathbf{v}\right|^2+\rho\hat{\phi}\right)+\left(\nabla\cdot\left(\frac{1}{2}\rho\left|\mathbf{v}\right|^2+\rho\hat{\phi}\right)\mathbf{v}\right)=-\left(\nabla\cdot p\mathbf{v}\right)-p\left(-\nabla\cdot\mathbf{v}\right)$$
$$-\left(\nabla\cdot\left[\tau\cdot\mathbf{v}\right]\right)-\left(-\tau:\nabla\mathbf{v}\right) \quad (14)$$

and Eq. (11) can be written as

$$\varepsilon\frac{\partial}{\partial t}\left(\frac{1}{2}\rho\frac{\left|\mathbf{v}\right|^2}{\varepsilon^2}+\rho\widehat{\phi}\right)+\left(\nabla\cdot\left(\frac{1}{2}\rho\frac{\left|\mathbf{v}\right|^2}{\varepsilon^2}+\rho\widehat{\phi}\right)\mathbf{v}\right)=-\left(\nabla\cdot p\mathbf{v}\right)$$
$$-p\left(-\nabla\cdot\mathbf{v}\right)-\left(\nabla\cdot\left(\tau_{eff}\cdot\mathbf{v}\right)\right)-\left(-\tau_{eff}:\nabla\mathbf{v}\right)-\left(\frac{\mu}{K}+\frac{\rho c_F}{\sqrt{K}}\left|\mathbf{v}\right|\right)\left|\mathbf{v}\right|^2, \quad (15)$$

which are the equations for the *mechanical* (kinetic plus potential) *energy*, as they contain only mechanical energy terms. Mechanical energy is, as generally accepted, intended as the form of energy that can be integrally and directly converted to mechanical useful work by an ideal (without losses) mechanical device [9, 10].

Terms in Eq. (14) are identified, from left to right, on a per unit volume basis, as (a) rate of increase of mechanical (kinetic plus gravitational) energy; (b) rate of mechanical (kinetic plus gravitational) energy leaving by convective transport; (c) rate of work done by pressure of surroundings on the fluid; (d) rate of *reversible* conversion of kinetic energy into internal energy; (e) rate of work done by viscous forces on the fluid; and (f) rate of *irreversible* conversion from kinetic to internal energy. Equation (15) has two additional terms, which are the rate of *irreversible* conversion from kinetic to internal energy due to the Darcy and Forchheimer terms.

If the Darcy flow model can be used, Eq. (12) becomes

$$\varepsilon\frac{\partial}{\partial t}\left(\rho\widehat{\phi}\right)+\left(\nabla\cdot\left(\rho\widehat{\phi}\right)\mathbf{v}\right)=-\left(\nabla\cdot p\mathbf{v}\right)-p\left(-\nabla\cdot\mathbf{v}\right)-\frac{\mu}{K}\left|\mathbf{v}\right|^2. \quad (16)$$

From this point forward, only the clear fluid domain model and the Darcy–Brinkman–Forccheimer model will be considered.

4 Total (Mechanical Plus Internal) Energy Balance Equation

Equation for the *total* [internal ($\rho\hat{u}$) plus kinetic ($\frac{1}{2}\rho\left|\mathbf{v}\right|^2$) plus (gravitational) potential ($\rho\hat{\phi}$)] *energy* for the flow in the clear fluid domain can be written, following Bird et al. [9] as

$$\frac{\partial}{\partial t}\left(\rho\hat{u}+\frac{1}{2}\rho\left|\mathbf{v}\right|^2+\rho\hat{\phi}\right)+\nabla\cdot\left(\left(\rho\hat{u}+\frac{1}{2}\rho\left|\mathbf{v}\right|^2+\rho\hat{\phi}\right)\mathbf{v}\right)=-\left(\nabla\cdot\mathbf{q}\right)$$
$$-\left(\nabla\cdot p\mathbf{v}\right)-\left(\nabla\cdot\left[\tau\cdot\mathbf{v}\right]\right). \quad (17)$$

The terms in this equation are identified, from left to right, on a per unit volume basis, as: (a) rate of increase of total (internal plus kinetic plus gravitational) energy; (b) rate of total (internal plus kinetic plus gravitational) energy leaving by convective transport; (c) rate of energy addition by heat conduction; (d) rate of work done on the fluid by pressure forces; and (e) rate of work done by viscous forces on the fluid.

For fluid-saturated porous domains, the similar equation for the fluid phase becomes

$$\varepsilon\frac{\partial}{\partial t}\left(\rho\hat{u}+\frac{1}{2}\rho\frac{|\mathbf{v}|^2}{\varepsilon^2}+\rho\widehat{\phi}\right)+\nabla\cdot\left(\left(\rho\hat{u}+\frac{1}{2}\rho\frac{|\mathbf{v}|^2}{\varepsilon^2}+\rho\widehat{\phi}\right)\mathbf{v}\right)$$
$$=ha_v\left(T_s-T_f\right)-\left(\nabla\cdot\mathbf{q}\right)-\left(\nabla\cdot p\mathbf{v}\right)-\left(\nabla\cdot\left[\tau_{eff}\cdot\mathbf{v}\right]\right). \tag{18}$$

In this case $\mathbf{q}$ is the conduction heat transfer vector in the fluid phase, and an additional term exists on the right-hand side of the equation expressing the heat released by the solid phase and received by the fluid phase, $ha_v\left(T_s-T_f\right)$, where a_v is the volumetric surface area of the interface between the solid and fluid phases and h is the corresponding convection heat transfer coefficient.

The total (internal plus mechanical) energy conservation equation is the mathematical form of the Energy Conservation Principle, sometimes, and in some contexts, referred also to as the First Law of Thermodynamics [10]. Energy can change from one form to another, but the total energy is conserved, and the Energy Conservation Principle is associated to the total (internal plus mechanical) energy conservation equation.

Solid phase is fixed, has no kinetic energy, and its gravitational potential energy is irrelevant, and the total energy conservation equation for the combined (fluid plus solid) medium is

$$\varepsilon\frac{\partial}{\partial t}\left(\rho\hat{u}+\frac{1}{2}\rho\frac{|\mathbf{v}|^2}{\varepsilon^2}+\rho\widehat{\phi}\right)+(1-\varepsilon)\frac{\partial}{\partial t}\left(\rho_s\hat{u}_s\right)$$
$$+\nabla\cdot\left(\left(\rho\hat{u}+\frac{1}{2}\rho\frac{|\mathbf{v}|^2}{\varepsilon^2}+\rho\widehat{\phi}\right)\mathbf{v}\right)=-\left(\nabla\cdot\mathbf{q}\right)-\left(\nabla\cdot p\mathbf{v}\right)-\left(\nabla\cdot\left[\tau_{eff}\cdot\mathbf{v}\right]\right), \tag{19}$$

where the term expressing the heat exchange between the fluid and solid phases disappeared (heat gained by one phase is heat lost by the other phase, with a null effect for the combined medium), and $\mathbf{q}=\mathbf{q}_f+\mathbf{q}_s$ is the total heat conduction occurring in the combined (fluid plus solid) medium.

5 Internal Energy Balance Equations

Subtracting the mechanical energy conservation equation (14) from the total energy conservation equation (17) the internal energy conservation equation in its conservative form [9] for the flow in the clear fluid domain is

$$\frac{\partial}{\partial t}(\rho\hat{u}) + (\nabla\cdot\rho\hat{u}\mathbf{v}) = -(\nabla\cdot\mathbf{q}) - p(\nabla\cdot\mathbf{v}) - (\tau:\nabla\mathbf{v}). \tag{20}$$

For fluid-saturated porous domains, the similar equation is obtained subtracting Eq. (15) from Eq. (19) to give

$$\varepsilon\frac{\partial}{\partial t}(\rho\hat{u}) + (1-\varepsilon)\frac{\partial}{\partial t}(\rho_s\hat{u}_s) + (\nabla\cdot\rho\hat{u}\mathbf{v}) = -(\nabla\cdot\mathbf{q}) - p(\nabla\cdot\mathbf{v}) - (\tau_{eff}:\nabla\mathbf{v}) + \left(\frac{\mu}{K} + \frac{\rho c_F}{\sqrt{K}}|\mathbf{v}|\right)|\mathbf{v}|^2. \tag{21}$$

The terms in Eq. (20) are identified, from left to right, on a per unit volume basis, as (a) rate of increase of internal energy; (b) rate of internal energy leaving by convective transport; (c) rate of energy addition by heat conduction; (d) *reversible* rate of internal energy increase by compression of the fluid (work of pressure forces); and (e) *irreversible* rate of internal energy increase by viscous dissipation. Only for incompressible fluids is $\nabla\cdot\mathbf{v} = 0$, and term $-p(\nabla\cdot\mathbf{v})$ is null. It can be seen that the symmetric of the term $-(-\tau:\nabla\mathbf{v})$ in Eq. (14) appears in Eq. (20), and this term represents in Eq. (14) a loss of mechanical energy which appears as an increase of the internal energy in Eq. (20), and it represents thus an *irreversible* conversion and loss of mechanical (kinetic plus gravitational) energy as heat. For the flow in the fluid-saturated porous domain, two additional terms exist, expressing the *irreversible* increase of the internal energy due to the Darcy and Forchheimer terms.

When the simpler Darcy flow model is used to describe the fluid flow, it is a usual practice to use a reduced version of Eq. (21) as

$$\varepsilon\frac{\partial}{\partial t}(\rho\hat{u}) + (1-\varepsilon)\frac{\partial}{\partial t}(\rho_s\hat{u}_s) + (\nabla\cdot\rho\hat{u}\mathbf{v}) = -(\nabla\cdot\mathbf{q}) - p(\nabla\cdot\mathbf{v}) + \left(\frac{\mu}{K}\right)|\mathbf{v}|^2, \tag{22}$$

without considering the Brinkman and Forchheimer terms. It is to be noted that this is not exactly the result obtained subtracting Eq. (16) from Eq. (19), with null Brinkman term, as no counterpart exists in Eq. (16) to the kinetic energy terms in Eq. (19). However, this is consistent with the use of the Darcy flow model, which does not consider any inertia terms or inertial effects.

6 Analysis, Notes, and Consequences of the Previous Equations

Considering the steady-state version of Eqs. (17) and (19) for the *total energy*, with null unsteady terms, and integrating over a closed domain with fixed boundaries, without any internal moving solid elements, noting that velocity is null over the boundaries of the domain, and using the Gauss Theorem to convert volume

integrals to surface integrals, one obtains that

$$\int_V -(\nabla \cdot \mathbf{q})\, dV = -\int_S \mathbf{q} \cdot \mathbf{n} dA = 0. \tag{23}$$

This result implies that no net heat inflow or outflow exists in the system.

Taking this result in mind, we consider similarly the steady-state version of Eqs. (20) and (21) for the *internal energy* to obtain respectively that

$$\int_V -p\,(\nabla \cdot \mathbf{v})\, dV + \int_V -(\tau : \nabla \mathbf{v})\, dV = 0, \tag{24}$$

$$\int_V -p\,(\nabla \cdot \mathbf{v})\, dV + \int_V -\left(\tau_{eff} : \nabla \mathbf{v}\right) dV + \int_V \left(\frac{\mu}{K} + \frac{\rho_f c_F}{\sqrt{K}}\,|\mathbf{v}|\right) |\mathbf{v}|^2\, dV = 0. \tag{25}$$

The main conclusions of the foregoing results, obtained for the steadystate situation in a closed domain of fixed boundaries, and without any internal moving solid parts, are as follows: (a) There is no net heat inflow or outflow to or from the system, no matter if the domain is filled with a clear fluid or with a fluid-saturated porous medium; (b) if the domain is filled with a clear fluid, the volume integral of the work of pressure forces equals the volume integral of the viscous dissipation, and both terms need to be considered in the internal energy conservation equation, Eq. (20); (c) if the domain is filled with a fluid-saturated porous medium, result of Eq. (25) needs to be verified, and all these terms need to be considered in the internal energy conservation equation, Eq. (21); and (d) work of pressure forces is relevant in natural or mixed convection problems, where density variations are totally or partially inducing the fluid motion, with associated expansions and contractions of the fluid, and its associated volume change work energy interaction.

The energy conservation formulation for the clear fluid domains as explained above is exact, the unique assumption is that the gravitational potential energy by unit mass $\widehat{\phi}$ is independent of time, and it shows that the correct energy formulation of the problem needs to consider the work of pressure forces if the viscous dissipation is considered. At a microscopic level, results obtained for the clear fluid domains apply also for the fluid-saturated porous domains. Developments made above for the flows in fluid-saturated porous domains are not exact, as the Darcy, Brinkman, and Forchheimer models are approximations, but the main conclusions obtained for the clear fluid domains remain also valid. In any problem, in open or closed fluid domains, or even in unsteady problems, if natural or mixed convection is present, work of pressure forces needs to be considered if the viscous dissipation is considered in the internal energy conservation equation. Equations (24) and (25) do not apply in all cases, but their validity for the steady situations and closed domains leads to very important conclusions for the energy conservation formulation even for other different cases. This is the main result and conclusion of the developments above and of this work.

7 Thermal Energy Balance Equations

Usual energy conservation equation taken for problems' solution is the internal energy conservation equation, but with temperature as the dependent variable. Thus, some more steps are needed to transform the *internal energy* conservation equations in the usual *thermal energy* conservation equations. However, it is to be retained that the aforementioned main issues concerning the energy conservation formulation remain independently of the particular form of the internal energy conservation equation used for practical purposes.

Using the mass conservation equation (2), Eq. (20) can be rewritten as

$$\rho \frac{D\hat{u}}{Dt} = -(\nabla \cdot \mathbf{q}) - p(\nabla \cdot \mathbf{v}) - (\tau : \nabla \mathbf{v}). \tag{26}$$

Noting that the specific enthalpy is [10]

$$\hat{h} = \hat{u} + \frac{p}{\rho}; \tag{27}$$

the internal energy conservation equation (26) can be cast as follows:

$$\rho \frac{D\hat{h}}{Dt} = -(\nabla \cdot \mathbf{q}) - (\tau : \nabla \mathbf{v}) + \frac{Dp}{Dt}, \tag{28}$$

which is the enthalpy counterpart of the internal energy conservation equation as given by Eq. (26).

From [10], if $\hat{h} = \hat{h}(T, p)$ it can be written as

$$d\widehat{h} = \left(\partial \widehat{h} / \partial T\right)_p dT + \left(\partial \widehat{h} / \partial p\right)_T dp = c_p dT + \left(\partial \widehat{h} / \partial p\right)_T dp,$$

where $c_p(T, p) = \left(\partial \widehat{h} / \partial T\right)_p$. Recalling that $Tds = d\widehat{u} + pdv$, and that $d\widehat{h} = d\widehat{u} + pdv + vdp$, and invoking the Maxwell relation $\left(\partial s / \partial p\right)_T = -\left(\partial v / \partial T\right)_p$ [10], it is obtained that $d\hat{h} = c_P dT + \left[(1 - \beta T) / \rho\right] dp$, where the volumetric thermal expansion coefficient is $\beta = -\left(1/\rho\right)\left(\partial \rho / \partial T\right)_p$, and then that

$$\rho \frac{D\hat{h}}{Dt} = \rho c_P \frac{DT}{Dt} + (1 - \beta T) \frac{Dp}{Dt}. \tag{29}$$

Combining Eqs. (28) and (29), the following form of the internal energy conservation equation, usually referred to as the c_P form of the *thermal energy conservation equation* as the explicit dependent variable in it is temperature, is obtained as

$$\rho c_P \frac{DT}{Dt} = -(\nabla \cdot \mathbf{q}) - (\tau : \nabla \mathbf{v}) + \beta T \frac{Dp}{Dt}, \tag{30}$$

where on the right-hand side, the presence of the viscous dissipation term and of the work of pressure forces term is clear.

If we are dealing with a fluid-saturated porous domain, similar developments can be conducted leading to

$$\rho c_P \frac{DT}{Dt} + (1-\varepsilon)\rho_s c_{P,s} \frac{\partial T_s}{\partial t} = -(\nabla \cdot \mathbf{q}) - \left(\boldsymbol{\tau}_{eff} : \nabla \mathbf{v}\right) + \beta T \frac{Dp}{Dt} + \left(\frac{\mu}{K} + \frac{\rho c_F}{\sqrt{K}} |\mathbf{v}|\right) |\mathbf{v}|^2 . \tag{31}$$

When solving this equation is usual to consider equal local temperatures of the solid and fluid phases (local thermal equilibrium), $T = T_f = T_s$, even if some models exist to consider the local thermal nonequilibrium [11].

8 Conclusions

Energy conservation formulation has some subtle details, especially when considering the viscous dissipation in natural or mixed convection problems. The unique energy conservation formulation compatible with the Energy Conservation Principle for such problems is that considering the work of pressure forces if the viscous dissipation is considered. If this is not the case, the domain behaves like an energy source or sink, energy emerging or disappearing continuously from nothing or to nothing, in a clear violation of the Energy Conservation Principle.

Starting from the basic principles associated with the energy conservation formulation it is given the answer for a question being debated in the recent literature. Main exact results are obtained for steady clear fluids in closed domains, highlighting that the main issues related with the viscous dissipation and the work of pressure forces apply also for fluid-saturated porous domains.

Models used to solve the equations as well as models used to describe the medium properties can induce some inconsistencies on the energy conservation formulation, but the problems of an incorrect energy conservation formulation cannot be mixed, or confused, with such approximations, and it is crucial to start problems' analysis with the correct energy conservation formulation respecting the Energy Conservation Principle.

Appendix

Main notation follows from [9]. Properties refer to the fluid phase, and only when strictly necessary the subscript s is used to denote that a particular property refers to the (rigid and fixed) solid phase.

Equations are mainly written in a compact vector and/or tensor form, using the notation as proposed by Bird et al. [9], where a term involving the vector differential operator ∇ inside a curved bracket means a scalar and a term involving the vector differential operator ∇ inside a square bracket means a vector.

a_v specific area, by unit volume
A surface area
c_F drag coefficient
c_P constant pressure specific heat
D substantial, or material, derivative
$\mathbf{g}$ gravitational acceleration vector
K permeability of the porous medium
h convection heat transfer coefficient
$\hat{h}$ specific enthalpy
p pressure
$\mathbf{q}$ conduction heat transfer vector
Re Reynolds number
s specific entropy
S area enclosing volume V
t time
T temperature
$\hat{u}$ specific internal energy
v specific volume ($= \frac{1}{\rho}$)
$\mathbf{v}$ velocity vector
V volume

Greek symbols
β volumetric expansion coefficient
ε porosity
μ dynamic viscosity
ρ density
τ stress tensor
ϕ generic variable
$\hat{\phi}$ potential gravitational energy by unit mass

Subscripts
eff effective
f fluid
s solid

Vector and tensor products:
$\mathbf{x}\cdot\mathbf{y}$—dot product of vectors $\mathbf{x}$ and $\mathbf{y}$ or dot product of a vector $\mathbf{x}$ and a tensor $\mathbf{y}$
$\mathbf{x}:\mathbf{y}$—double dot product of tensors $\mathbf{x}$ and $\mathbf{y}$
$\mathbf{xy}$—dyadic vector product of vectors $\mathbf{x}$ and $\mathbf{y}$

References

1. Costa, V.A.F.: Thermodynamics of natural convection in enclosures with viscous dissipation. Int. J. Heat Mass Transf. **48**, 2333–2341 (2005)
2. Costa, V.A.F.: On natural convection in enclosures filled with fluid-saturated porous media including viscous dissipation. Int. J. Heat Mass Transf. **49**, 2215–2226 (2006)
3. Nield, D.A.: Resolution of a paradox involving viscous dissipation and nonlinear drag in a porous medium. Transport Porous Med. **41**, 349–357 (2000)
4. Nield, D.A.: The modeling of viscous dissipation in a saturated porous medium. ASME J. Heat Transf. **129** 1459–1463 (2007)
5. Costa, V.A.F.: Discussion: "The modeling of viscous dissipation in a saturated porous medium" (Nield, D.A., ASME J. Heat Transfer **129**, 1459–1463 (2007)). ASME J. Heat Transfer **131**, 025502-1-2 (2009)
6. Nield, D.A.: Closure to "Discussion of 'The modeling of viscous dissipation in a saturated porous medium" (ASME J. Heat Transfer **131**, p. 025501 (2009)). ASME J. Heat Transfer **131**, 025502-1 (2009)

7. Costa, V.A.F.: Comment on the paper "I.A. Badruddin, Z.A. Zainal, Z.A. Khan, Z. Mallick, Effect of viscous dissipation and radiation on natural convection in a porous medium embedded within vertical annulus. Int. J. Thermal Sci. **46**(3) (2007) 221–227". Int. J. Thermal Sci. **49**, 1874–1875 (2010)
8. Nield, D.A., Barletta, A.: Comment on the comment by V.A.F. Costa, IJTS 49 (9) (2010) 1874-1875, on the paper by I.A. Badruddin, Z.A. Zainal, Z.A. Khan, Z. Mallick "Effect of viscous dissipation and radiation on natural convection in a porous medium embedded within vertical annulus" IJTS **46**(3), 221–227 (2007). Int. J. Thermal Sci. **49**, 2491–2492 (2010)
9. Bird, R.B., Stewart, W.E., Lightfoot, E.N.: Transport Phenomena, 2nd edn. Wiley, New York (2002)
10. Bejan, A.: Adv. Eng. Thermodyn, 3rd edn. Wiley, Hoboken (2006)
11. Nield, D.A., Bejan, A.: Convection in Porous Media, 3rd edn. Springer, New York (2006)

Analytical and Numerical Study of Memory Formalisms in Diffusion Processes

José A. Ferreira, E. Gudiño, and P. de Oliveira

Abstract In this chapter we study the diffusion of a liquid agent into a polymeric matrix. We propose an initial-boundary value problem to model the process. Numerical methods are obtained for solving it. The stability and the convergence of the methods are studied.

1 Introduction

An important problem in controlled release technology is the diffusion of a penetrant into a polymeric carrier where a drug is dispersed. A suitable choice for simulating drug delivery can be the classical Fick's law. However to model the sorption of the liquid agent an equation that takes into account the viscoelastic nature of polymers and consequently its non Fickian behavior is needed [5–8, 11]. As the fluid penetrates the matrix, the polymeric structure changes, and the flux is not simply proportional to the concentration gradient. To obtain a more accurate description of the fluid penetration several modifications of the flux have been proposed in the literature by introducing a memory formalism [5, 6].

The main idea is that flux depends not only on the concentration gradient but also on the viscoelastic stress. In [6] the authors use a 3-parameter solid model [2] to describe the stress–strain relaxation. However the stability of the continuous model has not been studied. Also the authors do not develop specific numerical algorithms to discretize the non-Fickian model. When highly heterogeneous systems are considered [4] the memory formalism is introduced via factorial derivatives.

In this chapter we study a non-Fickian diffusion mechanism described by a modified law for flux where diffusive and mechanical properties are coupled.

J.A. Ferreira (✉) • E. Gudiño • P. de Oliveira
CMUC, Department of Mathematics, University of Coimbra, Coimbra, Portugal
e-mail: ferreira@mat.uc.pt; egudino@gmail.com; poliveir@mat.uc.pt

J.A. Ferreira et al. (eds.), *Modelling and Simulation in Fluid Dynamics in Porous Media*, Springer Proceedings in Mathematics & Statistics 28, DOI 10.1007/978-1-4614-5055-9_4,

We address the stability of the continuous problem and we develop numerical methods for which discrete energy estimates mimic the continuous ones. To take into account a wide range of mechanical behaviors we consider a general viscoelastic model [2] to describe the stress–strain relation. In particular the model in [5] can be obtained as a special case of the viscoelastic model studied here. Our results can be easily adapted to other mechanical models based on Maxwell generalized models [2]. We note that the class of models studied here can be used to simulate fluid flow in a porous media [9, 10, 13].

Let us recall that the Fickian diffusion of a penetrant is described by the conservation law:

$$\frac{\partial C}{\partial t} = -\nabla \cdot J_F \ , \tag{1}$$

where $C = C(t,x)$ is the fluid concentration and $J_F = J_F(t,x)$ represents the flux and is defined by

$$J_F(t,x) = -D\nabla C(t,x) \ , \tag{2}$$

where D is the diffusion coefficient for the penetrant fluid.

To take into account viscoelastic effects we consider a modified flux [3] expressed as the sum of a Fickian flux J_F and a non-Fickian contribution J_{NF} defined by

$$J_{NF}(t,x) = -D_v \nabla \sigma(t,x) \ , \tag{3}$$

where $\sigma = \sigma(t,x)$ represents the stress and D_v stands for a stress-driven diffusion coefficient. The balance equation describing the behavior of the penetrant fluid is represented by (1) with J given by $J = J_F + J_{NF}$.

In our model we assume that the change of volume due to the relaxation of the polymeric matrix is instantaneous [11]. Both D and D_v can depend in some cases on C; nevertheless, for analytical purposes these parameters can be considered to be positive constants. In fact although solvent diffusion coefficient depends on solvent concentration the hypothesis of a constant solvent diffusion can be accepted if the swelling process does not take place from a dry condition up to a swelling equilibrium, but takes place from a partially swollen condition to another one (Grassi, M., personal communication).

From (1)–(3), we have

$$\frac{\partial C}{\partial t} = D\Delta C + D_v \Delta \sigma \ . \tag{4}$$

To model the viscoelastic polymeric behavior a variety of arrangements built with springs and damper elements are used [2]. We will consider a family of models, known as the 4-parameter solid model [2] that accounts for a wide range of viscoelastic behaviors. The arrangement is shown in Fig. 1.

The parameters E_1 and E_2 are nonnegative constants related with the elastic behavior of the polymer. The parameters μ_1 and μ_2 are also nonnegative constants related with the viscous behavior of the polymer (for more details see [2]). Note that different linear viscoelastic models can be obtained as a particular case of Fig. 1.

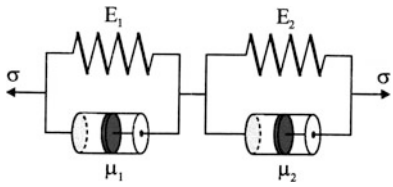

Fig. 1 Four-parameter solid model for viscoelastic polymeric behavior

For example, taking $E_1 = \mu_2 = 0$, we obtain the Maxwell model. Let $\varepsilon(t,x)$ represent the strain. Assuming then that the strain and the concentration are proportional, that is, $\exists \alpha > 0$ such that $\varepsilon(t,x) = \alpha C(t,x)$, the family of models can be represented by the PDE [2]:

$$\frac{\partial \sigma}{\partial t} + p_1 \sigma = q_0 C + q_1 \frac{\partial C}{\partial t} + q_2 \frac{\partial^2 C}{\partial t^2} \,, \tag{5}$$

where

$$p_1 = \frac{E_1 + E_2}{\mu_1 + \mu_2} \,,\; q_0 = \alpha \frac{E_1 E_2}{\mu_1 + \mu_2} \,,\; q_1 = \alpha \frac{E_2 \mu_1 + E_1 \mu_2}{\mu_1 + \mu_2}, \;\; and \;\; q_2 = \alpha \frac{\mu_1 \mu_2}{\mu_1 + \mu_2} \,.$$

The constants q_0, q_1, q_2, and p_1 have a physical meaning for the model and therefore they satisfy the following inequalities [2]:

$$q_1^2 - 4 q_0 q_2 > 0 \quad and \quad q_1 p_1 - q_0 - q_2 p_1^2 > 0 \,. \tag{6}$$

2 The Model

We consider a polymer filling a bounded domain $\Omega \subset \mathbb{R}^n$ with boundary $\partial\Omega$. We study the diffusion of a penetrant in this polymer described by the following initial-boundary value problem:

$$\frac{\partial C}{\partial t} = D \Delta C + D_v \Delta \sigma \quad in \;\; (0,T] \times \Omega \,, \tag{7}$$

$$\frac{\partial \sigma}{\partial t} + p_1 \sigma = q_o C + q_1 \frac{\partial C}{\partial t} + q_2 \frac{\partial^2 C}{\partial t^2} \quad in \;\; (0,T] \times \Omega \,, \tag{8}$$

$$C(t,x) = C_b(t,x), \;\; \sigma(t,x) = \sigma_b, \quad (t,x) \in (0,T] \times \partial\Omega \,, \tag{9}$$

$$C(0,x) = C_0(x), \;\; \sigma(0,x) = \sigma_0, \quad x \in \Omega \,. \tag{10}$$

Here $C : [0,T] \times \bar{\Omega} \to \mathbb{R}$ is the unknown concentration of the penetrant, $\sigma : [0,T] \times \bar{\Omega} \to \mathbb{R}$ is the unknown stress, $C_0 : \bar{\Omega} \to \mathbb{R}$ is the given initial concentration of the liquid in the matrix, $\sigma_0 \in \mathbb{R}$ is the given initial stress in the matrix, C_b :

$(0,T]\times\partial\Omega\to\mathbb{R}$ is the given concentration of the liquid in the fully swollen matrix, and $\sigma_b\in\mathbb{R}$ is the given stress in the fully swollen gel. We observe that Ω is fixed in time because the change of volume due to swelling is supposed to occur instantaneously.

3 Energy Estimates for the Continuous Problem

By $C(t)$ we represent a function defined from $\bar{\Omega}\subset\mathbb{R}$ into $\mathbb{R}$ with t fixed. Using energy estimate techniques we study in this section the stability of model (7)–(10).

We begin by integrating equation (8) over the time to obtain

$$\begin{aligned}\sigma(t) = {} & (q_2p_1-q_1)C_0e^{-p_1t}+(q_1-q_2p_1)C(t)\\ & +(q_0+q_2p_1^2-q_1p_1)\int_0^t e^{p_1(s-t)}C(s)ds+q_2\frac{\partial C}{\partial t}(t)+e^{-p_1t}\sigma_0\ ,\end{aligned}$$

provided that $\frac{\partial C}{\partial t}(0,x)=0$.

Replacing this last equation in (7) and rearranging the terms, we have

$$\frac{\partial C}{\partial t}(t)=A\Delta\frac{\partial C}{\partial t}(t)+B\Delta C(t)+F\int_0^t e^{p_1(s-t)}\Delta C(s)ds+Ge^{-p_1t}\Delta C_0\ , \tag{11}$$

where

$$A=D_vq_2,\ B=D+D_v(q_1-q_2p_1),\ F=D_v(q_0+q_2p_1^2-q_1p_1) \tag{12}$$

and

$$G=D_v(q_2p_1-q_1)\ .$$

We note that from (6) we can conclude that $A,B>0$ and $F,G<0$.

As we are interested in studying the stability of (7)–(10) we assume without loss of generality that

$$C(t,x)=0,\quad (t,x)\in[0,T]\times\partial\Omega\ . \tag{13}$$

The initial-boundary value problem (10), (11), (13), with $A=0$, is a special case of the general parabolic integro-differential problem:

$$u_t=\nabla.\left\{a(u)\nabla u+\int_0^t b(s)\nabla u(s)ds\right\}+f(u)\quad in\ (0,T]\times\Omega\ , \tag{14}$$

$$u(t,x)=0,\quad (t,x)\in(0,T]\times\partial\Omega\ , \tag{15}$$

$$u(0,x)=u_0(x),\quad x\in\Omega\ , \tag{16}$$

where a, b, and f are known functions. Problems (14)–(16) can serve as a model of fluid flow in porous media problems, specially in physical processes where significant memory effects can occur. For the details of formulation and their physical interpretations we refer the reader to [9, 10, 13, 14].

Let $(.,.)$ denote the inner product in $L^2(\Omega)$ and $\|.\|_2$ the usual norm induced by $(.,.)$. Let $H_0^1(\Omega)$ be the usual Sobolev space. By $H^1(0,T;H_0^1(\Omega))$ we represent the space of functions $v:\ (0,T) \mapsto H_0^1(\Omega)$ such that

$$\sum_{i=0}^{1} \int_0^T \left\| \frac{d^i v}{dt^i} \right\|_{H^1}^2 < \infty .$$

We denote by $\mathscr{C}^1(0,T;L^2(\Omega))$ the space of functions $v:\ (0,T) \mapsto L^2(\Omega)$ which have first time continuous derivative with respect to the norm $\|.\|_2$. By $|.|_{H^1}$ we represent the usual semi-norm in $H_0^1(\Omega)$. We replace (10), (11), (13) by the following variational problem: find $C \in H^1(0,T;H_0^1(\Omega))$ such that

$$\left(\frac{dC}{dt}(t), v\right) + A\left(\nabla \frac{dC}{dt}(t), \nabla v\right) + B(\nabla C(t), \nabla v) + F\left(\int_0^t e^{p_1(s-t)} \nabla C(s) ds, \nabla v\right)$$
$$= G(e^{-p_1 t} \Delta C_0, v) \quad a.e\ in\ (0,T), \ \ \forall\, v \in H_0^1(\Omega) \tag{17}$$

and

$$C(0) = C_0(x) , \tag{18}$$

where

$$(\nabla u, \nabla v) = \sum_{i=1}^{n} \left(\frac{\partial u}{\partial x_i}, \frac{\partial v}{\partial x_i}\right), \ \ u, v \in H_0^1(\Omega) .$$

We establish in what follows an estimate for the energy functional

$$\mathbb{E}(C)(t) = \|C(t)\|_2^2 + A\,|C(t)|_{H^1}^2 + 2B \int_0^t |C(s)|_{H^1}^2\, ds , \tag{19}$$

where A and B are defined in (12).

Theorem 3.1. *Let C be a solution of (17), (18) in $\mathscr{C}^1(0,T;L^2(\Omega)) \cap H^1(0,T;H_0^1(\Omega))$, then*

$$\mathbb{E}(C)(t) \le \left(\|C_0\|_2^2 + A\,|C_0|_{H^1}^2 + \frac{3\,|G|^2}{2p_1 A \phi}\, |C_0|_{H^1}^2 \right) e^{t\phi} , \tag{20}$$

where $\phi = \sqrt{\frac{3|F|^2}{8BAp_1}}$.

Proof. Considering in (17) $v = C(t)$ we easily deduce

$$\frac{d}{dt}\|C(t)\|_2^2 + A\frac{d}{dt}|C(t)|_{H^1}^2 + 2B|C(t)|_{H^1}^2$$
$$= 2|F|\int_0^t e^{p_1(s-t)}(\nabla C(s), \nabla C(t))ds + 2|G|e^{-p_1 t}(\nabla C_0, \nabla C(t)) \ . \quad (21)$$

Let us estimate the two terms in the second member of (21). We have

$$2|F|\int_0^t e^{p_1(s-t)}|(\nabla C(s), \nabla C(t))|\,ds \le 2|F|\int_0^t e^{p_1(s-t)}|C(s)|_{H^1}|C(t)|_{H^1}\,ds$$
$$\le 2\varepsilon|C(t)|_{H^1}^2 + \frac{|F|^2}{2\varepsilon}\left(\int_0^t e^{p_1(s-t)}|C(s)|_{H^1}\,ds\right)^2$$
$$\le 2\varepsilon|C(t)|_{H^1}^2 + \frac{|F|^2}{2\varepsilon}\psi\left(\int_0^t |C(s)|_{H^1}^2\,ds\right) \ ,$$

where $\varepsilon > 0$ is an arbitrary constant and ψ satisfies

$$\psi = \int_0^t e^{2p_1(s-t)}ds \le \frac{1}{2p_1} \ .$$

As we also have that

$$2|G|e^{-p_1 t}(\nabla C_0, \nabla C(t)) \le \frac{|G|^2 e^{-2p_1 t}}{\varepsilon}|C_0|_{H^1}^2 + \varepsilon|C(t)|_{H^1}^2 \ ,$$

we can establish from (21) that

$$\frac{d}{dt}\left(\|C(t)\|_2^2 + A|C(t)|_{H^1}^2 + 2B\int_0^t |C(s)|_{H^1}^2\,ds\right)$$
$$\le 3\varepsilon|C(t)|_{H^1}^2 + \frac{|F|^2}{4p_1\varepsilon}\left(\int_0^t |C(s)|_{H^1}^2\,ds\right) + \frac{|G|^2 e^{-2p_1 t}}{\varepsilon}|C_0|_{H^1}^2 \ .$$

Adding the term $\frac{3\varepsilon}{A}\|C(t)\|_2^2$ to the right-hand side and integrating and rearranging the terms we get

$$\|C(t)\|_2^2 + A|C(t)|_{H^1}^2 + 2B\int_0^t |C(s)|_{H^1}^2\,ds$$
$$\le \int_0^t \frac{3\varepsilon}{A}\left(\|C(s)\|_2^2 + A|C(s)|_{H^1}^2 + \frac{|F|^2 A}{12p_1\varepsilon^2}\int_0^s |C(r)|_{H^1}^2\,dr\right)ds$$
$$+ \|C_0\|_2^2 + A|C_0|_{H^1}^2 + \frac{|G|^2}{2p_1\varepsilon}|C_0|_{H^1}^2 \ .$$

Since ε is an arbitrary constant, we take $\varepsilon = \sqrt{\frac{|F|^2 A}{24Bp_1}}$. Then we finally conclude

$$\mathbb{E}(C)(t) \leq \|C_0\|_2^2 + A\,|C_0|_{H^1}^2 + \frac{|G|^2}{2p_1\varepsilon}\,|C_0|_{H^1}^2 + \int_0^t \phi\,\mathbb{E}(C)(s)ds\ ,$$

where $\phi = \sqrt{\frac{3|F|^2}{8BAp_1}}$, and by the Gronwall lemma [12], Eq. (20) holds. □

We note that under the assumptions of Theorem 3.1, if (17), (18) has a solution C in $H^1(0,T;H_0^1(\Omega))$, then C is unique. In fact let C and $\hat{C}$ be two different solutions of (17), (18) such that both of them are in $H^1(0,T;H_0^1(\Omega))$; then $w = C - \hat{C} \in H^1(0,T;H_0^1(\Omega))$ is a solution of (17) with homogeneous initial condition. By Theorem 3.1 we conclude that

$$\mathbb{E}(w)(t) = 0\ ;$$

consequently

$$C = \hat{C}\ ,\ \ \nabla C = \nabla \hat{C}\ \ in\ L^2(\Omega)\ .$$

In what follows we consider the stability behavior of C under perturbations in the initial condition C_0. Let C and $\hat{C}$ be solutions of (17), (18) in $H^1(0,T;H_0^1(\Omega))$ with initial conditions C_0 and $\hat{C}_0$, respectively. Then $w = C - \hat{C} \in H^1(0,T;H_0^1(\Omega))$ satisfies (17) with $w = 0$ in $(0,T] \times \partial\Omega$ and $w(0) = C_0 - \hat{C}_0$ in Ω. Consequently from the proof of Theorem 3.1 it follows that

$$\mathbb{E}(w)(t) \leq \left(\|C_0 - \hat{C}_0\|_2^2 + A\,|C_0 - \hat{C}_0|_{H^1}^2 + \frac{3\,|G|^2}{2p_1 A\phi}\,|C_0 - \hat{C}_0|_{H^1}^2 \right) e^{t\phi}\ ,$$

which implies that (17), (18) is stable in bounded time intervals.

4 Energy Estimates for the Semi-discrete Approximation

The semi-discrete problem is studied for $n = 1$ and $\Omega = [a,b]$. Let us consider in $[a,b]$ a grid $I_h = \{x_i,\ i = 0,1,..,N\}$ with $x_0 = a$, $x_N = b$ and $x_i - x_{i-1} = h$. Let u_h be a function defined over I_h and $L^2(I_h)$ the space of grid functions defined in I_h. For $u_h \in L^2(I_h)$ we introduce the following finite-difference operators:

$$D_{-x}u_h(x_i) = \frac{u_h(x_i) - u_h(x_{i-1})}{h}\ ,$$

$$D_{2,x}u_h(x_i) = \frac{u_h(x_{i+1}) - 2u_h(x_i) + u_h(x_{i-1})}{h^2}\ .$$

By $L_0^2(I_h)$ we represent the subspace of $L^2(I_h)$ of functions null on the boundary points. For grid functions u_h and v_h in $L_0^2(I_h)$ we introduce the inner product

$$(u_h, v_h)_h = \sum_{i=1}^{N-1} h u_h(x_i) v_h(x_i) \ .$$

We denote by $\|.\|_h$ the norm induced by the above inner product. For grid functions u_h and v_h in $L^2(I_h)$ we introduce the notations

$$(u_h, v_h)_+ = \sum_{i=1}^{N} h u_h(x_i) v_h(x_i) \ ,$$

and

$$\|u_h\|_+^2 = \sum_{i=1}^{N} h (u_h(x_i))^2 \ .$$

Discretizing the partial spatial derivative that arise in (17) we introduce the semi-discrete approximation $C_h(t)$ for the solution C of (17), (18). The semi-discrete variational problem has the form

$$\begin{aligned} &\left(\frac{dC_h}{dt}(t), v_h\right)_h + A\left(D_{-x}\frac{dC_h}{dt}(t), D_{-x}v_h\right)_+ + B(D_{-x}C_h(t), D_{-x}v_h)_+ \\ &+F\left(\int_0^t e^{p_1(s-t)} D_{-x}C_h(s)ds, D_{-x}v_h\right)_+ = G(e^{-p_1 t} D_{2,x}C_0, v_h)_h \\ &a.e\ in\ (0,T]\ \ \forall\ v_h \in L_0^2(I_h), \end{aligned} \tag{22}$$

and

$$C_h(0) = R_h C_0 \ , \tag{23}$$

where $R_h : \mathscr{C}([a,b]) \mapsto \mathbb{R}$ denote the pointwise restriction operator

$$R_h u(x_i) = u(x_i) \ \ for\ \ i = 1, 2, .., N.$$

It can be shown that if $C_h \in \mathscr{C}^1(0,T; L_0^2(I_h))$ which denotes the space of functions $u_h : [0,T] \mapsto L_0^2(I_h)$ which have first time continuous derivative with respect to the norm $\|.\|_h$, then C_h is solution of the following ordinary differential problem:

$$\begin{aligned} \frac{dC_h}{dt}(t) &= AD_{2,x}\frac{dC_h}{dt}(t) + BD_{2,x}C_h(t) + F\int_0^t e^{p_1(s-t)} D_{2,x}C_h(s)ds \\ &\quad + Ge^{-p_1 t} D_{2,x}C_h(0) \ , \end{aligned} \tag{24}$$

for $t \in (0,T]$,

$$C_h(t,x_0) = C_h(t,x_N) = 0, \ for\ all\ t \in [0,T]\ , \tag{25}$$

$$C_h(0,x_i) = C_0(x_i), \ for\ \ i = 1,2,\ldots,N-1\ . \tag{26}$$

In what follows we establish an estimate for a semi-discrete version of (19),

$$\mathbb{E}(C_h)(t) = \|C_h(t)\|_h^2 + A\,\|D_{-x}C_h(t)\|_+^2 + 2B\int_0^t \|D_{-x}C_h(s)\|_+^2\,ds\ .$$

Theorem 4.1. *Let C_h be a solution of (22), (23), then*

$$\mathbb{E}(C_h)(t) \le \left(\|C_h(0)\|_h^2 + A\,\|D_{-x}C_h(0)\|_+^2 + \frac{3\,|G|^2}{2p_1A\phi}\,\|D_{-x}C_h(0)\|_+^2\right) e^{t\phi}\ , \tag{27}$$

where $\phi = \sqrt{\frac{3|F|^2}{8BAp_1}}$.

Proof. Let C_h be a solution of (22), (23). Then considering $v_h = C_h(t)$ we have

$$\begin{aligned}&\frac{d}{dt}\left(\|C_h(t)\|_h^2 + A\,\|D_{-x}C_h(t)\|_+^2 + 2B\int_0^t \|D_{-x}C_h(s)\|_+^2\,ds\right)\\ &= 2\,|F|\int_0^t e^{p_1(s-t)}\,(D_{-x}C_h(s), D_{-x}C_h(t))_+\,ds + 2\,|G|\,e^{-p_1t}\,(D_{-x}C_0, D_{-x}C_h(t))_+\ .\end{aligned} \tag{28}$$

As

$$\begin{aligned}&2\,|F|\int_0^t e^{p_1(s-t)}\,(D_{-x}C_h(s), D_{-x}C_h(t))_+\,ds\\ &\le 2\varepsilon\,\|D_{-x}C_h\|_+^2 + \frac{|F|^2}{2\varepsilon}\left(\int_0^t e^{2p_1(s-t)}ds\right)\int_0^t \|D_{-x}C_h(s)\|_+^2\,ds\end{aligned}$$

and

$$\begin{aligned}2\,|G|\,e^{-p_1t}\sum_{i=1}^{N} h\,|D_{-x}C_0(x_i)D_{-x}C_h(t,x_i)| \le \frac{|G|^2\,e^{-2p_1t}}{\varepsilon}\,\|D_{-x}C_0(x)\|_+^2\\ +\varepsilon\,\|D_{-x}C(t,x)\|_+^2\ ,\end{aligned}$$

where $\varepsilon > 0$ is an arbitrary constant, we have from (28)

$$\begin{aligned}\frac{d}{dt}\mathbb{E}(C_h(t)) \le 3\varepsilon\,\|D_{-x}C_h(t)\|_+^2 + \frac{|F|^2}{4p_1\varepsilon}\int_0^t \|D_{-x}C_h(s)\|_+^2\,ds\\ +\frac{|G|^2\,e^{-2p_1t}}{\varepsilon}\,\|D_{-x}C_h(0)\|_+^2\ .\end{aligned}$$

Following the proof of Theorem 3.1, we conclude (27). □

Analogously as in the continuous case we consider the stability behavior of C_h under perturbations in the initial condition $C_h(0)$. Let C_h and $\hat{C}_h$ be solutions of (22), (23) with initial conditions $C_h(0)$ and $\hat{C}_h(0)$, respectively. Then $w_h = C_h - \hat{C}_h$ satisfies (22) with $w_h(0) = C_h(0) - \hat{C}_h(0)$ in $[a,b]$. Consequently from the proof of Theorem 4.1 it follows that

$$\mathbb{E}(w_h)(t) \leq \left(\left\| C_h(0) - \hat{C}_h(0) \right\|_h^2 + A \left\| D_{-x}(C_h(0) - \hat{C}_h(0)) \right\|_+^2 + \frac{3|G|^2}{2p_1 A\phi} \left\| D_{-x}(C_h(0) - \hat{C}_h(0)) \right\|_+^2 \right) e^{t\phi} , \tag{29}$$

which implies that (22), (23) is stable in bounded time intervals.

5 Error Estimates for the Semi-discrete Approximation

By $E_h(t)$ we represent the error induced by the spatial discretization introduced before. $E_h(t) = R_h C(t) - C_h(t)$ where $C_h(t)$ is the solution of (22)–(23).

In the convergence analysis we will assume that the solution of (10), (11), (13), C belongs to the space $H^1(0,T;H_0^3(a,b))$ which is defined as $H^1(0,T;H_0^1(a,b))$ replacing $H_0^1(a,b)$ by $H_0^3(a,b)$.

Theorem 5.1. *Let C and C_h be the solutions of (17), (18) and (22), (23), respectively. If $C \in H^1(0,T;H_0^3(a,b))$, then*

$$\mathbb{E}(E_h(t)) \leq e^{\phi t} \left(\|E_h(0)\|_h^2 + A \|D_{-x}E_h(0)\|_+^2 \right) + h^4 \int_0^t K(z) e^{\phi(t-z)} dz , \tag{30}$$

where

$$K(t) = \frac{20\beta_1^2}{\phi A} \left[A^2 \left| \frac{\partial C}{\partial t}(t) \right|_{H^3}^2 + B^2 |C(t)|_{H^3}^2 + F^2 \int_0^t e^{p_1(s-t)} |C(s)|_{H^3}^2 ds + G^2 |C_0|_{H^3}^2 \right] + \frac{4\beta_2^2}{\phi} \left| \frac{\partial C}{\partial t}(t) \right|_{H^2}^2 ,$$

with ϕ, β_1, and β_2 positive constants.

Proof. As we have

$$\frac{dE_h}{dt}(t) = R_h \frac{\partial C(t)}{\partial t}(t) - \left[AD_{2,x} \frac{dC_h}{dt}(t) + BD_{2,x}C_h(t) + F \int_0^t e^{p_1(s-t)} D_{2,x}C_h(s) ds + Ge^{-p_1 t} D_{2,x}C_0 \right] ,$$

we easily deduce that

$$\left(\frac{dE_h}{dt}(t),E_h(t)\right)_h = \left(R_h\frac{\partial C}{\partial t}(t),E_h(t)\right)_h + A\left(D_{-x}\frac{dC_h}{dt}(t),D_{-x}E_h(t)\right)_+ + B(D_{-x}C_h(t),D_{-x}E_h(t))_+ + F\int_0^t e^{p_1(s-t)}(D_{-x}C_h(s),D_{-x}E_h(t))_+ds + Ge^{-p_1t}(D_{-x}C_0,D_{-x}E_h(t))_+ . \quad (31)$$

Let $\left(\widehat{\frac{\partial C}{\partial t}}\right)_h(t)$ be the following grid function:

$$\left(\widehat{\frac{\partial C}{\partial t}}\right)_h(t,x_i) = \frac{1}{h}\int_{x_{\frac{i-1}{2}}}^{x_{\frac{i+1}{2}}}\frac{\partial C}{\partial t}(t)dx ,$$

where $x_{\frac{i-1}{2}} = \frac{x_{i-1}+x_i}{2}$ and $x_{\frac{i+1}{2}} = \frac{x_i+x_{i+1}}{2}$, for $i = 1,2,..,N-1$.

Introducing $\left(\widehat{\frac{\partial C}{\partial t}}\right)_h(t)$ in (31) we deduce

$$\left(\frac{dE_h}{dt}(t),E_h(t)\right)_h = (R_h\frac{\partial C}{\partial t}(t) - \left(\widehat{\frac{\partial C}{\partial t}}\right)_h(t),E_h(t))_h + (\left(\widehat{\frac{\partial C}{\partial t}}\right)_h(t),E_h(t))_h + A(D_{-x}\frac{dC_h}{dt}(t),D_{-x}E_h(t))_+ + B(D_{-x}C_h(t),D_{-x}E_h(t))_+ + F\int_0^t e^{p_1(s-t)}(D_{-x}C_h(s),D_{-x}E_h(t))_+ds + Ge^{-p_1t}(D_{-x}C_0,D_{-x}E_h(t))_+ . \quad (32)$$

We remark that

$$\left(\left(\widehat{\frac{\partial C}{\partial t}}\right)_h(t),E_h(t)\right)_h = \sum_{i=1}^{N-1}h\int_{x_{\frac{i-1}{2}}}^{x_{\frac{i+1}{2}}}\frac{\partial C}{\partial t}(t)dxE_h(t,x_i) = \sum_{i=1}^{N-1}h\int_{x_{\frac{i-1}{2}}}^{x_{\frac{i+1}{2}}}\left(A\frac{\partial^2}{\partial x^2}\left(\frac{\partial C}{\partial t}\right)(t) + B\frac{\partial^2 C}{\partial x^2}(t) + F\int_0^t e^{p_1(s-t)}\frac{\partial^2 C}{\partial x^2}(s)ds + Ge^{-p_1t}\frac{\partial^2 C_0}{\partial x^2}\right)dxE_h(t,x_i) . \quad (33)$$

Using summation by parts it is easy to see that

$$\sum_{i=1}^{N-1}\left(\int_{x_{\frac{i-1}{2}}}^{x_{\frac{i+1}{2}}}\frac{\partial^2 g}{\partial x^2}(x)dx\right)E_h(t,x_i)=-\sum_{i=1}^{N}h\frac{\partial g}{\partial x}(x_{\frac{i-1}{2}})D_{-x}E_h(t,x_i)\ . \tag{34}$$

Let $\hat{R}_h$ be defined by $\hat{R}_h g(x_i)=g(x_{\frac{i-1}{2}})$. Applying (34) to each term of (33) we easily establish the following:

$$\begin{aligned}\left(\left(\widehat{\frac{\partial C}{\partial t}}\right)_h(t),E_h(t)\right)_h &= -A\left(\hat{R}_h\left(\frac{\partial^2 C}{\partial x\partial t}\right)(t),D_{-x}E_h(t)\right)_+\\ &\quad -B(\hat{R}_h\left(\frac{\partial C}{\partial x}\right)(t),D_{-x}E_h(t))_+\\ &\quad -F\int_0^t e^{p_1(s-t)}(\hat{R}_h\left(\frac{\partial C}{\partial x}\right)(s),D_{-x}E_h(t))_+ds\\ &\quad -Ge^{-p_1 t}(\hat{R}_h\left(\frac{\partial C_0}{\partial x}\right),D_{-x}E_h(t))_+\\ &= A(D_{-x}R_h\left(\frac{\partial C}{\partial t}\right)(t)-\hat{R}_h\left(\frac{\partial^2 C}{\partial x\partial t}\right)(t),D_{-x}E_h(t))_+\\ &\quad +B(D_{-x}R_hC(t)-\hat{R}_h\left(\frac{\partial C}{\partial x}\right)(t),D_{-x}E_h(t))_+\\ &\quad +F\int_0^t e^{p_1(s-t)}(D_{-x}R_hC(s)\\ &\quad -\hat{R}_h\left(\frac{\partial C}{\partial x}\right)(s),D_{-x}E_h(t))_+ds\\ &\quad -Ge^{-p_1 t}(\hat{R}_h\left(\frac{\partial C_0}{\partial x}\right),D_{-x}E_h(t))_+\\ &\quad -A(D_{-x}R_h\left(\frac{\partial C}{\partial t}\right)(t),D_{-x}E_h(t))_+\\ &\quad -B(D_{-x}R_hC(t),D_{-x}E_h(t))_+\\ &\quad -F\int_0^t e^{p_1(s-t)}(D_{-x}R_hC(s),D_{-x}E_h(t))_+ds\ . \end{aligned}\tag{35}$$

From (32) and (35) we obtain

$$\begin{aligned}\left(\frac{dE_h}{dt}(t),E_h(t)\right)_h &= -A(D_{-x}\frac{dE_h}{dt}(t),D_{-x}E_h(t))_+ - B(D_{-x}E_h(t),D_{-x}E_h(t))_+\\ &\quad +|F|\int_0^t e^{p_1(s-t)}(D_{-x}E_h(s),D_{-x}E_h(t))_+ds+T\ ,\end{aligned}\tag{36}$$

where $T = T_1 + T_2 + T_3 + T_4 + T_5$, with

$$T_1 = \left(R_h \frac{\partial C(t)}{\partial t} - \left(\widehat{\frac{\partial C}{\partial t}} \right)_h (t), E_h(t) \right)_h ,$$

$$T_2 = A \left(D_{-x} R_h \left(\frac{\partial C}{\partial t} \right)(t) - \hat{R}_h \left(\frac{\partial^2 C}{\partial x \partial t} \right)(t), D_{-x} E_h(t) \right)_+ ,$$

$$T_3 = B(D_{-x} R_h C(t) - \hat{R}_h \left(\frac{\partial C}{\partial x} \right)(t), D_{-x} E_h(t))_+ ,$$

$$T_4 = F \int_0^t e^{p_1(s-t)} (D_{-x} R_h C(s) - \hat{R}_h \left(\frac{\partial C}{\partial x} \right)(s), D_{-x} E_h(t))_+ ds ,$$

$$T_5 = G e^{-p_1 t} (D_{-x} C_0 - \hat{R}_h \left(\frac{\partial C_0}{\partial x} \right), D_{-x} E_h(t))_+ .$$

As

$$2|F| \int_0^t e^{p_1(s-t)} (D_{-x} E_h(s), D_{-x} E_h(t))_+ ds$$
$$\leq 2\varepsilon \|D_{-x} E_h(t)\|_+^2 + \tfrac{|F|^2}{4 p_1 \varepsilon} \int_0^t \|D_{-x} E_h(s)\|_+^2 ds ,$$

where ε is an arbitrary positive constant, then by (36)

$$\frac{d}{dt} \left(\|E_h(t)\|_h^2 + A \|D_{-x} E_h(t)\|_+^2 + 2B \int_0^t \|D_{-x} E_h(s)\|_+^2 ds \right)$$
$$\leq 2\varepsilon \|D_{-x} E_h(t)\|_+^2 + \tfrac{|F|^2}{4 p_1 \varepsilon} \int_0^t \|D_{-x} E_h(s)\|_+^2 ds + 2|T| . \tag{37}$$

To estimate $T_2,\ T_3,\ T_4$, and T_5 we observe that

$$\lambda(g) = D_{-x} g(x_i) - g(x_{\frac{i-1}{2}}) = \frac{1}{h} \left[V(0) - V(1) + V'(\frac{1}{2}) \right] ,$$

with $V(\xi) = g(x_i - h\xi)$.

Let $\lambda(V) = V(0) - V(1) + V'(\frac{1}{2})$. As we have

$$\lambda(1) = 0,\ \ \lambda(\xi) = 0,\ \ \lambda(\xi^2) = 0,\ \ \textit{and}\ \ \lambda(\xi^3) \neq 0 ,$$

by the Bramble–Hilbert lemma [1] we deduce

$$|\lambda(v)| \leq \beta \int_0^1 \left| V'''(\xi) \right| d\xi = h^2 \beta \int_{x_{\frac{i-1}{2}}}^{x_{\frac{i+1}{2}}} \left| g'''(x) \right| dx ,$$

then

$$\begin{aligned}
&\left|\sum_{i=1}^{N} h\left(D_{-x}g(x_i) - g(x_{\frac{i-1}{2}})\right) D_{-x}E_h(t,x_i)\right| \\
&\leq \beta \sum_{i=1}^{N} h^2 \int_{x_{\frac{i-1}{2}}}^{x_{\frac{i+1}{2}}} \left|g'''(x)\right| dx \, |D_{-x}E_h(t,x_i)| \\
&\leq \beta \sum_{i=1}^{N} h^2 \left(\int_{x_{\frac{i-1}{2}}}^{x_{\frac{i+1}{2}}} \left|g'''(x)\right|^2 dx\right)^{\frac{1}{2}} \sqrt{h}\,|D_{-x}E_h(t,x_i)| \\
&\leq \frac{\beta^2 h^4}{\varepsilon} \sum_{i=1}^{N} |g|^2_{H^3\left[x_{\frac{i-1}{2}}, x_{\frac{i+1}{2}}\right]} + \varepsilon \, \|D_{-x}E_h(t)\|_+^2 \ ,
\end{aligned}$$

that is,

$$\left|\sum_{i=1}^{N} h\left(D_{-x}g(x_i) - g(x_{\frac{i-1}{2}})\right) D_{-x}E_h(t,x_i)\right| \leq \frac{\beta^2 h^4}{\varepsilon} \, |g|^2_{H^3} + \varepsilon \, \|D_{-x}E_h(t)\|_+^2 \ . \tag{38}$$

Considering (38) for $T_2,\ T_3,\ T_4$, and T_5 we obtain

$$\begin{aligned}
&\sum_{i=2}^{5} |T_i| \\
&\leq \frac{\beta_1^2}{\varepsilon} h^4 \left[A^2 \left|\frac{\partial C}{\partial t}(t)\right|^2_{H^3} + B^2 \, |C(t)|^2_{H^3} + F^2 \int_0^t e^{p_1(s-t)} \, |C(s)|^2_{H^3} \, ds + G^2 \, |C_0|^2_{H^3}\right] \\
&\quad + 4\varepsilon \, \|D_{-x}E_h(t)\|_+^2 \ ,
\end{aligned} \tag{39}$$

for certain positive constant β_1.

To estimate T_1 we introduce now $l(g)$ defined by

$$\begin{aligned}
l(g) &= hg(x_i) - \int_{x_{\frac{i-1}{2}}}^{x_{\frac{i+1}{2}}} g(x)dx \\
&= hg(x_i) - h\int_0^1 g(x_{\frac{i-1}{2}} + h\xi)d\xi \\
&= h(V(\frac{1}{2}) - \int_0^1 V(\xi)d\xi) \ ,
\end{aligned}$$

with $V(\xi) = g(x_{\frac{i-1}{2}} + h\xi)$.

For $\lambda(V) = V(\frac{1}{2}) - \int_0^1 V(\xi)d\xi$ holds the following:

$$\lambda(1) = 0,\ \ \lambda(\xi) = 0,\ \ and\ \ \lambda(\xi^2) \neq 0\,,$$

then by the Bramble–Hilbert lemma [1] we obtain

$$|\lambda(V)| \leq \beta_2 \int_0^1 \left|V''(\xi)\right| d\xi = h\beta_2 \int_{x_{\frac{i-1}{2}}}^{x_{\frac{i+1}{2}}} \left|g''(x)\right| dx;$$

consequently we deduce for T_1

$$\begin{aligned} |T_1| &\leq \left| \beta_2 \sum_{i=1}^{N} h^2 \int_{x_{\frac{i-1}{2}}}^{x_{\frac{i+1}{2}}} \frac{\partial^3 C}{\partial^2 x \partial t}(x) dx E_h(t, x_i) \right| \\ &\leq \frac{\beta_2^2 A}{5\varepsilon} h^4 \left| \frac{\partial C}{\partial t}(t) \right|_{H^2}^2 + \frac{5\varepsilon}{A} \|E_h(t)\|_+^2 \,. \end{aligned} \tag{40}$$

Replacing (39) and (40) in (37) we obtain

$$\begin{aligned} &\frac{d}{dt}\left(\mathbb{E}(E_h(t))\right) \\ &\leq \tfrac{10\varepsilon}{A} \|E_h(t)\|_h^2 + 10\varepsilon \|D_{-x}E_h(t)\|_+^2 + \tfrac{|F|^2}{4p_1\varepsilon} \int_0^t \|D_{-x}E_h(s)\|_+^2 ds + h^4 K(t)\,, \end{aligned} \tag{41}$$

where

$$\begin{aligned} K(t) = \frac{2\beta_1^2}{\varepsilon} &\left[A^2 \left| \frac{\partial C}{\partial t}(t) \right|_{H^3}^2 + B^2 |C(t)|_{H^3}^2 + F^2 \int_0^t e^{p_1(s-t)} |C(s)|_{H^3}^2 ds + G^2 |C_0|_{H^3}^2 \right] \\ &+ \frac{2\beta_2^2 A}{5\varepsilon} \left| \frac{\partial C}{\partial t}(t) \right|_{H^2}^2 . \end{aligned}$$

From (41) we have that

$$\begin{aligned} &\frac{d}{dt}\left(\mathbb{E}(E_h(t))\right) \\ &\leq \tfrac{10\varepsilon}{A} \left(\|E_h(t)\|_h^2 + A \|D_{-x}E_h(t)\|_+^2 + \tfrac{|F|^2 A}{40 p_1 \varepsilon^2} \int_0^t \|D_{-x}E_h(s)\|_+^2 ds \right) + h^4 K(t)\,, \end{aligned}$$

and taking $\varepsilon = \sqrt{\frac{F^2 A}{80 p_1 B}}$ we obtain

$$\frac{d}{dt}\left(\mathbb{E}(E_h(t))\right) \leq \phi \mathbb{E}(E_h(t) + h^4 K(t)\,,$$

where $\phi = \frac{10\varepsilon}{A}$. Finally multiplying by $e^{-\phi t}$ and integrating with respect to t we conclude (30). □

6 Numerical Results

To illustrate the qualitative behavior of the model studied in this chapter we present in this section numerical results for the solutions of the initial-boundary value problem (7)–(10) using method (24). We consider in [0,1] a spatial grid $I_h = \{x_i,\ i = 0, 1, .., N\}$ with $x_0 = 0$, $x_N = 1$ and a time grid in [0,1] with $\{t_n,\ n = 0, 1, \ldots, M\}$ such that $t_0 = 0$ and $t_M = 1$.

In Figs. 2 and 3 we plot the numerical results obtained with $\sigma_b = 0$, $C_b = 0$, $C_0(x) = 0.5$, $\alpha = 1$, $D = 1 \times 10^{-15}$, $D_v = 1 \times 10^{-4}$, $E_1 = 8 \times 10^{-5}$, $E_2 = 2 \times 10^{-5}$,

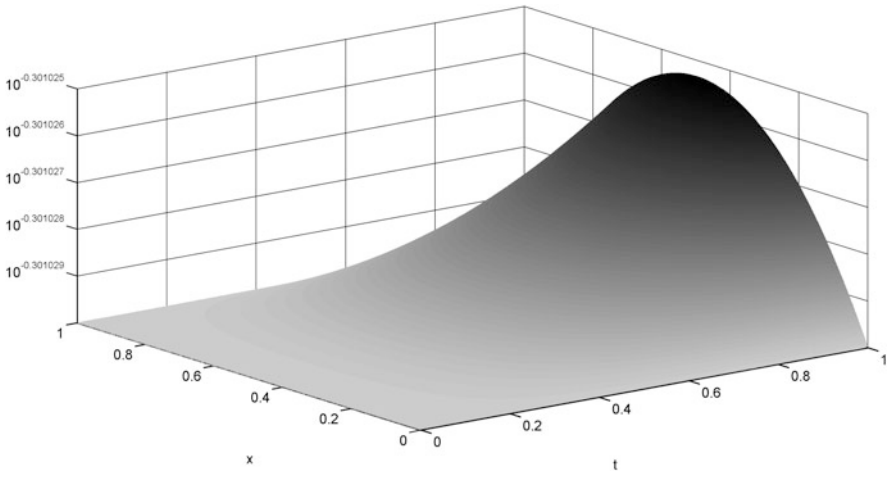

Fig. 2 Numerical solution for the concentration

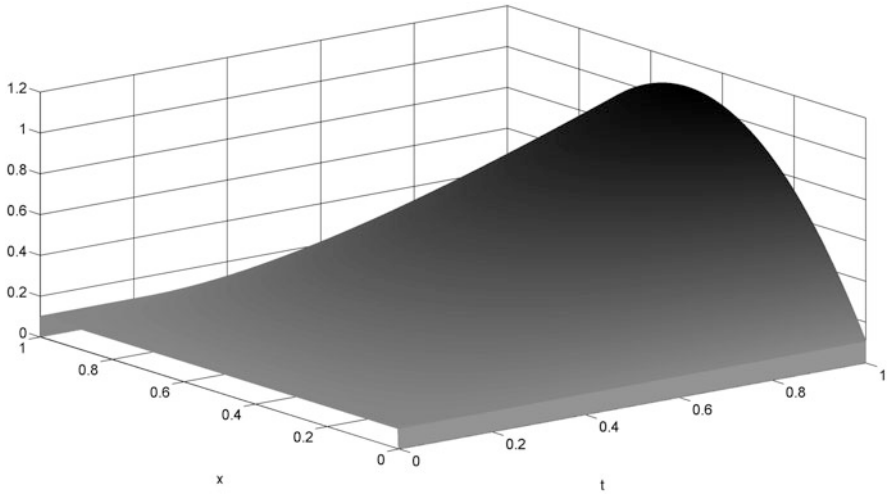

Fig. 3 Numerical solution for the stress

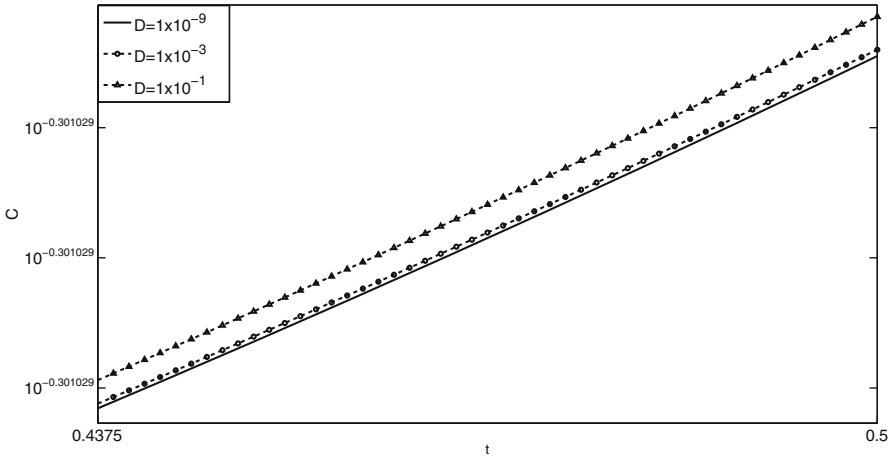

Fig. 4 Numerical solution for the concentration for different values of D

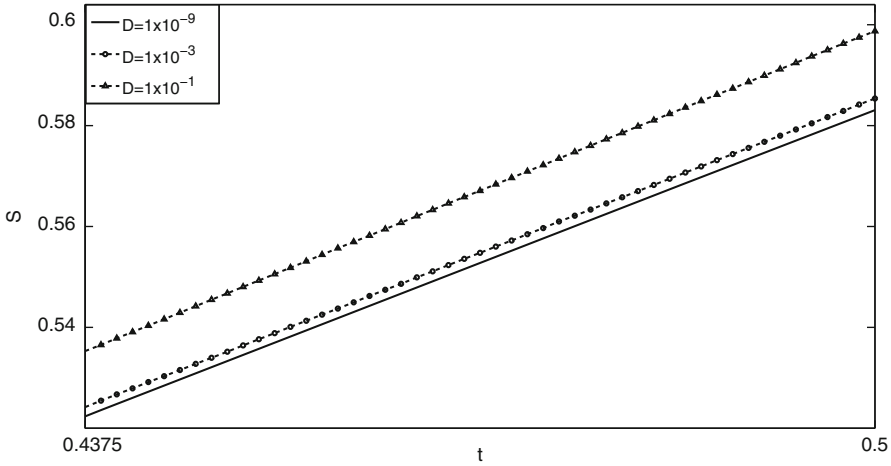

Fig. 5 Numerical solution for the stress for different values of D

$\mu_1 = 1 \times 10^5$, $\mu_2 = 1 \times 10^6$, $\Delta t = 13 \times 10^{-4}$, and $h = 17 \times 10^{-4}$. The two plots present similar behavior. As expected, high stress regions correspond to regions where the concentration is higher.

In Figs. 4 and 5 we plot a comparison of the numerical results for the concentration and the stress for different values of D at a fixed point of the spatial grid $x = 0.5$ and for a subinterval of the time grid $t \in [0, 1]$. The remaining constants assume the values previously defined. We observe that the concentration and the stress are increasing functions of the diffusion coefficient. The results are physically sound,

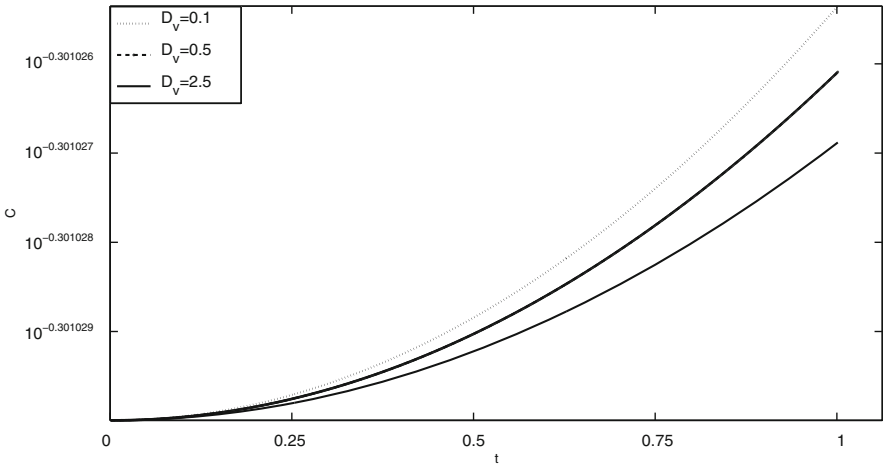

Fig. 6 Numerical solution for the concentration for different values of D_v

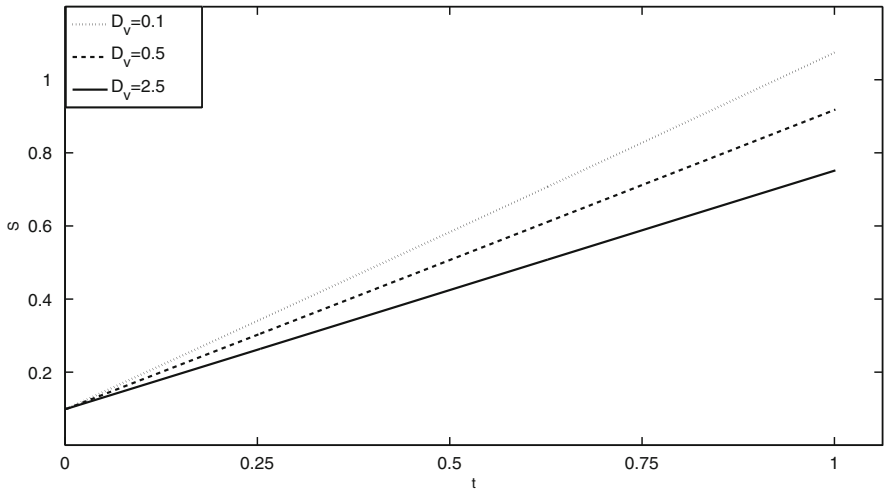

Fig. 7 Numerical solution for the stress for different values of D_v

because if the liquid diffuses more rapidly into the polymer, the concentration and the stress also increase more rapidly.

In Figs. 6 and 7 we plot a comparison of the numerical results for the concentration and the stress for different values of D_v at a fixed point of the spatial grid $x = 0.5$ and for $t \in [0, T]$. The other constants remain fixed with the same values as before. In this case we observe that the concentration and the stress are decreasing functions of the diffusion coefficient.

Acknowledgements Research supported by CMUC and FCT (Portugal), through European program COMPETE/FEDER and by the research project UTAustin/MAT/066/2008.

References

1. Bramble, J.H., Hilbert, S.R.: Estimation of linear functionals on Sobolev spaces with application to Fourier transforms and spline interpolation. SIAM J. Numer. Anal. **7**, 112–124 (1970)
2. Brinson, H.F., Brinson, L.C.: Polymer Engineering Science and Viscoelasticity, An Introduction. Springer, New York (2008)
3. Camera-Roda, G., Sarti, G.C.: AIChE J. **36**, 851–862 (1990)
4. Cametti, C., Caputo, M., Cesarone, F.: Memory formalism in the passive diffusion across highly heterogeneous systems. J. Membrane Sci. **250**, 79–84 (2005)
5. Cohen, D.S., White Jr., A.B.: Sharp fronts due to diffusion and viscoelastic relaxation in polymers. SIAM J. Appl. Math. **51**, 472–483 (1991)
6. Cohen, D.S., Edwards, D.A.: A mathematical model of a dissolving polymer. AIChE J. **41**, 2345–2355 (1995)
7. Crank, J.: The Mathematics of Diffusion. Oxford University Press, Oxford (1976)
8. Crank, J., Park, G.S.: Diffusion in Polymers. Academic Press, New York (1968)
9. Cushman, J.: Nonlocal dispersion in media with continuously evolving scales of heterogeneity. Transport Porous Med. **13**, 123–138 (1993)
10. Cushman, J., Hu, X., Ginn, T.: Nonequilibrium statistical mechanics of preasymptotic dispersion. J. Statist. Phys. **75**, 859–878 (1994)
11. Grassi, G., Grassi, M.: Mathematical modelling and controlled drug delivery: matrix systems. Curr. Drug Deliv. **2**, 97–116 (2005)
12. Gronwall, T.H.: Note on the derivative with respect to a parameter of the solutions of a system of differential equations. Ann. Math. **20**, 292–296 (1919)
13. Hassanizadeh, S.M.: On the transient non-Fickian dispersion theory. Transport Porous Med. **23**, 107–124 (1996)
14. Raynal, M.: On some nonlinear problems of diffusion in Volterra equations. In: London, S., Staffans, O. (eds.) Lecture Notes in Mathematics, pp. 251–266. Springer, Berlin, New York (1979)

Super-diffusive Transport Processes in Porous Media

E. Sousa

Abstract The basic assumption of models for the transport of contaminants through soil is that the movements of solute particles are characterized by the Brownian motion. However, the complexity of pore space in natural porous media makes the hypothesis of Brownian motion far too restrictive in some situations. Therefore, alternative models have been proposed. One of the models, many times encountered in hydrology, is based in fractional differential equations, which is a one-dimensional fractional advection diffusion equation where the usual second-order derivative gives place to a fractional derivative of order α, with $1 < \alpha \leq 2$. When a fractional derivative replaces the second-order derivative in a diffusion or dispersion model, it leads to anomalous diffusion, also called super-diffusion. We derive analytical solutions for the fractional advection diffusion equation with different initial and boundary conditions. Additionally, we analyze how the fractional parameter α affects the behavior of the solutions.

1 Fractional Advection Diffusion Equation

An equation commonly used to describe solute transport is the classical advection diffusion (or dispersion) equation

$$\frac{\partial u}{\partial t}(x,t) = -V\frac{\partial u}{\partial x}(x,t) + D\frac{\partial^2 u}{\partial x^2}(x,t), \tag{1}$$

where u is the concentration, V is the average linear velocity, x is the spatial domain, t is the time, and $D > 0$ is a constant diffusion (or dispersion) coefficient. The classical advection diffusion equation uses second-order Fickian diffusion

E. Sousa (✉)
CMUC, Department of Mathematics, University of Coimbra, 3001-454 Coimbra, Portugal
e-mail: ecs@mat.uc.pt

J.A. Ferreira et al. (eds.), *Modelling and Simulation in Fluid Dynamics in Porous Media*, Springer Proceedings in Mathematics & Statistics 28, DOI 10.1007/978-1-4614-5055-9_5,

which is based on the assumption that solute particles undergo an addition of successive increments that are independent, where identically distributed random variables have finite variance and the distribution of the sum of such increments is a normal distribution. Therefore, the fundamental solutions of the classical advection diffusion equation will be Gaussian densities with means and variations based on the values of the coefficients V and D.

The anomalous diffusion extends the capabilities of models built on the stochastic process of Brownian motion. For instance, the movement of particles may not follow Brownian motion because high-velocity regions in soil tend to be spatially continuous at all scales. A particle traveling faster or slower than the mean is much more likely to do so over a large distance and it seems to have a spatial memory, a feature that is absent in Brownian motion. Motions with the persistence in movements can be simulated with Lévy motion which assumes that significant deviations from the mean can occur, where large jumps are more frequent than in the Brownian motion. When describing scale-dependent transport in porous media, Lévy motion can be seen as a generalization of Brownian motion.

Fractional diffusion was firstly proposed by Chaves [3]. He presents an advection diffusion equation able to generate the Lévy distribution, with the purpose of having a model suitable to investigate the mechanism of super-diffusion. The classical advection diffusion (1) can be seen as the combination of the continuity equation

$$\nabla \cdot \mathbf{j} + \frac{\partial u}{\partial t} = 0, \tag{2}$$

with the Fick's empirical law

$$\mathbf{j} = -D\frac{\partial u}{\partial x} + Vu. \tag{3}$$

Chaves [3] proposes to generalize Fick's law to the form

$$\mathbf{j} = -\frac{D}{2}\left(\frac{\partial^{\alpha-1}u}{\partial x^{\alpha-1}} + \frac{\partial^{\alpha-1}u}{\partial(-x)^{\alpha-1}}\right) + Vu, \tag{4}$$

where u is the resident solute concentration, V is the average pore-water velocity, x is the spatial coordinate, t is the time, D is the diffusion coefficient, α is the order of the fractional differentiation, and $1 < \alpha \leq 2$. The fractional advection diffusion equation was later generalized by Benson et al. [1, 2], to include a parameter β, given by

$$\frac{\partial u}{\partial t} + V\frac{\partial u}{\partial x} = D\left(\frac{1}{2} + \frac{\beta}{2}\right)\frac{\partial^{\alpha} u}{\partial x^{\alpha}} + D\left(\frac{1}{2} - \frac{\beta}{2}\right)\frac{\partial^{\alpha} u}{\partial(-x)^{\alpha}}, \tag{5}$$

where β is the relative weight of solute particle forward versus backward transition probability. For $-1 \leq \beta \leq 0$, the transition probability is skewed backward, while

for $0 \leq \beta \leq 1$ the transition probability is skewed forward. For $\beta = 0$, we obtain the model presented in [3], that is, the transition of the solute particles is symmetric.

If we define the fractional operator by

$$2\nabla_{\beta}^{\alpha} = (1+\beta)\frac{\partial^{\alpha} u}{\partial x^{\alpha}} + (1-\beta)\frac{\partial^{\alpha} u}{\partial(-x)^{\alpha}},$$

the equation can be defined in a simple form:

$$\frac{\partial u}{\partial t} + V\frac{\partial u}{\partial x} = D\nabla_{\beta}^{\alpha} u. \tag{6}$$

Let us now define the fractional derivatives. The Riemann–Liouville fractional derivatives of order α of a function $u(x,t)$, for $x \in [a,b]$, $-\infty \leq a < b \leq \infty$, are in general defined by

$$\frac{\partial^{\alpha} u}{\partial x^{\alpha}}(x,t) = \frac{1}{\Gamma(n-\alpha)}\frac{\partial^{n}}{\partial x^{n}}\int_{a}^{x}\frac{u(\xi,t)}{(x-\xi)^{\alpha-n+1}}d\xi,\ n = [\alpha]+1,\ x > a, \tag{7}$$

$$\frac{\partial^{\alpha} u}{\partial(-x)^{\alpha}}(x,t) = \frac{(-1)^{n}}{\Gamma(n-\alpha)}\frac{\partial^{n}}{\partial x^{n}}\int_{x}^{b}\frac{u(\xi,t)}{(\xi-x)^{\alpha-n+1}}d\xi,\ n = [\alpha]+1,\ x < b, \tag{8}$$

where $\Gamma(\cdot)$ is the Gamma function. Therefore, in our case, for $1 < \alpha \leq 2$ we have

$$\frac{\partial^{\alpha} u}{\partial x^{\alpha}}(x,t) = \frac{1}{\Gamma(2-\alpha)}\frac{\partial^{2}}{\partial x^{2}}\int_{a}^{x}\frac{u(\xi,t)}{(x-\xi)^{\alpha-1}}d\xi \quad x > a, \tag{9}$$

$$\frac{\partial^{\alpha} u}{\partial(-x)^{\alpha}}(x,t) = \frac{1}{\Gamma(2-\alpha)}\frac{\partial^{2}}{\partial x^{2}}\int_{x}^{b}\frac{u(\xi,t)}{(\xi-x)^{\alpha-1}}d\xi, \quad x < b. \tag{10}$$

There are a number of interesting books describing the analytical properties of fractional derivatives, such as [5, 8, 13, 14, 16, 18].

2 Exact Solutions

In this section we show how to obtain exact solutions for some problems involving the fractional advection diffusion equation. The first problem is related to models that appear in works such as Benson et al. [2], Huang et al. [6], Pachepsky et al. [15], San Jose Martinez et al. [19], and Zhou et al. [24]. The second problem considers the Dirac delta function as the initial condition, which is of interest in many applications. Although we consider exact solutions, numerical solutions have also been investigated for super-diffusive models represented by (5) and for some values of β, namely finite element methods [4,7,17,23], finite volume methods [22], spectral methods [9], and finite difference methods [11, 20, 21].

Let us now consider the problem which consists of (5) defined in the whole real line, $x \in \mathbb{R}$, and $t > 0$, with the initial condition

$$u(x,0) = \begin{cases} u_0, & x < 0 \\ m_0, & x = 0 \\ 0, & x > 0, \end{cases} \tag{11}$$

where u_0 and m_0 are constants. The boundary conditions are given by

$$\lim_{x \to -\infty} u(x,t) = u_0, \qquad \lim_{x \to \infty} u(x,t) = 0. \tag{12}$$

We derive the exact solution for this problem by using the Fourier transform. If we consider a function defined in $\mathbb{R}$, then we can define its Fourier transform which is given by

$$\mathscr{F}[f(x)] = \hat{f}(k) = \int_{-\infty}^{+\infty} f(\tau) \mathrm{e}^{ik\tau} d\tau,$$

and its inverse is given by

$$f(x) = \mathscr{F}^{-1}[\hat{f}(k)] = \frac{1}{2\pi} \int_{-\infty}^{+\infty} \hat{f}(\xi) \mathrm{e}^{-ix\xi} d\xi.$$

The well-known Fourier transforms for integer derivatives are given by

$$\mathscr{F}\left[\frac{\partial^n f}{\partial x^n}\right] = (-ik)^n f(k).$$

They can be extended to rational order such as

$$\mathscr{F}\left[\frac{\partial^\alpha f}{\partial x^\alpha}\right] = (-ik)^\alpha \hat{f}(k), \qquad \mathscr{F}\left[\frac{\partial^\alpha f}{\partial (-x)^\alpha}\right] = (ik)^\alpha \hat{f}(k).$$

In the next proposition we state the solution for the problem (5), (11), (12).

Proposition 2.1. *The exact solution for the fractional advection diffusion (5), where $1 < \alpha \leq 2$ and $-1 \leq \beta \leq 1$, subject to the initial condition (11) and with boundary conditions (12), is of the form*

$$u(x,t) = u_0 \left[1 - F_{\alpha\beta}\left(\frac{x - Vt}{(RDt)^{1/\alpha}}\right)\right], \tag{13}$$

where $F_{\alpha\beta}$ is the cumulative probability function and $R = |\cos(\frac{\pi\alpha}{2})|$. For $\alpha \neq 1$ and $x \geq 0$ the cumulative probability function is defined by

$$F_{\alpha\beta}(x) = 1 - \frac{1}{2} \int_{-\theta}^{1} \exp\left[-(cx)^{\alpha/(\alpha-1)} U_\alpha(\phi, \theta)\right] d\phi, \tag{14}$$

where

$$c = \left[1 + \left(\beta \tan \frac{\pi\alpha}{2}\right)^2\right]^{-1/2\alpha},$$

$$\theta = \frac{2}{\pi\alpha} \tan^{-1}\left[\beta \tan \frac{\pi\alpha}{2}\right],$$

$$U_\alpha(\phi,\theta) = \left[\frac{\sin(\pi\alpha(\phi+\theta)/2)}{\cos(\pi\phi/2)}\right]^{\frac{\alpha}{1-\alpha}} \frac{\cos(\pi(\alpha-1)\phi/2+\alpha\theta)}{\cos(\pi\phi/2)}.$$

The function $F_{\alpha\beta}(x)$ for $\alpha \neq 0$ and $x < 0$ is computed using the identity

$$F_{\alpha\beta}(-x) = 1 - F_{\alpha,-\beta}(x)$$

and $F_{\alpha\beta}(-\infty) = 0, \quad F_{\alpha\beta}(\infty) = 1$.

Note that in order to have $u(x,t) \to u(x^0,0)$ as $(x,t) \to (x^0,0)$, for each $x^0 \in \mathbb{R}$, the constant m_0, in the initial condition (11), is defined as

$$m_0 = \frac{u_0}{2}(1+\theta).$$

Proof. Applying the Fourier transform at (5) we obtain

$$\frac{d}{dt}\hat{u}(k,t) = ikV\hat{u}(k,t) + \frac{1}{2}(1+\beta)D(-ik)^\alpha\hat{u}(k,t) + \frac{1}{2}(1-\beta)D(ik)^\alpha\hat{u}(k,t). \quad (15)$$

This is an ordinary differential equation for which the solution is given by

$$\hat{u}(k,t) = A\exp\left(\frac{1}{2}(1+\beta)(-ik)^\alpha Dt + \frac{1}{2}(1-\beta)(ik)^\alpha Dt + ikVt\right), \quad (16)$$

and the constant A is determined using the initial condition, that is, $A = \hat{u}(k,0)$. We have

$$\hat{u}(k,t) = \hat{u}(k,0)\exp\left(\frac{1}{2}|k|^\alpha Dt\left(\cos\left(\alpha\frac{\pi}{2}\right) - i\beta\sin\left(\text{sign}(k)\alpha\frac{\pi}{2}\right)\right) + ikVt\right).$$

After some algebra this can be written as

$$\hat{u}(k,t) = \hat{u}(k,0)\exp\left(\cos(\pi\alpha/2)Dt|k|^\alpha(1 - i\beta(sign(k))\tan(\pi\alpha/2)) + ikVt\right). \quad (17)$$

Therefore, noticing that $\cos(\alpha\pi/2)$ is negative for $1 < \alpha \leq 2$, we have

$$\hat{u}(k,t) = \hat{u}(k,0)\psi_\beta(k), \quad (18)$$

where

$$\psi_\beta(k) = \exp\left(-|\cos(\pi\alpha/2)|Dt|k|^\alpha(1 - i\beta(sign(k))\tan(\pi\alpha/2)) + ikVt\right).$$

We note $\psi_\beta(k)$ is a characteristic function. The cumulative probability function determined by the characteristic function and the densities, which are the differentiation of the cumulative probability, will be denoted by $F_{\alpha,\beta}$ and $f_{\alpha,\beta}$, respectively. According to McCulloh et al. [10] (p. 308, (3)), for the characteristic function $\psi_\beta(k)$ we obtain

$$\mathscr{F}^{-1}[\psi_\beta(k)] = f_{\alpha\beta}(x,\sigma,\delta),$$

and

$$F'_{\alpha\beta}(x,\sigma,\delta) = f_{\alpha\beta}(x,\sigma,\delta),$$

for

$$\delta = Vt \quad , \quad \sigma = (RDt)^{1/\alpha} \quad \text{and} \quad R = |\cos(\pi\alpha/2)|.$$

Note that

$$F'_{\alpha\beta}(x,\sigma,\delta) = F_{\alpha\beta}\left(\frac{x-\delta}{\sigma},1,0\right) := F_{\alpha\beta}\left(\frac{x-\delta}{\sigma}\right),$$

where $F_{\alpha\beta}$ is defined by (14). Consequently, using the convolution property for Fourier transforms, the inversion of (18) is given by

$$u(x,t) = \int_{-\infty}^{\infty} u(\tau,0) f_{\alpha\beta}(x-\tau,\sigma,\delta)d\tau.$$

Since $u(x,0) = 0$ for $x > 0$ and $u(x,0) = u_0$ for $x < 0$ we have

$$u(x,t) = \int_{-\infty}^{0} u_0 f_{\alpha\beta}(x-\tau,\sigma,\delta)d\tau.$$

Changing variables, by considering $\xi = x - \tau$, we have

$$u(x,t) = u_0 \int_{x}^{\infty} f_{\alpha\beta}(\xi,\sigma,\delta)d\xi.$$

Therefore

$$\begin{aligned} u(x,t) &= u_0[\lim_{\xi\to\infty} F_{\alpha\beta}(\xi,\sigma,\delta) - F_{\alpha\beta}(x,\sigma,\delta)] \\ &= u_0[1 - F_{\alpha\beta}(x,\sigma,\delta)] := u_0\left[1 - F_{\alpha\beta}\left(\frac{x-Vt}{(RDt)^{1/\alpha}}\right)\right]. \end{aligned}$$

Finally

$$u(x,t) = u_0\left[1 - F_{\alpha\beta}\left(\frac{x-Vt}{(RDt)^{1/\alpha}}\right)\right]. \tag{19}$$

Let us now consider the problem when the transition of the solute particle is symmetric, that is, $\beta = 0$. The problem is defined in the whole line, $x \in \mathbb{R}$, and $t > 0$, with initial conditions (11) and boundary conditions (12). This example was considered in [20].

Corollary 2.1. *The exact solution for the fractional advection diffusion (5), with $\beta = 0$, subject to the initial condition (11) and with boundary conditions (12) is of the form*

$$u(x,t) = u_0 \left[1 - F_\alpha \left(\frac{x - Vt}{(RDt)^{1/\alpha}} \right) \right], \tag{20}$$

where F_α is the cumulative probability function and $R = |\cos(\frac{\pi\alpha}{2})|$. For $\alpha \neq 1$ and $x \geq 0$ the cumulative probability function is defined by

$$F_\alpha(x) = 1 - \frac{1}{2} \int_0^1 \exp\left[-x^{\alpha/(\alpha-1)} U_\alpha(\phi) \right] d\phi, \tag{21}$$

where

$$U_\alpha(\phi) = \left[\frac{\sin(\pi\alpha\phi/2)}{\cos(\pi\phi/2)} \right]^{\frac{\alpha}{1-\alpha}} \frac{\cos(\pi(\alpha-1)\phi/2)}{\cos(\pi\phi/2)}.$$

The function $F_\alpha(x)$ for $\alpha \neq 0$ and $x < 0$ is computed using the identity

$$F_\alpha(-x) = 1 - F_\alpha(x)$$

and $F_\alpha(-\infty) = 0, \quad F_\alpha(\infty) = 1$.

Note that in order to have $u(x,t) \to u(x^0,0)$ as $(x,t) \to (x^0,0)$, for each $x^0 \in \mathbb{R}$, the constant m_0, in the initial condition (11), is defined as

$$m_0 = \frac{u_0}{2}.$$

Consider now the definition of an α-stable error function, Serf_α,

$$\mathrm{Serf}_\alpha(z) = 2 \int_0^z f_\alpha(x) dx,$$

where $f_\alpha(x) := F'_\alpha(x)$. Note that

$$\mathrm{Serf}_\alpha(z) = 2 \int_0^z f_\alpha(x) dx = 2 \left(\int_{-\infty}^z f_\alpha(x) dx - \frac{1}{2} \right).$$

Therefore we can also write the solution (20) in the form

$$u(x,t) = \frac{u_0}{2} \left[1 - \mathrm{Serf}_\alpha \left(\frac{x - Vt}{(RDt)^{1/\alpha}} \right) \right].$$

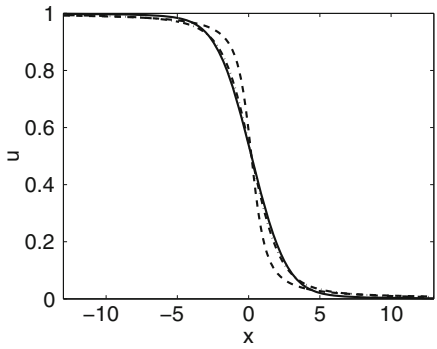

Fig. 1 Solutions for problem (5), (11), (12) for $t = 2$ with $V = 0.1$, $D = 1$, $\beta = 0$, and for different values of α: $\alpha = 1.8$ $(-)$, $\alpha = 1.5$ $(-\cdot-)$, $\alpha = 1.2$ $(--)$

For $\alpha = 2$, we have

$$u(x,t) = \frac{u_0}{2}\left[1 - \text{Erf}\left(\frac{x - Vt}{2\sqrt{Dt}}\right)\right],$$

where Erf is the error function. Note that in this case we have the usual advection diffusion equation with the second-order derivative.

A similar solution is named Ogata and Banks solution [12]

$$u(x,t) = \frac{u_0}{2}\left[1 - \text{Erf}\left(\frac{x - Vt}{2\sqrt{Dt}}\right) + e^{Vx/D}\text{Erfc}\left(\frac{x + Vt}{2\sqrt{Dt}}\right)\right],$$

where Erfc is the complementary error function. However, this is a solution of a slightly different problem. This is a solution for a problem defined in the half-line, that is, $x \geq 0$, with initial condition

$$u(x,0) = 0, \tag{22}$$

and boundary conditions

$$u(0,t) = u_0, \qquad u(\infty,t) = 0. \tag{23}$$

We note that for very small diffusion the solutions are basically the same. Nevertheless, if we want to consider such initial and boundary conditions, (22) and (23), with the fractional advection diffusion equation, we need to derive a different exact solution and we cannot use Fourier transforms.

In Figs. 1 and 2 we plot the effect of the fractional order α and the effect of the skewness parameter β on the solution of the problem. To compute the integrals in (13) we have used Gauss–Legendre quadrature. In Fig. 1 we observe how the α affects the solution for a fixed β, namely $\beta = 0$. As α gets larger we see the diffusive effects increase. In Fig. 2 we show how the β affects the solution, for a fixed α. The solution moves backward or forward according to the sign of the parameter β.

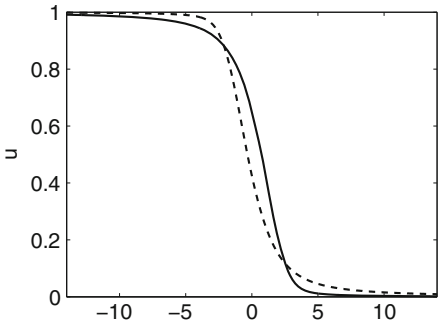

Fig. 2 Solutions for problem (5), (11), (12) for $t = 2$ with $V = 0.1$, $D = 1$, $\alpha = 1.5$, and for different values of β: $\beta = 0.6$ $(--)$, $\beta = -0.6$ $(-)$

Next, we present the solution of the problem that considers the fractional advection diffusion equation with the Dirac delta function as the initial condition, that is,

$$u(x,0) = \delta(x), \tag{24}$$

and subject to the boundary conditions,

$$\lim_{x\to-\infty} u(x,t) = 0, \qquad \lim_{x\to\infty} u(x,t) = 0. \tag{25}$$

Similarly to what we have done previously, we use Fourier transforms to derive the exact solution.

Proposition 2.2. *The exact solution for the problem (5), (24), (25) is given by*

$$u(x,t) = \frac{1}{2\pi}\int_0^\infty \mathrm{e}^{(1/2)\xi^\alpha Dt\cos(\alpha\pi/2)}\cos(\beta\xi^\alpha DT\sin(\alpha\pi/2) + \xi(x-Vt))d\xi. \tag{26}$$

Proof. Following the same steps as in the previous proposition and knowing that $\hat{u}(k,0) = \hat{\delta}(k) = 1$, we have

$$\hat{u}(k,t) = \exp\left(\frac{1}{2}(1+\beta)(-ik)^\alpha Dt + \frac{1}{2}(1-\beta)(ik)^\alpha Dt + ikVt\right). \tag{27}$$

After some algebra this can be written as

$$\hat{u}(k,t) = \exp\left(\frac{1}{2}|k|^\alpha Dt\left(\cos\left(\alpha\frac{\pi}{2}\right) - i\beta\sin\left(\mathrm{sign}(k)\alpha\frac{\pi}{2}\right)\right) + ikVt\right). \tag{28}$$

By the Fourier inversion

$$u(x,t) = \frac{1}{2\pi}\int_{-\infty}^\infty \mathrm{e}^{(1/2)\xi^\alpha Dtg(\xi,\alpha,\beta)}\mathrm{e}^{-i\xi(x-Vt)}d\xi,$$

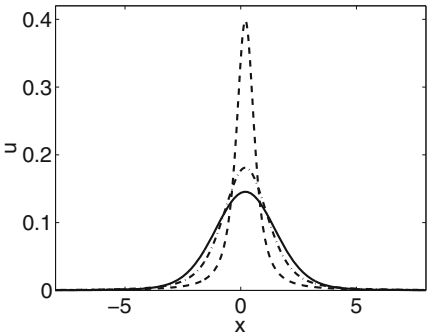

Fig. 3 Solutions for the problem (5), (24), (25) for $t = 2$ with $V = 0.1$, $D = 1$, $\beta = 0$ for different values of α: $\alpha = 1.8$ $(-)$, $\alpha = 1.5$ $(-\cdot-)$, $\alpha = 1.2$ $(--)$

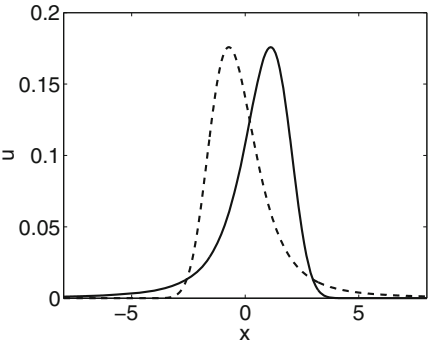

Fig. 4 Solutions for the problem (5), (24), (25) for $t = 2$ with $V = 0.1$, $D = 1$, $\alpha = 1.5$ for different values of β: $\beta = 0.5$ $(--)$, $\beta = -0.5$ $(-)$

where $g(\xi,\alpha,\beta) = \cos(\alpha\pi/2) - i\beta\sin(sign(\xi)\alpha\pi/2))$. Then

$$u(x,t) = \frac{1}{2\pi}\left[\int_0^\infty e^{(1/2)\xi^\alpha Dtg(-\xi,\alpha,\beta)} e^{i\xi(x-Vt)} d\xi + \int_0^\infty e^{(1/2)\xi^\alpha Dtg(\xi,\alpha,\beta)} e^{-i\xi(x-Vt)} d\xi\right].$$

After some calculations we get the result (26).

For the particular case, when $\beta = 0$, where the transition probability is symmetric, we have the following result.

Corollary 2.2. *The exact solution for the problem (5), (24), (25), with $\beta = 0$, is given by*

$$u(x,t) = \frac{1}{2\pi}\int_0^\infty e^{(1/2)\xi^\alpha Dt\cos(\alpha\pi/2)}\cos(\xi(x-Vt))d\xi. \tag{29}$$

In Figs. 3 and 4 we represent the behavior of the exact solution for the problem (5), (24), (25). Again the integral in (26) has been computed with Gauss–Legendre quadrature. In Fig. 3 we observe the effect of α for a fixed β. For larger values of α we have a more diffusive behavior. However, the shape of the function does not change too much apart from the expected damping. In Fig. 4 we display the effect of changing β assuming a fixed α. We observe the shape changes forming long tails on the left or right according to the sign of β.

3 Final Remarks

We have presented a fractional advection diffusion equation subject to different initial conditions and boundary conditions and have shown how we can obtain exact solutions by using Fourier transforms. We have also observed how the parameters α and β affects the shape of the solution. This model is more suitable to describe certain real-world problems than the classical advection diffusion equation as shown in many examples in literature. When adjusting the model to some physical problem, additionally to the estimation of the parameters V and D, we can also estimate the parameters α and β to obtain the model that more successfully describe our physical situation.

Acknowledgments Research supported by CMUC and FCT (Portugal), through European program COMPETE/FEDER and by the research project UTAustin/MAT/066/2008.

References

1. Benson, D.A.: The fractional advection-dispersion equation: development and application. Ph.D. dissertation, University of Nevada, Reno, USA (1998)
2. Benson, D.A., Wheatcraft, S.W., Meerschaert, M.M.: Application of a fractional advection-dispersion equation. Water Resour. Res. **36**, 1403–1412 (2000)
3. Chaves, A.S.: A fractional diffusion equation to describe Lévy flights. Phys. Lett. A. **239**, 13–16 (1998)
4. Deng,W.: Finite element method for the space and time fractional Fokker–Planck equation. SIAM J. Numer. Anal. **47**, 204–226 (2008)
5. Diethelm, K.: The analysis of fractional differential equations. Lecture Notes in Mathematics, vol. 2004. Springer, Heidelberg (2010)
6. Huang, G., Huang, Q., Zhan, H.: Evidence of one-dimensional scale-dependent fractional advection-dispersion. J. Contam. Hydrol. **85**, 53–71 (2006)
7. Huang, Q., Huang, G., Zhan, H.: A finite element solution for the fractional advection-dispersion equation. Adv. Water Resour. **31**, 1578–1589 (2008)
8. Kilbas, A.A., Srivastava, H.M., Trujillo, J.J.: Theory and Applications of Fractional Differential equations. Elsevier, Amsterdam (2006)
9. Li, X., Xu, C.: A space-time spectral method for the time fractional diffusion equation. SIAM J. Numer. Anal. **47** 2108–2131 (2009)
10. McCulloch, J.H., Panton, D.P.: Precise tabulation of the maximally-skewed stable distributions and densities. Comput. Stat. Data An. **23**, 307–320 (1997)
11. Meerschaert, M.M., Tadjeran, C.: Finite difference approximations for fractional advection-dispersion flow equations. J. Comput. Appl. Math. **172**, 65–77 (2004)
12. Ogata, A., Banks, R.B.: A solution of the differential equation of longitudinal dispersion in porous media. U.S. Geological Survey, Professional Paper No. 411-A A1–A7 (1961)
13. Oldham, K.B., Spanier, J.: The Fractional Calculus. Academic Press, New York-London (1974)
14. Ortigueira, M.D.: Fractional calculus for scientists and engineers. Lecture Notes in Electrical Engineering, vol. 84, Springer, Heidelberg (2011)
15. Pachepsky, Y., Benson, D., Rawls, W.: Simulating scale-dependent solute transport in soils with the fractional advective-dispersive equation. Soil Sci. Soc. Am. J. **4**, 1234–1243 (1997)
16. Podlubny, I.: Fractional Differential Equations. Academic Press, San Diego (1999)

17. Roop, J.P.: Computational aspects of FEM approximation of fractional advection dispersion equations on bounded domains in $\mathbb{R}^2$. J. Comput. Appl. Math. **193**, 243–268 (2006)
18. Samko, S.G., Kilbas, A.A., Marichev, O.I.: Fractional Integrals and Derivatives: Theory and Applications. Gordon and Breach Science Publishers, Amsterdam (1993)
19. San Jose Martinez, F., Pachepsky, Y.A., Rawls, W.J.: Fractional Advective-dispersive equations as a model of solute transport in porous media. In: Sabatier, J., Agrawal, O.P., Machado, J.A. (eds.) Advances in Fractional Calculus: Theoretical Developments and Applications in Physics and Engineering. pp. 199–212. Springer, Dordrecht (2007)
20. Sousa, E.: Finite difference approximations for a fractional advection diffusion problem. J. Comput. Phys. **228** 4038–4054 (2009)
21. Tadjeran, C., Meerschaert, M.M., Scheffler, H-P.: A second-order accurate numerical approximation for the fractional diffusion equation. J. Comput. Phys. **213**, 205–213 (2006)
22. Zhang, X., Mouchao, L., Crawford, J.W., Young, I.M.: The impact of boundary on the fractional advection-dispersion equation for solute transport in soil: defining the fractional dispersive flux with the Caputo derivatives. Adv. Water Resour. **30**, 1205–1217 (2007)
23. Zhang, H., Fawang, L., Anh, V.: Galerkin finite element approximation of symmetric space-fractional partial differential equations. Appl. Math. Comput. **217**, 2534–2545 (2010)
24. Zhou, L., Selim, H.M.: Application of the fractional advection-dispersion equation in porous media. Soil Sci. Soc. Am. J. **67**, 1079–1084 (2003)

Stochastic Forecasting of Algae Blooms in Lakes

P. Wang, D.M. Tartakovsky, and A.M. Tartakovsky

Abstract We consider the development of harmful algal blooms (HABs) in a lake with uncertain nutrients inflow. To quantify the impact of this uncertainty on predictions of the concentrations of various algae groups, we explore two alternative approaches based on the Fokker–Planck equation and PDF methods. Both approaches quantify predictive uncertainty by deriving deterministic equations for joint probability density functions of the algae concentrations. As an example, we study the impact of uncertain initial concentration and inflow–outflow ratio on the evolution of cyanobacteria (the blue-green algae).

1 Introduction

Anthropogenic stresses, such as discharge of wastewater, significantly accelerated eutrophication of many aquatic systems worldwide [1]. As a result, there is an explosion of harmful algae blooms (HABs) that pose serious risks to human and animal health and to ecosystem sustainability. A conservative estimate of annual economic costs of HABs and eutrophication in the USA. alone amounts to $2.2–4.6 billion [2]. Ironically, on the other end of the spectrum, recent research suggests various potential uses of algal biomass, such as biodiesel, animal feed, heating, electricity, and even pharmaceutical and cosmetic products.

Like most eco-dynamics systems, HABs involve complex interactions between different biological species and their predictions rely on mathematical models with a

P. Wang (✉) • A.M. Tartakovsky
Pacific Northwest National Laboratory, P.O. Box 999, MSIN K7-90, Richland, WA 99352, USA
e-mail: peng.wang@pnnl.gov; alexandre.tartakovsky@pnnl.gov

D.M. Tartakovsky
Department of Mechanical and Aerospace Engineering, University of California,
San Diego, 9500 Gilman Drive, La Jolla, CA 92093, USA
e-mail: dmt@ucsd.edu

J.A. Ferreira et al. (eds.), *Modelling and Simulation in Fluid Dynamics in Porous Media*,
Springer Proceedings in Mathematics & Statistics 28, DOI 10.1007/978-1-4614-5055-9_6,

large number of uncertain parameters. A number of recent studies [3–6] employed a probabilistic framework to quantify parametric uncertainty in predictions of HABs. These analyses are typically based on simplifying assumptions and rely on the ensemble variance of concentrations to quantify predictive uncertainty. Since the concentrations of multiple competing algae species are described by a system nonlinear differential equations with multiplicative noise, their probability density functions (PDFs) are typically highly non-Gaussian. Therefore, the concentration variances do not provide information necessary to predict extreme events and to conduct risk assessments of HABs.

We present two alternative frameworks, the Fokker–Planck equation and PDF methods, that enable probabilistic forecasting of HABs in natural environments. Section 2 contains a mathematical formulation of the problem and a brief overview of their uncertain parameterizations. In Sect. 3 we derive the Fokker–Planck (Sect. 3.1) and PDF (Sect. 3.2) equations that are applicable for uncorrelated and correlated system parameters, respectively. Both deterministic equations describe the temporal evolution of the joint PDF of the concentrations of competing algae species. In Sect. 4, we use the Fokker–Planck equation to quantify the impact of uncertain initial concentration and inflow–outflow ratio on the evolution of cyanobacteria (the blue-green algae). Section 5 consists of major conclusions drawn from this study.

2 Problem Formulation

HABs typically occur when nutrients (nitrogen and phosphorous) are abundant, water is warm ($>20^{\circ}$C) and either stagnant or quiescent, and sunlight is present [7]. It is often assumed that an aquatic system is well mixed throughout or at the top layer of water. This assumption allows one to model HABs with a system of ordinary differential equations (ODEs).

To be concrete, we base our analysis on a model of the growth of four competing algae groups: Diatoms, Chrysophyceae, nitrogen-fixing cyanobacteria, and minor species [4]. This model is generalized to account for the temporal evolution of n algae groups with biomass concentrations $c_i(t)$ $(i = 1, \ldots, n)$ in a lake of volume V and average depth h. Then the model [4] consists of a system of n coupled ODEs,

$$\frac{\mathrm{d}c_i}{\mathrm{d}t} = \left(\tilde{\mu}_i - \frac{\tilde{\sigma}_i}{h} - \frac{q_{\text{out}}}{V} - f_i C_{\text{z}}\right) c_i, \qquad i = 1, \ldots, n, \tag{1}$$

where $\tilde{\mu}_i$ is the natural growth rate of the ith algae group, $\tilde{\sigma}_i$ is its non-predatory loss rate, q_{out} denotes the outflow rate, and $f_i C_{\text{z}}$ is the zooplankton predator rate.

The natural growth rate $\tilde{\mu}_i$ and the non-predatory loss rate $\tilde{\sigma}_i$ vary with the average temperature in the lake, T, in accordance with

$$\tilde{\mu}_i = \mu_i \theta_i^{T-T_{\text{ref}}} \frac{I}{K_{I_i} + I} \frac{P}{K_{P_i} + P} \frac{N}{K_{N_i} + N}, \qquad \tilde{\sigma}_i = \sigma_i \theta_\sigma^{T-T_{\text{ref}}}, \tag{2}$$

Table 1 Model parameters and variables and their units (Table 3 in [4])

Parameter	Unit	Description
c_i	(mg m^{-3})	Biomass concentration of the ith algae group
μ_i	(day^{-1})	Maximum growth rate at 20°C
σ_i	(day^{-1})	Maximum non-predatory loss rate at 20°C
θ_i		Temperature coefficients for growth rate
θ_σ		Temperature coefficients for non-predatory loss rate
K_{I_i}	(W m^{-2})	Global irradiance half-saturation coefficient
K_{P_i}	(mg m^{-3})	Phosphorus half-saturation coefficient
K_{N_i}	(mg m^{-3})	Nitrogen half-saturation coefficient
$f_i C_z$	(day^{-1})	Zooplankton rate
α_i		Relative phosphorus content of algae
β_i		Relative nitrogen content of algae
P	(mg m^{-3})	Total phosphorus concentration available for the algae
P_{tot}	(mg m^{-3})	Total phosphorus concentration in the lake
P_0	(mg m^{-3})	Initial phosphorus concentration in the lake
c_P	(mg m^{-3})	Phosphorus concentration of inflow
N	(mg m^{-3}]	Total nitrogen concentration available for the algae
N_{tot}	(mg m^{-3})	Total nitrogen concentration in the lake
N_0	(mg m^{-3})	Initial nitrogen concentration in the lake
c_N	(mg m^{-3})	Nitrogen concentration of inflow
T, T_{ref}	(°C)	Temperature and the reference temperature (20°C)
q_{out}	(m^3 day^{-1})	Outflow rate
Q	(m^3)	Inflow volume
$\bar{Q}$	(m^3)	Mean inflow volume
I	(W m^{-2})	Global irradiance
V	(m^3)	Volume of lake
h	(m)	Depth of lake

where the rate coefficients K with various subscripts are defined in Table 1. Temperature coefficients for the growth and non-predatory loss rate are denoted by θ_i and θ_σ, respectively. Concentrations of available (nonabsorbed) nutrients (phosphorus P and nitrogen N) for algae are related to the concentrations of the algae groups by

$$P = P_{\text{tot}} - \sum_{i=1}^{n} \alpha_i c_i, \qquad N = N_{\text{tot}} - \sum_{i=1}^{n} \beta_i c_i, \tag{3}$$

where P_{tot} and N_{tot} are the overall nutrient concentrations in the lake; and the constants α_i and β_i denote the phosphorus and nitrogen contents of the ith algae group, respectively. The Monod form of algae growth rate (2) varies almost linearly with irradiance I and the phosphorous (P) and nitrogen (N) concentrations when these quantities are small.

Insufficient site characterization and temporal fluctuations render various parameters in (1) uncertain. The data reported in [4, 5] suggest that over the summer, temperature T, global irradiance I, outflow rate q_{out}, and predatory

loss $f_i C_z$ typically exhibit much smaller variation than the fluctuations of nutrients. Consequently, we treat the total nutrients contents (P_{tot} and N_{tot}) as random functions of time t and assume the remaining parameters to be deterministic. Our goal is to compute the joint PDF of the concentrations of various algae groups, $W(\{\mathbf{C}\},t)$, where $\{\mathbf{C}\} = C_1, C_2, \ldots, C_n$ denote deterministic values (outcomes) of random algae population concentrations.

3 Stochastic Models

In many bodies of water, nutrient inflow through surface runoff and wastewater discharge is the leading factor to eutrophication. Temporal fluctuations of inflow volume $Q(t)$ is identified as the common source of uncertainty for P_{tot} and N_{tot} via relationships

$$P_{tot} = P_0 + \frac{c_P Q}{V}, \qquad N_{tot} = N_0 + \frac{c_N Q}{V}, \tag{4}$$

where P_0 and N_0 are the initial phosphorus and nitrogen concentrations in the lake, respectively; and c_P and c_N denote the inflow concentrations of nutrients.

Using a Reynolds decomposition to represent the runoff volume $Q(t) = \bar{Q} + Q'$ as the sum of its ensemble mean $\bar{Q}$ and zero-mean fluctuations Q', and employing a Taylor expansion of the random growth rates $\tilde{\mu}_i$ around $\bar{Q}$ yields

$$\tilde{\mu}_i = \tilde{\mu}_i(\bar{Q}) + \frac{\mathrm{d}\tilde{\mu}_i}{\mathrm{d}Q}(\bar{Q})Q' + \mathscr{O}(Q'^2). \tag{5}$$

Substitution of (5) into (1) leads to a system of n nonlinear Langevin equations with multiplicative noise $Q'(t)$,

$$\frac{\mathrm{d}c_i}{\mathrm{d}t} = h_i(\mathbf{c},t) + g_i(\mathbf{c},t)Q'(t), \qquad i = 1,\ldots,n, \tag{6}$$

where $\mathbf{c} = (c_1, c_2, \ldots, c_n)$ and

$$h_i(\mathbf{c},t) \equiv \left[\tilde{\mu}_i(\bar{Q}) - \frac{\tilde{\sigma}_i}{h} - \frac{q_{out}}{V} - f_i C_z\right] c_i, \qquad g_i(\mathbf{c},t) \equiv \frac{\mathrm{d}\tilde{\mu}_i}{\mathrm{d}Q}(\bar{Q})c_i. \tag{7}$$

3.1 Fokker–Planck Equation

Following the standard procedure outlined in [8], we define the mth Kramers–Moyal expansion coefficients as

$$D^{(m)}_{i_1\ldots i_m}(\mathbf{C},t) = \frac{1}{m!}\lim_{\tau\to 0}\frac{\langle [c_{i_1}(t+\tau) - C_{i_1}]\cdots[c_{i_m}(t+\tau) - C_{i_m}]\rangle|_{c_{i_k}=C_{i_k}}}{\tau}, \tag{8}$$

where $\mathbf{C}$ is a deterministic outcome of random $\mathbf{c}$, $\langle\cdot\rangle$ denotes the ensemble mean, and $k = 1,\ldots,m$. Let us suppose that $Q'(t)$ is uncorrelated Gaussian-distributed white noise,

$$\langle Q'(t)\rangle = 0\,, \qquad \langle Q'(t_1)Q'(t_2)\rangle = 2\delta(t_1 - t_2), \tag{9}$$

where $\delta(\cdot)$ is the Dirac delta function. Then all but the first two of the Kramers–Moyal expansion coefficients vanish [8]. The nonzero coefficients are referred to as drift D_i and diffusion coefficients D_{ij}. This yields the Fokker–Planck equation for the joint PDF of the algae concentrations, $W(\mathbf{C},t)$,

$$\frac{\partial W}{\partial t} = -\sum_{i=1}^{n} \frac{\partial}{\partial C_i}\left[D_i(\mathbf{C},t)W\right] + \sum_{i,j=1}^{n} \frac{\partial^2}{\partial C_i \partial C_j}\left[D_{ij}(\mathbf{C},t)W\right] \tag{10}$$

where

$$D_i(\mathbf{C},t) = h_i(\mathbf{C},t) + g_k \frac{\partial}{\partial C_k} g_i(\mathbf{C},t), \qquad D_{ij}(\mathbf{C},t) = g_i(\mathbf{C},t)g_j(\mathbf{C},t). \tag{11}$$

3.2 PDF Method

For the correlation function $\langle Q'(t_1)Q'(t_2)\rangle$ that cannot be treated as white noise, we use the PDF method [9–11] to derive a deterministic equation for $W(\mathbf{C},t)$. We expand the concept of fine-grained single-point PDF [9–11] by introducing a fine-grained joint PDF of the concentrations of competing algae groups,

$$\Pi = \prod_{i=1}^{n} \delta[C_i - c_i(t)]. \tag{12}$$

Its ensemble average yields $W(\mathbf{C},t)$:

$$\langle \Pi\rangle = \int_{-\infty}^{\infty} \cdots \int_{-\infty}^{\infty} \prod_{i=1}^{n} \delta(C_i - c_i')W(c_1',\ldots,c_n',t)\mathrm{d}c_1' \cdots \mathrm{d}c_n' = W(C_1,\ldots,C_n,t). \tag{13}$$

We show in the Appendix that the coupled system of nonlinear stochastic ODEs (6) gives rise to a linear stochastic partial differential equation (PDE) for Π,

$$\frac{\partial \Pi}{\partial t} + \sum_{i=1}^{n} \frac{\partial}{\partial C_\mathrm{i}}[\phi_i(\mathbf{C},t)\Pi] = 0, \qquad \phi_i(\mathbf{C},t) \equiv h_i(\mathbf{C},t) + g_i(\mathbf{C},t)Q'(t). \tag{14}$$

This PDE is subject to appropriate initial and boundary conditions.

Employing Reynolds decompositions $\Pi = W + \Pi'$ and $\phi_i = \bar{\phi}_i + \phi_i'$, and taking the ensemble average of (14), leads to a deterministic equation for W,

$$\frac{\partial W}{\partial t} + \sum_{i=1}^{n} \frac{\partial}{\partial C_i}[W\bar{\phi}_i(\mathbf{C},t)] = \sum_{i=1}^{n} \frac{\partial}{\partial C_i}\langle \Pi'\phi_i'\rangle, \tag{15}$$

which contains the unknown covariance $\langle \Pi' \phi_i' \rangle$. A closure approximation for this term can be drawn from the rich literature on stochastic averaging of linear advective transport in random velocity fields. Here we adopt the large-eddy-diffusivity (LED) approximation [11],

$$\frac{\partial W}{\partial t} + \sum_{i=1}^{n} \frac{\partial}{\partial C_i}[\bar{\phi}_i(\mathbf{C},t)W] = \sum_{i,j=1}^{n} \frac{\partial}{\partial C_i}\left(D_{ij}\frac{\partial W}{\partial C_j}\right), \tag{16}$$

where D_{ij} are components of the effective eddy-diffusivity tensor. This closure becomes exact in the limit of the correlation length of $Q'(t)$ going to zero [9]. One can verify that in this limit the PDF equation (16) reduces to the Fokker–Planck equation (10).

4 Results and Discussion

We demonstrate our approach on a relatively simple example of cyanobacteria (blue-green algae) bloom that is caused by (uncertain) inflow of nutrients. The inflow rate $Q(t)$ is modeled as white noise, so that the PDF of the cyanobacteria concentration is governed by a simplified version of the Fokker–Planck equation (10),

$$\frac{\partial W}{\partial t} = -\frac{\partial}{\partial C}[D_1(C,t)W] + \frac{\partial^2}{\partial C^2}[D_2(C,t)W], \tag{17}$$

where the drift (D_1) and diffusion (D_2) coefficients take the form (see equation (3.95) in [8])

$$D_1 = \left(\tilde{\mu}_1 - \frac{\tilde{\sigma}_1}{h} - \frac{q_{\text{out}}}{V} - f_1 C_z\right)C + \left(\frac{\partial^2 \tilde{\mu}_1}{\partial Q \partial C}C + \frac{\partial \tilde{\mu}_1}{\partial Q}\right)\frac{\partial \tilde{\mu}_1}{\partial Q}C, \tag{18a}$$

$$D_2 = \left(\frac{\partial \tilde{\mu}_1}{\partial Q}C\right)^2. \tag{18b}$$

Numerical simulations are performed with the data from previous investigations [4, 5]. A lognormal distribution $\mathcal{N}(5,1)$ is prescribed to the initial concentration. Figure 1 exhibits temporal snapshots of the PDF of the cyanobacteria concentration, $W(C,t)$, at $t = 0$, 5, and 10 days. The continuous nutrient inflow leads to rapid growth of blue-green algae from its initial mean concentration of 5–33 mg m^{-3} over a week. Widening distributions indicate rising uncertainty in the forecast. Overall, the shape of W gradually diffuses and propagates with time, as expected from the advection-diffusion (17).

Figure 2 elucidates the effects of uncertainty in the initial algae concentration. The latter is quantified in terms of the coefficient of variation (CV, standard deviation divided by mean). The PDFs $W(C,t)$ in Fig. 2 correspond to $t = 10$ days and three

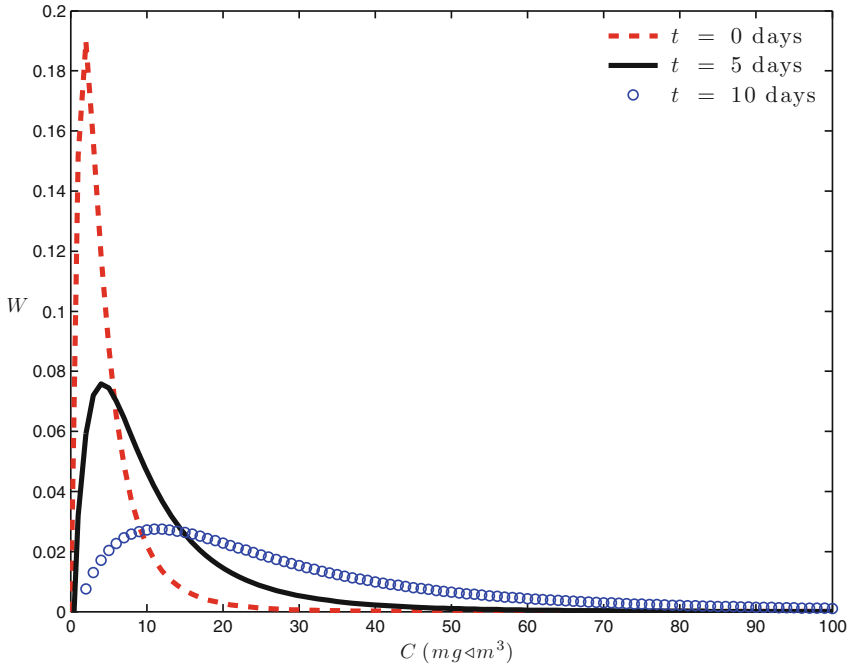

Fig. 1 Temporal snapshots of the cyanobacteria concentration PDF $W(C,t)$ at (**a**) $t = 0$ days, (**b**) $t = 5$ days, and (**c**) t 10 days

levels of CV of the initial concentration. Not surprisingly, larger initial fluctuations (CV$= 2$) lead to greater uncertainty, i.e., to longer distribution tails.

Figure 3 demonstrates the effect of average inflow on the algae growth for a fixed outflow volume. At $t = 10$ days, greater inflows ($\bar{Q}/Q_{\text{out}} = 2$) introduce more predictive uncertainty, as indicated by a wider breadth (longer tails) of the PDF $W(C,t)$. This is to be expected, because nutrient inflow is the primary factor leading to algae bloom in lakes, and the random inflow volume is identified as the sole source of uncertainty here. Reduction of average inflow ($\bar{Q}/Q_{\text{out}} = 0.5$) leads to smaller predictive uncertainty. However, its overall impact is limited (comparing to the time factor and initial condition) due to its small volume relative to the volume of the lake.

5 Conclusions

We present two alternative frameworks to quantify uncertainty in predictions of the concentration of various algae groups via their joint probabilistic density function (PDF). Based on a physical model routinely used for algae population dynamics in a lake, deterministic equations for the joint concentration PDF are

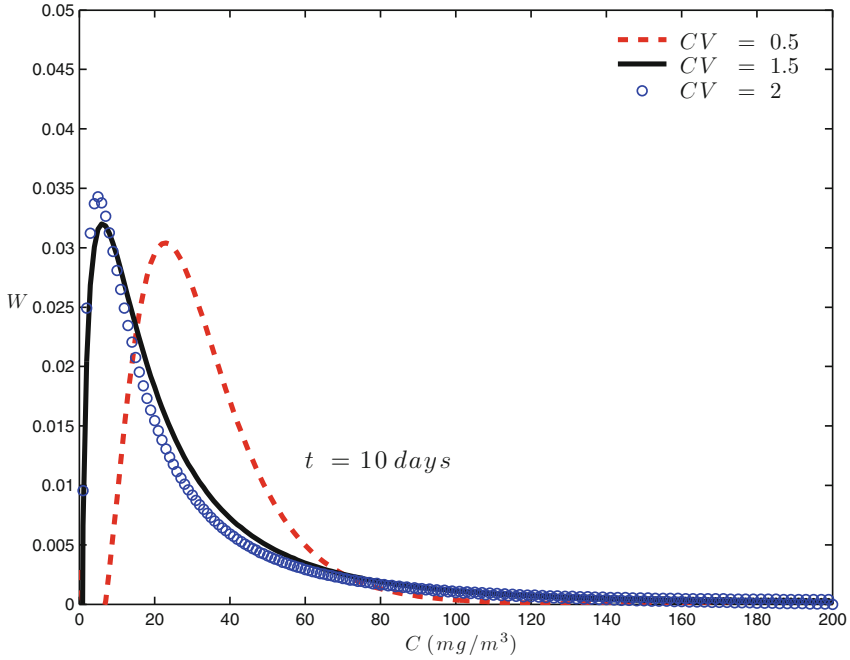

Fig. 2 The cyanobacteria concentration PDF $W(C,t)$ at $t = 10$ days for different levels of uncertainty about the initial concentration

derived by two methods, the Fokker–Planck equation and PDF method, for the uncorrelated and correlated input parameters, respectively. Our analysis leads to the following major conclusions:

1. The proposed approach provides full statistical information on the bloom of various algae species and facilitates probabilistic risk assessments by enabling computation of probabilities of rare events.
2. Uncertainty of initial population density is found to significantly affect overall predictive uncertainty.
3. Average inflow volume has limited impact on predictive uncertainty if its value is much smaller that the lake volume.

Acknowledgements This work was supported by the Office of Advanced Scientific Computing Research, the U.S. Department of Energy.

Appendix

We note that the derivatives of the raw joint PDF are

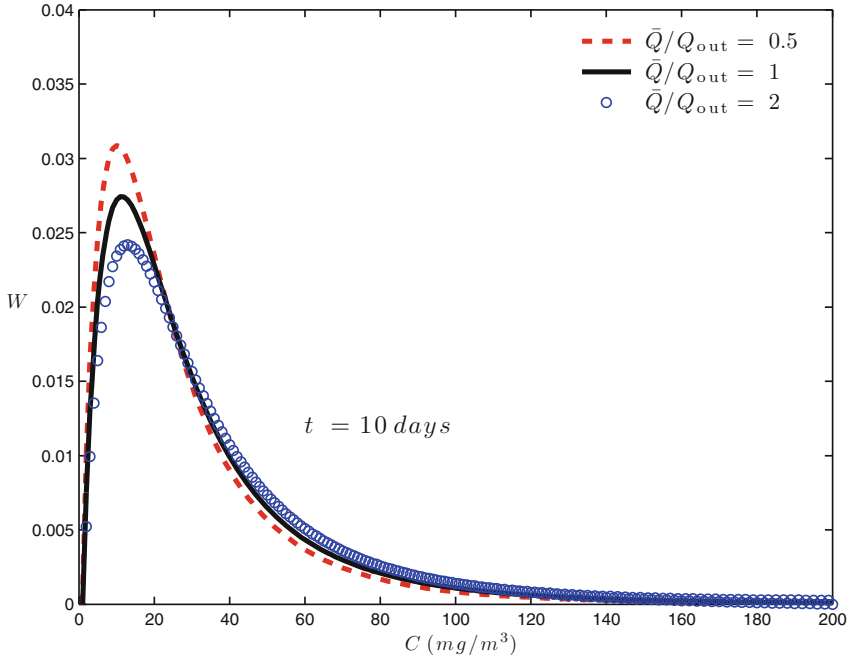

Fig. 3 Effects of average runoff $\bar{Q}$ on the cyanobacteria concentration PDF $W(C,t)$ at $t = 10$ days

$$\frac{\partial \Pi}{\partial C_i} = \frac{\partial \delta}{\partial C_i} \prod_{j=1, j\neq i}^{n} \delta(C_j - c_j), \qquad i = 1, \ldots, n, \tag{19}$$

$$\frac{\partial \Pi}{\partial t} = -\sum_{i=1}^{n} \left[\frac{\partial \delta}{\partial C_i} \frac{\mathrm{d}c_i}{\mathrm{d}t} \prod_{j=1, j\neq i}^{n} \delta(C_j - c_j) \right]. \tag{20}$$

Multiplying the ith equation (6) with $\partial \Pi / \partial C_\mathrm{i}$ yields the following equations:

$$\frac{\partial \delta}{\partial C_i} \prod_{j=1, j\neq i}^{n} \delta(C_j - c_j) \frac{\mathrm{d}c_i}{\mathrm{d}t} = \frac{\partial \Pi}{\partial C_i} \phi_i(\mathbf{c}, t) = \frac{\partial [\Pi \phi_i(\mathbf{c}, t)]}{\partial C_i} = \frac{\partial [\Pi \phi_i(\mathbf{C}, t)]}{\partial C_i}. \tag{21}$$

Summation over all n equations gives

$$\frac{\partial \Pi}{\partial t} = -\sum_{i=1}^{n} \frac{\partial}{\partial C_i} [\phi_i(\mathbf{C}, t) \Pi]. \tag{22}$$

Rearrangement of the above equation leads to (14).

References

1. Carmichael, W.: A world overview—One-hundred-twenty-seven years of research on toxic cyanobacteria—Where do we go from here? In: Hudnell, H.K. (ed.) Cyanobacterial Harmful Algal Blooms: State of the Science and Research Needs, pp. 105–125. Springer, New York (2008)
2. Dodds, W., Bouska, W., Eitzmann, J., Pilger T., Pitts, K., Riley, A., Schloesser, J., Thornbrugh, D.: Eutrophication of U.S. freshwaters: analysis of potential economic damages. Environ. Sci. Technol. **43**, 12–19 (2009)
3. Marshall, J.S., Sala, K.: A stochastic Lagrangian approach for simulating the effect of turbulent mixing on algae growth rate in photobioreactors. Chem. Eng. Sci. **66**, 384–392 (2011)
4. Malve, O., Laine, M., Haario, H., Kirkkala, T., Sarvala, J.: Bayesian modelling of algal mass occurrences: using adaptive MCMC methods with a lake water quality model. Environ. Model. Software. **22**, 966–977 (2007)
5. Haario, H., Kalachev, L., Laine, M.: Reduced models of algae growth. Bull. Math. Biol. **71**, 1626–1648 (2007)
6. Huang, D.W., Wang, H.L., Feng, J.F., Zhu, Z.W.: Modelling algal densities in harmful algal blooms (HAB) with stochastic dynamics. Appl. Math. Model. **32**, 1318–1326 (2008)
7. Hudnell, H., Jones, C., Labisi, B., Lucero, V., Hill, D.R., Eilers, J.: Freshwater harmful algal bloom (FHAB) suppression with solar powered circulation (SPC). Harmful Algae **9**, 208–217 (2010)
8. Risken, H.: The Fokker–Planck Equation: Methods of Solutions and Applications. Springer, Heidelberg (1989)
9. Kraichnan, R.H.: Eddy Viscosity and Diffusivity: Exact Formulas and Approximations. Complex Systems **1**, 805–820 (1987)
10. Pope, S.B.: Turbulent Flows. Cambridge University Press, Cambridge (2000)
11. Tartakovsky, D.M., Broyda, S.: PDF equations for advective-reactive transport in heterogeneous porous media with uncertain properties. J. Contam. Hydrol. **120–121**, 129–140 (2011)

Unfolding Method for the Homogenization of Bingham Flow

R. Bunoiu, G. Cardone, and C. Perugia

Abstract We are interested in the homogenization of a stationary Bingham flow in a porous medium. The model and the formal expansion of this problem are introduced in Lions and Sanchez-Palencia (J. Math. Pures Appl. 60:341–360, 1981) and a rigorous justification of the convergence of the homogenization process is given in Bourgeat and Mikelic (J. Math. Pures Appl. 72:405–414, 1993), by using monotonicity methods coupled with the two-scale convergence method. In order to get the homogenized problem, we apply here the unfolding method in homogenization, method introduced in Cioranescu et al. (SIAM J. Math. Anal. 40:1585–1620, 2008).

1 Introduction

The aim of our chapter is to study the homogenization of the Bingham flow in porous media. The porous media that we consider here are classical periodic porous media containing solid inclusions of the same size as the period, namely ε, where ε is a small real positive parameter.

R. Bunoiu (✉)
LMAM, UMR 7122, Université de Lorraine et CNRS Ile du Saulcy,
F-57045 METZ Cedex 1, France
e-mail: bunoiu@univ-metz.fr

G. Cardone
Department of Engineering, University of Sannio, Corso Garibaldi,
107, 82100 Benevento, Italy
e-mail: giuseppe.cardone@unisannio.it

C. Perugia
DSBGA, University of Sannio, Via Dei Mulini, 59/A, 82100 Benevento, Italy
e-mail: cperugia@unisannio.it.

J.A. Ferreira et al. (eds.), *Modelling and Simulation in Fluid Dynamics in Porous Media*, Springer Proceedings in Mathematics & Statistics 28, DOI 10.1007/978-1-4614-5055-9_7,

In the fluid part of the porous media we consider the stationary flow of the Bingham fluid, under the action of external forces. The Bingham fluid is an incompressible fluid which has a nonlinear constitutive law. So it is a non-Newtonian fluid and it moves like a rigid body when a certain function of the stress tensor is below a given threshold. Beyond this threshold, it obeys a nonlinear constitutive law.

As an example of such fluids we can mention some paints, the mud which can be used for the oil extraction and the volcanic lava.

The mathematical model of the Bingham flow in a bounded domain was introduced in [6] by Duvaut and Lions. The existence of the velocity and of the pressure for such a flow was proved in the case of a bi-dimensional and of a three-dimensional domain.

The homogenization problem was first studied in [8] by Lions and Sanchez-Palencia. The authors did the asymptotic study of the problem by using a multiscale method, involving a "macroscopic" variable x and a "microscopic" variable $y = \frac{x}{\varepsilon}$, and associated to the dimension of the pores. The study is based on a multiscale "ansatz", which allows to get to the limit a nonlinear Darcy law. There is no convergence result proved.

The rigorous justification of the convergence of the homogenization process of the results presented in [8] is given by Bourgeat and Mikelic in [2]. In order to do it, the authors used monotonicity methods coupled with the two-scale convergence method introduced by Nguetseng in [9] and further developed by Allaire in a series of papers, as for example [1]. The limit problem announced in [8] was obtained.

We use in our chapter the unfolding method introduced by Cioranescu et al. in [5] in order to get the homogenized limit problem. The basic idea of the method is to perform a change of scale which blows up the microscopic scale in a periodic fashion. The first advantage of the method is that by using an unfolding operator, functions defined on perforated domains are transformed into functions defined on a fixed domain. The second advantage of the method is that it reduces two-scale convergence to a mere weak convergence in an appropriate space and so general compactness results can be applied. Therefore, no extension operators are required and so the regularity hypotheses on the boundary of the perforated domain, necessary for the existence of such extensions, are not needed. We intend to study some other cases of Bingham flow in porous media, for which we expect that the unfolding method fits better than the two-scale convergence method.

This chapter is organized as follows. In Sect. 2 we describe the problem and we give the preliminary results, namely a priori estimates for the velocity and the pressure on one side and a presentation of the unfolding method introduced in [5], on the other side.

In Sect. 3 we state the main result of the chapter, which is the limit problem obtained after applying the unfolding method for the homogenization of the Bingham flow in the porous media. Mathematically, this corresponds to the passage to the limit as ε tends to zero in the initial problem.

In Sect. 4 we conclude our chapter.

2 Statement of the Problem and Preliminary Results

Let $\Omega \subseteq \mathbb{R}^n$ be a bounded open set with Lipschitz boundary, and let ε be a small real positive parameter.

We denote by $Y =]0,1[^n$ the unitary cell in $\mathbb{R}^n$, Y_S is an open set strictly included in Y, $Y_F = Y \setminus \overline{Y}_S$ is a connected open set and Γ is the interface between Y_S and Y_F that we assume to be Lipschitz. Let $\varepsilon Y_k = \varepsilon (Y + k)$, $\varepsilon Y_{S,k} = \varepsilon (Y_S + k)$, $\varepsilon Y_{F,k} = \varepsilon (Y_F + k)$, where $k \in \mathbb{Z}^n$.

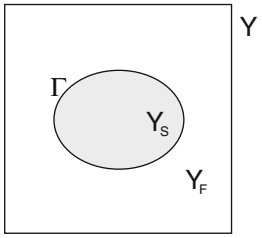

Elementary cell
$Y =]0,1[^2$.

We consider the set

$$K_\varepsilon = \{k \in \mathbb{Z}^n : \varepsilon Y_k \subset \Omega\},$$

and we define the fluid part of the porous media, denoted by Ω_ε as follows:

$$\Omega_{S,\varepsilon} = \bigcup_{k \in K_\varepsilon} \varepsilon Y_{S,k}, \ \Omega_\varepsilon = \Omega \setminus \overline{\Omega}_{S,\varepsilon}, \ \partial\Omega_\varepsilon = \partial\Omega \cup \partial\Omega_{S,\varepsilon}.$$

We assume that Ω_ε is a connected set.

In Ω_ε we consider a Bingham fluid. If u_ε and p_ε are the velocity and pressure respectively for such a fluid, then the stress tensor is written as

$$\sigma_{ij} = -p_\varepsilon \delta_{ij} + g \frac{D_{ij}(u_\varepsilon)}{(D_{II}(u_\varepsilon))^{\frac{1}{2}}} + 2\mu D_{ij}(u_\varepsilon), \tag{1}$$

where δ_{ij} is the Kronecker symbol and g and μ are real positive constants. The constant g represents the yield stress of the fluid and the constant μ is its viscosity. Relation (1) represents the constitutive law of the Bingham fluid.

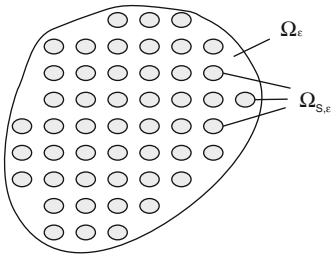

Ω_ε: fluid part;
$\Omega_{S,\varepsilon}$: the union of solid inclusions.

Moreover, we define

$$D_{ij}(u_\varepsilon) = \frac{1}{2}\left(\frac{\partial u_{\varepsilon,i}}{\partial x_j} + \frac{\partial u_{\varepsilon,j}}{\partial x_i}\right), 1 \le i,j \le n,$$

$$D_{II}(u_\varepsilon) = \frac{1}{2}\sum_{i,j=1}^{n} D_{ij}(u_\varepsilon) D_{ij}(u_\varepsilon)$$

$$\sigma_{ij}^D = g\frac{D_{ij}}{(D_{II})^{\frac{1}{2}}} + 2\mu D_{ij}$$

$$\sigma_{II} = \frac{1}{2}\sum_{i,j=1}^{n} \sigma_{ij}^D \sigma_{ij}^D.$$

Let us note that the constitutive law (1) is valid only if $D_{II}(u_\varepsilon) \neq 0$. In [6] it is shown that this constitutive law is equivalent with the following one:

$$\begin{cases} (\sigma_{II})^{\frac{1}{2}} < g\varepsilon \Leftrightarrow D_{ij}(u_\varepsilon) = 0 \\ \\ (\sigma_{II})^{\frac{1}{2}} \ge g\varepsilon \Leftrightarrow D_{ij}(u_\varepsilon) = \dfrac{1}{2\mu}\left(1 - \dfrac{g\varepsilon}{(\sigma_{II}^\varepsilon)^{\frac{1}{2}}}\right)\sigma_{ij}^D. \end{cases}$$

We see that this is a threshold law: as long as the shear stress is below $g\varepsilon$, the fluid behaves as a rigid solid. When the value of the shear stress exceeds $g\varepsilon$, the fluid flows and obeys a nonlinear law.

Moreover, the fluid is incompressible, which means that its velocity is divergence free

$$\operatorname{div} u_\varepsilon = 0 \text{ in } \Omega_\varepsilon.$$

In [6] it is shown that the velocity u_ε satisfies the following inequality when we apply to the porous media an external force denoted by f and belonging to $\left(L^2(\Omega)\right)^n$:

$$\begin{cases} a_\varepsilon(u_\varepsilon, v-u_\varepsilon) + j_\varepsilon(v) - j_\varepsilon(u_\varepsilon) \geq (f, v-u_\varepsilon)_{\Omega_\varepsilon}, \ \forall v \in V(\Omega_\varepsilon) \\ u_\varepsilon \in V(\Omega_\varepsilon), \end{cases} \tag{2}$$

where

$$a_\varepsilon(u,v) = 2\mu\varepsilon^2 \int_{\Omega_\varepsilon} \nabla u \cdot \nabla v dx, \quad j_\varepsilon(v) = g\varepsilon \int_{\Omega_\varepsilon} |\nabla v| dx, \quad (u,v)_{\Omega_\varepsilon} = \int_{\Omega_\varepsilon} u \cdot v dx,$$
$$V(\Omega_\varepsilon) = \left\{ v \in \left(H_0^1(\Omega_\varepsilon)\right)^n : \operatorname{div} v = 0 \text{ in } \Omega_\varepsilon \right\}.$$

If $f \in \left(L^2(\Omega)\right)^n$, we know from [6] that for $n = 2$ or 3 and every fixed ε there exists a unique $u_\varepsilon \in V(\Omega_\varepsilon)$ solution of problem (2) and that if p_ε is the pressure of the fluid in Ω_ε, then the problem (2) is equivalent to the following one:

$$a_\varepsilon(u_\varepsilon, v-u_\varepsilon) + j_\varepsilon(v) - j_\varepsilon(u_\varepsilon) \geq (f, v-u_\varepsilon)_{\Omega_\varepsilon} + (p_\varepsilon, \operatorname{div}(v-u_\varepsilon))_{\Omega_\varepsilon}, \tag{3}$$

for all $v \in \left(H_0^1(\Omega_\varepsilon)\right)^n$, $u_\varepsilon \in V(\Omega_\varepsilon)$ and $p_\varepsilon \in L_0^2(\Omega_\varepsilon)$, which admits a unique solution $(u_\varepsilon, p_\varepsilon)$. Here $L_0^2(\Omega_\varepsilon)$ denotes the space of functions belonging to $L^2(\Omega_\varepsilon)$ and of mean value zero.

The aim of our chapter is to pass to the limit as ε tends to zero in problem (3). In order to do this, we first need to get a priori estimates for the velocity u_ε and the pressure p_ε.

Let us recall that the Poincaré inequality for functions in $\left(H_0^1(\Omega_\varepsilon)\right)^n$ reads

$$\|u_\varepsilon\|_{L^2(\Omega_\varepsilon)^n} \leq C\varepsilon \|\nabla u_\varepsilon\|_{L^2(\Omega_\varepsilon)^{n\times n}}.$$

Setting $v = 2u_\varepsilon$ and $v = 0$ successively in (2) and using the Poincaré inequality, we easily find that the velocity satisfies the a priori estimates below:

$$\|u_\varepsilon\|_{L^2(\Omega_\varepsilon)^n} \leq C$$
$$\varepsilon \|\nabla u_\varepsilon\|_{L^2(\Omega_\varepsilon)^{n\times n}} \leq C.$$

Let $v_\varepsilon \in \left(H_0^1(\Omega_\varepsilon)\right)^n$. Setting $v = v_\varepsilon + u_\varepsilon$ in (3) and using estimates on the velocity, we get the estimate for the pressure:

$$\|\nabla p_\varepsilon\|_{H^{-1}(\Omega_\varepsilon)^n} \leq C\varepsilon.$$

Then we extend the velocity u_ε by zero to $\Omega \setminus \Omega_\varepsilon$ and denote the extension by the same symbol and we have the following estimates:

$$\|u_\varepsilon\|_{L^2(\Omega)^n} \leq C$$
$$\varepsilon \|\nabla u_\varepsilon\|_{L^2(\Omega)^{n\times n}} \leq C.$$

Moreover $\operatorname{div} u_\varepsilon = 0$ in Ω.

For the pressure p_ε, we know (see [10]) that there exists an extension $\widetilde{p}_\varepsilon \in L^2_0(\Omega)$ such that

$$\|\widetilde{p}_\varepsilon\|_{L^2_0(\Omega)} \leq C$$
$$\|\nabla \widetilde{p}_\varepsilon\|_{H^{-1}(\Omega)^n} \leq C\varepsilon$$

and

$$\langle \nabla p_\varepsilon, v\rangle_{\Omega_\varepsilon} = -\left(\widetilde{p}_\varepsilon, \operatorname{div} v\right)_\Omega,$$

for every v that is the extension by zero to the whole Ω of a function in $H^1_0(\Omega_\varepsilon)^n$.

For an open set D, the brackets $\langle\cdot,\cdot\rangle_D$ denote the duality product between the spaces $H^{-1}(D)^n$ and $H^1_0(D)^n$, where $H^{-1}(D)^n$ denotes the dual of $H^1_0(D)^n$.

The extension $\widetilde{p}_\varepsilon$ can be defined as in [4] by

$$\widetilde{p}_\varepsilon = p_\varepsilon \text{ in the fluid part } \Omega_\varepsilon,$$
$$\widetilde{p}_\varepsilon(x) = \frac{1}{|Y_F|}\int_{Y_F} p_\varepsilon\left(\varepsilon\left[\frac{x}{\varepsilon}\right] + \varepsilon y\right) dy \text{ in the solid part } \Omega_{S,\varepsilon} \text{ of the porous media,}$$

where $\left[\frac{x}{\varepsilon}\right]$ is defined as below.

According to these extensions, problem (3) can be written as

$$2\mu\varepsilon^2 \int_\Omega \nabla u_\varepsilon \cdot \nabla (v - u_\varepsilon)\, dx + g\varepsilon \int_\Omega |\nabla v|\, dx - g\varepsilon \int_\Omega |\nabla u_\varepsilon|\, dx \tag{4}$$
$$\geq \int_\Omega f_\varepsilon (v - u_\varepsilon)\, dx + \int_\Omega \widetilde{p}_\varepsilon \operatorname{div}(v - u_\varepsilon)\, dx,$$

for every v that is the extension by zero to the whole Ω of a function in $H^1_0(\Omega_\varepsilon)^n$.

In order to pass to the limit as ε tends to zero in problem (4), we will use the unfolding method introduced in [5].

The idea of the unfolding method is to transform oscillating functions defined on the domain Ω into functions defined on the domain $\Omega \times Y$, in order to isolate the oscillations in the second variable. This transformation, together with a priori estimates, will allow us to use compactness results and then to get the limits of u_ε and p_ε when ε tends to zero.

We recall the results concerning the unfolding operator that we will use in the sequel.

We know that every real number a can be written as the sum between his integer part $[a]$ and his fractionary part $\{a\}$ which belongs to the interval $[0,1)$.

For $x=(x_1,\dots,x_n)\in\mathbb{R}^n$, we apply this result to every real number $\frac{x_i}{\varepsilon}$ for $i=1,\dots,n$ and we get

$$x=\varepsilon\left[\frac{x}{\varepsilon}\right]_Y+\varepsilon\left\{\frac{x}{\varepsilon}\right\}_Y,$$

where $\left[\frac{x}{\varepsilon}\right]_Y\in\mathbb{Z}^n$ and $\left\{\frac{x}{\varepsilon}\right\}_Y\in Y$.

Let $w\in L^2_{loc}(\mathbb{R}^n)$ and let us introduce the operator

$$\widetilde{T}_\varepsilon(w)(x,y)=w\left(\varepsilon\left[\frac{x}{\varepsilon}\right]_Y+\varepsilon y\right)\ \text{for } x\in\mathbb{R}^n \text{ and } y\in Y.$$

Then, for $w\in L^2(\Omega)$, denoting in the same way its extension by zero outside of Ω, the unfolding operator T_ε is defined by

$$T_\varepsilon(w)=\widetilde{T}_\varepsilon(w)|_{\Omega\times Y}.$$

According to [5], this operator has the following properties:

(p_1) T_ε is linear and continuous from $L^2(\Omega)$ to $L^2(\Omega\times Y)$.
(p_2) $T_\varepsilon(\varphi\phi)=T_\varepsilon(\varphi)T_\varepsilon(\phi)$, $\forall\varphi,\phi\in L^2(\Omega)$.
(p_3) If $\varphi\in L^2(\Omega)$, then $T_\varepsilon(\varphi)\to\varphi$ strongly in $L^2(\Omega\times Y)$.
(p_4) If $\varphi\in L^2(Y)$ is a Y-periodic function and $\varphi^\varepsilon(x)=\varphi\left(\frac{x}{\varepsilon}\right)$, $x\in\mathbb{R}^n$, then

$$T_\varepsilon(\varphi^\varepsilon_{|_\Omega})\to\varphi \text{ strongly in } L^2(\Omega\times Y).$$

(p_5) If $\varphi_\varepsilon\in L^2(\Omega)$ and $\varphi_\varepsilon\to\varphi$ strongly in $L^2(\Omega)$, then

$$T_\varepsilon(\varphi_\varepsilon)\to\varphi \text{ strongly in } L^2(\Omega\times Y).$$

Moreover, the following results hold (see Proposition 2.9(iii) in [5]):

Proposition 2.1. *Let $\{\varphi_\varepsilon\}_\varepsilon$ be a bounded sequence in $L^2(\Omega)$ such that*

$$T_\varepsilon(\varphi_\varepsilon)\to\widehat{\varphi}\ \textit{weakly in}\ L^2(\Omega\times Y).$$

Then

$$\varphi_\varepsilon\to\mathscr{M}_Y(\widehat{\varphi})\ \textit{weakly in}\ L^2(\Omega),$$

where the mean value operator $\mathscr{M}_Y(\widehat{\varphi})$ is defined by

$$\mathscr{M}_Y(\widehat{\varphi})=\frac{1}{|Y|}\int_Y\widehat{\varphi}(x,y)\,dy\ \textit{a.e. for}\ x\in\Omega.$$

Let us observe that for a function $\varphi \in H^1(\Omega)$, one has

$$\nabla_y(T_\varepsilon(\varphi)) = \varepsilon T_\varepsilon(\nabla\varphi) \quad \text{a.e. } (x,y) \in \Omega \times Y.$$

According to Corollary 3.2 in [5], we have

Proposition 2.2. *Let $\{\varphi_\varepsilon\}_\varepsilon$ be a sequence in $H^1(\Omega)$ bounded in $L^2(\Omega)$. Let us assume that*

$$\varepsilon \|\nabla\varphi_\varepsilon\|_{L^2(\Omega)^n} \leq C.$$

Then, there exists $\widehat{\varphi}$ in $L^2(\Omega; H^1(Y))$ such that, up to a subsequence still denoted by ε

$$T_\varepsilon(\varphi_\varepsilon) \to \widehat{\varphi} \text{ weakly in } L^2(\Omega; H^1(Y)),$$
$$\varepsilon T_\varepsilon(\nabla_x\varphi_\varepsilon) \to \nabla_y\widehat{\varphi} \text{ weakly in } (L^2(\Omega \times Y))^n,$$

where $y \mapsto \widehat{\varphi}(\cdot, y) \in L^2(\Omega; H^1_{per}(Y))$, $H^1_{per}(Y)$ being the Banach space of Y-periodic functions in $H^1_{loc}(\mathbb{R}^n)$ with the $H^1(Y)$ norm.

In what follows, in order to replace integrals over the domain Ω by integrals over the domain $\Omega \times Y$, we use the relation below proved in [7]:

$$\int_\Omega \varphi dx \sim \frac{1}{|Y|} \int_{\Omega \times Y} T_\varepsilon(\varphi)\, dxdy, \quad \forall \varphi \in L^1(\Omega), \tag{5}$$

which is true for ε sufficiently small. Indeed, it is true for every cell $\varepsilon\xi + \varepsilon Y, \xi \in Z$ strictly included in Ω that

$$\int_{\varepsilon\xi+\varepsilon Y} \varphi(x)dx = \varepsilon^n \int_Y \varphi(\varepsilon\xi + \varepsilon y)dy = \frac{1}{|Y|} \int_{(\varepsilon\xi+\varepsilon Y)\times Y} T_\varepsilon(\varphi)(x,y)dxdy.$$

By using this equality for every cell strictly included in Ω and by denoting $\widehat{\Omega}_\varepsilon$ the largest union of such $\varepsilon\xi + \varepsilon Y$ cells strictly included in Ω, the following exact formula is obtained:

$$\int_{\widehat{\Omega}_\varepsilon} \varphi(x)dx = \frac{1}{|Y|} \int_{\widehat{\Omega}_\varepsilon \times Y} T_\varepsilon(\varphi)(x,y)dxdy.$$

This implies

$$\left| \int_\Omega \varphi(x)dx - \frac{1}{|Y|} \int_{\Omega\times Y} T_\varepsilon(\varphi)(x,y)dxdy \right| \leq 2\|\varphi\|_{L^1(\Omega\setminus\widehat{\Omega}_\varepsilon)},$$

and so any integral on Ω of a function from $L^1(\Omega)$ is "almost equivalent" to the integral of its unfolded on $\Omega \times Y$.

3 Main Result

Now we can state the main result of this chapter in the following theorem:

Theorem 3.1. *Let u_ε and $\widetilde{p}_\varepsilon$ verify relation (4) given in previous section. Then there exist $\widehat{u} \in L^2\left(\Omega;(H^1_{per}(Y_F))^n\right)$ and $\widehat{p} \in L^2_0(\Omega) \cap H^1(\Omega)$ such that $u_\varepsilon \to \frac{1}{|Y|}\int_{Y_F} \widehat{u}(\cdot,y)\,dy$ weakly in $(L^2(\Omega))^n$, $\widetilde{p}_\varepsilon \to \widehat{p}$ strongly in $L^2_0(\Omega)$ and satisfy the limit problem*

$$2\mu \int_{Y_F} \nabla_y \widehat{u} \cdot \nabla_y (\psi - \widehat{u})\,dy + g\int_{Y_F} \left|\nabla_y(\psi)\right| dy - g\int_{Y_F} \left|\nabla_y \widehat{u}\right| dy$$
$$\geq \langle f - \nabla_x \widehat{p}, \psi - \widehat{u}\rangle_{Y_F} \tag{6}$$

for every $\psi \in (H^1_{per}(Y))^n$ such that $\psi = 0$ in $\overline{Y}_S$ and $\operatorname{div}_y \psi = 0$. The function $\widehat{u}$ satisfies the following conditions:

$$\widehat{u}(x,y) = 0 \text{ in } Y_S, \text{ a.e. in } \Omega, \tag{7}$$
$$\widehat{u}(x,y) = 0 \text{ on } \Gamma, \text{ a.e. in } \Omega, \tag{8}$$
$$\operatorname{div}_y \widehat{u}(x,y) = 0 \text{ in } Y_F, \text{ a.e. in } \Omega, \tag{9}$$
$$\operatorname{div}_x \int_{Y_F} \widehat{u}(x,y)dy = 0 \text{ in } \Omega, \tag{10}$$
$$\nu \cdot \int_{Y_F} \widehat{u}(x,y)dy = 0 \text{ on } \partial\Omega. \tag{11}$$

Proof. Taking into account the a priori estimates and using Propositions 2.1 and 2.2 we have the following convergences for the velocity and for the pressure:

$$\|u_\varepsilon\|_{L^2(\Omega)^n} \leq C \Rightarrow T_\varepsilon(u_\varepsilon) \to \widehat{u} \text{ weakly in } (L^2(\Omega \times Y))^n,$$
$$\varepsilon \|\nabla u_\varepsilon\|_{L^2(\Omega)^{n\times n}} \leq C \Rightarrow \varepsilon T_\varepsilon(\nabla u_\varepsilon) \to \nabla_y \widehat{u} \text{ weakly in } (L^2(\Omega \times Y))^{n\times n},$$
$$\widehat{u} \in L^2\left(\Omega;\left(H^1_{per}(Y)\right)^n\right),$$
$$u_\varepsilon \to \frac{1}{|Y|}\int_Y \widehat{u}(\cdot,y)\,dy \text{ weakly in } (L^2(\Omega))^n,$$

and according to [10], we have

$$\widetilde{p}_\varepsilon \to \widehat{p} \text{ strongly in } L^2_0(\Omega).$$

Using property p_5 of the unfolding method we get

$$T_\varepsilon(\widetilde{p}_\varepsilon) \to \widehat{p} \text{ strongly in } L^2_0(\Omega \times Y).$$

In order to prove relation (7) let us recall that

$$\lim_{\varepsilon\to 0} \int\limits_{\Omega\times Y} T_\varepsilon(u_\varepsilon)(x,y)T_\varepsilon(\Psi)(x,y)T_\varepsilon(\psi)(x,y)dxdy = \int\limits_{\Omega\times Y} \widehat{u}(x,y)\Psi(x)\psi(y)dxdy,$$

for all $\Psi \in \mathscr{D}(\Omega)$, the space of infinitely differentiable functions with compact support in Ω and for all $\psi \in (H^1_{per}(Y))^n$. By choosing a function $\psi(y)$ such that $\psi = 0$ in Y_F we deduce

$$\int\limits_{\Omega\times Y_S} \widehat{u}(x,y)\Psi(x)\psi(y)dxdy = 0,$$

which proves (7).

Relation (8) is a consequence of the fact that $u_\varepsilon = 0$ at the interface between the fluid and the solid part and of the definition and properties of the unfolding boundary operator. This operator was first defined in [3] and we refer to it for the proof.

In order to prove relation (9), let us observe that $\operatorname{div} u_\varepsilon = 0$ implies $\varepsilon T_\varepsilon (\operatorname{div} u_\varepsilon) = 0$. But

$$\varepsilon T_\varepsilon (\operatorname{div} u_\varepsilon) = \varepsilon T_\varepsilon \left(\sum_{i=1}^n \frac{\partial u_{\varepsilon,i}}{\partial x_i} \right) = \varepsilon T_\varepsilon \left(\sum_{i=1}^n \frac{1}{\varepsilon} \frac{\partial u_{\varepsilon,i}}{\partial y_i} \right) = \operatorname{div}_y T_\varepsilon (u_\varepsilon)$$

and so $\operatorname{div}_y T_\varepsilon (u_\varepsilon) = 0$.

We pass to the limit as ε tends to zero in this last equality and by using (7) we get $\operatorname{div}_y \widehat{u} = 0$ in Y_F, a.e. in Ω.

In order to prove relation (10), let us take $\Psi \in \mathscr{D}(\Omega)$.

We have

$$0 = \int_\Omega \operatorname{div} u_\varepsilon \Psi dx = \int_\Omega u_\varepsilon \nabla \Psi dx.$$

By applying the unfolding we get

$$0 = \int_\Omega \int_Y T_\varepsilon (u_\varepsilon) T_\varepsilon (\nabla \Psi) dxdy.$$

We pass to the limit as ε tends to zero and taking into account relation (7) we get

$$0 = \int_{\Omega}\int_{Y_F} \widehat{u}\nabla_x \Psi dxdy,$$

$$0 = \int_{\Omega} \mathrm{div}_x \left(\int_{Y_F} \widehat{u}(x,y)\, dy \right) \Psi dx, \quad \forall\, \Psi \in \mathscr{D}(\Omega),$$

which implies (10).

In order to prove relation (11), we use the following assertions:

$$\widehat{u}(x,y) = 0 \text{ in } Y_S, \text{ a.e. in } \Omega,$$

$$u_\varepsilon \to \frac{1}{|Y|}\int_{Y_F} \widehat{u}(x,y)\, dy \text{ weakly in } (L^2(\Omega))^n,$$

the linearity and continuity of the normal trace from the space

$$H(\mathrm{div},\Omega) = \left\{ \varphi \in \left(L^2(\Omega)\right)^n : \mathrm{div}\,\varphi \in L^2(\Omega) \right\}$$

into $H^{-1/2}(\partial\Omega)$.

By applying now the unfolding operator to the inequality (4), we get

$$\begin{aligned} &2\mu\varepsilon^2 \int_{\Omega\times Y_F} T_\varepsilon(\nabla u_\varepsilon)\cdot T_\varepsilon(\nabla(v-u_\varepsilon))\, dxdy \\ &+ g\varepsilon \int_{\Omega\times Y_F} T_\varepsilon(|\nabla v|)\, dxdy - g\varepsilon \int_{\Omega\times Y_F} T_\varepsilon(|\nabla u_\varepsilon|)\, dxdy \\ &\geq \int_{\Omega\times Y_F} T_\varepsilon(f_\varepsilon)\, T_\varepsilon(v-u_\varepsilon)\, dxdy + \int_{\Omega\times Y_F} T_\varepsilon(\widetilde{p}_\varepsilon)\, T_\varepsilon(\mathrm{div}\,(v-u_\varepsilon))\, dxdy. \end{aligned} \tag{12}$$

In order to pass to the limit in relation (12), we will consider a test function $v = v^\varepsilon$ of the form

$$v^\varepsilon(x) = \Psi(x)\,\psi\left(\frac{x}{\varepsilon}\right), \text{ with } \Psi \in D(\Omega) \text{ and } \psi \in V(Y_F), \tag{13}$$

where $V(Y_F) = \left\{ \varphi \in (H^1_{per}(Y))^n : \varphi = 0 \text{ on } \overline{Y}_S \text{ and } \mathrm{div}_y\,\varphi = 0 \right\}$.

We have

$$\nabla_x v^\varepsilon = \nabla_x\left(\Psi(x)\,\psi\left(\frac{x}{\varepsilon}\right)\right) = \nabla_x\Psi(x)\,\psi\left(\frac{x}{\varepsilon}\right) + \Psi(x)\,\nabla_x\psi\left(\frac{x}{\varepsilon}\right). \tag{14}$$

Let us remark that due to condition (7) and to the choice of the test function v^ε, we can write the integrals either on $\Omega \times Y$ or on $\Omega \times Y_F$.

By using this test function we get for the first term in relation (12):

$$
\begin{aligned}
&2\mu\varepsilon^2\int_{\Omega\times Y_F} T_\varepsilon\left(\nabla u_\varepsilon\right)\cdot T_\varepsilon\left(\nabla\left(v-u_\varepsilon\right)\right)dxdy\\
&=2\mu\varepsilon^2\int_{\Omega\times Y_F} T_\varepsilon\left(\nabla u_\varepsilon\right)\cdot T_\varepsilon\left(\nabla v\right)dxdy-2\mu\varepsilon^2\int_{\Omega\times Y_F} T_\varepsilon\left(\nabla u_\varepsilon\right)\cdot T_\varepsilon\left(\nabla u_\varepsilon\right)dxdy\\
&=2\mu\varepsilon^2\int_{\Omega\times Y_F} T_\varepsilon\left(\nabla u_\varepsilon\right)\cdot\left[T_\varepsilon\left(\nabla_x\Psi\right)T_\varepsilon\left(\psi\right)+\frac{1}{\varepsilon}T_\varepsilon\left(\Psi\right)T_\varepsilon\left(\nabla_y\psi\right)\right]dxdy\\
&\quad-2\mu\varepsilon^2\int_{\Omega\times Y_F} T_\varepsilon\left(\nabla u_\varepsilon\right)\cdot T_\varepsilon\left(\nabla u_\varepsilon\right)dxdy\\
&=2\mu\int_{\Omega\times Y_F}\varepsilon T_\varepsilon\left(\nabla u_\varepsilon\right)\cdot\varepsilon T_\varepsilon\left(\nabla_x\Psi\right)\psi dxdy+2\mu\int_{\Omega\times Y_F}\varepsilon T_\varepsilon\left(\nabla u_\varepsilon\right)\cdot T_\varepsilon\left(\Psi\right)\nabla_y\psi dxdy\\
&\quad-2\mu\int_{\Omega\times Y_F}\left|\varepsilon T_\varepsilon\left(\nabla u_\varepsilon\right)\right|^2dxdy.
\end{aligned}
$$

According to the general convergence results for the unfolding, we have that the first term tends to zero and the second one to the following limit:

$$
2\mu\int_{\Omega\times Y_F}\nabla_y\widehat{u}\cdot\Psi\nabla_y\psi\left(y\right)dxdy.
$$

By using now the fact that the function $B(\varphi)=|\varphi|^2$ is proper convex continuous, we have for the third term

$$
\liminf_{\varepsilon\to 0}2\mu\int\limits_{\Omega\times Y_F}|\varepsilon T_\varepsilon(\nabla u_\varepsilon)|^2dxdy\geq 2\mu\int\limits_{\Omega\times Y_F}|\nabla_y\widehat{u}|^2dxdy.
$$

In order to pass to the limit in the nonlinear terms, let us first remark that for a function v in $\left(H^1(\Omega)\right)^n$, we have

$$
\begin{aligned}
\left[T_\varepsilon(|\nabla v|)\right]^2&=T_\varepsilon(|\nabla v|)T_\varepsilon(|\nabla v|)=T_\varepsilon(|\nabla v|^2)=T_\varepsilon\Big(\sum_{i,j=1}^n\Big(\frac{\partial v_i}{\partial x_j}\Big)^2\Big)=\\
&=\sum_{i,j=1}^n\Big(T_\varepsilon\Big(\frac{\partial v_i}{\partial x_j}\Big)\Big)^2=\sum_{i,j=1}^n\Big(\frac{1}{\varepsilon}\frac{\partial}{\partial y_j}T_\varepsilon(v_i)\Big)^2=\frac{1}{\varepsilon^2}|\nabla_y T_\varepsilon(v)|^2,
\end{aligned}
$$

and we deduce

$$
\varepsilon T_\varepsilon(|\nabla v|)=|\nabla_y T_\varepsilon(v)|. \tag{15}
$$

In order to pass to the limit in the first nonlinear term, by using the previous identity for the function v^ε given by (13), we have

$$
\begin{aligned}
&\left| g\varepsilon \int_{\Omega\times Y_F} T_\varepsilon\left(|\nabla v_\varepsilon|\right) dxdy - g\int_{\Omega\times Y_F} \left|\nabla_y\left(\Psi\psi\right)\right| dxdy \right| \\
&= \left| g\int_{\Omega\times Y_F} \left|\nabla_y T_\varepsilon\left(v_\varepsilon\right)\right| dxdy - g\int_{\Omega\times Y_F} \left|\nabla_y\left(\Psi\psi\right)\right| dxdy \right| \\
&\leq g\int_{\Omega\times Y_F} \left|\nabla_y T_\varepsilon\left(v_\varepsilon\right) - \nabla_y\left(\Psi\psi\right)\right| dxdy = \\
&= g\int_{\Omega\times Y_F} \left|\varepsilon T_\varepsilon\left(\nabla_x\Psi\right)(x,y)\cdot\psi(y) + T_\varepsilon\left(\Psi\right)(x,y)\nabla_y\psi(y) - \Psi(x)\nabla_y\psi(y)\right| dxdy \\
&\leq g\int_{\Omega\times Y_F} \left|T_\varepsilon\left(\varepsilon\nabla_x\Psi\right)(x,y)\cdot\psi(y)\right| dxdy \\
&\qquad + \int_{\Omega\times Y_F} \left|\left(T_\varepsilon\left(\Psi\right)(x,y) - \Psi(x)\right)\nabla_y\psi(y)\right| dxdy \\
&\leq g\left\|T_\varepsilon\left(\varepsilon\nabla_x\Psi\right)\right\|_{\left(L^2(\Omega\times Y_F)\right)^n} \left\|\psi\right\|_{\left(L^2(\Omega\times Y_F)\right)^n} + \\
&\qquad\qquad + \left\|T_\varepsilon\left(\Psi\right) - \Psi\right\|_{L^2(\Omega\times Y_F)} \left\|\nabla_y\left(\psi\right)\right\|_{\left(L^2(\Omega\times Y_F)\right)^{n\times n}}.
\end{aligned}
$$

Passing to the limit as $\varepsilon\to 0$, by property p_5, we have that $T_\varepsilon\left(\varepsilon\frac{\partial\Psi}{\partial x_i}\right)\to 0$ strongly in $L^2\left(\Omega\times Y_F\right)$ and so

$$\left\|T_\varepsilon\left(\varepsilon\nabla_x\Psi\right)\right\|_{\left(L^2(\Omega\times Y_F)\right)^n}\to 0.$$

Moreover, by property p_3, $T_\varepsilon(\Psi)\to\Psi$ strongly in $L^2\left(\Omega\times Y_F\right)$ and so

$$\left\|T_\varepsilon\left(\Psi\right) - \Psi\right\|_{L^2(\Omega\times Y_F)}\to 0.$$

Then

$$\lim_{\varepsilon\to 0} g\varepsilon\int_{\Omega\times Y_F} T_\varepsilon\left(|\nabla v_\varepsilon|\right) dxdy = g\int_{\Omega\times Y_F}\left|\nabla_y\left(\Psi\psi\right)\right| dxdy.$$

In order to pass to the limit in the second nonlinear term, we use identity (15) for the function u_ε and the fact that the function $E(\varphi)=|\varphi|$ is proper convex continuous. We then deduce

$$\liminf_{\varepsilon\to 0} g\varepsilon\int_{\Omega\times Y_F} T_\varepsilon\left(|\nabla u_\varepsilon|\right) dxdy \geq g\int_{\Omega\times Y_F}\left|\nabla_y\widehat{u}\right| dxdy.$$

Moreover,

$$\int_{\Omega\times Y_F} T_\varepsilon\left(f_\varepsilon\right) T_\varepsilon\left(v\right) dxdy - \int_{\Omega\times Y_F} T_\varepsilon\left(f_\varepsilon\right) T_\varepsilon\left(u_\varepsilon\right) dxdy \to \int_{\Omega\times Y_F} f\Psi\psi dxdy - \int_{\Omega\times Y_F} f\widehat{u} dxdy.$$

We consider now the term $\int_{\Omega\times Y_F} T_\varepsilon\left(\widetilde{p}_\varepsilon\right) T_\varepsilon\left(\operatorname{div}\left(v-u_\varepsilon\right)\right) dxdy$. Using $\operatorname{div}_x u_\varepsilon = 0$, we obtain

$$\begin{aligned}
&\int_{\Omega\times Y_F} T_\varepsilon\left(\widetilde{p}_\varepsilon\right) T_\varepsilon\left(\operatorname{div}_x\left(v-u_\varepsilon\right)\right) dxdy = \int_{\Omega\times Y_F} T_\varepsilon\left(\widetilde{p}_\varepsilon\right) T_\varepsilon\left(\operatorname{div}_x v\right) dxdy \\
&= \int_{\Omega\times Y_F} T_\varepsilon\left(\widetilde{p}_\varepsilon\right) T_\varepsilon\left(\operatorname{div}_x\left(\Psi(x)\,\psi\left(\frac{x}{\varepsilon}\right)\right)\right) dxdy \\
&= \int_{\Omega\times Y_F} T_\varepsilon\left(\widetilde{p}_\varepsilon\right) T_\varepsilon\left(\nabla_x\Psi(x)\,\psi\left(\frac{x}{\varepsilon}\right) + \Psi(x)\operatorname{div}_x\psi\left(\frac{x}{\varepsilon}\right)\right) dxdy \\
&= \int_{\Omega\times Y_F} T_\varepsilon\left(\widetilde{p}_\varepsilon\right) T_\varepsilon\left(\nabla_x\Psi\right)\psi dxdy.
\end{aligned}$$

Passing to the limit as ε tends to zero and using (10) the last term tends to

$$\begin{aligned}
\int_{\Omega\times Y_F} \widehat{p}\nabla_x\Psi(x)\,\psi(y)\,dxdy &= \int_{\Omega\times Y_F} \widehat{p}\nabla_x\Psi(x)\,\psi(y)\,dxdy \\
&\quad - \int_\Omega \widehat{p}\left(\operatorname{div}_x\int_{Y_F}\widehat{u}dy\right)dx \\
&= -\left\langle \nabla_x\widehat{p}, \int_{Y_F}\left(\Psi(x)\,\psi(y)-\widehat{u}\right)dy\right\rangle_\Omega.
\end{aligned}$$

Finally we obtain

$$\begin{aligned}
&2\mu\int_{\Omega\times Y_F}\nabla_y\widehat{u}\cdot\nabla_y\left(\Psi\psi-\widehat{u}\right)dxdy + g\int_{\Omega\times Y_F}\left|\nabla_y\left(\Psi\psi\right)\right|dxdy - g\int_{\Omega\times Y_F}\left|\nabla_y\widehat{u}\right|dxdy \\
&\geq \left\langle f-\nabla_x\widehat{p}, \int_{Y_F}\left(\Psi(x)\,\psi(y)-\widehat{u}\right)dy\right\rangle_\Omega,\ \forall\Psi\in\mathscr{D}(\Omega),\ \psi\in V(Y_F),
\end{aligned}$$

relation which by density is always true for a test function $\widehat{v}\in L^2(\Omega, V(Y_F))$.

Then we easily find that the function $\widehat{u}$ is the unique solution of the problem

$$\begin{aligned}
&2\mu\int_{\Omega\times Y_F}\nabla_y\widehat{u}\cdot\nabla_y\left(\widehat{v}-\widehat{u}\right)dxdy + g\int_{\Omega\times Y_F}\left|\nabla_y\left(\widehat{v}\right)\right|dxdy - g\int_{\Omega\times Y_F}\left|\nabla_y\widehat{u}\right|dxdy \\
&\geq \int_{\Omega\times Y_F} f\left(\widehat{v}-\widehat{u}\right)dxdy,
\end{aligned}$$

for every $\widehat{v} \in L^2(\Omega, V(Y_F))$ such that $div_x \int_{Y_F} \widehat{v}(x,y)dy = 0$ and $\nu \cdot \int_{Y_F} \widehat{v}(x,y)dy = 0$ on $\partial\Omega$.

The pressure $\widehat{p} \in H^1(\Omega)$, nonunique, and relation (6) are recovered as in [8]. □

4 Conclusion

We gave in this chapter the proof of the homogenization of the Bingham flow in porous media, by using the unfolding method, an alternative method to the two-scale convergence method, which was already used in [2] in order to solve the same problem. Our aim is to continue to work on the homogenization of the Bingham flow with different boundary conditions than the one treated in this chapter and for which we expect that the unfolding method will fit better than the two-scale convergence method.

Acknowledgments The authors would like to thank the referee for the valuable remarks and suggestions.

References

1. Allaire, G.: Homogenization of the unsteady Stokes equations in porous media. In: Bandle, C., Bemelmans, J., Chipot, M., Grüter, M., Saint Jean Paulin, J. (eds.) Progress in Partial Differential Equations: Calculus of Variations, Applications, pp. 109–123. Longman Scientific & Technical, New York (1992)
2. Bourgeat, A., Mikelic, A.: A note on homogenization of Bingham flow through a porous medium. J. Math. Pures Appl. **72**, 405–414 (1993)
3. Cioranescu, D., Damlamian, A., Donato, P., Griso, G., Zaki, R.: The periodic unfolding method in domains with holes. hal.archives-ouvertes.fr/docs/00/59/16/32/PDF/TrousDV2010-12-11.pdf
4. Cioranescu, D., Damlamian, A., Griso, G.: The Stokes problem in perforated domains by the periodic unfolding method. In: Mihailescu-Suliciu, M. (ed.) New Trends in Continuum Mechanics, pp. 67–80. Theta Foundation, Romania (2003)
5. Cioranescu, D., Damlamian, A., Griso, G.: The periodic unfolding method in homogenization. SIAM J. Math. Anal. **40**, 1585–1620 (2008)
6. Duvaut, G., Lions, J.L.: Les Inéquations en Mécanique et en Physique. Dunod, Paris (1972)
7. Griso, G.: Habilitation à Diriger les Recherches. Université de Lille I, Lille (2005)
8. Lions, J.L., Sanchez-Palencia, E.: Ecoulement d'un fluide viscoplastique de Bingham dans un milieu poreux. J. Math. Pures Appl. **60**, 341–360 (1981)
9. Nguetseng, G.: A general convergence result for a functional related to the theory of homogenization. SIAM J. Math. Anal. **20**, 608–623 (1989)
10. Tartar, L.: Convergence of the homogenization process. In: Sanchez-Palencia, E. (ed.) Non-homogeneous Media and Vibration Theory. Lecture Notes in Physics, vol. 127. Springer, Heidelberg (1980)

An Integrated Capillary, Buoyancy, and Viscous-Driven Model for Brine/CO_2 Relative Permeability in a Compositional and Parallel Reservoir Simulator

X. Kong, M. Delshad, and M.F. Wheeler

Abstract The effectiveness of CO_2 storage in the saline aquifers is governed by the interplay of capillary, viscous, and buoyancy forces. Recent experimental study reveals the impact of pressure, temperature, and salinity on interfacial tension (IFT) between CO_2 and brine. The dependence of CO_2-brine relative permeability and capillary pressure on pressure (IFT) is also clearly evident in published experimental results. Improved understanding of the mechanisms that control the migration and trapping of CO_2 in subsurface is crucial to design future storage projects that warrant long-term and safe containment. Simulation studies ignoring the buoyancy and also variation in interfacial tension and the effect on the petrophysical properties such as trapped CO_2 saturations, relative permeability, and capillary pressure have a poor chance of making accurate predictions of CO_2 injectivity and plume migration. We have developed and implemented a general relative permeability model that combines effects of pressure gradient, buoyancy, and IFT in an equation of state (EOS) compositional and parallel simulator. The significance of IFT variations on CO_2 migration and trapping is assessed.

1 Introduction

Saline aquifers can provide vast and safe storage for carbon dioxide pending a proper understanding of the displacement mechanisms of CO_2-brine binary system at in situ conditions [3]. These aquifers are widely distributed, have reasonable

X. Kong (✉) • M. Delshad
Petroleum and Geosystems Engineering Department, The University of Texas at Austin, TX, USA
e-mail: xhkong@utexas.edu; delshad@mail.utexas.edu

M.F. Wheeler
Center for Subsurface Modeling, The University of Texas at Austin, TX, USA
e-mail: mfw@ices.utexas.edu

J.A. Ferreira et al. (eds.), *Modelling and Simulation in Fluid Dynamics in Porous Media*, Springer Proceedings in Mathematics & Statistics 28, DOI 10.1007/978-1-4614-5055-9_8,

permeability and porosity values, and have good thickness with large storage capacity [16, 20, 28]. Geological carbon sequestration involves injecting the produced CO_2 into subsurface formations and trapping it through many geological and chemical mechanisms. CO_2 injection in subsurface invokes multiphase flow, fluid phase behavior, relative permeability, wettability, gravity and buoyancy, capillary pressure, and geochemical reactions. Several research groups have studied the interplay of the capillary, gravity, viscous forces, and other factors that may affect the trapping [4, 19, 30]. Much experimental research is focusing on interfacial tension of oil, water, and gas phases [32]. Many achievements have been made to understand the subsurface interaction between CO_2 and formation brine [2, 17, 22]. Based on these findings, the injected CO_2 in saline aquifers could be characterized in the following forms: dissolved in formation brine, trapped by capillary forces in the pore space as residual saturation, adsorbed on minerals by chemical trapping, and free phase that is mobile. However, because the chemical trapping is significant for CO_2 sequestration only in geological time scale, it is sometimes neglected for short-time behavior studies.

The injectivity of CO_2 into an aquifer is greatly affected by the relative permeability and interplay of capillary, gravity, and viscous forces. During injection into the aquifers, CO_2 displaces formation water at the leading edge of the plume as a drainage process. On the other hand during post injection, the formation brine displaces CO_2 at the trailing end as in an imbibition direction. Several hysteresis models have been developed to capture the saturation history-dependent relative permeability and capillary pressure relationships [14]. Experimental results show the change in both drainage and imbibition capillary pressure and relative permeability as the results of variations in pressure, salinity, and temperature [5]. In many simulation studies, relative permeability curves are, however, defined at the beginning of the simulation study and only the variations due to saturation are modeled and the changes of pressure, salinity, and temperature are typically ignored. With the exception of the simulators with hysteretic models, the residual CO_2 saturation in many simulators is also fixed for a given rock type. However, the residual saturation is affected by the interfacial tension between CO_2 and water and many experimental results reveal that IFT between CO_2 and brine varies at different pressure, salinity, and temperature conditions [1, 6, 18, 26]. These results show that the IFT decreases with increasing pressure and increases with increasing temperature and salinity. The results also show that the relative permeability curves are also greatly affected by the same variables.

In this chapter, we used an integrated parallel accurate reservoir simulator (IPARS) to model the fate and transport of CO_2 in saline aquifers. IPARS is an advanced computer framework that serves as a test bed for multiphase compositional flow models, advanced discretizations, efficient solvers, and upscaling techniques among others. The simulator is capable of modeling domains with millions of grids using multiple processors with an impressive parallel scalability. Numerical models with compositional phase behavior and composition-dependent relative permeability and capillary pressure are required for a better understanding and more accurate predictions of CO_2 flow and transport in saline aquifers. It would be very

difficult to model all of these interacting effects analytically since heterogeneity, pressure, phase behavior, interfacial tension, and relative permeability are all coupled in a complex and nonlinear way. Here we discuss:

1. The improvement in CO_2 solubility and brine density calculations as a function of salinity.
2. IFT calculations using several correlations.
3. Implementation of trapping number and the change in relative permeability and capillary pressure relations.
4. Large scale simulation of CO_2 injection scenarios.

2 Mathematical Formulations

The CO_2 module of IPARS-v3 is non-isothermal compositional EOS coupled with geochemical reactions [13, 33]. An iteratively coupled implicit-pressures, explicit-concentrations is applied to solve the flow and concentration equations, which is then sequentially coupled to a time-split method for solving the temperature energy balance and explicit ODE numerical integration method for chemical reactions. The Peng–Robinson cubic equation of state (PR-EOS) is used for phase behavior of binary system of CO_2 and water as a function of pressure and temperature followed by a flash algorithm to determine the mole fractions of CO_2 and water in two equilibrium phases. In this chapter, we discuss the improvements made to IPARS-v3 for fluid property calculations. We first added a new component to the water to model the brine salinity expressed as total dissolved solids (TDS). The EOS variables of binary interaction coefficients and volume shift parameters (VSPs) were then modified according to the salt concentration and temperature using published correlations [21,22]. These correlations proved to give more accurate CO_2 solubility in brine and brine density. Several correlations for interfacial tension between water and supercritical CO_2 were then implemented that account for pressure, temperature, and brine salinity. Once the interfacial tension is calculated, the next step is to calculate a dimensionless trapping number. The residual saturations of CO_2 and water are then calculated based on the trapping number, while the endpoints are shifted as well with the shifting of the residual saturations. Relative permeability and capillary pressure curves are subsequently adjusted as a function of trapping number because of the shifting of the residual phase saturations.

2.1 Effect of Salt on EOS Parameters

The binary interaction coefficient of EOS was first modified to model the solubility of CO_2 in brine as a function of temperature (T) and salinity (S) using the following empirical correlation [21]:

$$BIC_{H_2O-CO_2} = -0.093625 + 4.861 \times 10^{-4} \times (T - 113) + 2.29 \times 10^{-7} \times S. \quad (1)$$

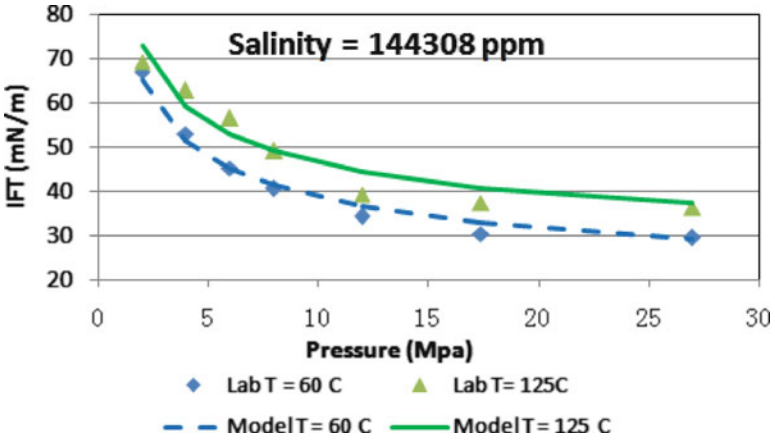

Fig. 1 Interfacial tension vs. pressure at two different temperatures (data from Bennion and Bachu [6])

A constant input VSP for CO_2 is used. However, to correct for the effect of CO_2 dissolution on brine density, the VSP for water is calculated using the following empirical correlation [21]:

$$VSP_{H_2O} = 0.179 + 2.2222 \times 10^{-4} \times (T - 113) + 4.9867 \times 10^{-7} S. \quad (2)$$

2.2 *Interfacial Tension*

There are several published models for calculating gas/liquid interfacial tension such as those proposed by Macleod–Sugden [27, 31], Bennion and Bachu [6], and Chalbaud [10], among others. We have implemented all existing correlations for comparison purposes but discuss only the one based on the work of Bennion and Bachu [6]. Bennion and Bachu [6] measured the IFT between supercritical CO_2 and brine and developed empirical correlations for IFT as a function of salinity, temperature, and pressure and IFT as a function of CO_2 solubility in water. We implemented both models but present only the one vs. P, T, and S. The correlation in Eq. 3 matched the measured IFT for a wide range of temperature (41 to 125°C), pressure (2,000–27,000 kPa), and salinity (fresh water to 34% TDS):

$$\sigma = 71.69243\, P^{-0.432629} + 0.210558\, T^{0.900261} + 0.075859\, S^{1.457937}, \quad (3)$$

where σ is the interfacial tension in mN/m, T is temperature in °C, P is pressure in Mpa, and S is salinity in wt %.

Figures 1 and 2 give comparison of some of the measured data with the correlation for different pressures, temperatures, and salinities. The results indicate

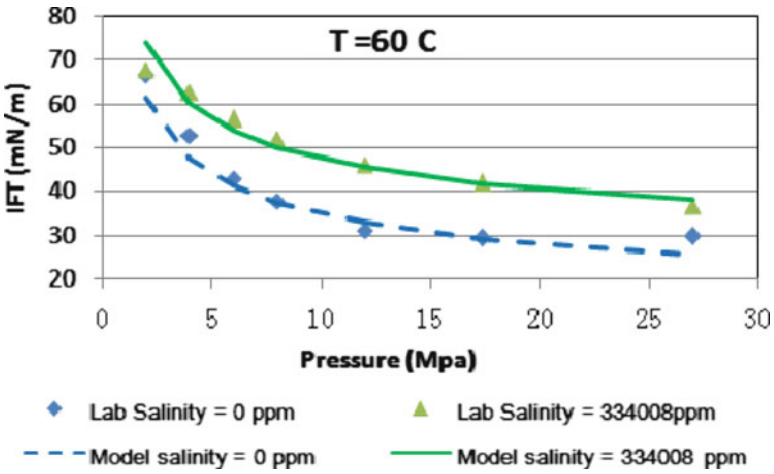

Fig. 2 Interfacial tension vs. pressure at different salinities (data from Bennion and Bachu [6])

threefold reduction in IFT with either increase in pressure or temperature or decrease in salinity.

2.3 Trapped Saturation and Trapping Number

Research shows that the trapped phase saturations should be a function of the ratio of viscous to capillary forces and defined a capillary number to capture this ratio [7]. Many variations of the definition have been published including the most recent one by Pope [29]. They generalized the capillary number by including the effect of gravity referred to as trapping number (N_T). The trapping number for water displaced by gas phase is defined as follows:

$$N_T = \frac{\left| \overrightarrow{\overrightarrow{K}} \cdot [\nabla \Phi + g\,(\rho_g - \rho_w)\,\nabla D] \right|}{\sigma} \tag{4}$$

where $\overrightarrow{\overrightarrow{K}}$ is the permeability tensor, $\nabla\Phi$ is the potential gradient, ρ is density, and D is the depth.

The trapped saturation is modeled as a function of trapping number as shown below:

$$S_{lr} = \min\left(S_l, S_{lr}^{high} + \frac{S_{lr}^{low} - S_{lr}^{high}}{1 + T_l (N_{Tl})^{\tau_l}} \right), \tag{5}$$

where trapping model parameters T_l and τ_l are obtained by fitting the trapped saturation data for phase l. Subscript l stands for either CO_2 (g) or water phase (w), and

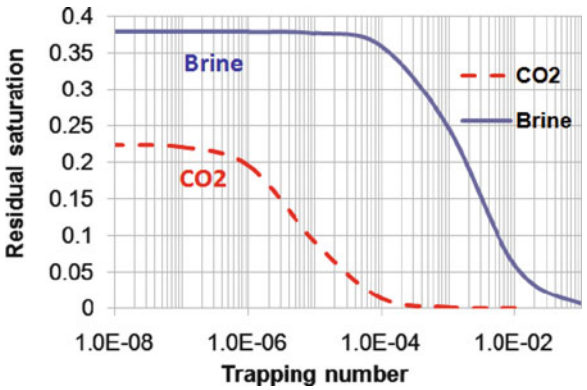

Fig. 3 Residual saturation vs. trapping number

S_{lr}^{high} and S_{lr}^{low} correspond to the trapped saturation at high and low trapping numbers. Figure 3 shows an example calculation for residual saturations vs. trapping number.

2.4 Relative Permeability

The next step for model improvement is to correlate the endpoint relative permeability of each phase, which increases in a very predictable way as trapping number increases (or interfacial tension decreases). The following is the correlation used to shift the endpoint relative permeability (K_r^0) for water (w) and CO_2 (g) as a function of residual saturation of the conjugate phase:

$$K_{rg}^{0} = K_{rg}^{0low} + \frac{S_{wr}^{low} - S_{wr}}{S_{wr}^{low} - S_{wr}^{high}} \left(K_{rg}^{0high} - K_{rg}^{0low} \right) \tag{6}$$

$$K_{rw}^{0} = K_{rw}^{0low} + \frac{S_{gr}^{low} - S_{gr}}{S_{gr}^{low} - S_{gr}^{high}} \left(K_{rw}^{0high} - K_{rw}^{0low} \right). \tag{7}$$

The exponent of relative permeability curves λ is also modified to reflect the change on the relative permeability curve

$$\lambda_g = \lambda_g^{low} + \frac{S_{wr}^{low} - S_{wr}}{S_{wr}^{low} - S_{wr}^{high}} \left(\lambda_g^{low} - \lambda_g^{high} \right) \tag{8}$$

$$\lambda_w = \lambda_w^{low} + \frac{S_{gr}^{low} - S_{gr}}{S_{gr}^{low} - S_{gr}^{high}} \left(\lambda_w^{low} - \lambda_w^{high} \right). \tag{9}$$

Figures 4 and 5 present example calculations for relative permeability endpoints and exponents as a function of trapping number.

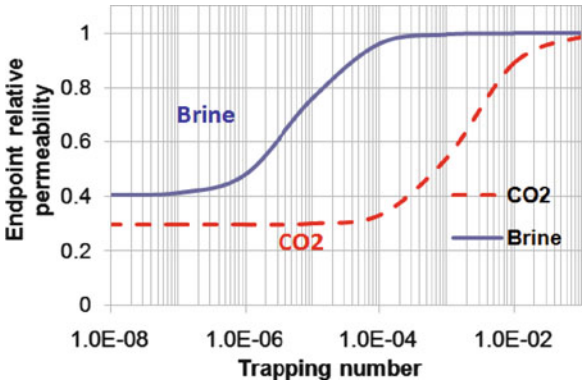

Fig. 4 Endpoint relative permeability vs. trapping number

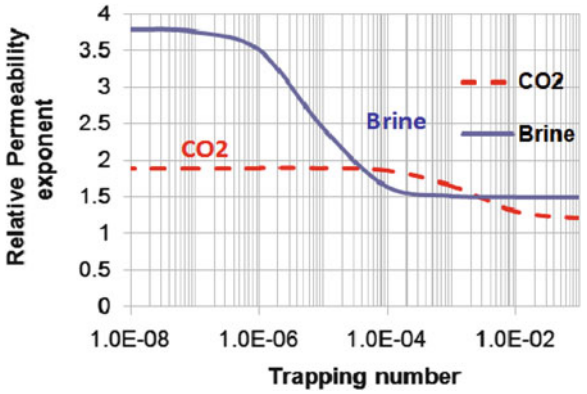

Fig. 5 Relative permeability exponent vs. trapping number

The next step is to calculate the relative permeability of each phase as a function of saturation. We assumed a [8] Corey-type relative permeability function where endpoint, exponent, and residual saturations are functions of trapping number as described in Eq. 10 . Example calculation results of CO_2-brine relative permeability at low and high trapping numbers are given in Figs. 6 and 7:

$$k_{rl} = k_{rl}^{0} \left(\overline{S_l}\right)^{\lambda_l} \tag{10}$$

where $\overline{S_l} = \frac{S_l - S_{lr}}{1 - S_{wr} - S_{gr}}$ is the normalized saturation.

2.5 Capillary Pressure

A Corey-type capillary pressure function was implemented. The effect of interfacial tension was accounted for by scaling the capillary pressure based on

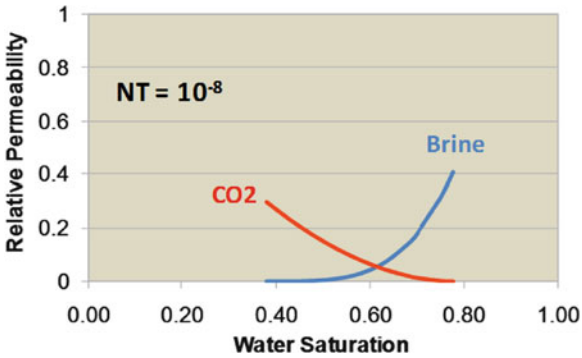

Fig. 6 Relative permeability at low trapping number of 10^{-8}

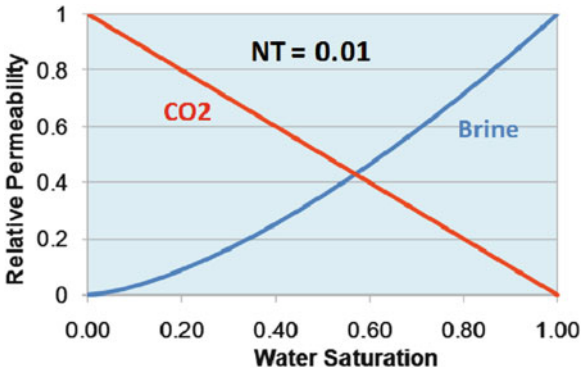

Fig. 7 Relative permeability at high trapping number of 0.01

Leverrett J-function such that the capillary pressure decreases as the interfacial tension decreases:

$$J(S_w) = \frac{P_c}{\sigma cos\theta}\left(\frac{K}{\phi}\right)^{0.5}. \tag{11}$$

Capillary pressure is then scaled based on the reference curve as

$$P_c = P_{c,ref}\frac{\sigma}{\sigma_{ref}}\left(\frac{K}{\phi}\right)^{0.5}_{ref}\left(\frac{\phi}{K}\right)^{0.5} \tag{12}$$

in which subscript *ref* stands for the measured properties of the reference rock.

3 Comparison with Experimental Data

We first compared the new trapping model with three relative permeability data sets provided by Bennion and Bachu [5]. Measured relative permeability curves are presented in Fig. 8.

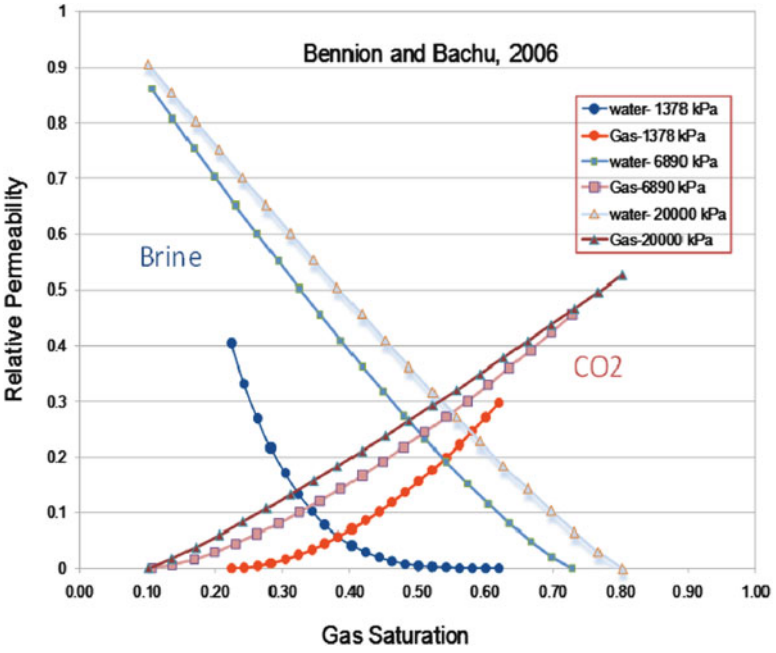

Fig. 8 Relative permeability curves at different pressure (data from Bennion and Bachu [5])

Table 1 Core data for the relative permeability experiments (Bennion and Bachu [5])

Core sample	Sandstone
Sample depth, m	1,626
Overburden pressure, kPa	11,000
In situ temperature, °C	43
In situ salinity, ppm	27,096
Core length, cm	3.73
Core diameter, cm	3.77
Cross-sectional area, cm^2	11.16
Injection rate, cm^3/h	10
Porosity	15.3%

The relative permeability curves were measured for a sample of sandstone rock at a temperature of 43°C and in situ salinity of 27,096 ppm. The core length was 3.73 cm with a diameter of 3.77 cm (Table 1). The three test cases outlined below correspond to different trapping numbers for the CO_2-brine system:

1. IFT = 56.2 mN/m, P = 1,378 kPa (200 psig), corresponding to low trapping number.
2. IFT = 33.2 mN/m, P = 6,890 kPa (1,000 psig), corresponding to medium-range trapping number.
3. IFT = 19.8 mN/m, P = 20,000 kPa (2,900 psig), corresponding to high trapping number.

Table 2 Relative permeability model parameters using Bennion and Bachu's data [5]

P (kPa)	IFT (mN/m)	S_{gr}	S_{wr}	k^0_{rg}	k^0_{rw}	λ_g	λ_w
1,378	56.2	0.225	0.379	0.298	0.405	1.9	3.8
6,890	33.2	0.107	0.271	0.456	0.861	1.5	1.3
20,000	19.8	0.102	0.197	0.527	0.905	1.1	1.1

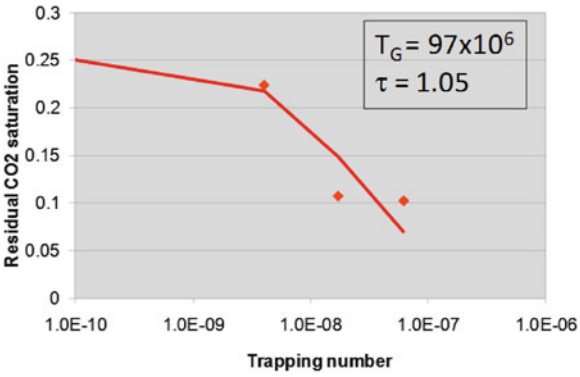

Fig. 9 Comparison of measured and calculated residual CO_2 saturation vs. trapping number

Examination of experimental results in Fig. 8 indicates the trend that endpoint relative permeability to CO_2 increases and relative permeability curvature reduces as IFT decreases (due to the pressure increase). The trends in experiments are consistent with the model predictions shown in Figs. 4 and 5. We used Eq. 10 to model the different relative permeability curves at different pressures. The relative permeability model parameters for these cases are given in Table 2.

To obtain the CO_2 trapping model parameters (T_2 and τ_2), we calculated the trapping number corresponding to each measured residual CO_2 saturation. The fit of data to Eq. 5 is shown in Fig. 9, which shows a reasonable match.

4 Simulation Cases

Three test cases were used to study the new trapping model and the impact on CO_2 sequestration.

Case 1. First test case is to show the parallel scalability of the IPARS simulator. We used over one million ($160\times160\times40$) grids with highly heterogeneous aquifer permeability (Fig. 10). There are four injection wells in the center of the model with constant CO_2 injection rate of 300 MSCF/D for 20 years. More details for this case are given in Table 3. The problem was run on 36, 48, and 72 processors. CPU time is shown in Table 4 and Fig. 11 with a very good parallel scalability.

Case 2. Second simulation case is to study the effect of IFT on flow and transport of CO_2. Four injectors are positioned in the center of the aquifer with a constant

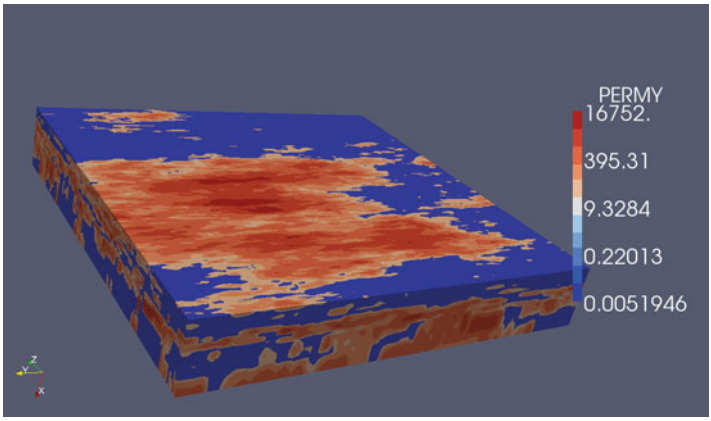

Fig. 10 Permeability distribution for one million grid Case 1

Table 3 Reservoir and fluid data for simulation Case 1

Aquifer size, L, W, H	32,500 ft × 32,500 ft × 500 ft
Mesh	3D with 10,240,000 cells (160× 160 × 40)
Dip angle	0
Depth (top corner)	5,000 ft
Aquifer temperature	100 C (212 F)
Initial aquifer pressure	2,500 psi
Horizontal permeability	SPE10 benchmark
K_v/K_h	0.1
Porosity	0.30
Vertical well completion length	256 ft
Initial water saturation	1.0
Residual water saturation, S_{ar}	0.379
Residual CO_2 saturation, S_{gr}	0.225
Injection rate	300 MSCF/D
Injection period	20 years

Table 4 CPU time using different number of processors

Number of processors	Run time (s)	Run time (h)	Total CPU (h)
36	55,519.78	15.42	555.12
48	46,259.06	12.85	616.8
72	30,844.94	8.57	617.04

injection pressure of 2900 psi and continuous injection for 3 years followed by 7 years of no injection. The boundary conditions of the model are constant pressure of 2500 psi. The reservoir has a 10 degree dip. The model parameters are in Table 5.

The permeability data is from SPE10 case [11]. Figure 12 shows the permeability distribution. Porosity is constant and the ratio of vertical permeability to horizontal permeability is 0.1.

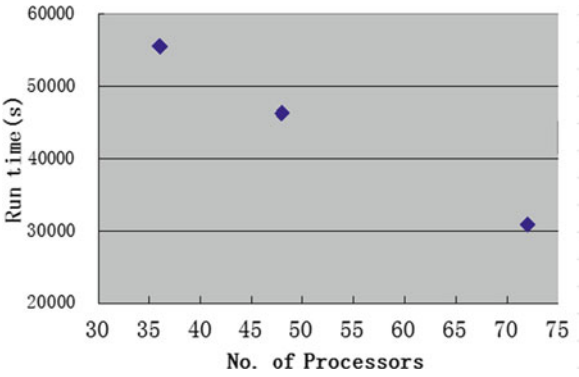

Fig. 11 Run times of IPARS for one million grid simulation with different number of processors

Table 5 Reservoir and fluid data for simulation Case 2

Aquifer size, e, W, H	32,500 ft × 32,500 ft × 500 ft
Mesh	120 × 220 × 40
Dip	10°
Depth (top corner)	5,000 ft
Surface temperature	10°C
Aquifer temperature	71°C (160°F)
Initial pressure	2500 psi
Horizontal permeability	Based on SPE10 benchmark
K_a/K_h ratio	0.1
Porosity	0.30
Vertical well length	256 ft
Initial water saturation	1.0
Residual water saturation, S_{wr}	0.379
Residual CO_2 saturation, S_{gr}	0.225
Injection pressure	2900 psi
Injection period	3 years injection, 7 years shut-in

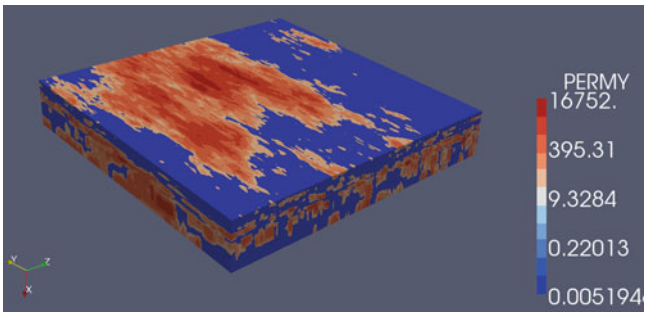

Fig. 12 Permeability distribution for Case 2

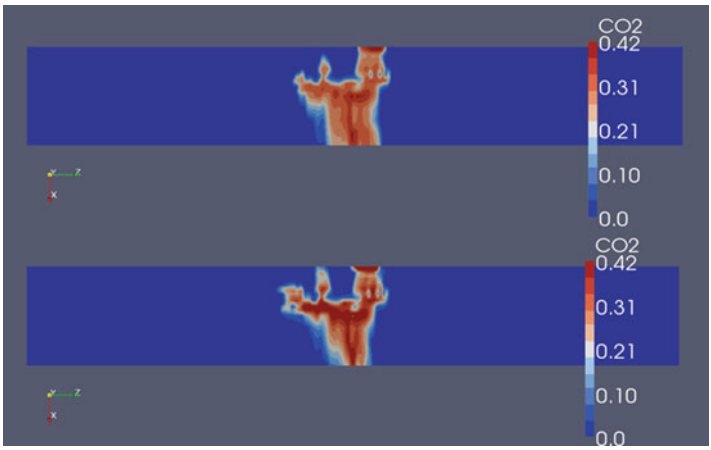

Fig. 13 CO_2 saturation for a vertical cross section through the injection well at the end of injection for Case 2: (*Top*) with no IFT effect; (*bottom*) with IFT effect

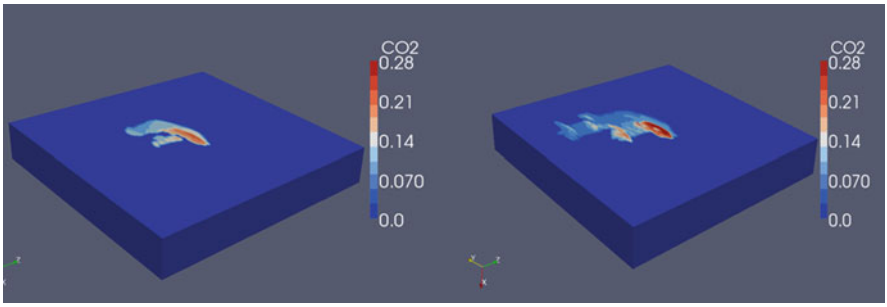

Fig. 14 Final CO_2 saturation for simulation Case 2: (*left*) no IFT effect; (*right*) with IFT effect

Results are shown in Figs. 13–15. The trapping number in the whole domain could vary from 1×10^{-8} to 1×10^{-4} during the injection period as shown in the simulation. Therefore, the trapping number plays a role for the sequestration process. The CO_2 saturation at vertical cross section through the injection wells indicates that CO_2 migrates further distances from the wells when the IFT effect is modeled (Fig. 13). The injected CO_2 is also spreading larger area when the effect of IFT is included (Fig. 14).

The inventory of CO_2 distribution in different forms is shown in Fig. 15 where the dissolved contribution increases whereas trapped contribution significantly decreases giving rise to more free CO_2 to flow when the effect of IFT is modeled.

Case 3. The third case is studying the effect of salinity and comparing the injection in aquifers with different salinity conditions and taking into account the IFT effect

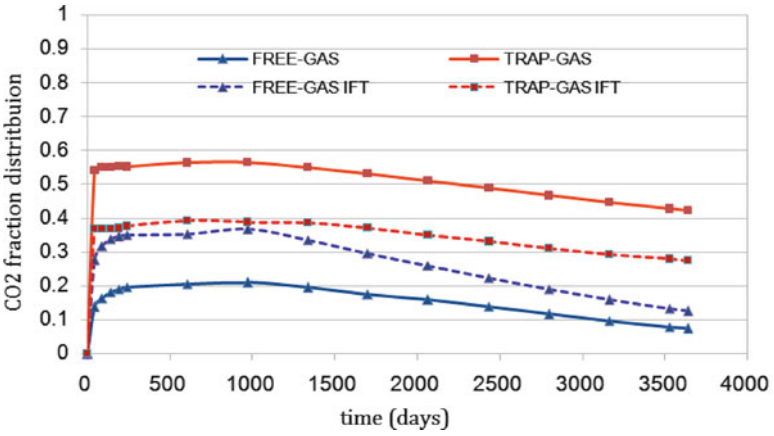

Fig. 15 Effect of IFT on CO_2 inventory for Case 2

Table 6 Reservoir and fluid data for Case 3

Aquifer size, L, W, H	3,500 ft ×3,500 ft ×100 ft
Mesh	3D (24 × 24 × 3)
Dip angle	0 %
Depth (top corner)	8,300 ft
Surface temperature	10°C
Aquifer temperature	43°C (110°F)
Initial aquifer pressure	1000 psi
Horizontal permeability	50 md
Kv/Kh	0.1
Porosity	0.30
Vertical well length	20 ft
Initial water saturation	1
Residual water saturation	0.379
Residual CO_2 saturation	0.225
Salinity	(1) 150,000 ppm, (2) 334,000 ppm
Injection rate	414 MSCF/D
Injection period	10 years injection, 20 years shut-in

on relative permeability curves. The aquifer has heterogeneous permeability and porosity. The aquifer salinity and temperature are uniform. The injection well is located in the center of the model with a constant injection rate of 414 MSCF/D. The initial aquifer pressure is 1000 psi and the boundary condition is no flow boundary at all sides of the reservoir model. The binary interaction parameter is modeled as a function of salinity and temperature. The model parameters are shown in Table 6.

Distributions of CO_2 as free, trapped, and dissolved are shown in Fig. 16. It is evident that the dissolution of CO_2 is decreasing with increased salinity, while the free phase is almost unchanged.

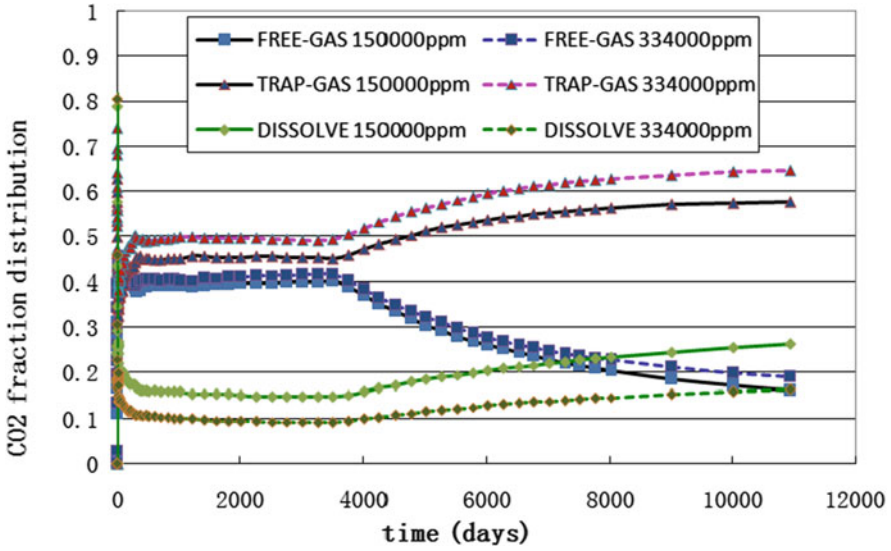

Fig. 16 Effect of salinity on CO_2 inventory (Case 3)

5 Other Model Enhancements

Hysteresis: We have already implemented a hysteretic relative permeability and capillary pressure model based on Land's correlation and the earlier experiences [9, 12, 15, 23, 24]. The Leverett J-function is also modeled [25]. However we focus on the effect of interfacial tension and the resulting shift in the residual saturation for this study.

Enhanced Velocity Method: IPARS has the capability of applying the enhanced velocity mixed finite element method where nonmatching multiblock grids are used to take advantage of different types of discretization in different parts of the simulation domain and maintaining the flux continuity along the interfaces [33, 34]. Figure 17 gives an example of such simulation that resulted in a significant computational time saving of about 81% compared to refining the whole region using the fine grid. We are in the process of testing this methodology for CO_2 injection where we can use very fine grid near injection wells and larger cell sizes further away from the wells to benefit from more accurate high-resolution near wells with more efficient CPU times.

6 Summary and Conclusion

The results presented in this research suggest that the sequestration and distribution of injected CO_2 as free, trapped, and dissolved is strongly affected by the aquifer conditions of pressure, temperature, and salinity. These factors affect the

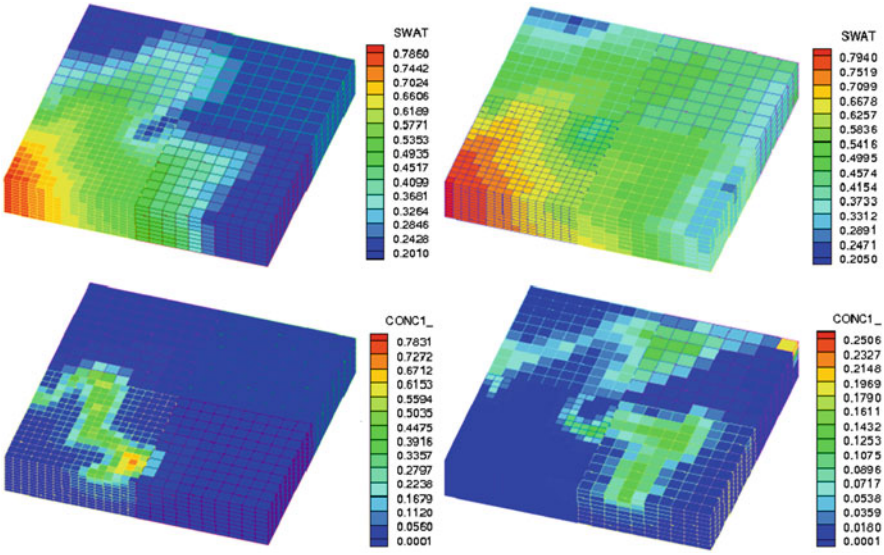

Fig. 17 Water phase saturations (*top* figures) and species concentration (*bottom* figures) profiles at 50 (*left*) and 100 (*right*) days using enhanced velocity multiblock

displacement characteristics of the two-phase flow by altering the relative permeability and capillary pressure curves. Further research is needed to fully understand the longtime impact of these effects on CO_2 sequestration. Few observations and conclusions are outlined as follows:

- Relative permeability model based upon trapping number was successfully tested for CO_2/brine to properly account for the changes in residual saturations and relative permeability endpoints.
- Key to the model is the dependence of CO_2 residual saturation on pressure (or IFT), viscous forces, and gravitational forces consistent with the published lab data for supercritical CO_2/brine.
- Phase behavior, trapping number, and heterogeneity interact in a complex way that requires compositional simulation to understand and predict the behavior of high-rate CO_2 injection wells.
- Effect of interfacial tension on capillary pressure and relative permeability hysteresis needs to be included.

Acknowledgments This work was supported in part by an Academic Excellence Alliance program award from King Abdullah University of Science and Technology (KAUST) Global Collaborative Research under the title X. A portion of this research was supported by the U.S. Department of Energy, Office of Science, Office of Basic Energy Sciences. The **Center for Frontiers of Subsurface Energy Security** (CFSES) is a DOE Energy Frontier Research Center, under contract number DE-SC0001114. The authors gratefully acknowledge the financial support provided by the NSF-CDI under contract number DMS 0835745.

References

1. Al-Abri, A., Amin, R.: Experimental investigation of interfacial interactions of condensate/brine/SC-CO_2 systems at high pressure and high temperature conditions. Society of Petroleum Engineers—International Petroleum Technology Conference, Doha, Qatar (2009)
2. Bachu, S.: CO_2 storage in geological media: role, means, status and barriers to deployment. Prog. Energ. Combust. Sci. **34**, 254–273 (2008)
3. Bachu, S., Adams, J.J.: Sequestration of CO_2 in geological media in response to climate change: capacity of deep saline aquifers to sequester CO_2 in solution. Energ. Convers. Manage. **44**, 3151–3175 (2003)
4. Bachu, S., Gunter, W.D., Perkings, E.H.: Aquifer disposal of CO_2: hydrodynamic and mineral trapping. Energ. Convers. Manage. **35**, 269–279 (1994)
5. Bennion, D.B., Bachu, S.: Dependence on temperature, pressure and salinity of the IFT and relative permeability displacement characteristics of CO_2 injected in deep saline aquifers. Paper SPE 102138 presented at the 2006 SPE Technical Conference and Exhibition, San Antonio, TX (2006)
6. Bennion, D.B., Bachu, S.: A correlation for the interfacial tension between supercritical phase CO_2 and equilibrium brines as a function of salinity, temperature and pressure. SPE 114479 presented at the 2008 SPE Annual Technical Conference, Denver, Colorado (2008)
7. Bownell, L.E., Ktz, D.L.: Flow of fluids through porous media: part II. Chem. Eng. Prog. **43**, 601–612 (1947)
8. Brooks, A.N., Corey, A.T.: Hydraulic Properties of Porous Media. Fort Collins, Colorado State University (1964)
9. Carlson, F.M.: Simulation of relative permeability hysteresis to the non-wetting phase. Paper SPE 10157, presented at the 1981 SPE Annual Technical Conference and Exhibition, San Antonio, TX (1981)
10. Chalbaud, C., Robin, M., Egermann, P.: Interfacial tension data and correlations of brine/CO_2 systems under reservoir conditions. Paper SPE 102918, presented at the 2006 SPE Annual Technical Conference and Exhibition, San Antonio, TX (2006)
11. Christie, M.A., Blunt, M.J.: Tenth SPE comparative solution project: a comparison of upscaling technique. SPE Reserv. Eval. Eng. **4**, 308–317 (2001)
12. Delshad, M., Lenhard, R.J., Oostrom, M., Pope, G.A.: A mixed-wet hysteretic relative permeability and capillary pressure model for reservoir simulations. SPE Reservoir Evaluation & Engineering. **6**, 328–334 (2003)
13. Delshad, M., Thomas, S.G., Wheeler, M.F.: Parallel numerical reservoir simulations of non-isothermal compositional flow and chemistry. SPE 118847-PA, SPE J. **16**, 239–248 (2011)
14. Doughty, C.: Modeling geological storage of carbon dioxide: comparison of non-hysteretic and hysteretic characteristic curves. Energ. Convers. Manage. **48**, 1768–1781 (2007)
15. Flett, M., Randal, G., Taggart, I.: The function of gas-water relative permeability hysteresis in the sequestration of carbon dioxide in saline formations. SPE Asia Pacific Oil and Gas Conference and Exhibition Perth, Australia, 18–20 October 2004
16. Ghomian, G., Pope, G.A., Sepehrnoori, K.: Reservoir simulation of CO_2 sequestration pilot in frio brine formation. Energy **33**, 1055–1067 (2008)
17. Gunter, W.D., Bachu, S., Benson, S.M.: The role of hydrogeological and geochemical trapping in sedimentary basin for secure geological storage for carbon dioxide. In: Baines, S.J., Wordern, R.H. (eds.) Geological Storage of Carbon Dioxide, pp. 129–145. Geological Society Special Publication, London (2004)
18. Hauser, E.A., Michaels, A.S.: Interfacial tension at elevated pressure and temperature. I. J. Phys. Chem. **52**, 1157–1165 (1948)
19. House, N.J., Faulder, D.D., Olson, G.L., Fanchi, J.R.: Simulation study of CO_2 sequestration in a north sea formation. Paper SPE 81202, presented at the 2003 SPE/EPA/DOE Exploration and Production Environmental Conferences, San Antonio, TX (2003)

20. Jones, J.A.A.: Climate change and sustainable water resources: placing the threat of global warming in perspective. Hydrolog. Sci. **44**, 541–571 (1999)
21. Kumar, A.: A simulation study of carbon sequestration in deep saline aquifers. M.S. Thesis. The University of Texas at Austin (2004)
22. Kumar, A., Ozah, R., Noh, M.H., Pope, G.A., Bryant, S.L., Sepehrnoori, K., Lake, L.W.: Reservoir simulation of CO_2 storage in deep saline aquifers. SPE J. **10**(3), 336–348 (2005)
23. Land, C.S.: Calculation of imbibition relative permeability for two- and three-phase flow from rock properties. SPE J. 149–156 (1968)
24. Land, C.S.: Comparison of calculated with experimental imbibition relative permeability. SPE J. 419–425 (1971)
25. Leverett, M.C.: Capillary behavior in porous solids. Trans. AIME **142**, 159–172 (1941)
26. Liu, N., Sachin, G., Lee, H., Liangxiong, L., Reid, G., Lee, R.: The effect of pressure and temperature on brine-CO_2 relative permeability and IFT at reservoir conditions. SPE 139029 (2010)
27. Macleod, D.B.: On a relation between surface tension and density. Trans. Faraday Soc. **19** 38–41 (1923)
28. Orr, F.: Storage of carbon dioxide in geologic formations. SPE J. **56**, 90–97 (2004)
29. Pope, G.A., Wu, W., Narayanaswamy, G., Delshad, M., Sharma, M.M., Wang, P.: Modeling relative permeability effects in gas-condensate reservoirs with a new trapping model. SPE Reserv. Eval. Eng. **3**, 171–178 (2000)
30. Pruess, K., Xu, T., Apps, J., Garcia, J.: Numerical Modeling of Aquifer Disposal of CO2, SPE 83695-PA, **8**(1), 49–60, (2003)
31. Sugden, S.: A relation between surface tension, density, and chemical composition. J. Chem. Soc., Trans., **125**, 1177–1189 DOI: 10.1039/CT9242501177 (1924)
32. Taha, M., Okasha Al-Shiwaish, A.A.: Effect of temperature and pressure on interfacial tension and contact angle of Khuff gas reservoir. SPE/DGS Saudi Arabia Section Technical Symposium and Exhibition, Al-Khobar, Saudi Arabia, 4–7 April (2010)
33. Thomas, S.G.: On some problems in the simulation of flow and transport through propose media. Ph.D. Dissertation. The University of Texas at Austin (2009)
34. Wheeler, J.A., Wheeler, M.F., Yotov, I.: Enhanced velocity mixed finite element methods for flow in multiblock domains. Comput. Geosci. **6**, 315–332 (2002)

Sneak Flow Simulations in the IXV′s Windward TPS Assembly

M. Patrício and R. Patrício

Abstract Upon reentering the terrestrial atmosphere, the IXV endures a sneak flow phenomenon which is a result of the existence of thermal protection joints in between the tiles that shield the spacecraft's cold structure from friction and high temperatures. Placing a low-permeability porous material as a sealer in between this structure and the tiles will prevent cold structure overheating but at the same time increase the global mass. To aid the selection of an adequate sealing foam-like material the relevant thermal phenomena which occur during the atmospheric reentry are translated into a boundary value problem which couples the Navier–Stokes, Brinkman and heat transfer equations. The resolution of this problem, accomplished resorting to finite element methods, provides tools to predict the maximum temperature achieved at the outer wall of the cold structure, for each set of material parameters. An algorithm that implements a domain decomposition approach is presented in order to increase the accuracy of the numerical solution and decrease the computational complexity of the problem. Finally, it is discussed how the ideal properties for a sealing material may be sought; a second algorithm is proposed to this end.

1 Introduction

The European Space Agency (ESA) has been developing a spacecraft, the so-called intermediate experimental vehicle (IXV), to test and develop technology for future spacecrafts, cf. [11]. One particular aspect that has to be taken into

M. Patrício (✉)
CMUC, Department of Mathematics, University of Coimbra, Coimbra, Portugal

School of Technology and Management, Polytechnic Institute of Leiria, Leiria, Portugal
e-mail: miguelpatricio@gmail.com

R. Patrício
Active Space Technologies S.A., Coimbra, Portugal
e-mail: ricardo.patricio@activespacetech.com

J.A. Ferreira et al. (eds.), *Modelling and Simulation in Fluid Dynamics in Porous Media*, Springer Proceedings in Mathematics & Statistics 28, DOI 10.1007/978-1-4614-5055-9_9,

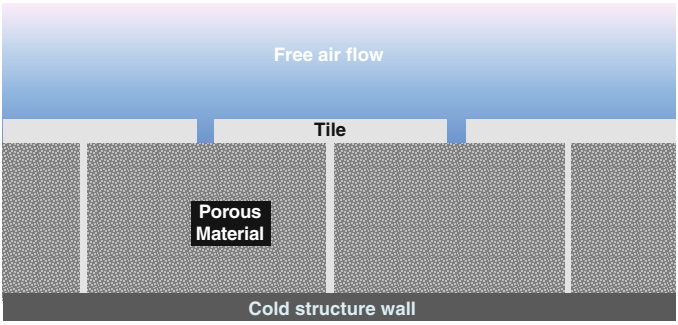

Fig. 1 Cold structure wall and TPS

consideration is the harsh reentry environment that will be sustained by the vehicle upon returning from outer space and reentering the atmosphere. It is estimated that it will encounter temperatures which rise above 1,500 °C as it slows down from a speed of over 7 km/s. With this in mind, besides the advanced ship design that aids enduring the severe friction and aerodynamic heating, the spacecraft is equipped with a thermal protection system (TPS). The outer layer of the TPS is made up of independent tiles, which are fixed externally to the primary structure of the capsule, the so-called cold structure (Fig. 1). The tiles cover the sections most exposed to high temperatures. However, thermal expansion joints that are left between the tiles allow for the flow of hot gas from the atmosphere. Due to this sneak flow, proper insulation to prevent the structure from being heated to temperatures that would lead to structural failure is required. The insulation may be provided by placing sealing porous materials between the TPS tiles and the primary structure of the capsule. It is crucial to choose an adequate material which offers low permeability without placing a great burden on the global mass. Porous lightweight foams are being considered as candidates to play the role of the desired sealer.

It is the goal of this chapter to provide tools for predicting the optimal characteristics for a sealer. Section 2 is devoted to the description of an experimental model which allows a simulation of the sneak flow phenomenon. This model is translated into a boundary value problem in Sect. 3. The airflow is assumed to be properly described by the coupled Navier–Stokes, Brinkman, and heat transfer equations. The physical processes at the subregions of the domain of interest are typically described by these equations, which link together to form a global heterogeneous partial differential model, [3, 9]. Numerical approaches to solve the resulting boundary value problem are proposed in Sect. 4. Here, besides focusing on the direct problem of computing the maximum temperature attained at the cold structure given the permeability of a chosen sealer material, we will also look at the inverse problem, which consists of determining the ideal permeability for a sealing material. Numerical examples are included in Sect. 5 and some concluding remarks are presented in Sect. 6.

2 Problem Description

It is required that a model for the sneak flow phenomenon should both give rise to meaningful numerical results without involving a prohibitive computational complexity and also be reproducible in practical experiments. Bearing that in mind, we adopt the model represented in Fig. 2. Three different regions are considered in the geometry: the free flow region Ω_f, the porous material region Ω_p, and the cold structure's wall Ω_C. The first is depicted in the figure by the upper two chambers, which represent the atmosphere outside of the spacecraft. As for the porous material region, it is depicted in the picture by the chamber beneath and it represents the region in between the TPS tiles and the cold structure's wall where the sealing material is placed. Finally, the wall is depicted by the dark grey region at the bottom of the figure. In this setup an inlet and an outlet are assumed to exist at the upper left chamber and the upper right chamber respectively, so that the air is forced to circulate from and back to the free flow region through the porous region. This fails to represent the fact that not all of the air outside of the spacecraft will pass through the thermal joints, but the idea is that by forcing the air to circulate through the sealing material the sneak flow is maximized, enabling the testing of the phenomena in meaningful, yet less complex and costly, experimental setups.

It is proposed that different porous materials be numerically tested as sealers. For each set of corresponding material parameters, we let hot air enter the upper left chamber of the computational domain. The goal is to determine, for various boundary conditions that are imposed at the inlet, the temperature that is attained at the outer wall of the cold structure of the spacecraft. Besides this problem, which we call the direct problem, one also wants to solve the inverse problem. This consists of the determination of the permeability of the porous material that ensures that the maximum temperature of the cold structure wall does not exceed a prescribed critical value.

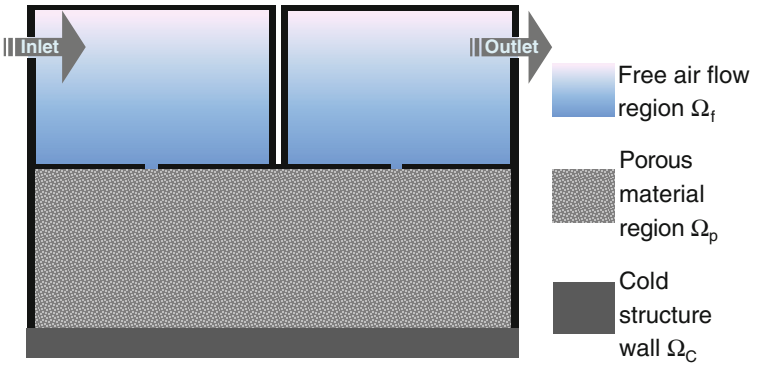

Fig. 2 Geometry of the model

3 Mathematical Model

One would like to determine the temperature T over $\overline{\Omega}$, the closure of the computational domain $\Omega = \Omega_f \cup \Omega_p \cup \Omega_C$, as well as the pressure and the velocity vector field of the air as it flows through Ω_f and Ω_p, denoted by p and $\mathbf{u} = (u, v)$, respectively.

We assume that the phenomena occurring over the free flow region Ω_f may be modeled by the Navier–Stokes and the heat transfer equations:

$$\rho(\mathbf{u}\cdot\nabla)\mathbf{u} = \nabla\cdot\left[-p\mathbf{I} + \mu(\nabla\mathbf{u} + (\nabla\mathbf{u})^T)\right], \quad \mathbf{x}\in\Omega_f, \tag{1}$$

$$\nabla\cdot\mathbf{u} = \mathbf{0}, \quad \mathbf{x}\in\Omega_f, \tag{2}$$

$$\rho C_p\mathbf{u}\cdot\nabla T = \nabla\cdot(k_f\nabla T), \quad \mathbf{x}\in\Omega_f. \tag{3}$$

Here, ρ, μ, C_p, and k_f are material parameters which represent the density, dynamic viscosity, specific heat capacity, and thermal conductivity of the fluid, respectively.

Over Ω_p, the air circulation is affected by the placement of a porous material in between the cold structure's wall and the tiles, implying that different partial differential equations have to be considered, cf. [1, 2, 8]. The unknowns are then assumed to satisfy the Brinkman equation, so that in this region one may write

$$-\nabla p + \frac{1}{\varepsilon_p}\nabla\cdot\left[\mu(\nabla\mathbf{u} + (\nabla\mathbf{u})^T - \frac{2}{3}\mu(\nabla\cdot\mathbf{u})\mathbf{I})\right] = \left(\frac{\mu}{k}\right)\mathbf{u}, \quad \mathbf{x}\in\Omega_p, \tag{4}$$

$$\rho\nabla\mathbf{u} = \mathbf{0}, \quad \mathbf{x}\in\Omega_p, \tag{5}$$

$$\rho C_p\mathbf{u}\cdot\nabla T = \nabla\cdot(k_{eq}\nabla T), \quad \mathbf{x}\in\Omega_p. \tag{6}$$

Here, ε_p, k, and k_{eq} denote the porosity, the permeability, and the equivalent thermal conductivity, respectively.

Finally, over the cold structure's wall region Ω_C, the temperature field T is assumed to be the solution of the partial differential equation:

$$-\nabla\cdot(k_C\nabla T) = \mathbf{0}, \quad \mathbf{x}\in\Omega_C, \tag{7}$$

where k_C is the thermal conductivity of the solid material.

In order to obtain a proper mathematical description of the sneak flow phenomenon that we are interested in, boundary conditions have to be added to the partial differential equations written above, cf. [5, 6]. At the internal boundary $\Gamma_{fp} = \overline{\Omega}_f \cap \overline{\Omega}_p$ between the free flow region and the porous material region, continuity of the velocity vector, of the normal component of the stress tensor, of the temperature and of the heat flux are enforced. At the internal boundary $\Gamma_{pC} = \overline{\Omega}_p \cap \overline{\Omega}_C$ between the porous material region and the cold structure region only the continuity of the temperature and of the heat flux is imposed. At the inlet of the computational domain, which we denote by Γ_{in}, both the temperature T_{in} and

the pressure p_{in} are assumed to be known. At the outlet Γ_{out}, both the temperature gradient in the normal direction and the pressure are prescribed to be equal to zero:

$$T(\mathbf{x}) = T_{in}; \qquad p(\mathbf{x}) = p_{in}, \quad \mathbf{x} \in \Gamma_{in}, \tag{8}$$

$$\frac{\partial}{\partial x} T(\mathbf{x}) = 0; \qquad p(\mathbf{x}) = 0, \quad \mathbf{x} \in \Gamma_{out}. \tag{9}$$

In order to describe the convective cooling that occurs at the lowest boundary of the cold structure's wall Γ_C, one has

$$k_C \frac{\partial}{\partial y} T(\mathbf{x}) = \alpha(T - T_C), \quad \mathbf{x} \in \Gamma_C, \tag{10}$$

where α and T_C are given scalars. At the left and right boundaries of the cold structure's wall Γ_{Clr}, the prescribed boundary condition reads

$$\frac{\partial}{\partial x} T(\mathbf{x}) = 0, \quad \mathbf{x} \in \Gamma_{Clr}. \tag{11}$$

All the remaining boundaries Γ_w are treated as solid walls where the following conditions hold

$$\mathbf{n} \cdot \Delta T(\mathbf{x}) = 0; \qquad \mathbf{u}(\mathbf{x}) = \mathbf{0}, \quad \mathbf{x} \in \Gamma_w. \tag{12}$$

Here, $\mathbf{n}$ denotes the outward pointing normal.

4 Solution Approaches

Determining the exact solution of the boundary value problem (1)–(12) with the internal boundary conditions that have been stated, which are hereforth suppressed for the sake of simplicity, is a rather daunting task. Here we opt to compute a numerical solution to the problem by resorting to finite element methods (FEM). In addition, a domain decomposition method is proposed to allow for greater accuracy with a smaller computational effort. The section is concluded with the presentation of an algorithm to solve the problem of predicting the ideal characteristics for a porous material that will keep the temperature of the cold structure's wall from exceeding a prescribed critical value.

4.1 The Direct Problem

Computing a finite element approximation to the solution of the problem at hand requires a great computational effort. One alternative is to employ domain decomposition, which allows for finer meshes to be used over subdomains of the computational domain at a lower cost, improving the global solution, cf., for

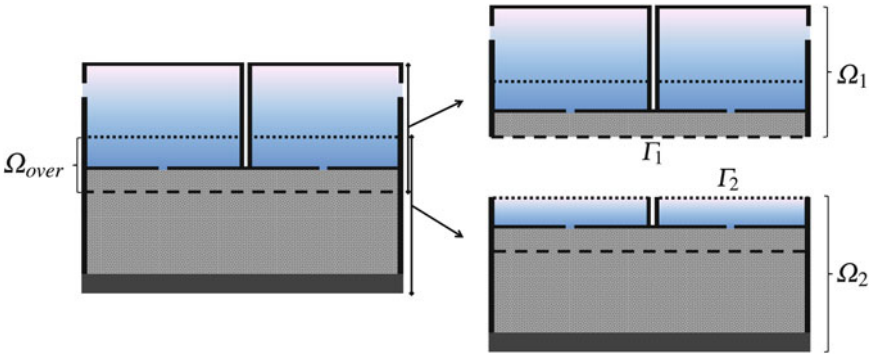

Fig. 3 Computational domain Ω and overlapping subdomains Ω_1 and Ω_2

example, [9, 10]. The idea is to divide Ω into two overlapping subdomains, Ω_1 and Ω_2, such that $\Omega = \Omega_1 \cup \Omega_2$ and the overlapping region is $\Omega_{over} = \Omega_1 \cap \Omega_2$. This introduces two artificial boundaries Γ_1 and Γ_2 (Fig. 3). By resolving the equations over each of the subdomains separately, the computational complexity of the problem is reduced.

The first step of the domain decomposition approach consists of determining a global approximation $\mathbf{u}^{(0)}$ and $T^{(0)}$ for the velocity vector field and for the temperature. This is done by resorting to FEM with a coarse mesh. The following step consists of resolving the coupled Navier–Stokes, Brinkman, and heat transfer equations over Ω_1, with $\mathbf{u}^{(0)}$, $T^{(0)}$ being used as input values over the artificial boundary Γ_1. This will allow the computation of approximations $\mathbf{u}_1^{(1)}$ and $T_1^{(1)}$, for the velocity field and the temperature over Ω_1, respectively. Finally, the coupled Navier–Stokes, Brinkman, and heat transfer equations are resolved over Ω_2, with $\mathbf{u}_1^{(1)}$ and $T_1^{(1)}$ being used as input values over the artificial boundary Γ_2 and resulting in the computation of $\mathbf{u}_2^{(1)}$ and $T_2^{(1)}$.

At the n^{th} iteration, the following boundary value problems are resolved:

$$
\begin{cases}
\rho(\mathbf{u}_1^{(n)} \cdot \nabla)\mathbf{u}_1^{(n)} = \nabla \cdot \left[-p_1^{(n)}\mathbf{I} + \mu(\nabla \mathbf{u}_1^{(n)} + (\nabla \mathbf{u}_1^{(n)})^T)\right], & \mathbf{x} \in \Omega_f \\
\nabla \cdot \mathbf{u}_1^{(n)} = \mathbf{0}, & \mathbf{x} \in \Omega_f \\
\rho C_p \mathbf{u}_1^{(n)} \cdot \nabla T_1^{(n)} = \nabla \cdot (k_f \nabla T_1^{(n)}), & \mathbf{x} \in \Omega_f \\
\frac{1}{\varepsilon_p}\nabla \cdot \left[\mu(\nabla \mathbf{u}_1^{(n)} + (\nabla \mathbf{u}_1^{(n)})^T - \frac{2}{3}\mu(\nabla \cdot \mathbf{u}_1^{(n)})\mathbf{I}\right] & \\
-\nabla p_1^{(n)} = (\frac{\mu}{k})\mathbf{u}_1^{(n)}, & \mathbf{x} \in \Omega_p \\
\rho \nabla \mathbf{u}_1^{(n)} = \mathbf{0}, & \mathbf{x} \in \Omega_p \\
\rho C_p \mathbf{u}_1^{(n)} \cdot \nabla T_1^{(n)} = \nabla \cdot (k_{eq} \nabla T_1^{(n)}), & \mathbf{x} \in \Omega_p \\
\mathbf{u}_1^{(n)} = \mathbf{u}_2^{(n-1)}; \quad T_1^{(n)} = T_2^{(n-1)}, & \mathbf{x} \in \Gamma_1 \\
T_1^{(n)}(\mathbf{x}) = T_{in}; \qquad p_1^{(n)}(\mathbf{x}) = p_{in}, & \mathbf{x} \in \Gamma_{in} \\
\frac{\partial}{\partial x} T_1^{(n)}(\mathbf{x}) = 0; \qquad p_1^{(n)}(\mathbf{x}) = 0, & \mathbf{x} \in \Gamma_{out} \\
\mathbf{n} \cdot \Delta T_1^{(n)}(\mathbf{x}) = 0; \qquad \mathbf{u}_1^{(n)}(\mathbf{x}) = \mathbf{0}, & \mathbf{x} \in \Gamma_w \cap \overline{\Omega_1}
\end{cases}
\tag{13}
$$

$$
\begin{cases}
\rho(\mathbf{u}_2^{(n)}\cdot\nabla)\mathbf{u}_2^{(n)} = \nabla\cdot\left[-p_2^{(n)}\mathbf{I}+\mu(\nabla\mathbf{u}_2^{(n)}+(\nabla\mathbf{u}_2^{(n)})^T)\right], & \mathbf{x}\in\Omega_f \\
\nabla\cdot\mathbf{u}_2^{(n)} = \mathbf{0}, & \mathbf{x}\in\Omega_f \\
\rho C_p\mathbf{u}_2^{(n)}\cdot\nabla T_2^{(n)} = \nabla\cdot(k_f\nabla T_2^{(n)}), & \mathbf{x}\in\Omega_f \\
\frac{1}{\varepsilon_p}\nabla\cdot\left[\mu(\nabla\mathbf{u}_2^{(n)}+(\nabla\mathbf{u}_2^{(n)})^T-\frac{2}{3}\mu(\nabla\cdot\mathbf{u}_2^{(n)})\mathbf{I}\right] & \\
-\nabla p_2^{(n)} = (\frac{\mu}{k})\mathbf{u}_2^{(n)}, & \mathbf{x}\in\Omega_p \\
\rho\nabla\mathbf{u}_2^{(n)} = \mathbf{0}, & \mathbf{x}\in\Omega_p \\
\rho C_p\mathbf{u}_2^{(n)}\cdot\nabla T_2^{(n)} = \nabla\cdot(k_{eq}\nabla T_2^{(n)}), & \mathbf{x}\in\Omega_p \\
-\nabla\cdot(k_C\nabla T_2) = \mathbf{0}, & \mathbf{x}\in\Omega_C \\
\mathbf{u}_2^{(n)} = \mathbf{u}_1^{(n)};\quad T_2^{(n)} = T_1^{(n)}, & \mathbf{x}\in\Gamma_2 \\
k_C\frac{\partial}{\partial y}T_2^{(n)}(\mathbf{x}) = \alpha(T_2^{(n)}-T_C), & \mathbf{x}\in\Gamma_C \\
\mathbf{n}\cdot\Delta T_2^{(n)}(\mathbf{x}) = 0; \qquad \mathbf{u}_2^{(n)}(\mathbf{x}) = \mathbf{0}, & \mathbf{x}\in\Gamma_w\cap\overline{\Omega_2} \\
\frac{\partial}{\partial x}T_2(\mathbf{x}) = 0, & \mathbf{x}\in\Gamma_{Clr}.
\end{cases}
\tag{14}
$$

The continuity conditions that were stated for the internal boundary conditions must also hold. The process is repeated until the following stopping criterion is reached:

$$
\| \left(\mathbf{u}_1^{(n)}-\mathbf{u}_2^{(n)}\right)|_{\Omega_{over}}\| < TOL_1, \tag{15}
$$

where TOL_1 is a given tolerance. The procedure described above allows establishing the following algorithm:

Algorithm 1

Let n=1. Given: TOL_1.

1. Compute a global solution $(\mathbf{u}^{(0)},\ T^{(0)})$ for (1)–(12).
2. Let $\mathbf{u}_2^{(n-1)} = \mathbf{u}^{(0)}|_{\overline{\Omega_2}}$, $T_2^{(n-1)} = T^{(0)}|_{\overline{\Omega_2}}$.
3. Solve the boundary value problem (13).
4. Solve the boundary value problem (14).
5. If (15) does not hold, let n=n+1 and return to 3.
6. Let $\mathbf{u} = \mathbf{u}_1^{(n)}$ and $T = T_1^{(n)}$ over $\overline{\Omega_1}\setminus\overline{\Omega_2}$ and $\mathbf{u} = \mathbf{u}_2^{(n)}$ and $T = T_2^{(n)}$ over $\overline{\Omega_2}$.

This algorithm allows determining a numerical solution $(\mathbf{u}, T)$ for the direct problem and, in particular, computing the maximum temperature that is reached over the wall of the cold structure that should remain below a given critical value.

4.2 The Inverse Problem

A choice has to be made for which foam to use as a sealer. This choice is twofold: the foam must on one hand provide the thermal protection required, as the temperature of the cold structure may not exceed a certain critical value, and it must also be as light as possible. Solving the inverse problem means finding the optimal permeability for each set of values for the temperature and pressure at the inlet, i.e., the value of permeability that will ensure that the temperature of the cold structure does not exceed a prescribed temperature T_{target}. This value for the permeability may be found by solving direct problems associated with different values of permeability in a trial and error type of approach. From the resolution of each of these problems a correspondence will be established between values of permeability k and the maximum of the temperature $T_{max}(k)$ that is reached over the wall of the cold structure. A desired approximation for the permeability k_d will be such that it satisfies $|T_{max}(k_d) - T_{target}| < TOL_2$, where TOL_2 is a given value for the tolerance. To systemize the computation of k_d we resort to classical fitting techniques, cf., for example, [4]. In particular, we resort to a monotonicity-preserving interpolation. The procedure is described in the following algorithm:

Algorithm 2

Let n=1. Given: $k^{(0)}$, $k^{(1)}$, TOL_2.

1. Compute $T^{(0)} = T_{max}(k^{(0)})$ and $T^{(1)} = T_{max}(k^{(1)})$.
2. Set n=n+1. Compute the shape-preserving spline S that fits the data $(k^{(i)}, T^{(i)})$, for $i = 0,\ 1,\ 2,\ \ldots,\ n-1$.
3. Let $k^{(n)} = S^{-1}(T_{target})$ and $T^{(n)} = T_{max}(k^{(n)})$.
4. If $|T^{(n)} - T_{target}| < TOL_2$ holds, set $k_d = k^{(n)}$. If not, return to 2.

We observe that $k^{(0)}$ and $k^{(1)}$ represent two initial approximations for the permeabilities, which should be chosen such that $k^{(0)} < k_d < k^{(1)}$.

5 Numerical Examples

We have assumed that the sneak flow phenomenon in the IXV is properly described by the boundary value problem (1)–(12). In what follows we will consider different values for the pressure and temperature at the input boundary Γ_{in}. As a first example of the numerical solutions that arise by employing the procedures described above, we begin by taking rather harsh conditions:

$$p_{in} = 10,000\,Pa; \quad T_{in} = 1,166\,K.$$

We assign the material properties of air and alumina to the fluid and to the cold structure, respectively. We also take

$$T_C = 293.15\ K; \quad \alpha = 1\ W/(m^2K); \quad k = 1 \times 10^{-8}\ m^2; \quad \varepsilon_p = 0.95.$$

As for the geometry that will be considered, it is characterized by

$$\Omega_f = ((]-288,-3.5[\cup]3.5,288[)\times]0,200[) \cup ((]-98,-95[\cup]95,98[)\times]-4,0]),$$
$$\Omega_p =]-288,288[\cup]-104,-4[, \qquad \Omega_C =]-288,288[\cup]-108,-104[,$$
$$\Gamma_{in} = \{-288\} \times [160,170], \qquad \Gamma_{out} = \{288\} \times [160,170].$$

We start by taking a coarse triangular mesh, refined over the most critical regions, and refine it further into finer meshes, so that the maximum element size varies. For each of these meshes a numerical solution is found for both the velocity and the temperature of the airflow, resorting to the FEM commercial package COMSOL 4.0a and Matlab scripts. The unavailability of an analytical solution led us to seek out a reference solution, obtained classically by the consecutive refinement of meshes. The magnitude of the velocity of the airflow of the reference solution is represented in Fig. 4. For better visualization, the arrows in the figure have been included to represent the direction of the airflow. We note that the color range in the figure has been taken less broad than the range of values of the reference solution. In fact, the ranges of the horizontal and vertical components of the velocity and of the temperature, computed over $\overline{\Omega_f \cup \Omega_p}$, are actually $[-160,137]$, $[-187,140]$, and $[420,896]$, respectively.

For each mesh, the error E_u of the numerical approximation for the horizontal component of the velocity is obtained by taking the L^2 norm of its difference to the reference solution. Likewise, the errors E_v and E_T for the vertical component of the velocity and for the temperature, respectively, are also computed (Table 1). The values of the errors obtained for the different meshes are displayed in Table 2. Clearly, as expected, the errors decrease with the maximum mesh size. Also, when compared to the range of the values of the velocity components and the temperature, the approximations may be considered to be quite accurate.

As was seen in Sect. 4, one may employ the domain decomposition approach set in Algorithm 1 to obtain a computationally cheaper and more accurate solution for

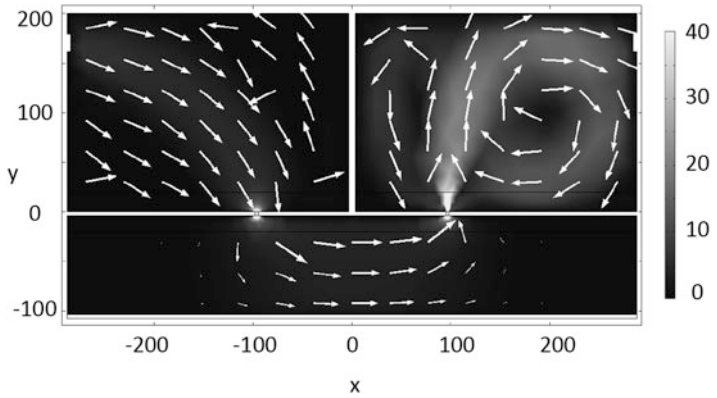

Fig. 4 Magnitude of the velocity field

Table 1 Errors of the FEM approximations

	Maximum mesh size			
Error	0.33	0.17	0.13	0.10
E_u	1.94	0.99	0.70	0.68
E_v	1.83	0.81	0.65	0.37
E_T	7.31	1.08	0.51	0.16

Table 2 Errors of the domain decomposition method approximations

	Iteration				
Error	0	1	2	3	4
E_u	0.78	0.33	0.27	0.26	0.25
E_v	0.35	0.15	0.11	0.10	0.09
E_T	3.89	0.55	0.40	0.38	0.37

the boundary value problem. We start by taking a course grid to obtain a FEM global approximations $\mathbf{u}^{(0)}$ and $T^{(0)}$ for the velocity and the temperature, respectively. The artificial boundaries are taken:

$$\Gamma_1 = \{(x,y) \in \mathbb{R}^2 : x \in [-288,-3.5] \cup [3.5,288] \ \wedge \ \ y = 20\},$$
$$\Gamma_2 = \{(x,y) \in \mathbb{R}^2 : x \in [-288,288] \ \wedge \ \ y = -20\ \}.$$

Table 2 displays the errors of the approximations obtained at each iteration of the algorithm in the L^2 norm. Clearly, the errors decrease with the increase of the iteration number. We note that the rate of convergence may be increased by taking a larger overlapping region. However, this would result in a greater computational cost, cf. [7].

We conclude this section by examining at how one may determine the ideal permeability for a sealer material for the IXV, i.e., we look at the so-called inverse problem. We start by taking $p_{in} = 100\ Pa$ and $T_{in} = 873\,\mathrm{K}$ for the pressure and the temperature at the input Γ_{in}. Our goal is to determine the ideal permeability k_d

Table 3 Permeabilities and corresponding temperatures, resulting from Algorithm 2

n	$k^{(n)}$	$T_{max}(k^{(n)})$
0	1E−7	763.6
1	1E−12	293.4
2	2.4E−8	738.5
3	4.8E−9	592.4
4	1.5E−9	463.3
5	8.8E−10	417.9
6	7.9E−10	409.3
7	7.8E−10	408.9

Table 4 Predicted permeabilities for different input pressure values, resulting from Algorithm 2

p_{in}	k_d
100	7.8E−10
250	1.7E−10
500	4.5E−11
750	2.1E−11
1,000	1.2E−11
2,000	3.2E−12

for which the maximum temperature $T_{max}(k_d)$ reached at the boundary of the cold structure is $T_{target} = 408$ K, up to a given tolerance. We follow the steps of Algorithm 2 in which we take $k^{(0)} = 10^{-7}$, $k^{(1)} = 10^{-12}$, and $TOL_2 = 1$ K, thus obtaining the values included in Table 3.

Note that it was required that eight direct problems be solved in order to find the desired approximation. In general, it is important to have good initial guesses $k^{(0)}$ and $k^{(1)}$ in order to reduce the number of iterations. Moreover, different boundary conditions at the input require the repetition of the procedure above to determine the corresponding ideal permeabilities. However, by storing and using these permeabilities, it is possible to find a predictor that avoids the unnecessary resolution of more direct problems. In fact, let us focus on the varying pressure values that may be read on the first row of Table 4, for which we have employed Algorithm 2 to compute the optimized permeabilities. All of these values were obtained for a fixed temperature of $T_{in} = 873$ K, like before. An estimator $k_d = k_d(p_{in})$ for the permeability of the sealer as a function of the pressure is found by fitting the values that are found in the table:

$$k_d(p_{in}) = 4 \times 10^{-6} \times p_{in}^{-1.844}. \tag{16}$$

The fitting above is illustrated in Fig. 5, where dots were used to represent the data that is contained in Table 4 and the predictor given by (16) is depicted as a full line. To test its effectiveness as a predictor for the desired permeability, we use (16) to compute the permeabilities for other values of pressure, namely $p_1 = 200$, $p_2 = 300$, $p_3 = 400$, $p_4 = 600$, $p_5 = 800$, and $p_6 = 900$ Pa. The maximum temperatures attained at the cold structure are then computed for each value of

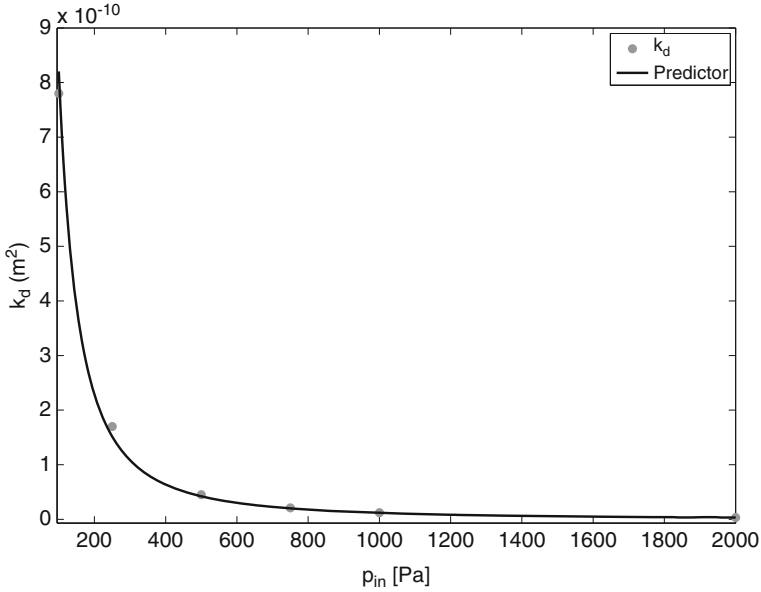

Fig. 5 Fitting for the permeability

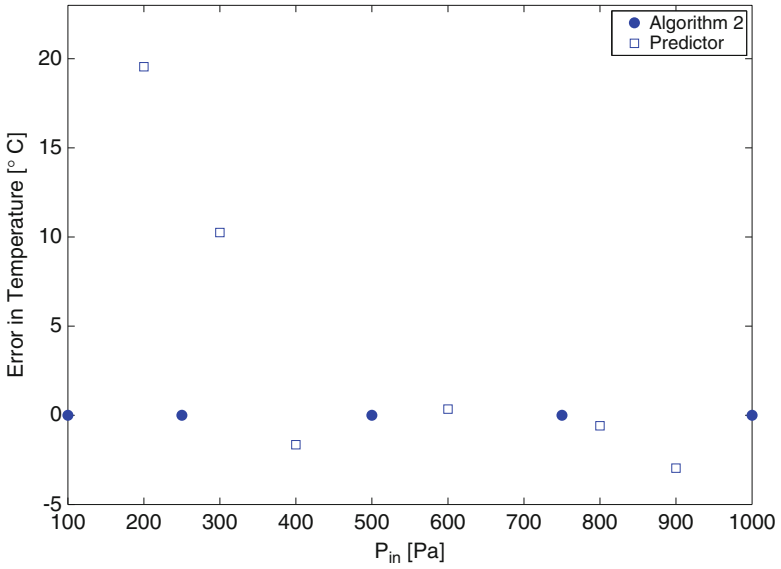

Fig. 6 Error arising from the predicted permeabilities

pressure by solving a direct problem in which the predicted permeability has been given as input. The difference between each of these temperatures and T_{target} is

displayed in Fig. 6 by a square. The full circles correspond to the data included in Table 4 and the corresponding temperatures.

Clearly, while porous materials with the predicted permeabilities do a good job at preventing the cold structure from attaining temperatures that differ much from T_{target} for $p > 400$ Pa, this is not so clear when the pressure equals to 200 or 300. Note however that the slope of the predictor for the permeability increases for smaller values of pressure. For such values one may obtain an improvement by having more data available in this region.

6 Concluding Remarks

The temperature attained at the outer wall of the cold structure of the IXV during its atmospheric reentry must be kept sufficiently low. In this chapter we have set out to provide tools to aid the selection of a porous lightweight sealing material for the IXV. A mathematical description of the thermal phenomena was presented. Given the material parameters, it is then possible to predict the cold structure's wall temperature. Two numerical techniques were employed to solve the mathematical problems: standard FEM and a simple domain decomposition approach. The latter was based on the classical Schwarz iterative scheme that dates back to the nineteenth century. The idea consists of dividing the computational domain into two overlapping subdomains. The size of the overlapping region plays a crucial role in the convergence of the scheme. The larger it is, the faster the scheme should converge. However, this comes at the cost of increasing the computational complexity for each of the problems solved at the subdomains. Note that it is possible to adopt different domain decomposition techniques, namely, nonoverlapping subdomains may be considered, as long as the conditions imposed at the artificial boundary between the two subdomains assure convergence to the matching conditions. Decomposing the computational domain into more subdomains, and eventually resorting to parallelization, will again reduce the complexity of the problem and allow for finer meshes to be employed.

Solving the inverse problem equals answering the question of which should be the permeability for a sealing material once the other material parameters and the boundary conditions are set. The computed permeability should hint into which of the existing materials under consideration should be tested, both numerically using the direct approach described above and experimentally.

Acknowledgements Research supported by CMUC and FCT (Portugal), through European program COMPETE/FEDER.

References

1. Auriault, J.-L.: On the domain of validity of Brinkman's equation. Transport Porous Med. **79**, 215–223 (2009)
2. Brinkman, H.C.: A calculation of the viscous force exerted by a flowing fluid on a dense swarm of particles. Appl. Sci. Res. **1**, 27–34 (1949)
3. Discacciati, M., Quarteroni, A.: Navier-Stokes/Darcy coupling: modeling, analysis, and numerical approximation. Rev. Mat. Complutense **22**, 315–426 (2009)
4. Fritscht, F.N., Carlson, R.E.: Monotone piecewise cubic interpolation. SIAM J. Numer. Anal. **17**, 238–246 (1980)
5. Guta, M., Sundar, S.: Navier-Stokes-Brinkman system for interaction of viscous waves with a submerged porous structure. Tamkang J. Math. **41**, 217–243 (2010)
6. Neale, G., Nader, W.: Practical significance of Brinkman's extension of Darcy's law: coupled parallel flows within a channel and a bounding porous medium. Canadian J. Chem. Eng. **52**, 475–478 (1974)
7. Patrício, M., Mattheij, R.M.M., de With, G.: Solutions for periodically distributed materials with localized imperfections. Comput. Model. Eng. Sci. **38**, 89–118 (2008)
8. Popov, P., Qin, Q., Bi, L., Efendiev, Y., Kang, Z., Li, J.: Multiphysics and multiscale methods for modeling fluid flow through naturally fractured carbonate karst reservoirs. SPE Reserv. Eval. Eng. **12**, 218–231 (2009)
9. Quarteroni, A., Valli, A.: Domain Decomposition Methods for Partial Differential Equations. Clarendon Press, Oxford (1999)
10. Schwarz, H.A.: Über einen grenzübergang durch alternierendes verfahren. Vierteljahrsschr. Naturforsch. Ges. Zür. **15**, 272–286 (1870)
11. Tumino, G., Angelino, E., Leleu, F., Angelini, R., Plotard, P., Sommer, J.: The IXV project, the ESA re-entry system and technologies demonstrator paving the way to European autonomous space transportation and exploration endeavours. 3rd Future Launchers Preparatory Programme Industrial Workshop, Glasgow (2008)

Implementing Lowest-Order Methods for Diffusive Problems with a DSEL

J.-M. Gratien

Abstract Industrial simulation software has to manage: (1) the complexity of the underlying physical models, (2) the complexity of numerical methods used to solve the PDE systems, and finally (3) the complexity of the low-level computer science services required to have efficient software on modern hardware. Nowadays, some frameworks offer a number of advanced tools to deal with the complexity related to parallelism in a transparent way. However, high-level complexity related to discretization methods and physical models lacks tools to help physicists to develop complex applications. Generative programming and domain-specific languages (DSL) are key technologies allowing to write code with a high-level expressive language and take advantage of the efficiency of generated code for low-level services. Their application to scientific computing has been up to now limited to finite element (FE) methods and Galerkin methods, for which a unified mathematical framework has been existing for a long time (see projects like `Freefem++`, `Getdp`, `Getfem++`, `Sundance`, `Feel++` Aavatsmark et al. (SIAM J. Sci. Comput., 19:1700–1716, 1998), `Fenics` project). In reservoir and basin modeling, lowest-order methods are promising methods allowing to handle general meshes. Extending finite volume (FV) methods, Aavatsmark, Barkve, Bøe, and Mannseth propose consistent schemes for nonorthogonal meshes while stability problems are solved with the mimetic finite difference method (MFD) and the mixed/hybrid finite volume methods (MHFV) (Aavatsmark et al. Discretization on non-orthogonal, curvilinear grids for multi-phase flow. In: Christie, M.A., Farmer, C.L., Guillon, O., Heinmann, Z.E. (eds.) Proceedings of the 4th European Conference on the Mathematics of Oil Recovery, Norway, 1994). However, the lack of a unified mathematical frame was a serious limit to the extension all of these methods to a large variety of problems. In Aavatsmark et al. (J. Comput. Phys., 127:2–14, 1996), the authors propose a unified way to express FV multipoint scheme and

J.-M. Gratien (✉)
IFP Energies nouvelles, 1 et 4 av Bois Préau 92500 Rueil-Malmaison, France
e-mail: jean-marc.gratien@ifpen.fr

J.A. Ferreira et al. (eds.), *Modelling and Simulation in Fluid Dynamics in Porous Media*, Springer Proceedings in Mathematics & Statistics 28, DOI 10.1007/978-1-4614-5055-9_10,

DFM/VFMH methods. This mathematical frame allows us to extend the DSL used for FE and Galerkin methods to lowest-order methods. We focus then on the capability of such language to allow the description and the resolution of various and complex problems with different lowest-order methods. We validate the design of the DSL that we have embedded in C++, on the implementation of several academic problems. We present some convergence results and compare the performance of their implementation with the DSEL to their hand-written counterpart.

1 Introduction

Industrial simulation software has to manage: (1) the complexity of the underlying physical models, usually expressed in terms of a PDE system completed with algebraic closure laws, (2) the complexity of numerical methods used to solve the PDE systems, and finally (3) the complexity of the low-level computer science services required to have efficient software on modern hardware. Robust and effective finite volume (FV) methods as well as advanced programming techniques need to be combined in order to fully benefit from massively parallel architectures (implementation of parallelism, memory handling). Moreover, the above methodologies and technologies become more and more sophisticated and too complex to be handled by physicists alone. Nowadays, this complexity management becomes a key issue for the development of scientific software (Fig. 1).

Some frameworks already offer a number of advanced tools to deal with the complexity related to parallelism in a transparent way. Hardware complexity is hidden and low-level algorithms which need to deal directly with hardware specificity, for performance reasons, are provided. They often offer services to manage mesh data services and linear algebra services which are key elements

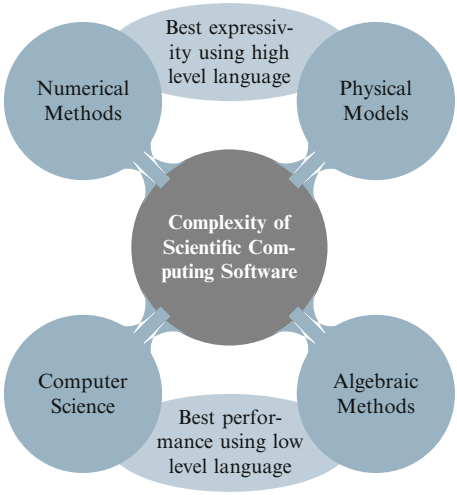

Fig. 1 Complexity management

to have efficient parallel software. Among such kind of framework, the Arcane platform is a parallel C++ framework, co-developed by CEA (Commissariat à l'Energie Atomique) and IFP Energies Nouvelles, designed to develop applications based on 1D, 2D, and 3D unstructured grids. It provides services to manage meshes, groups of mesh elements, discrete variables representing discrete fields on mesh elements, parallelism, and network communication between processors and IO services. A linear algebra layer developed above this platform, provides also a unified way to handle standard parallel linear solver packages such as Petsc, Hypre, MTL4, UBlas, and IFPSolver an in house linear solver package. However, all these frameworks often provide only partial answers to the problem as they only deal with hardware complexity and low-level numerical complexity like linear algebra. The complexity related to discretization methods and physical models lacks tools to help physicists to develop complex applications. New paradigms for scientific software must be developed to help them to seamlessly handle the different levels of complexity so that they can focus on their specific domain. Generative programming, component engineering, and domain-specific languages (either DSL or DSEL) are key technologies to make the development of complex applications easier to physicists, hiding the complexity of numerical methods and low-level computer science services. These paradigms allow to write code with a high-level expressive language and take advantage of the efficiency of generated code for low-level services close to hardware specificities (Fig. 1). Their application to scientific computing has been up to now limited to finite element (FE) methods, for which a unified mathematical framework has been existing for a long time. Such kind of DSL has been developed for finite element or Galerkin methods in projects like `Freefem`, `Getdp`, `Getfem++`, `Sundance`, `Feel++`, and `Fenics` project. They are used for various reasons, teaching purposes, designing complex problems, or rapid prototyping of new methods, schemes, or algorithms, the main goal being always to hide technical details behind software layers and providing only the relevant components required by the user or program [21, 22].

We try to extend this kind of approach to lowest-order methods to solve the PDE systems of geo-modeling applications. These kinds of methods seem to be very promising for geoscience application as they allow to handle general meshes which is an important issue for reservoir and basin modeling. The first extension of FV methods is due to Aavatsmark et al. [1–4] and to Edwards and Rogers [17, 18]) in reservoir simulation. The main idea is to transform the classical two-point flux approximation into a multi-point flux approximation. This idea solves the consistency problem for nonorthogonal meshes but does not guaranty the stability of the resulting method. This can be solved with mimetic finite difference method (MFD) [8, 9] and mixed/hybrid finite volume methods (MHFV) [15, 16, 19]. These methods are elaborated, adding face unknowns and using a variational formulation approach instead of the classical conservative balance approach on each cell. However the lack of a unified mathematical frame was a serious limit to the extension all of these methods to a large variety of problems. A partial answer was recently proposed by Di Pietro in [12, 13], by introducing a new class of methods inspired from nonconforming finite element, see also Di Pietro and

Gratien [14]. These formulations enable to express in a unified way VF multipoint scheme and DFM/VFMH methods and allow to extend them to various problems in fluid and solid mechanics. This consistent unified mathematical frame allows a unified description of a large family of lowest-order methods. It is possible then, as for FE methods, to design of a high-level language inspired from the mathematical notation, that could help physicist to implement their application. We have developed a language based on that frame, which we have embedded in the C++ language. This approach, used in projects like `Feel++`, `Fenics`, or `Sundance`, has several advantages over generating a specific language. Embedded in the C++ language, (1) It avoids the compiler construction complexities, taking advantage of the generative paradigm of the C++ language and allowing grammar checking at compile time. (2) It allows to use other libraries concurrently which is often not the case for specific languages, our implementation heavily relies, in particular, on the tools provided by the `boost` library. (3) It exploits the optimization capabilities of the C++ compiler, thereby allowing to tackle large study cases which is not possible with interpreted language. (4) It allows to mix the object-oriented programming and the functional programming paradigm. New concepts provided by the standard C++0x (the keyword `auto`, lambda functions, ...) make C++ very competitive as its syntax becomes comparable to that of interpreted languages like `Python` or `Ruby` used in projects like `FreeFem++` or `Fenics`, while performance issues remain preserved thanks to compiler optimizations.

The proposed DSEL has been developed on top of Arcane platform [20]. It is based on useful concepts inspired from the unified mathematical frame. We focus on their capability to allow the description and the resolution of various and complex problems with different lowest-order methods. We validate the design of the DSEL on the implementation of different methods on two diffusion problems. We present some convergence results and analyze some performance criteria.

2 Mathematical Setting

Let $\Omega \subset \mathbb{R}^d$, $d \geq 2$, and $\mathscr{T}_h = \{T\}$ be a given mesh partitioning Ω. Mesh faces with a $(d-1)$-dimensional measure, defined by $T_1, T_2 \in \mathscr{T}_h$ such that $F \subset \partial T_1 \cap \partial T_2$ (interface) or $T \in \mathscr{T}_h$ such that $F \subset \partial T \cap \partial \Omega$ (boundary), are, respectively, collected in the set $\mathscr{F}_h^i$ and $\mathscr{F}_h^b$. Let $\mathscr{F}_h \stackrel{\text{def}}{=} \mathscr{F}_h^i \cup \mathscr{F}_h^b$.

For all $k \geq 0$, we define the broken polynomial spaces of total degree $\leq k$ on $\mathscr{S}_h$,

$$\mathbb{P}_d^k(\mathscr{S}_h) \stackrel{\text{def}}{=} \{v \in L^2(\Omega) \mid \forall S \in \mathscr{S}_h,\, v|_S \in \mathbb{P}_d^k(S)\},$$

with $\mathbb{P}_d^k(S)$ given by the restriction to $S \in \mathscr{S}_h$ of the functions in $\mathbb{P}_d^k$.

We introduce trace operators which are of common use in the context of nonconforming FE methods. Let v be a scalar-valued function defined on Ω smooth

enough to admit on all $F \in \mathscr{F}_h$ a possibly two-valued trace. To any interface $F \subset \partial T_1 \cap \partial T_2$ we assign two nonnegative real numbers $\omega_{T_1,F}$ and $\omega_{T_2,F}$ such that

$$\omega_{T_1,F} + \omega_{T_2,F} = 1,$$

and define the jump and weighted average of v at F for a.e. $\mathbf{x} \in F$ as

$$[\![v]\!]_F(\mathbf{x}) \stackrel{\text{def}}{=} v|_{T_1} - v|_{T_2}, \qquad \{v\}_{\omega,F}(\mathbf{x}) \stackrel{\text{def}}{=} \omega_{T_1,F} v|_{T_1}(\mathbf{x}) + \omega_{T_2,F} v|_{T_2}(\mathbf{x}). \tag{1}$$

If $F \in \mathscr{F}_h^b$ with $F = \partial T \cap \partial \Omega$, we conventionally set $\{v\}_{\omega,F}(\mathbf{x}) = [\![v]\!]_F(\mathbf{x}) = v|_T(\mathbf{x})$. The index ω is omitted from the average operator when $\omega_{T_1,F} = \omega_{T_2,F} = \frac{1}{2}$, and we simply write $\{v\}_F(\mathbf{x})$. The dependence on both the point $\mathbf{x}$ and the face F is also omitted from both the jump and average trace operators if no ambiguity arises.

The unified mathematical frame presented in [13,14] allows a unified description of a large family of lowest-order methods. The key idea is to reformulate the method at hand as a (Petrov)–Galerkin scheme based on a possibly incomplete, broken affine space. This is done by introducing a piecewise constant gradient reconstruction, which is used to recover a piecewise affine function starting from cell (and possibly face)-centered unknowns.

For example, we consider the following heterogeneous diffusion model problem:

$$\begin{aligned} -\nabla\cdot(\kappa\nabla u) &= f \quad \text{in } \Omega, \\ u &= 0 \quad \text{on } \partial\Omega, \end{aligned} \tag{2}$$

with source term $f \in L^2(\Omega)$. Here, κ denotes a uniformly elliptic tensor field piecewise constant on the mesh $\mathscr{T}_h$.

The continuous weak formulation reads: Find $u \in [H_0^1(\Omega)]$ such that

$$a(u,v) = b(v) \quad \forall v \in [H_0^1(\Omega)],$$

with

$$a(u,v) \stackrel{\text{def}}{=} \int_\Omega \kappa\nabla u\cdot\nabla v,$$

$$b(v) \stackrel{\text{def}}{=} \int_\Omega f * v.$$

In this framework, a specific lowest-order is defined by (1) Setting $U_h(\mathscr{T}_h)$ and $V_h(\mathscr{T}_h)$ a trial and a test function space. (2) Defining for all $(u_h, v_h) \in U_h \times V_h$ a bilinear form $a_h(u_h, v_h)$ and a linear form $b_h(v_h)$, and (3) solving the discrete problem consists then in finding $u_h \in U_h$ such that:

$$a_h(u_h, v_h) = b_h(v_h) \quad \forall v_h \in V_h.$$

The setting of a discrete function space U_h is based on three main ingredients:

- $\mathscr{T}_h$ the mesh partitioning Ω, $\mathscr{S}_h$ a submesh of $\mathscr{T}_h$ where $\forall S \in \mathscr{S}_h, \exists T_S \in \mathscr{T}_h, S \subset T_S$ (we will consider two choices: the identity $\mathscr{S}_h = \mathscr{T}_h$, and the pyramidal $\mathscr{S}_h = \mathscr{P}_h$ where cells $S \subset T_S$ are built with the center of T and a face $F \subset \partial T_S$).
- $\mathbb{V}_h$ the space of vector of DOF where the components of the vectors can be indexed by the mesh entities (cells, faces, or nodes).
- $\mathfrak{G}_h$ a linear gradient operator that defines for each vector $v \in V_h$ a constant gradient on each element of $\mathscr{S}_h$ a submesh of $\mathscr{T}_h$.

The key idea to get a unifying perspective is to consider lowest-order methods as nonconforming methods based on incomplete broken affine spaces that are defined starting from the space of degrees of freedom (DOFs) $\mathbb{V}_h$. More precisely, we let

$$\mathbb{T}_h \stackrel{\text{def}}{=} \mathbb{R}^{\mathscr{T}_h}, \qquad \mathbb{F}_h \stackrel{\text{def}}{=} \mathbb{R}^{\mathscr{F}_h},$$

and consider the following choices:

$$\mathbb{V}_h = \mathbb{T}_h \text{ or } \mathbb{V}_h = \mathbb{T}_h \times \mathbb{F}_h. \tag{3}$$

The choice $\mathbb{V}_h = \mathbb{T}_h$ corresponds to cell-centered finite volume (CCFV) and cell-centered Galerkin (ccG) methods, while the choice $\mathbb{V}_h = \mathbb{T}_h \times \mathbb{F}_h$ leads to MFD and mixed/hybrid finite volume (MHFV) methods.

The key ingredient in the definition of a broken affine space is a piecewise constant linear gradient reconstruction $\mathfrak{G}_h : \mathbb{V}_h \to [\mathbb{P}^0_d(\mathscr{S}_h)]^d$ with suitable properties. We emphasize that the linearity of $\mathfrak{G}_h$ is a fundamental assumption for the implementation discussed in Sect. 3.

Using the above ingredients, we can define the linear operator $\mathfrak{R}_h : \mathbb{V}_h \to \mathbb{P}^1_d(\mathscr{S}_h)$ such that, for all $\mathbf{v}_h \in \mathbb{V}_h$,

$$\forall S \in \mathscr{S}_h, S \subset T_S \in \mathscr{T}_h, \forall \mathbf{x} \in S, \qquad \mathfrak{R}_h(\mathbf{v}_h)|_S = v_{T_S} + \mathfrak{G}_h(\mathbf{v}_h)|_S \cdot (\mathbf{x} - \mathbf{x}_{T_S}), \tag{4}$$

where v_{T_S} is the component of $\mathbf{v}_h$ indexed by T_S and $\mathbf{x}_{T_S}$ is the barycenter of T_S. The operator $\mathfrak{R}_h$ maps every vector of DOFs $\mathbf{v}_h \in \mathbb{V}_h$ onto a piecewise affine function $\mathfrak{G}_h(\mathbf{v}_h)$ belonging to $\mathbb{P}^1_d(\mathscr{S}_h)$. Hence, we can define a broken affine space as follows:

$$V_h = \mathfrak{R}_h(\mathbb{V}_h) \subset \mathbb{P}^1_d(\mathscr{S}_h). \tag{5}$$

With this framework, the model problem (2) can be solved with various methods:

- The G-method, see [6], is based on an space V_h^{g} defined setting $\mathbb{V}_h = \mathbb{T}_h$, $\mathscr{S}_h = \mathscr{P}_h$ and giving an operator $\mathfrak{G}_h^{\mathrm{g}}$ based on a L-construction.

  This method leads to the following Petrov–Galerkin method:

$$\text{Find } u_h \in V_h^{\mathrm{g}} \text{ s.t. } a_h^{\mathrm{g}}(u_h, v_h) = \int_\Omega f v_h \text{ for all } v_h \in \mathbb{P}^0_d(\mathscr{T}_h),$$

  where $a_h^{\mathrm{g}}(u_h, v_h) \stackrel{\text{def}}{=} \sum_{F \in \mathscr{F}_h} \int_F \{\kappa \nabla_h u_h\} \cdot \mathrm{n}_F [\![v_h]\!]$ with ∇_h broken gradient on $\mathscr{P}_h$.

- The cell-centered Galerkin method, see [11,13], is based on a space V_h^{ccg} defined setting $\mathbb{V}_h = \mathbb{T}_h$, $\mathscr{S}_h = \mathscr{T}_h$ and giving an operator $\mathfrak{G}_h^{\mathrm{ccg}}$ obtained with the Green formula and a trace operator.

  The method reads:

$$\text{Find } u_h \in V_h^{\mathrm{ccg}} \text{ s.t. } a_h^{\mathrm{ccg}}(u_h, v_h) = \int_\Omega f v_h \text{ for all } v_h \in V_h^{\mathrm{ccg}}, \tag{6}$$

  where

$$\begin{aligned} a_h^{\mathrm{ccg}}(u_h, v_h) \stackrel{\mathrm{def}}{=} & \int_\Omega \kappa \nabla_h u_h \cdot \nabla_h v_h \\ & - \sum_{F \in \mathscr{F}_h} \int_F [\{\kappa \nabla_h u_h\}_\omega \cdot \mathrm{n}_F [\![v_h]\!] + [\![u_h]\!] \{\kappa \nabla v_h\}_\omega \cdot \mathrm{n}_F] \\ & + \sum_{F \in \mathscr{F}_h} \eta \frac{\gamma_F}{h_F} \int_F [\![u_h]\!][\![v_h]\!], \end{aligned} \tag{7}$$

  with:

  - ∇_h broken gradient on $\mathscr{T}_h$.
  - The weights in the average operator defined as follows: For all $F \in \mathscr{F}_h^i$ such that $F \subset \partial T_1 \cap \partial T_2$,

$$\omega_{T_1,F} = \tfrac{\lambda_2}{\lambda_1+\lambda_2}, \qquad \omega_{T_2,F} = \tfrac{\lambda_1}{\lambda_1+\lambda_2},$$

    where $\lambda_i \stackrel{\mathrm{def}}{=} \kappa|_{T_i} \mathrm{n}_F \cdot \mathrm{n}_F$ for $i \in \{1,2\}$.
  - $\gamma_F = \frac{2\lambda_1\lambda_2}{\lambda_1+\lambda_2}$ on internal faces $F \subset \partial T_1 \cap \partial T_2$.
  - $\gamma_F = \kappa|_T \mathrm{n}_F \cdot \mathrm{n}_F$ on boundary faces $F \subset \partial T \cap \partial \Omega$.
  - η is a (strictly positive) penalty parameter.

- The hybrid finite volume method, recovering the SUSHI scheme, see[19], [16], and [8,9], is based on the space V_h^{hyb} defined setting $\mathbb{V}_h = \mathbb{T}_h \times \mathbb{F}_h$, $\mathscr{S}_h$ pyramidal and giving the operator $\mathfrak{G}_h^{\mathrm{hyb}}$ obtained with the green formula.

  This method reads:

$$\text{Find } u_h \in V_h^{\mathrm{hyb}} \text{ s.t. } a_h^{\mathrm{sushi}}(u_h, v_h) = \int_\Omega f v_h \text{ for all } v_h \in V_h^{\mathrm{hyb}},$$

  with $a_h^{\mathrm{sushi}}(u_h, v_h) \stackrel{\mathrm{def}}{=} \int_\Omega \kappa \nabla_h u_h \cdot \nabla_h v_h$ and ∇_h broken gradient on $\mathscr{P}_h$.

As in all of these lowest-order methods, gradient reconstructions are piecewise constant, integrals appearing in the defined bilinear forms are evaluated exactly using the barycenter of the mesh item (cell or face) as a quadrature node. This remark is an important point in the implementation details of forms in Sect. 3.

3 Implementation

The framework described in Sect. 2 allows a unified description for a large family of lowest methods and as for FE/DG methods the design of a high-level language inspired from the mathematical notation. Such language enables to express the variational discretization formulation of PDE problem with various methods defining bilinear and linear forms. Algorithms are then generated to solve the problems, evaluating the forms representing the discrete problem. The language is based on concepts (mesh, function space, test trial functions, differential operators) close to their mathematical counterpart. They are the front end of the language. Their implementations use algebraic objects (vectors, matrices, linear operators) which are the back end of the language. Linear and bilinear forms are represented by expressions built with the terminals of the language linked with unary and binary operators (`+,-,*,/,`**dot**`(.,.)`) and with free functions like **grad**`(.)`, **div**`(.)`, `and` **integrate**`(.,.)`. The purpose of these expressions is first to express the variational discretization formulation of the problem but also to solve and find its solution.

In the first part of this section, we present the different C++ concepts defining the front end of our language, their mapping onto their mathematical counterpart and their links with algebraic objects corresponding to the back end of the language. We then introduce the DSEL that enables to manipulate these concepts to build complex expressions close to the mathematical discretization formulation of continuous PDE problems. We finally explain how, evaluating these expressions, we can generate source codes that solve discrete problems.

For our diffusion model problem (2), such DSEL will for instance achieve to express the variational discretization formulation (6) with the programming counterpart in listing 1.

Listing 1 Diffusion problem implementation

```
MeshType Th;
Real K;
auto Vh = newCCGSpace(Th);
auto u = Vh->trial(''U'');
auto v = Vh->test(''V'');
auto lambda = eta*val(gamma)/val(H());
BilinearForm a =
  integrate(allCells(Th),dot(K*grad(u),grad(v))) +
  integrate(allFaces(Th),jump(u)*dot(N(Th),avg(grad(v))) -
                         dot(N(Th),avg(K*grad(u)))*jump(v) +
                         lambda*jump(u)*jump(v);
LinearForm b =
  integrate(allCells(Th),f*v);
```

3.1 Algebraic Back End

In this section we focus on the elementary ingredients used to build the terms appearing in the linear and bilinear forms of Sect. 2, which constitute the back end of the DSEL presented in Sect. 3.3.

3.1.1 Mesh

The mesh concept is an important ingredient of the mathematical frame. Mesh types and data structures are a very standard issue and different kinds of implementation already exist in various framework. We developed above Arcane mesh data structures a **mesh concept** defining (1) `MeshType::dim` the space dimension, (2) the subtypes `Cell`, `Face`, and `Node` for mesh element of dimension, respectively, `MeshType::dim`, `MeshType::dim-1` and 0. Some free functions like `allCells(<mesh>)`, `allFaces(<mesh>)`, `boundaryCells(<mesh>)`, `boundaryFaces(<mesh>)`, and `internalCells(<mesh>)` are provided to manipulate the mesh, to extract different parts of the mesh.

3.1.2 Vector Spaces, Degrees of Freedom, and Discrete Variables

The `class Variable` with template parameters `ItemT` and `ValueT` manages vectors of values of type `ValueT` and provides data accessors to these values with either mesh elements of type `ItemT`, integer ids, or iterators identifying these elements. Instances of the class `Variable` are managed by `VariableMng`, a class that associates each variable to its unique string key label corresponding to the variable name.

3.1.3 Linear Combination, Linear, and Bilinear Contribution

The point of view presented in Sect. 2 naturally leads to a finite element-like assembly of local contributions stemming from integrals over elements or faces. This procedure leads to manipulate local vectors indexed by mesh entities represented by the concept of linear combination
`template<ValueT,ItemT> class LinearCombT`. Associated to an efficient linear algebra, this concept enables to create `LinearContribution` (local vectors) and `BilinearContribution` (local matrices) used in the assembly procedure of the global matrix and vector of the global linear system.

3.2 Functional Front End

3.2.1 Function Spaces

Incomplete broken polynomial spaces defined by (5) are mapped onto C++ types according to the `FunctionSpace` concept. The key role of `FunctionSpace` is to bridge the gap between the algebraic representation of DOFs and the functional representation used in the methods of Sect. 2. This is achieved by the functions **grad** and **eval**, which are the C++ counterparts of the linear operators $\mathfrak{G}_h$ and $\mathfrak{R}_h$, respectively; see Sect. 2. More specifically:

1. For all $S \in \mathscr{S}_h$, **grad** (S) returns a vector-valued linear combination corresponding to the (constant) restriction $\mathfrak{G}_h|_S$.
2. For all $S \in \mathscr{S}_h$ and all $\mathbf{x} \in S$, **eval** $(S, \mathbf{x})$ returns a scalar-valued linear combination corresponding to $\mathfrak{R}_h|_S(\mathbf{x})$ defined according to (4).

The linear combinations returned by **grad** and **eval** can be used to build `LinearContributions` and `BilinearContributions` as described in the previous sections.

A function space types also defines the subtypes `TestFunctionType`, `FunctionType`, and `TrialFunctionType` corresponding to the mathematical notions of discrete functions and test and trial functions in variational formulations. Instances of `TrialFunctionType` and `FunctionType` are associated to a `Variable` object containing a vector of DOFs associated to a string key corresponding to the variable name. For functions, the vector of DOFs is used in the evaluation on a point $x \in \Omega$ while for trial functions, this vector is used to receive the solution of the discrete problem. Test functions implicitly representing the space basis are not associated to any `Variable` objects, neither vector of DOFs. Unlike `FunctionType`, the evaluation of `TrialFunctionType` and `TestFunctionType` is lazy in the sense that it returns a linear combination. This linear combination can be used to build local linear or bilinear contributions to the global system, or enables to postpone the evaluation with the variable data.

3.2.2 Bilinear and Linear Forms

Bilinear and linear forms described in Sect. 2 result from the integration of, respectively, bilinear and linear terms on groups of mesh items. A **BilinearForm** and a **LinearForm** concept have been developed to represent these forms. They enable to store mesh item groups, expressions built with test, trial functions, and unary and binary operators. They are the link between the numerical representation of the problem with forms and its algebraic representation with a matrix and a vector.

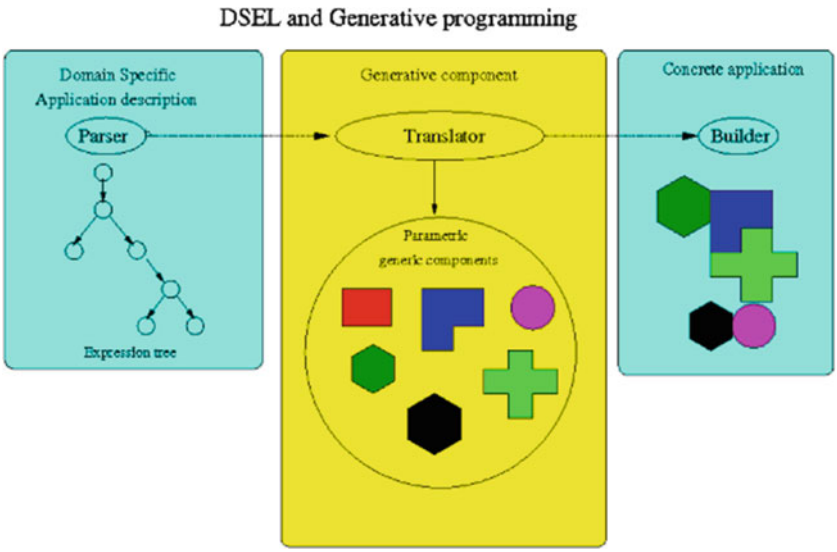

Fig. 2 Generative programming

3.3 DSEL Implementation

The **key ingredients** to design a DSEL are:

1. Meta-programming techniques that consist in writing programs that transform types at compile time.
2. Generic programming techniques that consist in designing generic components composed of abstract programs with generic types.
3. Generative programming techniques that consist in generating concrete programs, transforming types with meta-programs to create concrete types to use with abstract programs of generic components.
4. Expression template techniques [5, 7, 23] that consist in representing problems with expression tree and using tools to describe, parse, and evaluate these trees.

Applying all these techniques, it is possible to represent a problem with an expression tree. Parsing this tree at compile time, using meta-programming tools to introspect the expression, it is possible to select generic components, to link them together to assemble and generate a concrete program (Fig. 2). The execution of this program consists in evaluating the tree at the run time, executing the concrete instance of the selected components to build a linear system and solve it to find the solution of the problem.

Using these principles, we have designed a DSEL that enables to express and define linear and bilinear forms. The terminals of our language are composed of symbols representing C++ objects with base types (real or integer) and with types representing discrete variables, functions, and test and trial functions. Our language

uses the standard C++ binary operators (+,-,*,/), the binary operator **dot**`(.,.)` representing the scalar product of vector expressions, and unary operators representing standard differential operators like **grad**`(.)` and **div**`(.)`. The language is completed by a number of specific keywords **integrate**`(.,.)`, **N**`()`, and **H**`()`.

The **integrate**`(.,.)` keyword associates a collection of mesh entities to linear and bilinear expressions.

N`()` and **H**`()` are free functions returning discrete variable containing, respectively, the precomputed values of n_F and h_F of the mesh faces of $\mathscr{T}_h$.

Our DSEL has been implemented with tools and concepts provided by the Boost::Proto template library, a powerful framework to build DSEL in C++ based on expression templates techniques. This library provides a collection of generic concepts and meta-functions that help to design a DSEL, its grammar and tools to parse and evaluate expressions with a tree representation. We used these tools to design the DSEL front end that enables to create expressions with terminals, unary and binary operators, and predefined free functions used as specific keywords. The grammar of the DSEL is based on tag structures and on meta functions allowing the introspection of the nodes of the expression tree. The DSEL back ends are composed of algebraic structures (matrices, vectors, linear combinations) used in algorithms. We use `Evaluation Context` object, kind of function objects that are passed along expression trees. They associate behaviors to node types; in other words they enable to call specific piece of algorithm regarding the type of the node expression. When an expression is evaluated, the context is invoked at each node of the tree. Algorithms are then implemented as specific expression tree evaluation, as a sequence of piece of algorithms associated to the behavior of the `Evaluation Context` on each node.

Algorithms associated to linear variational formulation were implemented with `LinearContext` and `BilinearContext` objects. These objects, with a reference to a linear system back-end object, allow to build a global linear system with different linear algebra packages.

Let us consider for instance the bilinear form defined in listing 2:

Listing 2 Expression defining a bilinear form

```
BilinearForm ah = integrate(allCells(Th), dot(K*grad(u),grad(v));
```

`allCells(Th)`, `K`, `u`, and `v` are terminals of the language. **integrate**, **dot**, and **grad** are specific keywords of the language. The expression defined in listing 2 has a tree structure which has the following representation (Fig. 3).

When the expression is evaluated, the behavior associated to these context objects can be described as follows:

1. The root node of the expression tree is associated to the tag `tag::`**integrate** composed of an expression (`allCells(Th)`) and the expression (**dot**`(K*`**grad**`(u),`**grad**`(v))`).
2. The integration algorithm consists in iterating on the cell elements of the `allCells(Th)` and evaluating the bilinear expression on each cell. This bilinear expression is composed of:

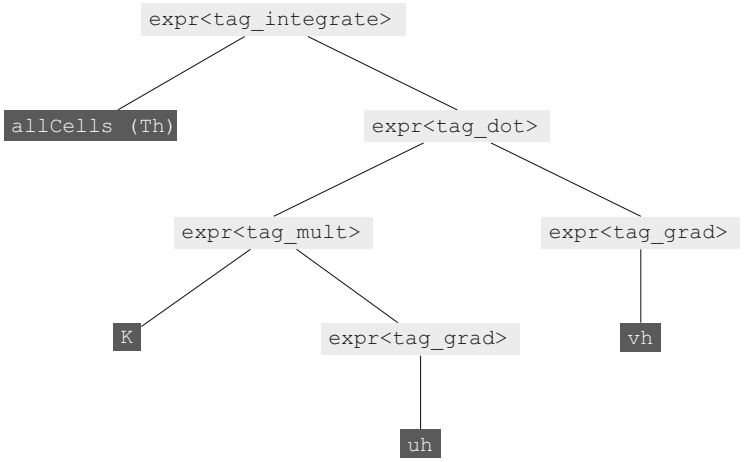

Fig. 3 Expression tree for the bilinear form 2. Expressions are in *light gray*, language terminals in *dark gray*

- A trial function expression: `K*`**grad**`(u)`.
- A test function expression: **grad**`(v)`.
- A binary operator associated to the tag: `tag::`**dot**.

With a linear context object, the evaluation of the trial function and of the test function on a cell returns two linear combination objects which, associated to the binary operator tag, lead to a bilinear contribution which is a local matrix contributing to the global linear system of the linear context with a factor equal to the measure of the cell.

This algorithm is generated with the simple following template function:

```
template<typename ItemT,
         typename BilinearExprT,
         typename LinearContextT>
void integrate(Mesh const& mesh,
               GroupT<ItemT> const& group,
               BilinearExprT const& expr,
               LinearContextT& ctx)
{
  static const Context::ePhaseType
       phase = LinearContextT::phase_type;
  typedef tag_of<BilinearExprT>::type tag_op;
  auto test = TestFunction(expr);
  auto trial = TrialFunction(expr);
  auto system = ctx.getSystem();
  std::for_each(group.begin(),
                group.end(),
                [&system,&mesh](ItemT& cell)
```

```
  {
    assemble<tag_op, phase>(system,                    //! linear system
                            measure(mesh, cell), //! cell measure
                            proto::eval(trial, cell), //! trial linear com-
bination
                            proto::eval(test, cell)); //! test linear com-
bination
  }
}
```

In the same way the evaluation of a linear form expression with a linear context leads to the construction of the right hand side of a global linear system.

Once built, the global linear system can be solved with a linear system solver provided by the linear algebra layer.

3.3.1 Boundary Condition Management

In Sect. 2 we have presented only homogeneous boundary conditions. In fact most of these methods are easily extended to more general boundary conditions. Let $\partial\Omega_d \subset \partial\Omega$ and $\partial\Omega_n \subset \partial\Omega$, and let us consider the following conditions:

$$u = g \text{ on } \partial\Omega_d,\ g \in L^2(\partial\Omega_d) \tag{8}$$

$$\frac{\partial u}{\partial n} = h \text{ on } \partial\Omega_n,\ h \in L^2(\partial\Omega_n) \tag{9}$$

To manage such conditions, we introduce (1) Extra DOF on boundary faces, (2) Constraints on the bilinear form, or (3) Extra terms in the linear form. These constraints and terms lead to add or remove some equations in the matrix and to add extra terms in the right hand side of the linear system.

In our DSEL, the keywords **trace**`(u)` enable to recover DOF on mesh elements, and **on**`(..,.)` enable to had constraints on group of on mesh elements. For example, with the hybrid method the boundary conditions (8) and (9) are expressed with the expressions of listing 3.

Listing 3 Boundary conditions management

```
BilinearForm ah = integrate(allCells(Th), dot(K*grad(u),grad(v)) ;
LinearForm bh = integrate(allCells(Th),f*v) ;

//Dirichlet condition on ∂Ω_d
ah += on(boundaryFaces(Th,''dirichlet''),trace(u)=g) ;

//Neumann condition on ∂Ω_n
bh += integrate(boundaryFaces(Th,''neumann''),h*trace(v)) ;
```

4 Applications

In this section we validate the design of our DSEL. We implement and compare different lowest-order methods on a pure diffusion problem then present the results of a diffusion problem with a heterogenous permeability field coming from a more realistic reservoir model.

The prototypes implemented are compiled with the `gcc` 4.5 compiler with the following compile options:

```
-03 -fno-builtin
-mfpmath=sse -msse -msse2 -msse3 -mssse3 -msse4.1
-msse4.2 -fno-check-new -g -Wall -std=c++0x
--param -max-inline-recursive-depth=32
--param max-inline-insns-single=2000
```

The benchmark test cases are run on a work station with a quad-core Intel Xeon processor Genuine Intel W3530, 2.80GHz, 8MB for cache size.

4.1 Pure Diffusion

We present for the diffusion problem different variational discrete formulations that we compare to their programming counterpart.

We present some numerical results, run on a family of meshes of increasing sizes $h \in \mathscr{H}$. We list in tables the value of different error norms regarding an analytical solution. For each kind of error, we estimate the order of convergence as $\text{order} = d \ln(e_1/e_2) / \ln\left(\text{card}(\mathscr{T}_{h_2})/\text{card}(\mathscr{T}_{h_1})\right)$, where e_1 and e_2 denote, respectively, the errors committed on $\mathscr{T}_{h_1}$ and $\mathscr{T}_{h_2}$, $h_1, h_2 \in \mathscr{H}$. We check the theoretical convergence results detailed in [11].

To evaluate errors, we consider the norms

$$\|u\|_{L^2}^2 = \int_\Omega u^2 \quad \text{and} \quad \|u\|_L^2 = \sum_{T \in \mathscr{T}_h} \sum_{F \in \mathscr{F}_T} \int_F \frac{1}{d_{F,T}^2} \mathfrak{T}(u)^2,$$

where $\mathfrak{T}(u)$ is a trace operator on mesh faces, and $d_{F,T}$ is the distance of the center of a cell T to a face $F \subset \partial T$.

To analyze the performance of the framework, we evaluate the overhead of the language, the relative part of algebraic computations (defining, building, and solving linear systems) and linear combination computations, studying the following criteria:

- t_{start} the time to precompute trace and gradient operators, to build the expression tree describing linear and bilinear forms.
- t_{def} the time to compute the linear system profile.

- t_{build} the time to fill the linear system evaluating the expression tree.
- t_{solve} the time to solve the linear system with linear algebra layer.
- N_{it} the number of iterations of the linear solver, the ILU0 preconditioned BiCGStab algorithm with 10^{-6} tolerance.
- N_{nz} the number on nonzero entries of the linear system of the test case.

We compare all these times in seconds to $t_{ref} = \frac{t_{solver}}{N_{it}}$ the average time of one solver iteration approximatively equal to a fixed number of matrix vector multiplication operations.

In iterative methods (time integration, nonlinear solver), t_{start} and t_{def} correspond to computation phases only done once before the first iterative step, while the t_{build} corresponds to a computation phase done at each step. A careful attention is paid to the t_{build} results specially for such algorithms. *Nnz* is an important criterion to evaluate the amount of memory used by the method.

We consider the problem

$$\begin{cases} -\triangle u = 0 & \text{in } \Omega \subset \mathbb{R}^3, \\ u = g & \text{on } \partial\Omega. \end{cases}$$

The continuous weak formulation reads: find $u \in [H_0^1(\Omega)]$ such that

$$a(u,v) = 0 \quad \forall v \in [H_0^1(\Omega)],$$

with

$$a(u,v) \stackrel{\text{def}}{=} \int_\Omega \nabla u \cdot \nabla v.$$

The discrete formulations of the problem with the G-method, the ccG-method, and the hybrid method defined in Sect. 2 are represented by the definition of the bilinear forms a_h^{g}, a_h^{ccg}, and a_h^{hyb}. We can compare them to their programming counterpart in listings 4–6.

Listing 4 C++ implementation of a_h^{g} and b_h

```
MeshType Th; // declare T_h
BoundaryFaceVarType g; // declare boundary values
auto Vh = newP0Space(Th);
auto Uh = newGSpace(Th);
auto u = Uh->trial(``U'');
auto v = Vh->test(``V'');
BilinearForm ah_g =
 integrate(allFaces(Th),dot(N(),avg(grad(u)))*jump(v));
ah_g += on(boundaryfaces(Th),trace(u)=g) ;
```

Listing 5 C++ implementation of a_h^{ccg}

```
MeshType Th; // declare T_h
BoundaryFaceVarType g; // declare boundary values
auto Uh = newCCGSpace(Th);
auto u = Uh->trial(``U'');
auto v = Uh->test(``V'');
auto lambda = eta*gamma/H();
BilinearForm ah_ccg =
  integrate(allCells(Th),dot(grad(u),grad(v))) +
  integrate(allFaces(Th),-jump(u)*dot(N(),avg(grad(v)))
                         -dot(N(),avg(grad(u)))*jump(v)
                         +lambda*jump(u)*jump(v);
ah_ccg += on(boundaryfaces(Th),trace(u)=g) ;
```

Listing 6 C++ implementation of a_h^{hyb}

```
MeshType Th; // declare T_h
BoundaryFaceVarType g; // declare boundary values
auto Uh = newHybridSpace(Th);
auto u = Uh->trial(``U'');
auto v = Uh->test(``V'');
BilinearForm ah_hyb =
 integrate(allFaces(Th),dot(grad(u),grad(v));
ah_hyb += on(boundaryfaces(Th),trace(u)=g) ;
```

We consider the analytical solution $u(x,y,z) = sin(\pi x)sin(\pi y)sin(\pi z)$ of the diffusion problem on the square domain $\Omega = [0,1]^3$ with $f(x,y,z) = 3\pi u(x,y,z)$.

Tables 1–3 list the errors in the L^2 and L norm of, respectively, the G-method, the ccG-method, and the hybrid method.

In Fig. 4, we compare convergence error of the G-method, the ccG-method, the hybrid method, and a standard hand written L-Scheme FV method.

Table 1 Diffusion test case: G-method

card($\mathcal{T}_h$)	h	$\|u-u_h\|_L$	Order	$\|u-u_h\|_{L^2(\Omega)}$	Order
1,000	1.00e−01	1.58e−02		2.92e−03	
8,000	5.00e−02	3.96e−03	2.	7.28e−04	2.
64,000	2.50e−02	9.89e−04	2.	1.82e−04	2.
125,000	1.25e−02	6.32e−04	2.	1.16e−04	2.

Table 2 Diffusion test case: ccG-method

card($\mathcal{T}_h$)	h	$\|u-u_h\|_L$	Order	$\|u-u_h\|_{L^2(\Omega)}$	Order
1,000	1.00e−01	3.1474e−02		5.3866e−03	
8,000	5.00e−02	7.8977e−03	1.99	1.4257e−03	1.92
64,000	2.50e−02	1.9763e−03	2.	3.6157e−04	1.95
512,000	1.25e−02	1.2649e−03	2.	2.3180e−04	1.95

Table 3 Diffusion test case: hybrid method

card($\mathcal{T}_h$)	h	$\|u-u_h\|_L$	Order	$\|u-u_h\|_{L^2(\Omega)}$	Order
1,000	1.00e−01	1.58e−02		2.92e−03	
8,000	5.00e−02	3.95e−03	2.	7.28e−04	2.01
64,000	2.50e−02	9.87e−04	2.	1.82e−04	2.
512,000	1.25e−02	6.32e−04	2.	1.16e−04	2.

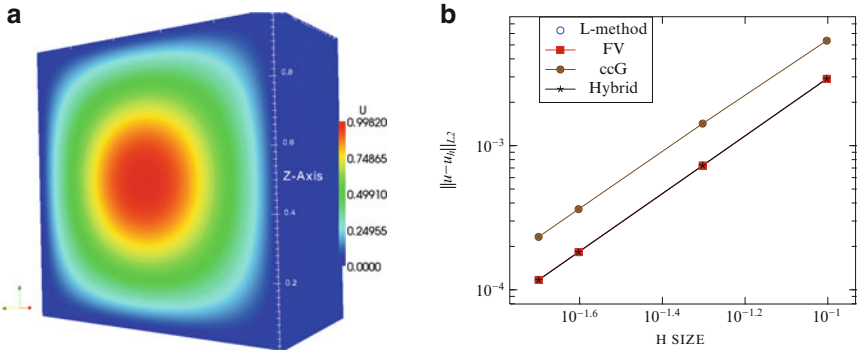

3D view convergence curves

Fig. 4 Diffusion problem

Table 4 Diffusion test case: G-method performance results

card($\mathcal{T}_h$)	N_{it}	N_{nz}	t_{start}	t_{build}	t_{solve}	t_{ref}	t_{start}/t_{ref}	t_{build}/t_{ref}
1,000	4	16,120	8.8987e−02	7.9980e−03	3.0000e−03	7.50e−04	118.65	10.66
8,000	8	140,240	6.0191e−01	6.4990e−02	1.6997e−02	2.12e−03	283.30	30.59
64,000	14	1,168,480	4.8033e+00	6.2190e−01	2.0097e−01	1.44e−02	334.61	43.32
125,000	25	2,300,600	7.0929e+00	1.1738e+00	5.9191e−01	2.37e−02	299.58	49.58

Table 5 Diffusion test case: ccG-method performance results

card($\mathcal{T}_h$)	N_{it}	N_{nz}	t_{start}	t_{build}	t_{solve}	t_{ref}	t_{start}/t_{ref}	t_{build}/t_{ref}
1,000	3	117,642	6.5990e−02	9.2986e−02	3.0995e−02	1.03e−02	6.39	9
8,000	5	1,145,300	5.2292e−01	8.0088e−01	2.9596e−01	5.92e−02	8.83	13.53
64,000	8	10,114,802	4.1344e+00	6.9929e+00	3.0625e+00	3.83e−01	10.8	18.27
125,000	10	20,017,250	8.1658e+00	1.3516e+01	6.3850e+00	6.39e−01	12.79	21.17

In Tables 4–7, we compare the performance of each methods. The analysis of these results shows that the G-method is comparable to the hand written FV method and the language implementation does not contribute to extra cost. The G-method and the hybrid method have equivalent convergence order. A closer look to the N_{nz} column shows that the ccG-method requires much more nonzero entries for the linear system than the G-method and the hybrid method, and we can see the effect on the cost of the linear system building phase which is more important for the ccG-method than for the G-method.

Table 6 Diffusion test case: hybrid-method performance results

card($\mathcal{T}_h$)	N_{it}	N_{nz}	t_{start}	t_{build}	t_{solve}	t_{ref}	t_{start}/t_{ref}	t_{build}/t_{ref}
1,000	7	16,120	4.6993e−02	4.0000e−03	2.1997e−02	3.14e−03	14.95	1.27
8,000	17	140,240	3.4095e−01	2.5996e−02	1.6098e−01	9.47e−03	36.01	2.75
64,000	33	1,168,480	2.8686e+00	2.1197e−01	2.4106e+00	7.30e−02	39.27	2.9
125,000	50	5,563,700	5.2122e+00	3.8094e−01	4.5323e+00	9.06e−02	57.5	4.2

Table 7 Diffusion test case: standard hand-written performance results

card($\mathcal{T}_h$)	N_{it}	N_{nz}	t_{start}	$t_{def+build}$	t_{solve}	t_{ref}	t_{start}/t_{ref}	t_{build}/t_{ref}
1,000	4	16,120	4.899e−02	3.399e−02	3.998e−03	1.00e−03	49.01	34.01
8,000	7	140,240	3.519e−01	2.149e−01	3.399e−02	4.86e−03	72.47	44.26
64,000	13	1,168,480	2.786e+00	1.861e+00	3.489e−01	2.68e−02	103.8	69.34
125,000	16	9,536,960	5.338e+00	3.893e+00	7.688e−01	4.81e−02	111.09	81.02

The inspection of the columns t_{start}/t_{ref} and t_{build}/t_{ref} shows that the implementation remains scalable regarding the size of the problem.

4.2 SPE10 Test Case

The test case is based on data taken from the second model of the 10^{th} SPE test case [10]. The geological model is a $1,200 \times 2,200 \times 170\,ft$ block discretized with a regular Cartesian grid with $60 \times 220 \times 85$ cells. This model is a part of a Brent sequence. The maps of porosity, horizontal and vertical permeability can be downloaded from the web site of the project [24].

Let Ω be the domain define by the layer 85 of the grid, $\partial\Omega_{xmin}$ and $\partial\Omega_{xmax}$, the left and right boundary of the layer. We consider the following heterogeneous diffusion model problem:

$$\begin{aligned} -\nabla\cdot(\kappa\nabla u) &= 0 && \text{in } \Omega, \\ u &= P_{min} = -10 && \text{on } \partial\Omega_{xmin}, \\ u &= P_{max} = 10 && \text{on } \partial\Omega_{xmax}, \\ \frac{\partial u}{\partial n} &= 0 && \text{on } \partial\Omega \setminus \{\partial\Omega_{xmin} \cup \partial\Omega_{xmax}\} \end{aligned} \tag{10}$$

where κ is associated to the map of the horizontal permeability field of the layer 85.

The discrete formulations of this problem (10) have been implemented with the hybrid method defined in Sect. 2 as in listing 7

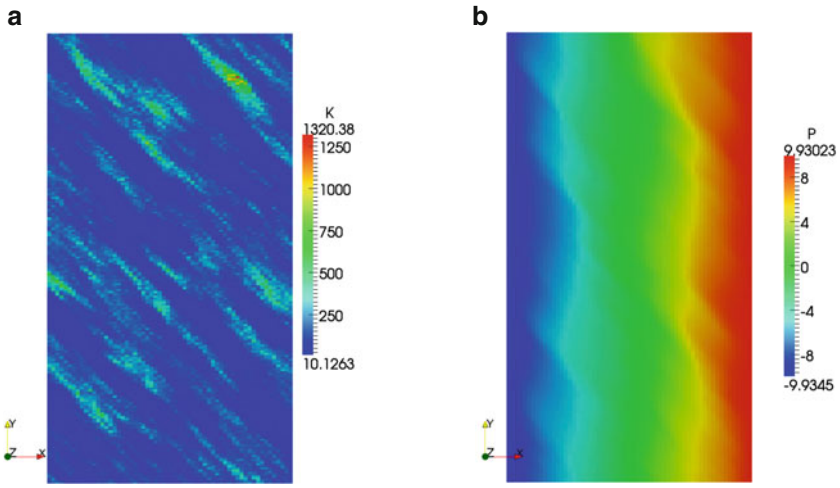

Fig. 5 SPE10 (**a**) permeability field and (**b**) pressure solution

Listing 7 C++ implementation of a_h^{hyb}

```
MeshType Th; // declare T_h
Real Pmin = -10, Pmax=10 ;
auto Uh = newHybridSpace(Th);
auto u = Uh->trial(''U'');
auto v = Uh->test(''V'');
BilinearForm ah_hyb =
  integrate(allFaces(Th),k*dot(grad(u),grad(v));
  ah_hyb += on(boundaryFaces(Th,''xmin''),trace(u)=Pmin) ;
  ah_hyb += on(boundaryFaces(Th,''xmax''),trace(u)=Pmax) ;
```

In Fig. 5, we have a 2D view of the permeability field and of the solution of the problem.

5 Conclusion and Perspectives

Our DSEL for lowest-order methods allows to describe and solve various diffusion problems. Different numerical methods recovering standard methods (L-scheme, ccG, Sushi method) have been implemented with a high-level language close to the one used in the unified mathematical framework. The analysis of the performance results of our study cases shows that the overhead of the language is not important regarding standard hand written codes.

In future works, we plan to extend our DSEL to take into account nonlinear formulations hiding the complexities of derivatives computation with Frechet's derivatives and to address new business applications with linear elasticity, poro-mechanic or dual medium model.

Within the HAMM project (hybrid architecture and multilevel model), we handle multi-level methods and illustrate the interest of our approach to take advantage of the performance of new hybrid hardware architecture with GP-GPU.

References

1. Aavatsmark, I., Barkve, T., Bøe, Ø., Mannseth, T.: Discretization on non-orthogonal, curvilinear grids for multi-phase flow. In: Christie, M.A., Farmer, C.L., Guillon, O., Heinmann, Z.E. (eds.) Proceedings of the 4th European Conference on the Mathematics of Oil Recovery, Norway (1994)
2. Aavatsmark, I., Barkve, T., Bøe, Ø., Mannseth, T.: Discretization on non-orthogonal, quadrilateral grids for inhomogeneous, anisotropic media. J. Comput. Phys. **127**, 2–14 (1996)
3. Aavatsmark, I., Barkve, T., Bøe, Ø., Mannseth, T.: Discretization on unstructured grids for inhomogeneous, anisotropic media, part I: derivation of the methods. SIAM J. Sci. Comput. **19**, 1700–1716 (1998)
4. Aavatsmark, I., Barkve, T., Bøe, Ø., Mannseth, T.: Discretization on unstructured grids for inhomogeneous, anisotropic media, part II: discussion and numerical results. SIAM J. Sci. Comput. **19**, 1717–1736 (1998)
5. Abrahams, D., Gurtovoy, I.: C++ template metaprogramming: concepts, tools, and techniques from Boost and beyond. In: C++ in Depth Series. Addison-Wesley Professional, Boston (2004)
6. Agélas, L., Di Pietro, D.A., Droniou, J.: The G method for heterogeneous anisotropic diffusion on general meshes. M2AN Math. Model. Numer. Anal. **44**, 597–625 (2010)
7. Aubert, P., Di Césaré, N.: Expression templates and forward mode automatic differentiation. In: Corliss, G., Faure, C., Griewank, A., Hascoët, L., Naumann, U. (eds.) Computer and Information Science, pp. 311–315. Springer, New York (2001)
8. Brezzi, F., Lipnikov, K., Shashkov, M.: Convergence of mimetic finite difference methods for diffusion problems on polyhedral meshes. SIAM J. Numer. Anal. **45**, 1872–1896 (2005)
9. Brezzi, F., Lipnikov, K., Simoncini, V.: A family of mimetic finite difference methods on polygonal and polyhedral meshes. Math. Mod. Meth. Appl. Sci. **15**, 1533–1553 (2005)
10. Christie, M.A., Blunt, M.J.: Tenth SPE comparative solution project: a comparison of upscaling techniques. In: SPE Reservoir Simulation Symposium, Houston, TX, pp. 308–317 (2001)
11. Di Pietro, D.A.: Cell centered Galerkin methods. C. R. Acad. Sci. Paris Ser. I **348**, 31–34 (2010)
12. Di Pietro, D.A.: Cell centered Galerkin methods for diffusive problems. ESAIM Math. Model. Numer. Anal. **46**, 111–144 (2012)
13. Di Pietro, D.A.: A compact cell-centered Galerkin method with subgrid stabilization. C. R. Acad. Sci. Paris Ser. I **349** 93–98 (2011)
14. Di Pietro, D.A., Gratien, J.-M.: Lowest order methods for diffusive problems on general meshes: a unified approach to definition and implementation. In: Fořt, J., Fürst, J., Halama, J., Herbin, R., Hubert, F. (eds.) Finite Volumes for Complex Applications VI: Problems and Perspectives, pp. 803–820. Springer, Heidelberg (2011)
15. Droniou, J., Eymard, R.: A mixed finite volume scheme for anisotropic diffusion problems on any grid. Num. Math. **105**, 35–71 (2006)
16. Droniou, J., Eymard, R., Gallouët, T., Herbin, R.: A unified approach to mimetic finite difference, hybrid finite volume and mixed finite volume methods. Math. Models Methods Appl. Sci. **20**, 265–295 (2010)

17. Edwards, M.G., Rogers, C.F.: A flux continuous scheme for the full tensor pressure equation. In: Christie, M.A., Farmer, C.L., Guillon, O., Heinmann, Z.E. (eds.) Proceedings of the 4th European Conference on the Mathematics of Oil Recovery, Norway (1994)
18. Edwards, M.G., Rogers, C.F.: Finite volume discretization with imposed flux continuity for the general tensor pressure equation. Comput. Geosci. **2**, 259–290 (1998)
19. Eymard, R., Gallouët, Th., Herbin, R.: Discretization of heterogeneous and anisotropic diffusion problems on general nonconforming meshes SUSHI: a scheme using stabilization and hybrid interfaces. IMA J. Numer. Anal. **30**, 1009–1043 (2010)
20. Grospellier, G., Lelandais, B.: The Arcane development framework. In: Proceedings of the 8th Workshop on Parallel/High-Performance Object-Oriented Scientific Computing, POOSC '09, vol. 4. p. 11 (2009)
21. Prud'homme, C.: A domain specific embedded language in C++ for automatic differentiation, projection, integration and variational formulations. Sci. Program. **2**, 81–110 (2006)
22. Prud'homme, C.: Life: overview of a unified C++ implementation of the finite and spectral element methods in 1D, 2D and 3D. In: Kågström, B., Elmroth, E., Dongarra, J.J., Waśniewski J. (eds.) Lecture Notes in Computer Science, vol. 4699, pp. 712–721. Springer, Heidelberg (2006)
23. Veldhuizen, T.: Using C++ template metaprograms. C++ Report **7**, 36–43 (1995)
24. Web site for the 10th SPE Comparative Solution Project: www.spe.org/csp/ Accessed On Sep 2000

Non-Darcian Effects on the Flow of Viscous Fluid in Partly Porous Configuration and Bounded by Heated Oscillating Plates

S. Panda, M.R. Acharya, and A. Nayak

Abstract This chapter deals with the fluid flow and heat transfer in a channel partially filled with porous material bounded by parallel heated oscillating plates. The Darcy–Forchheimer and the Navier–Stokes equations are employed in the porous and clear fluid domains, respectively. At the interface, the flow boundary condition imposed is a stress jump together with a continuity of velocity. The thermal boundary condition is continuity of temperature and heat flux. Solutions for the flow velocity and the solutions which take into account the convection term for the temperature field are obtained numerically. The effects of permeability parameter, Prandtl number, Reynolds number, Forchheimer coefficient, viscosity ratio and thermal conductivity ratio on the flow fields, skin friction, and heat transfer have been discussed. The results of the numerical calculations show good agreement with the analytical results for the simplified Darcy flow velocity.

1 Introduction

Analysis of fluid flow and heat transfer in porous medium or in partly porous configurations between two parallel plates has been a subject of fundamental importance. It is relevant to a lot of industrial applications such as heat exchangers, electronic cooling, heat pipes and many important thermal engineering applications.

S. Panda (✉)
NIT Calicut, NIT(P.O)-673601, Calicut, India
e-mail: satyanand@nitc.ac.in

M.R. Acharya
OUAT, Bhubaneswar-751003, India
e-mail: manasranjan_acharya@yahoo.co.in

A. Nayak
Silicon Institute of Technology, Bhubaneswar-751024, India,
e-mail: anitta_nayak@yahoo.co.in

J.A. Ferreira et al. (eds.), *Modelling and Simulation in Fluid Dynamics in Porous Media*, Springer Proceedings in Mathematics & Statistics 28, DOI 10.1007/978-1-4614-5055-9_11,

In many of such aforesaid applications Darcy's model (see, e.g., [23, 33]) is used to represent the fluid flow in porous media. This model equation describes the relation between the rate of flow and pressure gradient through porous medium. But, it has been observed that the Darcy model is not compatible with the existence of wall-bounded porous medium (Beavers et al. [4], Beavers et al. [5]). It has been also observed that proportionality between pressure gradient and fluid velocity does not hold for high-velocity fluid flow in porous media [13]. This phenomenon has been the subject of many theoretical and experimental investigations. Thus, in order to describe more complex situation, for example, to incorporate inertial effects and high-velocity flow, Darcy's law has been generalized for many such behaviors (see the exhaustive list of early works in [23]). Many earlier and recent investigations are mainly divided into two parts: firstly, to establish an upper bound (according to most of experiment critical value of Reynolds numbers Re in the range 1 to 15) for the range of validity of Darcy's equation and to provide relationship which predicts the nonlinear flow behavior [10]; secondly, to provide a physical basis for the generalized equation of motion and to identify mechanism which is responsible for the nonlinear flow behavior.

Opinions on the mechanism responsible for the onset of non-linearity at high flow velocities are diverse. Early descriptions of high-velocity flow attributing to the nonlinearity are due to the occurrence of turbulence. However, experiments have indicated that the onset of turbulence occurs at much higher velocity, i.e., Re $\approx$ 300 (Dybbs and Edwards [10]). Thus deviations from Darcy's law are not solely due to turbulence. They may be due to microscopic inertial forces. This concept has been widely accepted [7]. The rise of nonlinear terms are also due to increase of microscopic drag forces on the pore walls. The Forchheimer type of equations presented here support this point of view. In the most commonly used Forchheimer model inertia appears as a drag proportional to the square of the velocity [16]. In [4, 5] the authors have shown experimentally that for high velocity a quadratic term in the Darcy law is required for a fluid flow through porous medium bounded by wall and hence a modified form of Darcy's equation has been used. Joseph et al. [16] later presented Forchheimer modification of the Darcy law. Darcy–Forchheimer model in the context of forced convection partly filled with porous configurations has been studied by Kuznetsov [18, 19].

Considerable attention has also been given to the fluid flow in parallel-plate configuration, where fluid flow is induced by the motion of the plates. Sekharan et al. [29] have studied the unsteady flow between two oscillating plates and further it has been studied by Hayat [14] in the context of dipolar fluid. Debnath et al. [8] explained the flow between two oscillating plates in connection with hydromagnetic flow of a dusty fluid. Bujurke et al. [6] have included second-order fluid in a single domain (combining the terms for porous and fluid domain). Transport phenomena in a composite domain consisting of a porous layer exchanging momentum, heat, and/or constituents with an adjacent fluid layer are encountered in a wide range of industrial applications like thermal insulation, filtration processes, dendritic solidification, storage of nuclear waste, and spreading on porous substrate. Applications are extended to environmental problems like geothermal system, benthic

boundary layers, and ground water pollution. Recently a brief overview on natural convection in partially porous media (saturated) has been reported by Gobin and Goyeau [12]. Their discussion mostly includes clear fluid region described by the Stokes equation and momentum equation in the homogeneous porous layer by the Darcy law. The analytical solutions of the fluid flow and heat transfer of the viscous fluid in a partly porous configuration bounded by two oscillating plates have been recently reported by Sharma et al. [30]. Darcy's model is employed in their work to study the fluid velocity within the plates and the rate of heat transfer on the plates. Drag effects on the flow and heat transfer in such fluid and solid configuration have not been considered and therefore corresponding Darcy one-dimensional linear model is solved analytically. There is a lot of discussion [22] regarding inclusion of viscous dissipation term in energy equation. Hassanizadeh and Gray [13] pointed out that macroscopic intrafluid stress terms are not important in porous media flow and that in the case of very coarse soil with low value of specific surface of the solid phase and near the medium boundaries intrafluid stress terms are comparable to drag forces. Effects of viscous dissipation term have been studied by Murty and Singh [21] and they found that effect of viscous dissipation increases as the flow region changes from non-Darcy regime to Darcy regime. Aydin and Kaya [2] published a paper in which viscous dissipation term was included in energy equation. They observed that viscous dissipation enhances heat transfer for wall cooling case and reduces heat transfer for wall heating case. All such discussions were made in non-Darcian flow regime in a porous medium. After this paper was published Rees and Magyari [28] published a comment by stating that in the free stream region the viscous dissipation term $(\nu/c_p)(\partial u/\partial y)^2$ will be zero in the presence of $(\nu/Kc_p)u^2$. Here ν is the kinematic viscosity and the definition of the symbols K, c_p, u, and y is given in Eqs. 3–4. According to them in case of thermal equilibrium between porous medium and wall the first term will behave like a heat generation source and create heating effect like the adiabatic heating observed for a clear fluid. In a reply to Rees and Magyari's comment Aydin and Kaya [3] opined that viscous dissipation term would be included with Forchheimer term in the boundary layer region.

Rajagopal [27], while studying hierarchies of approximate models, proposed several models for flow of fluids in porous medium. One such model that can result under some assumptions is the Darcy–Forchheimer model. Some of the important assumptions considered in his study are:

- Only interacting forces that come into play are due to frictional forces, which the fluid encounters at the boundary of the pore. This is a drag-like force proportional to the difference in velocity between two constituents and the drag coefficient is a constant quantity.
- Frictional effects within the fluid due to viscosity are neglected.
- Due to slowness of fluid inertial nonlinearity can be ignored.

The assumption that the effects of viscosity can be neglected does not mean that fluid has no viscosity. First and second assumptions together imply that the viscosity of fluid and roughness of solid surface lead to greater frictional

resistance(dissipation) at the porous boundaries of solid than the frictional resistance in the fluid. Forchheimer pointed out that deviation from Darcy's law was largely due to kinetic effect of fluid. Accordingly kinetic energy term $(\rho C_F/\sqrt{K})u^2$ is included in Darcy's law. The definition of symbols ρ and C_F is defined in Eq. 3.

This presentation deals more specifically with problems of fluid flow and heat transfer in a channel involving clear fluid domain and porous domain. The flow within the porous domain is described by Darcy–Forchheimer model and the flow in clear fluid domain is formulated by Navier–Stokes equations. The heat convection and Forchheimer drag effects are studied particularly at low Reynolds number. The transition from clear fluid domain to porous domain is defined by the spatial variation of the thermophysical properties. In Sect. 2 governing equations for fluid flow in clear fluid domain and porous domain are formulated. Section 3 is devoted to solution procedure. Results, discussion and physical interpretations are given in Sect. 4 and finally conclusions are embedded in Sect. 5. The analytical results for the simplified Darcy one-dimensional linear equations of motion for velocity are given in the Appendix.

2 Governing Equations

A typical flow scenario is illustrated in Fig. 1: it shows the flow of a fully developed laminar flow in a region partially filled with porous medium of finite thickness of size h bounded by two parallel plates in the presence of oscillating wall temperature. The region between two plates is filled with fluid and initially both the fluid and plates are at rest. Flow is then induced by the motion of the plate in its own plane. Entire fluid region is divided equally into two regions, one is clear fluid region bounded by an upper wall and an interface and the other is the porous fluid region bounded by an interface and the bottom wall. The bottom and upper plates lie at $y^* = -h$ and $y^* = h$, respectively. The interface of the two regions lies at $y^* = 0$. The horizontal coordinate x^* is taken along the interface with y^* perpendicular to it. The fluid is assumed incompressible and Newtonian and the porous medium is isotropic and homogeneous. Let us consider two domain approaches in which the plates are long, impermeable and oscillating with uniform velocity u_0 and frequency w^*. The length of the channel is larger than the height. So buoyancy effect is safely neglected here.

The set of governing equations for the flow in the clear fluid region neglecting oscillatory body force can be presented as

$$\rho \frac{\partial u_1^*}{\partial t^*} = \mu_1 \frac{\partial^2 u_1^*}{\partial y^{*2}}, \quad 0 < y^* < h \tag{1}$$

$$\rho c_p \left(\frac{\partial T_1^*}{\partial t^*} + u_1^* \frac{\partial T_1^*}{\partial y^*} \right) = k_1 \frac{\partial^2 T_1^*}{\partial y^{*2}} + \mu_1 \left(\frac{\partial u_1^*}{\partial y^*} \right)^2, \quad 0 < y^* < h, \tag{2}$$

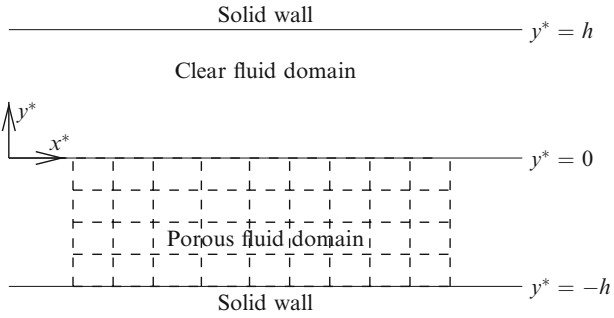

Fig. 1 Sketch of flow geometry

in which t^* is time, ρ is the density of the fluid, and c_p is the specific heat at constant pressure. Here, u_1^*, T_1^*, μ_1, and k_1 are the fluid velocity, temperature, coefficient of viscosity and thermal conductivity, respectively. Equation 2 is a thermal energy equation in clear fluid domain. The derivation of energy equation can be found, for example, in [1]. The index '1' is chosen here to specify the notations of the clear fluid domain. The index '2' will be used later for the porous domain. In the above equations the asterisk(*) implies dimensional variables.

The governing equations in the porous domain are the momentum equation which is due to the Darcy–Forchheimer equation and the temperature equation and can be given as

$$\rho \frac{\partial u_2^*}{\partial t^*} = \mu_2 \frac{\partial^2 u_2^*}{\partial y^{*2}} - \frac{\mu_1}{K^*} u_2^* - \rho \frac{C_F}{\sqrt{K^*}} u_2^{*2}, \quad -h < y^* < 0 \tag{3}$$

$$\rho\, c_p \left(\frac{\partial T_2^*}{\partial t^*} + u_2^* \frac{\partial T_2^*}{\partial y^*} \right) = k_2 \frac{\partial^2 T_2^*}{\partial y^{*2}} + \frac{\mu_1}{K^*} u_2^{*2} + \rho \frac{C_F}{\sqrt{K^*}} u_2^{*3}, \quad -h < y^* < 0, \tag{4}$$

where K^* is the permeability of the isotropic porous medium, k_2 is the effective thermal conductivity, and μ_2 is the effective viscosity for the porous region. Here the symbol C_F(nondimensional) stands for the Forchheimer coefficient (see, e.g., [32]), which is used in expressing the inertial term in Eq. 3. An empirically based correlation for this coefficient can be found in [31]. The fluid viscosity μ_1 is different from effective viscosity μ_2 of porous region (Martys et al. [20] and Givler et al. [11]). The formulation is an extension of the problem presented by Sharma et al. [30].

In the energy Eq. 4 the last two terms represent dissipation effect. The first term is the viscous dissipation in Darcy's limit ($K^* \to 0$)(see, e.g., Ingham et al. [15]), while the second term is the Forchheimer–Darcy dissipation term. The viscous dissipation term is neglected in Darcy–Forchheimer approximation (see, e.g., [27]). For the discussions and derivations of Eqs. 3–4, we refer the reader to Joseph et al. [16], Nield [22], Payne et al. [26], and Kaviany [17].

The corresponding boundary conditions for the velocity field and temperature at the upper plate are

$$\text{At } y^* = h: \; u_1^* = u_0 \cos(w^* t^*), \quad T_1^* = T_0(1 + \cos(w^* t^*)), \tag{5}$$

where u_0 and T_0 are the mean velocity and mean temperature of the plate, respectively, and w^* is the frequency of oscillation of the plate. The interface boundary conditions are due to the continuity of the velocity, temperature, and the balance of heat flux and the stress jump.

$$\text{At } y^* = 0: u_1^* = u_2^*, \; T_1^* = T_2^*, \; k_1 \frac{\partial T_1^*}{\partial y^*} = k_2 \frac{\partial T_2^*}{\partial y^*}, \; \mu_2 \frac{\partial u_2^*}{\partial y^*} - \mu_1 \frac{\partial u_1^*}{\partial y^*} = \beta \frac{\mu_1}{\sqrt{K^*}} u_1^*. \tag{6}$$

Here β is the adjustable parameter in the stress jump boundary condition. Such an imposition was justified and used previously by [19],[24] and [25].

Analogously, the boundary conditions at the bottom plate are

$$\text{At } y^* = -h: u_2^* = u_0 cos(w^* t^*), \quad T_2^* = T_0(1 + cos(w^* t^*)). \tag{7}$$

Equations 1–7 constitute the mathematical formulation of the problem under consideration. Nondimensionalizing the governing equations 1–4 using dimensionless (without asterisks) variables given by

$$\begin{aligned} y^* = hy, \quad t^* = \frac{h}{u_0} t, \quad w^* = \frac{u_0}{h} w \\ u_k^* = u_0 u_k, \quad T_k^* = T_0 T_k + T_0 \quad for\, k = 1, 2 \\ m = \frac{\mu_1}{\mu_2}, \quad n = \frac{k_1}{k_2}, \quad K^* = h^2 K. \end{aligned} \tag{8}$$

The equations are obtained as

$$\frac{\partial u_1}{\partial t} = \frac{1}{\text{Re}} \frac{\partial^2 u_1}{\partial y^2}, \quad 0 < y < 1 \tag{9}$$

$$\frac{\partial T_1}{\partial t} + u_1 \frac{\partial T_1}{\partial y} = \frac{1}{\text{Pr Re}} \frac{\partial^2 T_1}{\partial y^2} + \frac{\text{Ec}}{\text{Re}} \left(\frac{\partial u_1}{\partial y} \right)^2, \quad 0 < y < 1 \tag{10}$$

and

$$\frac{\partial u_2}{\partial t} = \frac{1}{m\text{Re}} \frac{\partial^2 u_2}{\partial y^2} - \frac{1}{\text{Re}\, K} u_2 - \frac{C_F}{\sqrt{K}} u_2^2, \quad -1 < y < 0 \tag{11}$$

$$\frac{\partial T_2}{\partial t} + u_2 \frac{\partial T_2}{\partial y} = \frac{1}{n\,\text{Pr Re}} \frac{\partial^2 T_2}{\partial y^2} + \frac{\text{Ec}}{K\,\text{Re}} u_2^2 + \text{Ec} \frac{C_F}{\sqrt{K}} u_2^3, \quad -1 < y < 0 \tag{12}$$

where $\mathrm{Re} = \rho u_0 h/\mu_1$ is the dimensionless Reynolds number that characterizes the relation between inertial and viscous forces, $\mathrm{Pr} = \mu_1 c_p/k_1$ is the dimensionless Prandtl number which expresses the ratio of kinematic viscosity to thermal diffusivity, and $\mathrm{Ec} = u_0^2/c_p T_0$ is the Eckert number that approximates the ratio of the kinematic energy and thermal energy. Here the viscosity ratio(m) and the thermal conductivity ratio(n) are defined in terms of the clear fluid with respect to the fluid in the porous domain.

Using Eq. 8, the boundary condition equations 5–7 can be written as

$$\text{At } y = 1: \; u_1 = \cos(wt), \quad T_1 = \cos(wt), \tag{13}$$

$$\text{At } y = 0: u_1 = u_2, \quad T_1 = T_2, \quad n\frac{\partial T_1}{\partial y} = \frac{\partial T_2}{\partial y}, \quad \frac{\partial u_2}{\partial y} - m\frac{\partial u_1}{\partial y} = \frac{\beta m}{\sqrt{K}}u_1, \tag{14}$$

$$\text{At } y = -1: \; u_2 = \cos(wt), \quad T_2 = \cos(wt). \tag{15}$$

3 Solution Procedure

In order to explain the given physical problem the model is reduced to suitable form. Since the flow of the fluid under consideration is due to the oscillations of the plates, the solution of the equations is presented in the following form:

$$u_j = f_j e^{iwt}, \qquad for \quad j = 1,2 \tag{16}$$

$$T_j = F_j e^{iwt}, \qquad for \quad j = 1,2 \tag{17}$$

where only the real part of the complex quantities has physical meaning. Here f_j and F_j are the complex amplitudes of the oscillation and they do not depend upon time t but depend only on space variable y and that w is a constant. The symbol i stands for the complex imaginary number. To obtain an expression for f_j and F_j, simply substitute Eqs. 16 and 17 in Eqs. 9–15. After simple calculation we find that the functions f_1, f_2, F_1, and F_2 must satisfy the following:

$$f_1'' - iw\,\mathrm{Re}\, f_1 = 0 \tag{18}$$

$$F_1'' - \mathrm{Pr}\,\mathrm{Re}\, e^{iwt} f_1 F_1' - iw\,\mathrm{Pr}\,\mathrm{Re}\, F_1 + \mathrm{Pr}\,\mathrm{Ec}\, e^{iwt} f_1'^2 = 0 \tag{19}$$

$$f_2'' - \left(\frac{m}{K} + iwm\,\mathrm{Re}\right) f_2 - \mathrm{Re}\, m e^{iwt} \frac{C_F}{\sqrt{K}} f_2^2 = 0 \tag{20}$$

$$F_2'' - n\mathrm{RePr}\left(e^{iwt} f_2 F_2' + iwF_2\right) + n\mathrm{EcPr}e^{iwt}\left(\frac{1}{K}f_2^2\right) + \frac{n\mathrm{PrReEc}C_F}{\sqrt{K}} e^{2iwt} f_2^3 = 0 \tag{21}$$

subject to the boundary and interface conditions:

$$f_1(1) = 1,\ F_1(1) = 1,\ f_2(-1) = 1,\ F_2(-1) = 1 \tag{22}$$

$$f_1(0) = f_2(0),\ F_1(0) = F_2(0),\ nF_1^{'}(0) = F_2^{'}(0), f_2^{'}(0) - mf_1^{'}(0) = \frac{\beta m}{\sqrt{K}} f_1(0), \tag{23}$$

where the prime stands for the derivative with respect to y.

The solution of the model equations 18–23 neglecting Forchheimer drag term reduces to Darcy flow and is a special case of the present problem. Eqs. 18–21 together with the boundary condition equations 22–23 are solved numerically to study the effect of C_F. First of all, velocity field in a complete domain is solved and subsequently temperature field is evaluated. For a numerical integration, the following procedure has been used which is similar to the one used by Deng et al. [9]:

- The constant $f_1^{'}(1) = f_0$ is first introduced. Now trial value for f_0 is assumed, and then Eq. 18 can be treated as initial value problem and may be solved by Runge–Kutta fourth-order method over the domain $0 \leq y \leq 1$.
- Next at $y = 0$ the interface conditions are evaluated using Eqs. 23 for a prescribed value of m.
- Equation 20 is now treated as initial value problem and integrated over the domain $-1 \leq y \leq 0$ using the Runge–Kutta method of order four, the same one that we used in the first step. The boundary conditions $f_2(0) = f_1(0)$ and $f_2^{'}(0) = mf_1^{'}(0) + \beta m f_1(0)/\sqrt{K}$ are used for the solution of Eq. 20.
- The solution with trial value of f_0 is computed with boundary condition at $y = -1$. Newton's Raphson method, a root finding procedure, is used to update the value of f_0 until the boundary condition at $y = -1$, i.e., $f_2(-1) = 1$ is satisfied with a tolerance of 1×10^{-6}.

The temperature equations are solved by the similar procedure.

4 Results and Discussion

4.1 Validation

To demonstrate the successful implementation of the numerical algorithm the numerical results are compared with those obtained from the analytical solutions for the Darcy flow velocity ($C_F = 0, \beta = 0$).

The algorithm is implemented in scientific computing program MATLAB. The details of analytical expression for the velocity field are given in Appendix. The numerical simulation for Eq. 16 is obtained by solving system of Eqs. 18 and 20 with corresponding boundary conditions using 201 grid points for each fluid domain. The simulation results for velocity profiles at two different phases for different values of

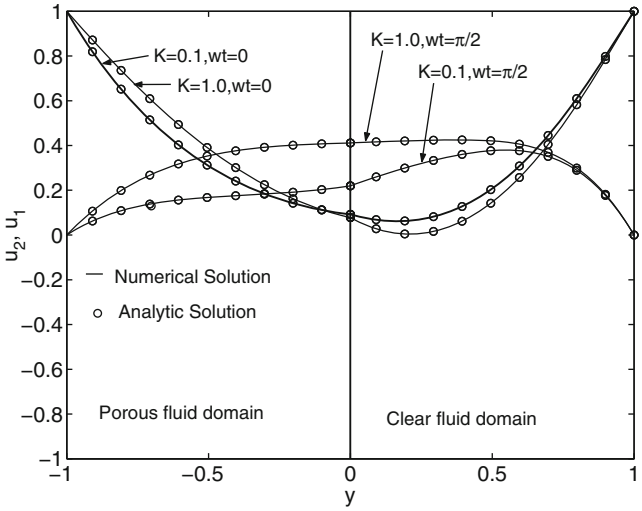

Fig. 2 Velocity profiles at two different phases for different values of permeability parameter K with $w = 8$, $m = 0.4$, Re $= 1$, $C_F = 0$, and $\beta = 0$

permeability parameters are shown in Fig. 2 and the flow parameters are reported in the figure caption. Comparison of results shows that numerical and analytical solutions are in close agreement and thereby validating numerical approach. It can be also observed that the fluid velocity increases with an increase in the permeability parameter due to the overall reduction in damping resistance offered by porous matrix. At the initial phase $wt = 0$, fluid attains maximum velocity on the plate and then decreases exponentially as the fluid moves towards interface. But when phase increases, for example, $wt = \pi/2$, the maximum velocity is observed in the middle of the domain.

4.2 Drag Effect and Velocity Distribution

The Fluid moving through a porous medium, it experiences a drag force which is due to frictional drag and form drag. Let us discuss quadratic drag effect on the flow pattern. The distribution of velocity is shown at different phases for different values of Forchheimer coefficient (Figs. 3–6).

The model parameters $m = 0.4$, Re $= 1$, $K = 0.5$, $w = 8$, and $\beta = 0.1$ are considered for the simulation. Clearly the fluid flow is parabolic in nature (Figs. 3 and 4) inside the channel. But, the presence of solid matrix inside the porous medium reduces the velocity field. Maximum velocity of the fluid flow is seen in the clear fluid region near to the axis. However, at the interface and inside the porous medium, the flow is obstructed due to frictional drag.

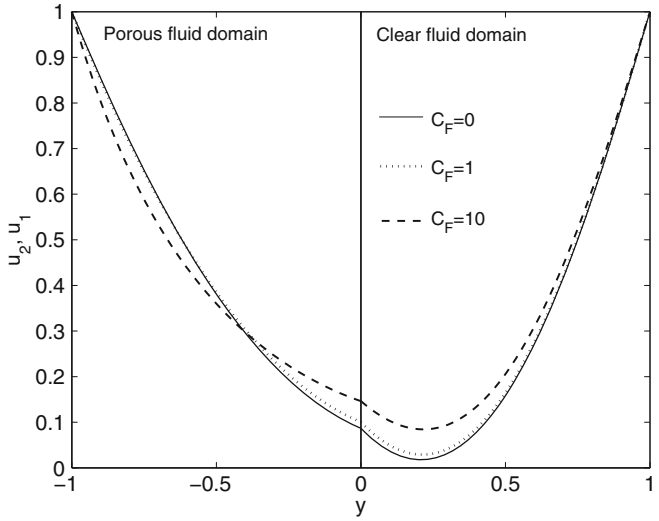

Fig. 3 Velocity profile at phase $wt = 0$

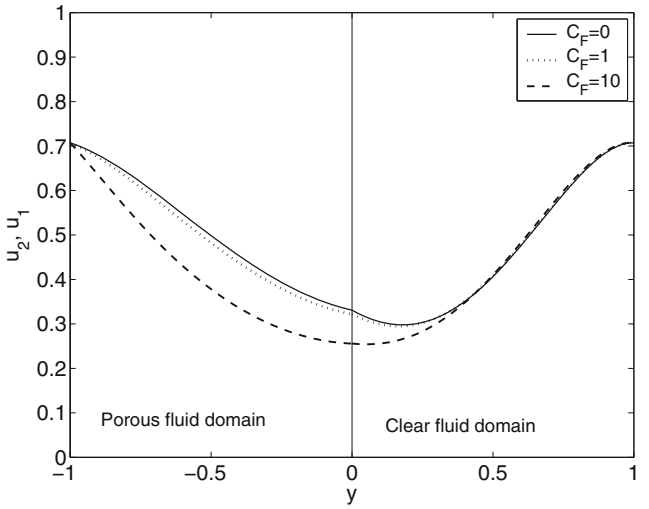

Fig. 4 Velocity profile at phase $wt = \pi/4$

Again comparing various curves in either of the plot, it is concluded that the higher the convective current, the greater is the drag effect, so also the thickness of the boundary layer decreases. It is interesting to note that oscillating plate for different phases wt produces reversal in the flow (Figs. 5 and 6).

Reynolds number frequently arise when performing dimensional analysis in the viscous flow equations. Figure 7 depicts the effect of Reynolds number in the clear

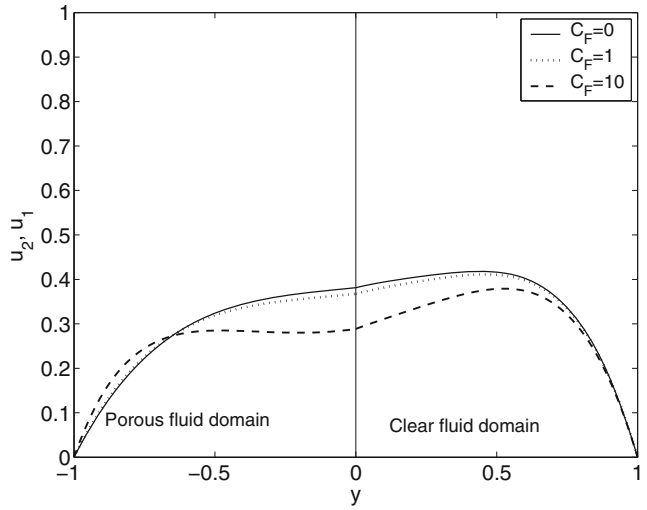

Fig. 5 Velocity profile at phase $wt = \pi/2$

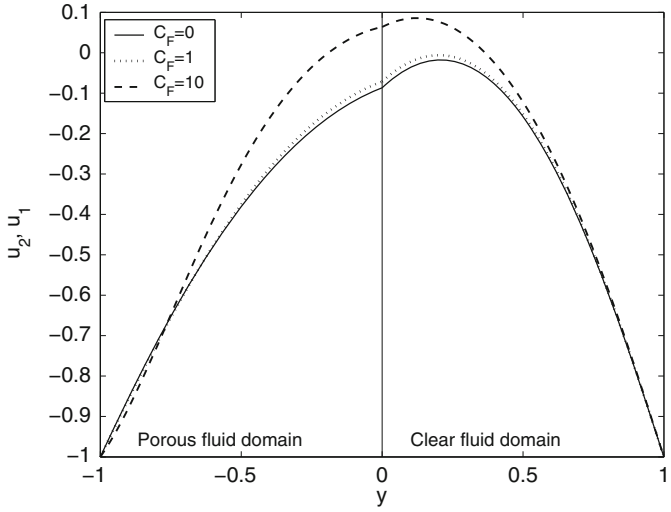

Fig. 6 Velocity profile at phase $wt = \pi$

fluid domain as well as porous fluid domain. Velocity field is higher in clear fluid domain than in porous fluid domain at a constant Reynolds number. Low Reynolds number indicate laminar flow, which is characterized by smooth constant flow. When Reynolds number increases gradually, in this context, viscous effect decreases and flow pattern is dominated by oscillating plate (for Re = 2 in Figure 7). It can be further seen that with the increase of Reynolds number the interface velocity decreases faster due to drag effects.

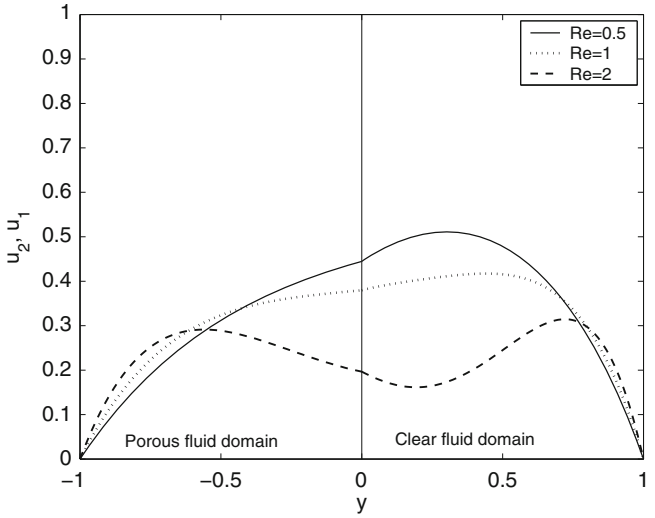

Fig. 7 Variation of velocity profiles with increase Reynolds numbers Re with $wt = \pi/2$, $w = 8$, $m = 0.4$, $K = 0.5$, $C_F = 0.1$, and $\beta = 0.1$

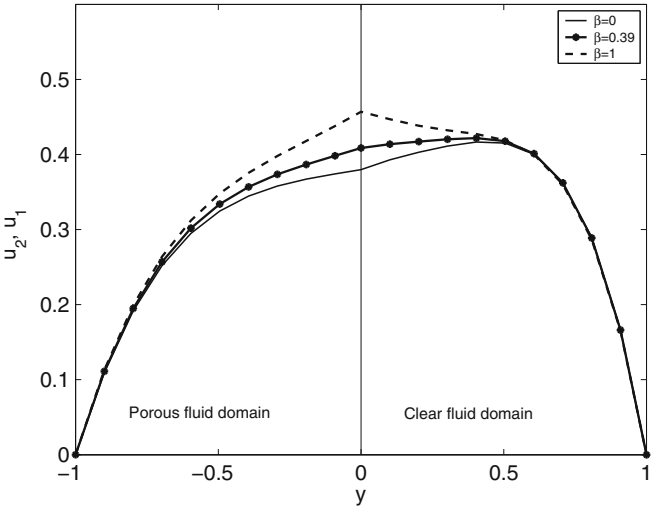

Fig. 8 Variation of velocity profiles for different values of stress jump parameter β

To conclude the discussion on velocity in two different domains we consider the effect of adjustable parameter β in the stress jump boundary condition (Fig. 8). The model parameters $w = 8$, $m = 0.4$, $K = 0.5$, $C_F = 0.1$, and $\mathrm{Re} = 1$ are considered for the simulation at phase $wt = \pi/2$. As evident, when $\beta = 0$, the transition of fluid flow from clear fluid domain to porous domain is not smooth. Slight increase of β from 0 to 0.39 makes the velocity gradient same in both regions causing a

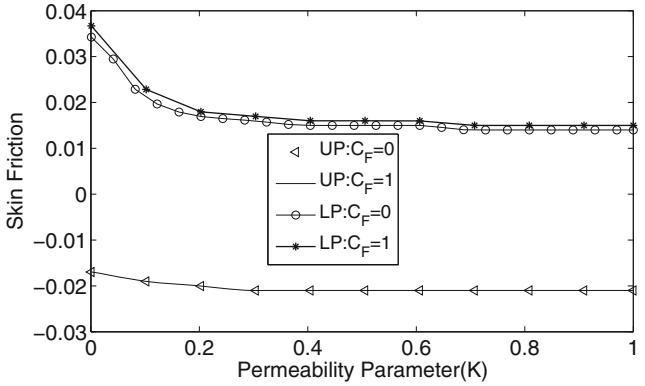

Fig. 9 Skin friction at the upper plate (UP) and lower plate (LP) at phase $wt = 0$

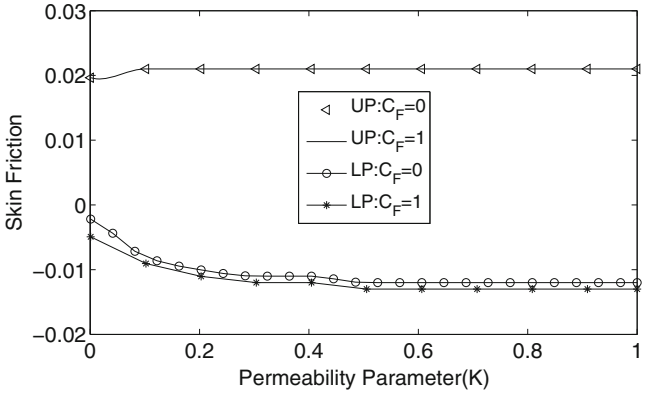

Fig. 10 Skin friction at the upper plate (UP) and lower plate (LP) at phase $wt = \pi/2$

smooth transition of fluid from one region to another. In case of $\beta = 1$, the velocity gradients of two regions are unequal and there is a misalignment. Physically there is a distortion for $\beta = 0$ and $\beta = 1$. However, at $\beta = 0.39$, the transition of the flow is smooth at the interface.

4.2.1 Skin Friction

The dimensionless skin friction at the upper and lower plates is given by $\left(\frac{\partial u_1}{\partial y}\right)_{y=1}$ and $\left(\frac{\partial u_2}{\partial y}\right)_{y=-1}$, respectively.

The computed values at two different phases $wt = 0$ and $wt = \pi/2$ for nondimensional parameters Re $= 1$, $w = 8$, $m = 0.4$, and $\beta = 0.1$ are visualized against the permeability parameter (K) in Figs. 9 and 10. As evident skin friction is independent of permeability parameter in clear fluid region (see skin friction in the upper plate

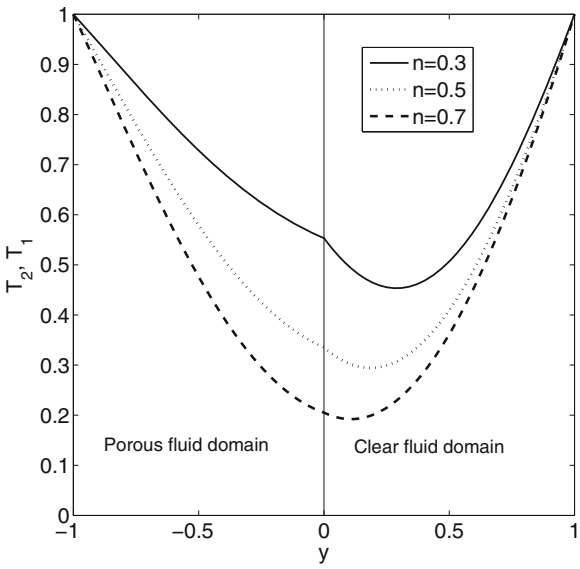

Fig. 11 Temperature profile for different conductivity ratios with Pr = 0.5 and Ec = 0.1

(UP) in Figs. 9 and 10). But this effect on lower plate is clearly visible. The skin friction almost attains constant values for $K > 0.4$ (Fig. 9) and it increases with the decrease of permeability parameter K. It is also interesting to analyze the differences between the profiles of the skin friction at lower plate(LP) with and without drag effects. As seen from Fig. 9 this difference is quite significant (see skin friction in the lower plate (LP) in Figs. 9 and 10). This is interesting because drag effect has no contribution in clear fluid region. The skin friction is greater in case of non-Darcian fluid($C_F = 1$) as compared to Darcian case ($C_F = 0$). Negative skin friction is observed in the clear fluid region at phase $wt = 0$ which may be attributed to the fact that there is a flow reversal at the boundary layer near the plate. With the advancement of phase wt from 0 to $\pi/2$ the reverse effect is observed in Fig. 10.

4.2.2 Temperature Distribution

In the following the simulated temperature distributions in the respective domains are analyzed. Figure 11 illustrates the profiles of temperature distribution at phase $wt = 0$ for various values of thermal conductivity ratios (n) for fixed $m = 0.4$, Re = 1, $C_F = 1$, $\beta = 0.1$, Pr = 0.5, and Ec = 0.1.

This temperature distributions correspond to the velocity distribution that is depicted in Fig. 12. It can be observed that the conductivity ratio substantially influences the temperature distribution in both the domains. The smaller the conductivity ratio implies the higher thermal conductivity of the porous domain. Since the porous medium is in direct contact with the heated wall heat is transferred by conduction through solid boundaries. So temperature of porous medium is higher

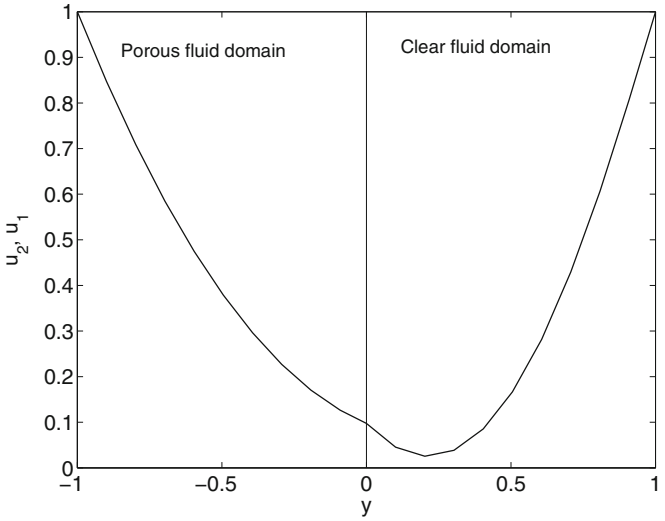

Fig. 12 Corresponding velocity profile for the computation of temperature distribution (Fig. 11) at phase $wt = 0$ with $m = 0.4$, Re $= 1$, $C_F = 1$, and $\beta = 0.1$

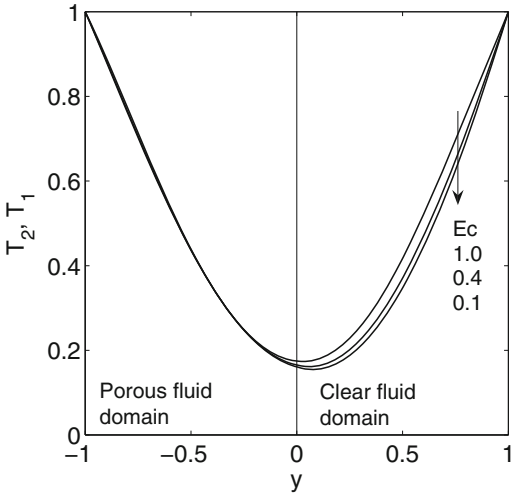

Fig. 13 Variation of temperature profiles with increasing Eckert numbers (Ec) for the velocity profile given in Fig. 12 with $n = 0.8$ and Pr $= 0.5$

than in the clear fluid domain close to the interface and for small n. It is further noticed that lower value of thermal conductivity ratio indicates a sharp jump of thermal boundary layer at the interface of two regions.

The effect of Eckert number (Ec) on the temperature distribution is described in Fig. 13. It is observed that the temperature increases in the clear fluid region with the increasing value of Ec. This effect is only visible at near to the interface in porous domain. Eckert number that measures the kinetic energy transformed into heat by viscous dissipation. In high Eckert number flow, frictional heating dominates the

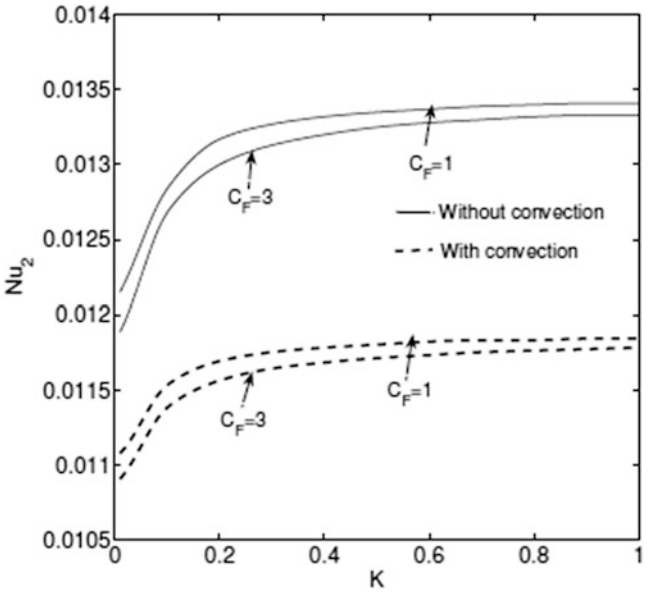

Fig. 14 Nusselt number at lower plate

boundary-layer fluid temperature and consequently rate of heat transfer to the fluid through the wall is higher.

Another physical quantity of interest in this problem, the local convective heat transfer rate at the surface characterized by the Nusselt number, is easily computed. The dimensionless Nusselt number at the respective plates are given by

$$\textit{At the upper plate}: \quad Nu_1 = -\left(\frac{\partial T_1}{\partial y}\right)_{y=1}.$$

$$\textit{At the lower plate}: \quad Nu_2 = -\left(\frac{\partial T_2}{\partial y}\right)_{y=-1}.$$

The dependence of Nusselt number on the permeability parameter for different values of the Forchheimer coefficient is described in Figs. 14 and 15. This figures are computed for $w = 8$, $m = 0.4$, $n = 0.8$, $\mathrm{Re} = 1$, $\mathrm{Pr} = 0.5$, $\mathrm{Ec} = 0.1$, and $\beta = 0.1$ at phase $wt = 0$. Moreover the effect of heat convection on the Nusselt number is analyzed. The results depicted in Fig. 14 correspond to the Nusselt number at the lower plate. The simulation result shows that the convection reduces the Nusselt number for all permeability parameter K. The reason is obvious that near the lower plate conduction dominates the flow and Nusselt number decreases. It is also evident that the higher the drag effect the lesser is the Nusselt number for both convection and without convection. It can be seen further that the increase in permeability

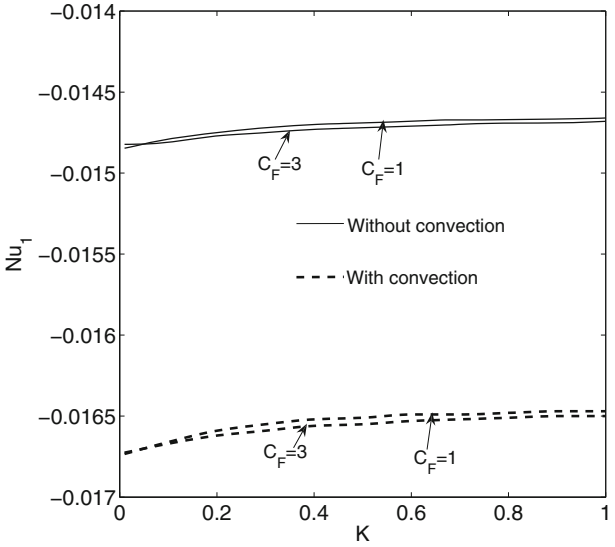

Fig. 15 Nusselt number at upper plate

results in the increase of rate of wall heat transfer as more heat is transferred away from the wall by convection. The wall effect due to solid wall is effective in a length scale of $K = 0.5$. In the clear fluid region convection dominates the flow. Decrease in Nusselt number is observed (Fig. 15) with convection than without convection because convection causes the motion to be turbulence. It is also observed that Nusselt number is all most independent of permeability parameter. Since drag effect has no role to play in the clear fluid region, therefore heat transfer rate is independent of drag coefficient.

5 Conclusion

Non-Darcian effects on the viscous fluid in partly porous configurations have been investigated numerically. The Navier–Stokes and Darcy–Forchheimer equations are employed in clear fluid and porous medium, respectively. Conclusion of this study is summarized below:

- Fluid flow is almost parabolic in nature between two oscillating plates. Clearly velocity field in the clear fluid region is larger than porous region and minimum value of thermal boundary layer shifts towards interface.
- Drag effect reduces the flow field. There exist three flow resistances, the bulk damping resistance due to porous structure, the viscous resistance due to boundary and the resistance due to inertial forces.

- In between the two oscillating plates clear fluid domain and porous fluid domain coexist. At the interface the transition of fluid is not smooth. This depends upon adjustable parameter, i.e., the stress jump boundary condition. Proper choice of adjustable parameter may give rise to smooth transition.
- The heat conductivity ratio also plays important role in temperature distribution. In the clear fluid region the thermal boundary layer attains minimum value near the axis $y = 0$ and minimum value of thermal boundary layer shifts towards interface, while in the porous domain the thermal boundary layer attains minimum value at the interface and gradually increases to unity at the plate.
- In case of lower plate flow is dominated by conductive heat transfer. The evolution of the flow with increasing permeability results from the competition between two opposing effects. Higher permeability results in a better penetration in porous layer by the flow and consequently the diffusive effect of the imposed temperature is lower. The flow is then accelerated resulting higher heat transfer. In case of upper plate heat transfer is independent of permeability parameter.

The present investigation of the study of non-Darcian effects on the viscous flow in partly porous configuration between two oscillating plates can be utilized as the basis for many scientific and engineering applications and for studying more complex problems.

Appendix

The analytical solutions for the Darcian velocity fields u_1 and u_2 are obtained by first solving Eqs. 18 and 20 with corresponding boundary conditions(with $C_F = 0$ and $\beta = 0$) and then the real part of Eq. 16 yields the following expression. These analytical results are compared with numerical simulations in Fig. 2, showing a good agreement.

$$u_1(y,t) = S_{11}\cos(wt) - S_{12}\sin(wt), \quad for \;\; 0 \le y \le 1$$
$$u_2(y,t) = S_{21}\cos(wt) - S_{22}\sin(wt), \quad for \;\; -1 \le y \le 0$$

where

$$S_{11} = \frac{(a_8 m_7 + b_8 n_7)}{m_7^2 + n_7^2}, \quad S_{12} = \frac{(b_8 m_7 - a_8 n_7)}{m_7^2 + n_7^2}$$
$$S_{21} = \frac{(p_5 m_7 + q_5 n_7)}{m_7^2 + n_7^2}, \quad S_{22} = \frac{(q_5 m_7 - p_5 m_7)}{m_7^2 + n_7^2}$$

with

$$m_7 = m_3 + m_6, \qquad n_7 = n_3 + n_6$$

$$m_3 = m_2 c_1 - n_2 d_1, \qquad n_3 = m_2 d_1 + n_2 c_1$$

$$m_6 = m_5 c_2 + n_5 d_2, \qquad n_6 = n_5 c_2 - m_5 d_2$$

$$m_2 = x_2 m_1 + y_2 n_1, \qquad n_2 = x_2 n_1 - y_2 m_1$$

$$c_2 = \sin(x_{22})\cosh(y_{22}), \qquad d_2 = \cos(x_{22})\sinh(y_{22})$$

$$c_1 = \cos(x_{22})\cosh(y_{22}), \qquad d_1 = \sin(x_{22})\sinh(y_{22})$$

$$m_1 = -1 + \alpha_3 \cos(2y_1), \qquad n_1 = \alpha_3 \sin(2y_1)$$

$$m_5 = m\sqrt{k}\,(y_1 m_4 - y_1 n_4), \qquad n_5 = m\sqrt{k}\,(y_1 m_4 + y_1 n_4)$$

$$m_4 = 1 + \alpha_3 \cos(2y_1), \qquad n_4 = \alpha_3 \sin(2y_1)$$

$$x_{22} = \frac{x_2}{\sqrt{k}}, \qquad y_{22} = \frac{y_2}{\sqrt{k}}$$

$$x_2 = \frac{1}{\sqrt{2}}\sqrt{\sqrt{m^2 + (mwk\,\mathrm{Re})^2} - m}, \qquad y_2 = \tfrac{1}{\sqrt{2}}\sqrt{\sqrt{m^2 + (mwk\,\mathrm{Re})^2} + m}$$

$$y_1 = \sqrt{\frac{w\,\mathrm{Re}}{2}}, \qquad \alpha_3 = exp(2y_1)$$

$$a_8 = a_{11} + a_4 + a_7, \qquad b_8 = b_{11} + b_4 + b_7$$

$$a_7 = a_6 c_2 + b_6 d_2, \qquad b_7 = b_6 c_2 - a_6 d_2$$

$$a_6 = m\sqrt{k}\,(y_1 a_5 - y_1 b_5), \qquad b_6 = m\sqrt{k}(y_1 a_5 + y_1 b_5)$$

$$a_5 = \beta_2 \cos(y_1(1-y)) + \alpha_2 \cos(y_1(1+y)), \qquad b_5 = \beta_2 \sin(y_1(1-y)) + \alpha_2 \sin(y_1(1+y))$$

$$\alpha_2 = exp(y_1(1+y)), \qquad \beta_2 = exp(y_1(1-y))$$

$$a_4 = a_3 c_1 - b_3 d_1, \qquad b_4 = a_3 d_1 + b_3 c_1$$

$$a_3 = x_2 a_2 + y_2 b_2, \qquad b_3 = x_2 b_2 - a_2 y_2$$

$$a_2 = \alpha_2 \cos(y_1(1+y)) - \beta_2 \cos(y_1(1-y)), \qquad b_2 = \alpha_2 \sin(y_1(1+y)) - \beta_2 \sin(y_1(1-y))$$

$$a_{11} = x_2 a_1 + y_2 b_1, \qquad b_{11} = x_2 b_1 - y_2 a_1$$

$$a_1 = \alpha_1 \cos(y_1(2-y)) - \beta_1 \cos(y_1 y), \qquad b_1 = \alpha_1 \sin(y_1(2-y)) - \beta_1 \sin(y_1 y)$$

$$\alpha_1 = exp(y_1(2-y)), \qquad \beta_1 = exp(y_1 y)$$

$$p_5 = p_1 - p_2 + p_4, \qquad q_5 = q_1 - q_2 + q_4$$

$$p_4 = p_3 c_5 + q_3 d_5, \qquad q_4 = q_3 c_5 - p_3 d_5$$

$$p_3 = 2m\sqrt{k}\,(\alpha_4 y_1 \cos(y_1) - \alpha_4 y_1 \sin(y_1)), \qquad q_3 = 2m\sqrt{k}\,(\alpha_4 y_1 \cos(y_1) + \alpha_4 y_1 \sin(y_1))$$

$$\alpha_4 = exp(y_1)$$

$$c_5 = \sin(x_{44})\cosh(y_{44}), \qquad d_5 = \cos(x_{44})\sinh(y_{44})$$

$$x_{44} = x_{22}(1+y), \qquad y_{44} = y_{22}(1+y)$$

$$p_2 = m_5 c_4 + n_5 d_4, \qquad q_2 = n_5 c_4 - m_5 d_4$$

$$c_4 = \sin(x_{33})\cosh(y_{33}), \qquad d_4 = \cos(x_{33})\sinh(y_{33})$$
$$x_{33} = y x_{22}, \qquad y_{33} = y y_{22}$$
$$p_1 = m_2 c_3 - n_2 d_3, \qquad q_1 = m_2 d_3 + n_2 c_3$$
$$c_3 = \cos(x_{33})\cosh(y_{33}), \qquad d_3 = \sin(x_{33})\sinh(y_{33})$$

References

1. Anderson, J.D. Jr.: Computational Fluid Dynamics: The Basic with Applications. McGraw-Hill, New York (1995)
2. Aydin, O., Kaya, A.: Non-Darcian forced convection flow of a viscous dissipating fluid over a flat plate embedded in a porous medium. Transport Porous Med. **73**, 173–186 (2008)
3. Aydin, O., Kaya, A.: Reply to comments on "Non-Darcian forced convection flow of viscous dissipating fluid over a flat plate embedded in a porous medium". Transport Porous Med. **73**, 191–193 (2008)
4. Beavers, G.S., Sparrow, E.M.: Non-Darcy flow through fibrous porous media. J. Appl. Mech. **36**, 711–714 (1969)
5. Beavers, G.S., Sparrow, E.M., Rodenz, D.E.: Influence of bed size on the flow characteristics and porosity of randomly packed beds of spheres. J. Appl. Mech. **40**, 655–660 (1973)
6. Bujurke, N.M., Hiremath, P.S., Biradar, S.N.: Impulsive motion of a non-Newtonian fluid between two oscillating parallel plates. Appl. Sc. Res. **45**, 211–231 (1988)
7. Cvetkovic, V.D.: A continuum approach to high velocity flow in a porous medium. Transport Porous Med. **1**, 63–97 (1986)
8. Debnath, L., Ghosh, A.K.: On unsteady hydromagnetic flows of a dusty fluid between two oscillating plates. Appl. Sc. Res. **45**, 353–365 (1988)
9. Deng, C., Martinez, D.M.: Viscous flow in a channel partially filled with a porous medium and with wall suction. Chem. Eng. Sci. **60**, 329–336 (2005)
10. Dybbs, A., Edwards, R.V.: A new look at porous media fluid mechanics—Darcy to turbulent. In Bear, J., Corapcioglu, M.Y. (eds.) Fundamentals of Transport Phenomena in Porous Media, pp. 199–256. Martinus Nijhoff, Dordrecht (1984)
11. Givler, R.C., Altobelli, S.A.: A determination of the effective viscosity for the Brinkman-Forchheimer flow model. J. Fluid Mech. **258**, 355–370 (1994)
12. Gobin, D., Goyeau, B.: Natural convection in partially porous media: a brief overview. Int. J. Num. Methods Heat Fluid Flow **18**, 465–490 (2008)
13. Hassanizadeh, S.M., Gray, W.G.: High velocity flow in porous media. Transport Porous Med. **2**, 521–531 (1987)
14. Hayat, T.: Exact solutions of a dipolar fluid flow. Acta Mec. Sin. **19**, 308–314 (2003)
15. Ingham, D.B., Pop, I., Cheng, P.: Combined free and forced convection in a porous medium between two vertical walls with viscous dissipation. Transport Porous Med. **5**, 381–398 (1990)
16. Joseph, D.D., Nield, D.A., Papanicolaou, G.: Nonlinear equation governing flow in a saturated porous medium. Water Resour. Res. **18**, 1049–1052 (1982)
17. Kaviany, M.: Principles of Heat Transfer in Porous Media, 2nd edn. Springer, New York (1995)
18. Kuznetsov, A.V.: Analytical investigation of Couette flow in a composite channel partially filled with a porous medium and partially with a clear fluid. Int. J. Heat Mass Transf. **41**, 2556–2560 (1998)
19. Kuznetsov, A.V.: Analytical studies of forced convection in partly porous configurations. In: Vafai, K. (ed.) Handbook of Porous Media, pp. 269–310. Mercel Dekker, New York (2000)
20. Martys, N., Bentz, D.P., Garboczi, E.J.: Computer simulation study of the effective viscosity in Brinkman's equation. Phys. Fluids **6**, 1434–1439 (1994)
21. Murty, P.V.S.N., Singh, P.: Effect of viscous dissipation on a non-Darcy natural convective regime. Int. J. Heat Mass Transf. **40**, 1251–1260 (1997)

22. Nield, D.A.: Resolution of a paradox involving viscous dissipation and non-linear drag in a porous medium. Transport Porous Med. **41**, 349–357 (2000)
23. Nield, D.A., Bejan, A.: Convection in Porous Media. Springer, New York (2006)
24. Ochoa-Tapia, J.A., Whitaker, S.: Momentum transfer at the boundary between a porous medium and a homogeneous fluid-I. Theoretical development. Int. J. Heat Mass Transf. **38**, 2635–2646 (1995)
25. Ochoa-Tapia, J.A., Whitaker, S.: Momentum transfer at the boundary between a porous medium and a homogeneous fluid-II. Comparison with experiment. Int. J. Heat Mass Transf. **38**, 2647–2655 (1995)
26. Payne, L.E., Rodrigues, J.F., Straughan, B.: Effect of anisotropic permeability on Darcy's law. Math. Method Appl. Sci. **24**, 427–438 (2001)
27. Rajagopal, K.R.: On a hierarchy of approximate models for flows of incompressible fluids through porous solids. Math. Method Appl. Sci. **17**, 215–252 (2007)
28. Rees, D.A.S., Magyari, E.: Comments on the paper "Non-Darcian forced-convection flow of viscous dissipating fluid over a flat plate embedded in a porous medium" by Aydin, O. and Kaya, A., Transport in Porous Media. Transport Porous Med. **73**, 187–189 (2008). doi:10.1007/s11242-007-9200-x
29. Sekharan, E.C., Ramanaiah, G.: Unsteady flow between two oscillating plates. Def. Sc. J. **32**, 99–104 (1982)
30. Sharma, P.K., Chaudhary, R.C., Sharma, B.K.: Flow of viscous incompressible fluid in a region partially filled with porous medium and bounded by two periodically heated oscillating plates. Bull. Cal. Math. Soc. **97**, 263–274 (2005)
31. Vafai, K.: Convective flow and heat transfer in variable porosity media. J. Fluid Mech. **147**, 233–259 (1984)
32. Vafai, K., Tien, C.L.: Boundary and inertia effects on flow and heat transfer in porous media. Int. J. Heat Mass Transf. **24**, 195–203 (1981)
33. Whitaker, S.: Flow in porous media: part-I, a theoretical derivation of Darcy's law. Transport Porous Med. **1**, 3–25 (1986)

Experimental and Numerical Study of the Salt Dissolution in Porous Media

F. Dorai, G. Debenest, H. Luo, H. Davarzani, R. Bouhlila, F. Laouafa, and M. Quintard

Abstract Dissolution in porous media is a complex phenomenon. In most of the approaches, density variations are ignored but they generate important convection structures like those presented in [5]. In this chapter, our aim is to develop an experimental approach in order to validate our numerical tool. To do so, we will make use of local measurments using microtomography in order to get the surface evolution of the dissolved medium. We will also get some results about the weight losses of salt dissolved and then try to compare to those predicted by numerical simulations.

F. Dorai
Université de Tunis El-Manar, ENIT LMHE BP 37, Le Belvédére-1002 Tunis, Tunisia

Université de Toulouse; INPT, UPS; IMFT; Toulouse, France
e-mail: ferdaous.dorai@yahoo.fr

G. Debenest (✉) • H. Davarzani • M. Quintard
Université de Toulouse; INPT, UPS; IMFT; Toulouse, France
e-mail: debenest@imft.fr

H. Luo
Université de Toulouse; INPT, UPS; IMFT; Toulouse, France

CNRS IMFT; Toulouse, France

IMFT-GEMP, 1 Allée du Pr Camille SOULA, 31400 Toulouse, France

R. Bouhlila
Université de Tunis El-Manar, ENIT LMHE BP 37, Le Belvédére-1002 Tunis, Tunisia

F. Laouafa
INERIS, Parc technologique ALATA BP2, F-60550 Verneuil-en-Halatte, France

J.A. Ferreira et al. (eds.), *Modelling and Simulation in Fluid Dynamics in Porous Media*, Springer Proceedings in Mathematics & Statistics 28, DOI 10.1007/978-1-4614-5055-9_12,

1 Introduction

Dissolution has several important environmental and industrial applications: mineral mining, dissolution of underground cavities, increasing the permeability of the oil field by acid injection and sequestration of carbon dioxide. These applications involve chemical reactions and various transport phenomena such as convection and diffusion. The porous medium evolution resulting from dissolution causes the modification of its hydrologic properties, mainly the porosity, and consequently its permeability. Because of the complexity of this phenomenon, many theoretical and experimental studies have been carried out to understand the relationship between dissolution and the parameters that influence it. For acid injection, it was noticed that dissolution of the porous medium leads to the formation of ramified channels called wormholes inside the rock. Many studies were interested in the effect of the rock mineralogy, the injected acid solution concentration and the injection rate on dissolution, and they all conclude that there are different dissolution regimes depending on the flow rate [1, 2]. This work is part of a project carried out by the National Institute of Industrial Environment and Risks (INERIS). In this chapter, we represent an experimental study to validate the mathematical binary system dissolution model developed for a Darcy scale which takes into account the density variation [4]. In fact, Golfier et al. (2002) developed a Darcy-scale local non-equilibrium model without density variation [2]. However, the variation of density can modify the results of dissolution as shown in Luo et al. (2010) [4]. We aim to study the impact of the Péclet number and the injected water density on the salt dissolution, qualitatively and quantitatively using the technique of X-ray microtomography to visualize the results.

2 Dissolution Model

2.1 Pore-Scale Dissolution Model for a Binary System

Luo et al. (2010) presented a model describing microscopic scale dissolution problem [4]. We consider, in this study, a two-phase flow: the solid phase (σ-phase) and the liquid phase (β-phase). In addition, β-phase contains two components: A which refers to the solid component (salt) and B which is the salty solution (Fig. 1).

Mass balance equations in the β-phase are written as follows:

- For the species A:

$$\frac{\partial \rho_\beta \omega_{A\beta}}{\partial t} + \nabla \cdot (\rho_\beta \omega_{A\beta} \boldsymbol{v}_{A\beta}) = 0 \tag{1}$$

- For the species B:

$$\frac{\partial \rho_\beta \omega_{B\beta}}{\partial t} + \nabla \cdot (\rho_\beta \omega_{B\beta} \boldsymbol{v}_{B\beta}) = 0 \tag{2}$$

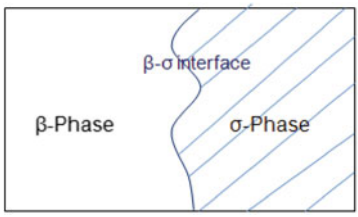

Fig. 1 Original solid/liquid dissolution problem

- Mass balance equations in the σ-phase:

$$\frac{\partial \rho_\sigma}{\partial t} + \nabla \cdot (\rho_\sigma \boldsymbol{v}_\sigma) = 0 \tag{3}$$

where ρ_β and ρ_σ are the β-phase and the σ-phase densities; $\boldsymbol{v}_{A\beta}$, $\boldsymbol{v}_{B\beta}$, $\boldsymbol{v}_\sigma$, $\omega_{A\beta}$ and $\omega_{B\beta}$ are the velocities and the mass fractions of the species A and B in the β-phase and the σ-phase, respectively. At the β–σ interface, we have:

- The equilibrium condition of the mass fraction imposing an equilibrium concentration for species A:

$$\omega_{A\beta} = \omega_{eq} \tag{4}$$

  where ω_{eq} is the mass fraction at equilibrium, i.e. when the salty solution is saturated.
- The mass balances for the species A and B:

$$\rho_\beta \omega_{A\beta} (\boldsymbol{v}_{A\beta} - \boldsymbol{w}) \cdot \boldsymbol{n}_{\beta\sigma} = \rho_\sigma \omega_{A\sigma} (\boldsymbol{v}_{A\sigma} - \boldsymbol{w}) \cdot \boldsymbol{n}_{\beta\sigma} \tag{5}$$

$$\rho_\beta \omega_{B\beta} (\boldsymbol{v}_{B\beta} - \boldsymbol{w}) \cdot \boldsymbol{n}_{\beta\sigma} = \rho_\sigma \omega_{B\sigma} (\boldsymbol{v}_{B\sigma} - \boldsymbol{w}) \cdot \boldsymbol{n}_{\beta\sigma} \tag{6}$$

where $\boldsymbol{w}$ is the velocity of the interface and $\boldsymbol{n}_{\beta\sigma}$ is the unit normal vector directed from the β-phase to the σ-phase. We use Navier–Stokes equation for flow motion at the pore-scale defined as:

$$\frac{\partial (\rho_\beta \boldsymbol{v}_\beta)}{\partial t} + \boldsymbol{v}_\beta \nabla \cdot (\rho_\beta \boldsymbol{v}_\beta) = -(\nabla P_\beta - \rho_\beta \boldsymbol{g}) + \mu_\beta \nabla^2 \boldsymbol{v}_\beta \tag{7}$$

$\boldsymbol{v}_\beta$, P_β and μ_β are the velocity, the pressure and the dynamic viscosity of the fluid, respectively, with a non-slip boundary condition at the β–σ interface:

$$\boldsymbol{v}_\beta = 0 \tag{8}$$

The velocity of the interface can be defined using the diffusion theory of Taylor and Krishna, 1993 [3]:

$$\boldsymbol{n}_{\beta\sigma} \boldsymbol{w} = \boldsymbol{n}_{\beta\sigma} \left(\frac{\rho_\beta}{\rho_\sigma (1 - \omega_{A\beta})} \boldsymbol{D}_{A\beta} \nabla \omega_{A\beta} \right). \tag{9}$$

2.2 Diffuse Interface Model

Many methods are used to express the microscopic equations in the Darcy scale. In fact, we need to develop the macroscopic description of the problem which represents the effective behaviour of the porous medium since the direct resolution of the microscopic equations on a large volume is usually impossible. The technique used in this work is the volume averaging. Recently, using this technique has attracted many attentions because of its simplicity and efficiency. It has been extensively used to predict the effective transport properties for many processes. It is based on the integration in the representative elementary volume (REV) of the microscopic conservation equations. Luo et al. (2010) [4] presented the diffuse interface model (DIM) model in the Darcy scale for solid/liquid dissolution in a binary system with variable density. It is described by the following equations: the mass balances for the phases σ and β and the mass balance for the species A:

$$\rho_{\sigma}^{*}\frac{\partial \varepsilon_{\sigma}}{\partial t} = \rho_{\beta}^{*}\alpha(\omega_{eq} - \Omega_{A\beta}) \tag{10}$$

$$\frac{\partial(\varepsilon_{\beta}\rho_{\beta}^{*})}{\partial t} + \nabla\cdot(\rho_{\beta}^{*}\boldsymbol{V}_{\beta}) = \rho_{\beta}^{*}\alpha(\omega_{eq} - \Omega_{A\beta}) \tag{11}$$

$$\varepsilon_{\beta}\rho_{\beta}^{*}\frac{\partial \Omega_{A\beta}}{\partial t} + \rho_{\beta}^{*}(\boldsymbol{V}_{\beta})\cdot\nabla\Omega_{A\beta} = \nabla\cdot(\varepsilon_{\beta}\rho_{\beta}^{*}\boldsymbol{D}_{A\beta}^{*}\cdot\nabla\Omega_{A\beta}) + \rho_{\beta}^{*}\alpha(1-\Omega_{A\beta})(\omega_{eq}-\Omega_{A\beta}). \tag{12}$$

The velocity $\boldsymbol{V}_{\beta}$ is given by the Darcy's law:

$$\boldsymbol{V}_{\beta} = -\frac{K}{\mu}(\nabla P_{\beta} - \rho_{\beta}\boldsymbol{g}) \tag{13}$$

where ε_{σ} is the volume fraction of the solid in the σ-phase, ε_{β} and $\Omega_{A\beta}$ are the volume fraction and the mass fraction of the component A in the β-phase, respectively, α is the mass exchange term, ρ_{σ}^{*} and ρ_{β}^{*} are the effective densities in the σ-phase and β-phase, K is the permeability, $\boldsymbol{D}_{A\beta}^{*}$ is the effective diffusion tensor for species A, μ is the viscosity and $\boldsymbol{g}$ is the gravity.

3 Material and Methods

3.1 X-ray Microtomography

In this study, we used the technique of X-ray microtomography to visualize the experimental results. This technique allows to reconstruct an object from its projections. For image processing and analysis, the Skyscan software and the CT-Analyser were used (www.skyscan.be/next/CTan_UserManual.pdf). Image

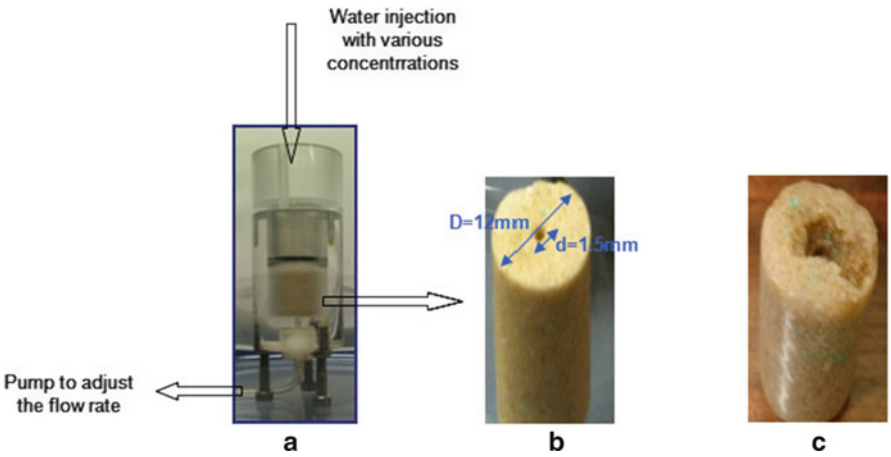

Fig. 2 Experimental setup (**a**) and the dissolution effect on the salt samples: (**b**) a sample before dissolution and (**c**) the same sample after dissolution

binarization was carried out on the smoothed 16-bit greyscale images obtained from the reconstruction step using Matlab software. Binarization is the process of converting greyscale images into black and white images by assigning 1 to all pixels whose intensity is below a given grey tone and 0 to all others.

3.2 Tube Dissolution

An experimental setup was realized for a three-dimensional dissolution through drilled cylindrical samples of salt. The diameter and length of the salt cylinder are chosen to be 12 mm and 20 mm, respectively. A hole of 1.5 mm has been created at the middle of salt cylinder. Water with various concentrations and velocity will be injected trough out this hole to study the influence of the Péclet number and the density on dissolution by changing the flow velocity and the concentration of the injected solution. The Péclet number is given by

$$Pe = \frac{Ud}{D} \tag{14}$$

where d is the hole diameter [m], U is the velocity inside the hole [m.s^{-1}] and D is the diffusion coefficient of salt in pure water [m^2.s^{-1}].

In order to observe the shape of solid/liquid interface, the sample was reconstructed using the X-ray microtomographic imaging. The experimental setup is shown in Fig. 2.

In this setup, we injected an undersaturated solution made of salt inside the hole in the centre of the cylinder. In practice, we vary the mass fraction of salt of the injected solution, ω, which refers to $\Omega_{A\beta}$ in the model given. Four values of were

considered: 0 for pure water, 0.1, 0.15 and 0.2. The flow rate is controlled with a pump from the bottom of the sample in order to modify the Péclet number inside the hole.

The Péclet numbers used were: 1000, 10 000 and 100 000. The experiments lasted 40 minutes for pure water injection ($\omega = 0$) and about 3 hours for the other cases. Then, the dissolution process was stopped by heating the sample during one hour in the oven. The shape of the dissolution fronts is observed with X-ray microtomography. In order to study the effect of gravity on the dissolution processes, two series of experiments were realized based on the position of the salt sample: the first was carried out with vertical cylindrical samples (the gravity parallel to their axis) and the second with horizontal samples (the gravity perpendicular to their axis).

4 Results and Discussions

In this section, we present the comparison of our results coming from the experimental with the ones of the numerical studies. Our simulation results are obtained using the DIM model coupled with the adaptative mesh refinement (AMR) technique (Luo et al. (2011) [5]) and the code was written in Fortran using a finite volume method. AMR is a technique developed to refine grid in zones where strong gradients are present. In our case, the dissolution is a dynamic phenomenon and the solid/liquid interface is moving with time (see [5] for more details).

4.1 The Dissolution Front Shapes

In order to compare qualitatively the shape of the dissolution fronts, the images generated from microtomography and those from numerical simulations are given in Tables 1 and 2. Only half of the domain is represented because the geometry is axial symmetric.

Qualitatively, an agreement between the results is observed when the images of microtomography or those of simulations were used, but there are some relevant differences near the boundary because of the structure of the salt used in experiments: the material is easily dissolved, especially when the Péclet number is high and convection is important (case of $\omega = 0.1$ and $Pe = 100000$). There is a change in the dissolution regimes depending on the Péclet number. When the Péclet number increases, the dissolution front is more spread in the porous medium.

The second comparison between the numerical and the experimental works is based on the position of some characteristic points on the front of dissolution in every cylinder of salt at the end of the experiment. The points are located at 25%, 50% and 75% of the height of the sample.

Table 1 Numerical and experimental comparison of the dissolution front shape—Vertical case

	Numerical results	Experimental results
$\omega = 0.1$, $Pe = 100,000$	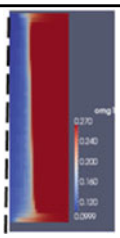	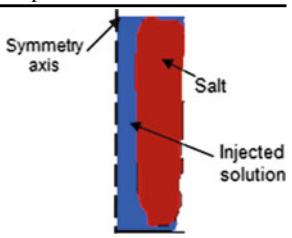
$\omega = 0.2$, $Pe = 10,000$	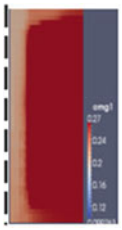	

Table 2 Numerical and experimental comparison of the dissolution front shape—Horizontal case

	Numerical results	Experimental results
$\omega = 0.2$, $Pe = 1000$		

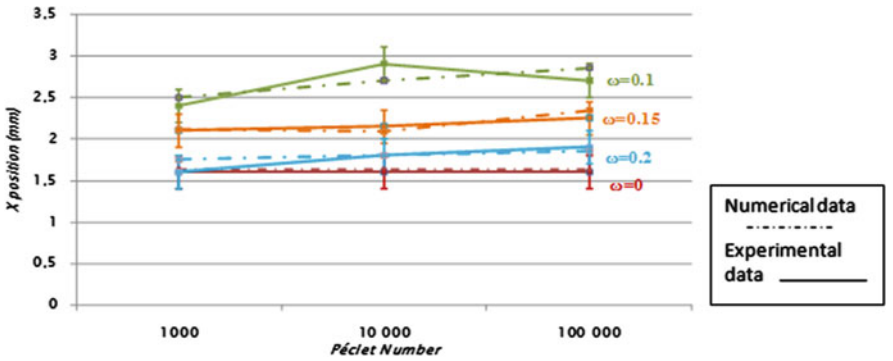

Fig. 3 Position of the point located at the half of the sample height

In Fig. 3, we chose to present the x-position of the point located at 50% of the total sample height with different Péclet numbers and injected water concentrations. To draw the numerical data, we used directly the x-position of the dissolution front stored at each time step in the output file. The experimental curve is obtained by

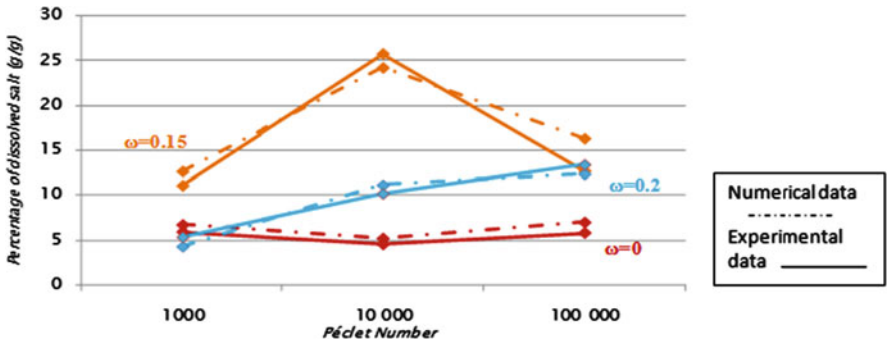

Fig. 4 Comparison of mass balances

direct measurements on the binarized images. The error due to the experimental data reading is 2%. For each concentration of the water injected, we compared the results of the numerical and the experimental studies with different Péclet numbers.

The numerical and experimental results are in good agreement in given accuracy and precision of experimental method. The position of the front is almost the same for the different concentrations and Péclet numbers used.

4.2 Study of the Mass Balance

In this section, the production of salt after dissolution was studied and results were compared with those of simulations. The difference between the sample masses before and after the experiment has been shown in Fig. 4.

From this figure, it appears that the Péclet number and the concentration of injected solution are sensitive parameters in the mechanism of salt production. It seems that increasing the Péclet number accelerates dissolution, convection becomes more important and the quantity of salt removed is bigger.

5 Conclusions

A DIM was developed to describe the dissolution problem with a binary system using the volume averaging technique [4]. To predict salt dissolution problem, numerical simulations were performed using the DIM model coupled with the AMR technique. An experimental study was carried out and its results were compared with numerical ones. A good agreement was observed between the two. The Péclet number and the concentration of the injected solution are important parameters in describing this kind of problems. They play also a key role in controlling the dynamics of the phenomenon and defining the regime of dissolution.

References

1. Fredd, C.N., Miller, M.J.: Validation of carbonate matrix simulation models. In: SPE International Symposium on Formation Damage Control, Lafayette, Louisiana (2000)
2. Golfier, F., Zarcone, C., Bazin, B., Lenormand, R., Lasseux, D., Quintard, M.: On the ability of a Darcy scale model to capture wormhole formation during the dissolution of a porous medium. J. Fluid Mech. **457**, 213–254 (2002)
3. Krishna, R., Taylor, R.: Multicomponent Mass Transfer. Wiley, New York (1993)
4. Luo, H., Quintard, M., Debenest, G., Laouafa, F., Dorai, F.: A diffuse interface model for dissolution processes with variable density. In: AICHE annual conference, Salt Lake City, USA (2010)
5. Luo et al. H., Quintard, M., Debenest, G., Laouafa, F.: The AMR technique for simulating dissolution processes with a diffuse interface model. In: Interpore conference, Computational Geosciences Bordeaux, **16**(4), 913–932 France (2011)